

# Norway's marine and terrestrial climate mapped with dynamical downscaling

Hilde Haakenstad

Thesis for the degree of Philosophiae Doctor (PhD)  
University of Bergen, Norway  
2022

UNIVERSITY OF BERGEN



# Norway's marine and terrestrial climate mapped with dynamical downscaling

Hilde Haakenstad



Thesis for the degree of Philosophiae Doctor (PhD)  
at the University of Bergen

Date of defense: 20.06.2022

© Copyright Hilde Haakenstad

The material in this publication is covered by the provisions of the Copyright Act.

Year: 2022

Title: Norway's marine and terrestrial climate mapped with dynamical downscaling

Name: Hilde Haakenstad

Print: Skipnes Kommunikasjon / University of Bergen

# Scientific environment

This study has been conducted at the Norwegian Meteorological Institute (MET Norway) at the Development Centre for Weather Forecasting (SUV) in Oslo and in the Division of Oceanography and Marine Meteorology (Bergen). The formal educational institution has been the Geophysical Institute, University of Bergen. During the PhD study, the author spent five weeks in Longyearbyen, Svalbard, where she participated at a course at the University Centre in Svalbard (UNIS). The work has been funded by the ERA4CS project WINDSURFER, the fjord-crossing project SVV-E39 of the Norwegian Public Roads Administration, the Stormrisk project (Research Council of Norway, grant no. 300608), Equinor, and the Norwegian Meteorological Institute. The author has been enrolled in the Norwegian Research School on Changing Climates in the coupled Earth System (CHESS).





# Acknowledgements

A great thanks to my main supervisor, Øyvind Breivik and the rest of my appreciated supervisor team; Harald Schyberg and Birgitte R. Furevik. Øyvind, thanks for always having time for discussions, to help me on the right track and for being a great mentor. Harald, thanks for your knowledge and discussions, and Birgitte, thanks for having good ideas and your advices. Thanks to my also very appreciated leader, Jørn Kristiansen, who let me do this PhD study, and also for help and support. A great thanks to my family; my husband, Håkan, for being supportive and patient and my daughters, Tuva and Linn for being encouraging. Thanks to the rest of my family and my friends for all support. Thanks to all my colleagues both in Bergen and Oslo who also made the work float easier. A special thanks to Ole Vignes for help to get the models run on new supercomputers. I also have to point out that I feel very privileged to have been given the opportunity to conduct the research for my PhD project at MET Norway. I gratefully acknowledge the financial support to this study from the ERA4CS WIND-SURFER project and the Norwegian Climate Service Centre (KSS). I also gratefully acknowledge the support from Equinor ASA who have co-funded the development of the NORA3 archive and the funding from the Norwegian Public Roads Administration through the project “E39 Coastal Highway Route”.

Hilde Haakenstad  
Oslo, 2022-03-25



# Abstract

Long-term numerical reconstructions on high spatial resolution of past weather are essential tools for studies of the local climate and climate extremes. The focus of this thesis has been to resolve the wind, precipitation, temperature and wave climate of Norway and Norwegian waters by high-resolution dynamical downscaling. Known as a hindcast archive, this is a well-known method to obtain local information based on more coarse atmospheric fields, typically reanalyses. Such reanalyses provide the state of the atmosphere as accurately as possible on meso-beta scale (20-200 km) whereas flow over complex terrain and along irregular coastlines requires resolutions on meso-gamma scale (2-20 km) or microscale (1 km or less) to be well represented. By using numerical weather prediction models tailored to high resolution modelling to downscale the reanalyses, we obtain far more detailed information than what a global reanalysis alone can give. In this thesis I focus on a convection-permitting non-hydrostatic downscaling and compare it to a hydrostatic hindcast as well as the host reanalysis. We see improvement in performance of the wind speed in both downscaling procedures, compared to the large scale reanalysis. However, extreme winds and precipitation are much better resolved by the convection-permitting non-hydrostatic model with better representation of convective features and the wind field in steep terrain and along irregular coastlines. We also find that the representation of polar lows is improved. Both atmospheric hindcasts are accompanied by wave hindcasts. We find that the wave field is sensitive to strong winds, and indeed the strongest winds (realistically) rendered by the non-hydrostatic NORA3 hindcast yields too strong wave growth. A new parameterization of the Charnock coefficient is explored and successfully used to generate a high-resolution wave hindcast based on the NORA3 atmospheric hindcast.





# Outline

This thesis consists of an introductory part (Chapters 1 to 3), four scientific papers (Chapter 4) and one appendix. Chapter 1 gives an introduction to hindcasting and the most important flow regimes of the atmosphere; both on large scale and also smaller local scale systems, together with the hydrological cycle. Chapter 1 also describes the technical information. Data and methods, as well as an introduction to the theory, are presented in chapter 2. This chapter also includes scientific achievements, further perspectives and conclusion. A brief summary of the papers is given in Chapter 3.

The papers included in this thesis are:

1. Haakenstad, H., Ø. Breivik, M. Reistad, and O. J. Aarnes (2020), NORA10EI: A revised regional atmosphere-wave hindcast for the North Sea, the Norwegian Sea and the Barents Sea, *International Journal of Climatology*, 40(10), DOI: 10.1002/joc.6458
2. Haakenstad, H., Ø. Breivik, B. R. Furevik, M. Reistad, P. Bohlinger, and O. J. Aarnes (2021), NORA3: A nonhydrostatic high-resolution hindcast of the North Sea, the Norwegian Sea, and the Barents Sea, *Journal of Applied Meteorology and Climatology*, 60(10), DOI: 10.1175/JAMC-D-21-0029.1
3. Haakenstad, H. and Ø. Breivik (2022). NORA3 Part II: Precipitation and temperature statistics in complex terrain modeled with a non-hydrostatic model, Submitted 2022-01-31 to *Journal of Applied Meteorology and Climatology* (under review)
4. Breivik, Ø, A. Carrasco, H. Haakenstad, M. Reistad, P. Bohlinger, O. J. Aarnes, B. R. Furevik, J.-R. Bidlot, J. Staneva, A. Behrens, and H. Günther (2022), The impact of a reduced high-wind Charnock parameter on wave growth with application to the North Sea, the Norwegian Sea and the Arctic Ocean, *Journal of Geophysical Research: Oceans*, 127(3), DOI: 10.1029/2021JC018196



# Contents

<b>Scientific environment</b>	<b>i</b>
<b>Acknowledgements</b>	<b>iii</b>
<b>Abstract</b>	<b>v</b>
<b>Outline</b>	<b>vii</b>
<b>1 Introduction</b>	<b>1</b>
1.1 Atmospheric circulation systems and hindcasting . . . . .	2
1.1.1 The general atmospheric circulation . . . . .	2
1.1.2 The hydrologic cycle . . . . .	3
1.1.3 Local climate . . . . .	4
1.1.4 Historical context . . . . .	5
1.1.5 Objectives . . . . .	6
1.1.6 Technical details . . . . .	6
<b>2 This study</b>	<b>9</b>
2.1 Scientific background . . . . .	9
2.1.1 HIRLAM . . . . .	10
2.1.2 HARMONIE-AROME . . . . .	10
2.1.3 The wave model WAM . . . . .	12
2.2 Scientific achievements . . . . .	12
2.3 Future perspectives and conclusions . . . . .	13
<b>3 Introduction to the papers</b>	<b>15</b>
<b>4 Scientific results</b>	<b>21</b>
<b>A Appendix</b>	<b>145</b>
A.1 Technical details of the supercomputer Nebula . . . . .	145
A.2 Calculation of vertical velocity in the hydrostatic model HIRLAM . . . . .	146
A.3 The fully compressible Euler equations and other relevant information . . . . .	146
A.4 HARMONIE-AROME configuration in NORA3 . . . . .	149
A.5 The choice of the NORSOK wind profile . . . . .	150
A.6 Abbreviations and relevant information . . . . .	155
A.7 List of symbols . . . . .	157



# Chapter 1

## Introduction

The local wind field is typically affected by small-scale features that violate the hydrostatic assumption usually applied in coarser atmospheric models. The vertical motions that are only inferred diagnostically in hydrostatic models also control the precipitation and the cloud formation. Wind and rainfall are perhaps the most important factors contributing to what is generally termed “dangerous weather” on the Norwegian mainland, with its multitude of valleys and fjords.

The Norwegian Meteorological Institute has as its foremost task to “help protect life and property” (<https://met.no/en>). High-resolution modelling of the atmosphere and the oceanic wave field is increasingly seen as essential ingredients in safety preparedness, for safe marine navigation and in the planning of maritime and coastal infrastructure. High-resolution wind and wave fields are of the utmost importance when mapping onshore and offshore wind energy (*Solbrekke et al., 2021*), and regarding climate change, it is further crucial to know the response in wind, waves and precipitation.

There is a long tradition for making reruns of past weather and the wave field, so called hindcasts, reanalyses or retrospective forecasts, to provide a full three-dimensional archive of the atmospheric wind field and the full sea state as accurately as possible. The optimal way to do this is to run a global reanalysis, using a consistent numerical weather prediction model with a fixed and comprehensive data assimilation scheme, utilizing quality-assured observations. In a reanalysis, the setup of the model and the data assimilation system is kept fixed during the whole run. Observations used in the data assimilation should also be as stable as possible over the period to keep the error statistics as stationary as possible. Impressive progress has been made in the generation of such reanalyses over the past decades. Here I mention the most well-known global reanalyses (see also Table 1.1). The American ones are the NCEP/NCAR reanalyses which consist of the 40-year reanalysis (*Kalnay et al., 1996*) (which was later extended), the Climate Forecast System Reanalysis, (CFSR, *Saha et al. (2010)* and CFSRv2, *Saha et al. (2014)*), and the Modern-Era Retrospective analysis for Research and Applications (MERRA, *Rienecker et al. (2011)* and MERRA-2, *Gelaro et al. (2017)*). The Japanese reanalyses are the JRA-25 (*Onogi et al., 2005*) and JRA-55 (*Kobayashi et al., 2015*). The European ECMWF series of reanalyses includes ERA-15 (*Gibson et al., 1997*), followed by ERA-40 (*Uppala et al., 2005*), ERA-Interim (*Dee et al., 2011*), and the latest, ERA5 (*Hersbach et al., 2020*). ECMWF has also produced several ocean reanalyses (ORAS3 (*Balmaseda et al., 2008*), ORAS4 (*Balmaseda et al., 2013*) and ORAS5 (*Zuo et al., 2018*)), atmospheric composition reanalyses (MACC

(*Inness et al.*, 2013), CAMS-Interim (*Flemming et al.*, 2017), CAMS (*Inness et al.*, 2019)) and centennial reanalyses and model-only climate integrations (ERA-20CM (*Hersbach et al.*, 2015), ERA20C (*Poli et al.*, 2016), CERA-20C (*Laloyaux et al.*, 2018) and CERA-SAT (*Schepers et al.*, 2018)).

Reanalysis	hres	nlev	period	m.version	assim.
NCEP/NCAR 40-yr	210 km	28L	1957–1996	1994	3D-Var
CFSR	38 km	64L	1979–2009	2004	3D-Var
MERRA	0.5°x0.666°	72L	1979–2010	2008	3D-Var
MERRA-2	0.5°x0.625°	72L	1979–	2014	3D-Var
JRA-25	110 km	40L	1979–2003	2004	3D-Var
JRA-55	55 km	60L	1958–2002	2009	4D-Var
ERA-15	125 km	31L	1979–1993	1995(Cy13r4)	OI
ERA-40	125 km	60L	1957–2002	2001(Cy23r4)	3D-Var
ERA-Interim	79 km	60L	1979–2019	2006(Cy31r2)	4D-Var
ERA5	31 km	137L	1950–	2016(Cy41r2)	4D-Var

Table 1.1: The table shows a list of the most commonly used global reanalyses. The columns indicate (from left to right) the name of the reanalysis, horizontal resolution, number of vertical levels, time period, model version and the assimilation method. If no end year is given, the reanalysis is still in production.

The generation of a reanalysis is expensive and cannot provide information on the resolution required to resolve typical topographical features in the coastal zone and in mountainous terrain. This is where dynamical downscaling, regional reforecasting or hindcasting as we also call it, comes into play. Regional hindcasts can, as they forgo data assimilation and rely instead on the boundary conditions and initial conditions of a global reanalysis, be run on much higher spatial resolution and are today capable of being run at resolutions past the hydrostatic limit. In this work we have produced two atmospheric hindcasts, one hydrostatic at approximately 10 km resolution, called NORA10EI (*Haakenstad et al.*, 2020), and one non-hydrostatic hindcast at 3 km resolution, called NORA3 (*Haakenstad and Breivik*, 2022; *Haakenstad et al.*, 2021). Both provide the full three-dimensional atmospheric state using a numerical weather prediction model to downscale a global reanalysis, ERA-Interim (*Dee et al.*, 2011) and ERA5 (*Hersbach et al.*, 2020), respectively. We have also generated two associated wave hindcasts on a resolution similar to that of their corresponding atmospheric hindcasts (*Breivik et al.*, 2022; *Haakenstad et al.*, 2020).

## 1.1 Atmospheric circulation systems and hindcasting

### 1.1.1 The general atmospheric circulation

The large scale atmospheric state follows the conservation laws of momentum, mass and energy, which determine the relationships among pressure, wind and temperature (*Holton*, 1992). The large scale atmospheric flow together with the ocean circulations work to redistribute the energy imbalance, which is set in motion due to the differential heating by the sun. The astronomical properties of the earth, as the rotation, the tilt

and the curvature, together with the atmospheric composition and the different albedo of the earth's surface, make the distinct part of the earth to be heated quite differently, setting up prevailing winds, weather patterns and jet streams.

In each hemisphere, the mean circulation is characterized by three meridional circulation cells extending through the whole troposphere; the Hadley, the Ferrel and the polar cell with the respectively inherent prevailing wind systems; the north-east trade winds, the westerlies and the polar easterlies (*Tarback and Lutgens, 1990*). The strongest wind speeds are found in jet streams, in the interface between the troposphere and the stratosphere, where thermal wind integrated through the troposphere has a maximum (*Holton, 1992*). This occurs in the separation zone between the Hadley cell and the Ferrel cell (the subtropical jet stream) and in the separation zone between the polar cell and the Ferrel cell (the polar jet stream). The polar jet do strongly affect the synoptic weather in our latitudes. Synoptic scale disturbances are typically growing in the region of jet maximum propagating downstream along storm tracks which roughly follows the jet stream (*Holton, 1992*). The polar jet normally runs directly from west to east with quick passing of weather systems, however, sometimes the steering flow of the jet can meander and a weather system can persist for longer time over a region. Whether this is happening more often in a warmer climate with Arctic amplification is expected (*Francis and Vavrus, 2012*). A change in the fundamental general circulation due to climate warming and sea ice retreat is also probable. Recently, a comprehensive study suggested a robust but weak change in the system (*Smith et al., 2022*). The work is based on extensive simulations from 16 different models contributing to the Polar Amplification Model Intercomparison Project (PAMIP) which is part of the sixth Coupled Model Intercomparison Project (CMIP6). The study shows an overall agreement between the different models of a robust equatorward shift, with a weakening of zonal winds around 55-65°N and a strengthening around 30-40°N, this is new information added to previous knowledge from the 5th IPCC report in which they found small or no changes in wind speed extremes across Europe, this conclusion was labeled with low confidence, while an increase in winter wind speed extremes over Central and Northern Europe was labeled medium confidence (*Kovats et al., 2014*).

### 1.1.2 The hydrologic cycle

The continuous circulation of water in the earth-atmosphere system is called the hydrologic cycle (*Peixoto and Oort, 1992*). Complex processes as precipitation, evaporation, transpiration, soil storage and dynamics are some of numerous processes that complete the cycle ([https://www.nwrfc.noaa.gov/info/water\\_cycle/hydrology.cgi](https://www.nwrfc.noaa.gov/info/water_cycle/hydrology.cgi)). The hydrologic cycle is a principal factor in the dynamics of climate.

The flow of water vapor in the atmosphere follows primarily the same planetary behaviour of the general circulation but in the lower half of the atmosphere since the water vapor pursue a weighting component for the wind field (*Peixoto and Oort, 1992*). Since the water vapor transport occurs mainly in the lower troposphere, it is clearly affected by the earth's topography. The western coast of Norway is typically experiencing large scale frontal precipitation related to north Atlantic extratropical cyclone track (*Hodges et al., 2011*). Here, the air is also experiencing orographic enhancement. These two combined effects typically results in extreme precipitation amounts



exceeding 2000 mm a year (*Heikkilä and Sorteberg, 2012*). The most extreme cases are often related to atmospheric rivers (AR) (*Azad and Sorteberg, 2017; Benedict et al., 2019; Zhu and Newell, 1994*). Even though the AR are mostly weak systems, they can also give rise to hazardous weather with heavy precipitation, flood and landslide risk. *Azad and Sorteberg (2017)* found that 55 out of 58 extreme daily precipitation events on the west coast of Norway were associated with atmospheric rivers. The southern coast of Norway and the eastern area typically experience extreme precipitation during summer time (*Dyrrdal et al., 2018*), related to convective precipitation. Heavy precipitation events are expected, with high confidence, to show a marked increase in the future (*IPCC-AR5 et al., 2014; Kovats et al., 2014*).

### 1.1.3 Local climate

Local wind systems are controlled by the general atmospheric circulation and the local forces which act on the flow. Inhomogeneous surface characteristics will affect the air above differently. Typical examples where the air flow is strongly influenced by abrupt changes from surface forcing are the shorelines and terrain with variations in vegetation and where lakes are present. The sea ice edge and the marginal ice zone represents a sharp temperature boundary between the cold ice and the relatively warm open ocean. However, the sea ice itself can also have strong gradients caused by leads and polynyas. These patches of open water strongly affect the temperature and the fluxes of latent and sensible heat to the air above, and the air above can also strongly affect the the different surface patches (*Wang et al., 2021*). High numerical resolution is therefore essential to realistically reproduce these interactions, together with relevant physics for the different surface characteristics and a coupling between the systems (*Vihma et al., 2014*). Along the shorelines, different heating processes can set up circulation patterns called land and sea breeze. Because of the smaller thermal conductivity and heat capacity of the soil compared to water, the temperature signal will remain in the upper part of the soil for a longer time. The land surface is therefore cooler than the ocean and lakes during night, and warmer during the day. This gives rise to land breeze during the night and sea breeze during the day (*Stull, 1988*).

Orography strongly controls the air flow. The speed and stability of the air flow upstream have a crucial influence on the flow downstream from an obstacle. Air can be forced to flow over the mountain, or it can be blocked or split to flow around the obstacle. Forced lifting of stably stratified air over a mountain barrier causes the development of buoyancy perturbations, and gravity waves can be formed (*Holton, 1992*). If the lifted air reaches a stagnation point aloft, wave breaking can occur and severe situations of clear air turbulence can arise and strong wind can blow down the lee slope of the barrier (*Durran, 1986; Sharman et al., 2012; Smith, 1989b*). Examples of strong down-slope wind events are the Foehn wind (*Elvidge and Renfrew, 2016*) in the Alps and the Bora (*Alpers et al., 2009*) in Croatia. Down-slope winds are also common features in Norway (*Sandvik and Harstveit, 2005*). Other orographically induced phenomena regarding wind, are gap winds (*Gaberšek and Durran, 2004*), valley winds (*Jackson and Steyn, 1994*), katabatic wind (*Parish and Cassano, 2003*), tip jets (*Reeve and Kolstad, 2011*) and mountain parallel jets (*Parish, 1982*).

### 1.1.4 Historical context

There has been a huge development in the modelling of marine wind and the oceanic wave field in the past three decades. The first reports of marine wind climatology were based on weather ship and oil platform measurements (*Eide et al.*, 1985; *Haug and Guddal*, 1981). The use of observations interpolated and extrapolated to obtain gridded maps was the standard method for creating wind climatologies in the 1990s. Important wind climatologies were provided from the European Wind Atlas (EWA) using the Wind Atlas analysis and application Programme (WaSP) (*Troen and Petersen*, 1989), and the Waves and Storms in the North Atlantic (WASA) project (WASA-group, 1998). The latter was started due to the challenges in interpreting inhomogeneous observations. A 40-year wave hindcast was produced on two different grids ( $1.5^\circ \times 1.5^\circ$  and  $0.5^\circ \times 0.75^\circ$ ) using wind forcing from kinematic estimates of surface winds (WASA-group, 1998). Their results showed a marked interdecadal variability with an intensification in storms and wave climate in the north east Atlantic in the past decades. However, the trend was not significant when compared with conditions earlier in the century, before 1930 (*Alexandersson et al.*, 1998). The main standards organization of Norway would as late as 2002 base their marine wind field on geostrophic winds, produced from surface pressure information taken from re-analyzed weather maps, calculated in cells of size  $75 \text{ km} \times 75 \text{ km}$  (*Harstveit*, 2005). Extreme value analyses were calculated by a Gumbel-Lieblein extreme value analysis.

At the Norwegian Meteorological Institute, reconstruction of the wind climate has since 2006 been based on numerical weather prediction models and downscaling of global reanalyses (*Haakenstad et al.*, 2020, 2021; *Reistad et al.*, 2011). The production of NORA10 (*Reistad et al.*, 2011) started in 2006 and provides today the longest Norwegian time series of the wind and wave fields on a 10 km grid for the North Sea, the Norwegian Sea and the Barents Sea, reaching back to September 1957. It is still in production. NORA10 runs the numerical weather prediction model HIRLAM (*Unden et al.*, 2002), forced with ERA-40 (*Uppala et al.*, 2005) between September 1957 and August 2002. After that operational analyses from ECMWF-IFS are used. The wave model WAM (*Günther et al.*, 1992; *Komen et al.*, 1994; *Wamdi-Group*, 1988) is forced with the down-scaled winds.

In the hindcast NORA10EI (*Haakenstad et al.*, 2020) (which is part of this thesis), ERA-Interim (*Dee et al.*, 2011) was instead used as forcing for the period 1979–2017. NORA10EI has the same configuration as NORA10. The use of ERA-Interim as forcing makes the errors in NORA10EI statistically more homogeneous.

Increased supercomputer resources have now allowed the hindcast archives to be built using more complex numerical weather prediction models with much higher spatial resolution. In 2018, the production of NORA3 (*Haakenstad et al.*, 2021) (which is also part of this thesis) started with the state-of-the-art numerical weather prediction model HARMONIE-AROME Cy 40h.1.2 (HA) (*Bengtsson et al.*, 2017; *Müller et al.*, 2017a; *Seity et al.*, 2011). The model is convection-permitting and non-hydrostatic. HARMONIE-AROME is forced with the latest reanalyses from ECMWF, called ERA5 (*Hersbach et al.*, 2020), and downscales the ERA5 to 3 km horizontal resolution. The wave field is produced with the wave model WAM Cy 4.7 with physics from *Ardhuin et al.* (2010).

Several other hindcasts have also been produced for the North Sea and the Nor-

wegian Sea. Except for the New European Wind Atlas (NEWA, <https://www.neweuropeanwindatlas.eu>) (Hahmann *et al.*, 2020; Hasager *et al.*, 2020), these hindcasts are typically focussed on smaller domains and cover considerably shorter periods. To be mentioned is the study by Byrkjedal and Kravik (2009) providing wind maps on  $4 \text{ km} \times 4 \text{ km}$  resolution for parts of the Norwegian Sea, based on a two-year simulation with the Weather Research and Forecasting model (WRF). Berge *et al.* (2009), in the NORSEWIND (NORthern SEas Wind Index Database) study, ran WRF with a fine nest of 2 km resolution. However, the run covers only four years, which is quite short in a climatological perspective. The work of Byrkjedal *et al.* (2015) is based on a five-year WRF simulation on  $4 \text{ km} \times 4 \text{ km}$  resolution for Scandinavia with the explicit objective to investigate the icing issue due to wind power at cold climates. Regarding the NEWA archive, despite running a 3 km horizontal resolution simulation with WRF over large parts of Europe, few parameters have been stored, and this archive is mostly aimed to provide wind maps in wind turbine heights. For the northern part of Norway, and the Arctic, a comprehensive regional reanalysis called CARRA (Køltzow *et al.*, 2022; Yang *et al.*, 2020) has recently been completed. However, CARRA is not covering the full Norwegian Sea and none of the North Sea.

## 1.1.5 Objectives

The objectives of this PhD project have been to

1. investigate the marine and terrestrial climate of Norway
2. investigate the effect of forcing data on trends in a regional hindcast
3. investigate the effect of increased resolution and the use of a convection-permitting non-hydrostatic numerical weather prediction model on 3 km resolution on the most important parameters for dangerous weather in Norway (wind and precipitation)

## 1.1.6 Technical details

The NORA10EI configuration of HIRLAM was set up on the Norwegian supercomputer vilje.ntnu.no in 2014. (The configuration was a copy of the NORA10 configuration of HIRLAM, which had been run for several years.) In 2017 production was moved to one of the Swedish National Supercomputer Centre (NSC) supercomputers, elvis.nsc.liu.se (Elvis), where the hindcast was completed in 2018. The 39-year hindcast used just over 200,000 CPU hours.

At the end of 2017, the final setup of NORA3 was determined through a number of tests. The plans started with a 2.5 km grid which was a bit smaller than the final grid. However, a desire for a larger domain led us to stretching it further north. This also meant we could not go for the 2.5 km resolution both because of computer resources and storage capacity. We finally decided on the 3 km grid shown together with the NORA10EI grid in Fig. 1.1. The grid is in the Lambert conformal conic projection with 900 longitudinal grid points and 1500 latitudinal grid points. The central meridian is  $42^\circ\text{W}$  and the central latitude is  $66.3^\circ\text{N}$ . The standard parallel (with the unit scale) is  $66.3^\circ\text{N}$ .

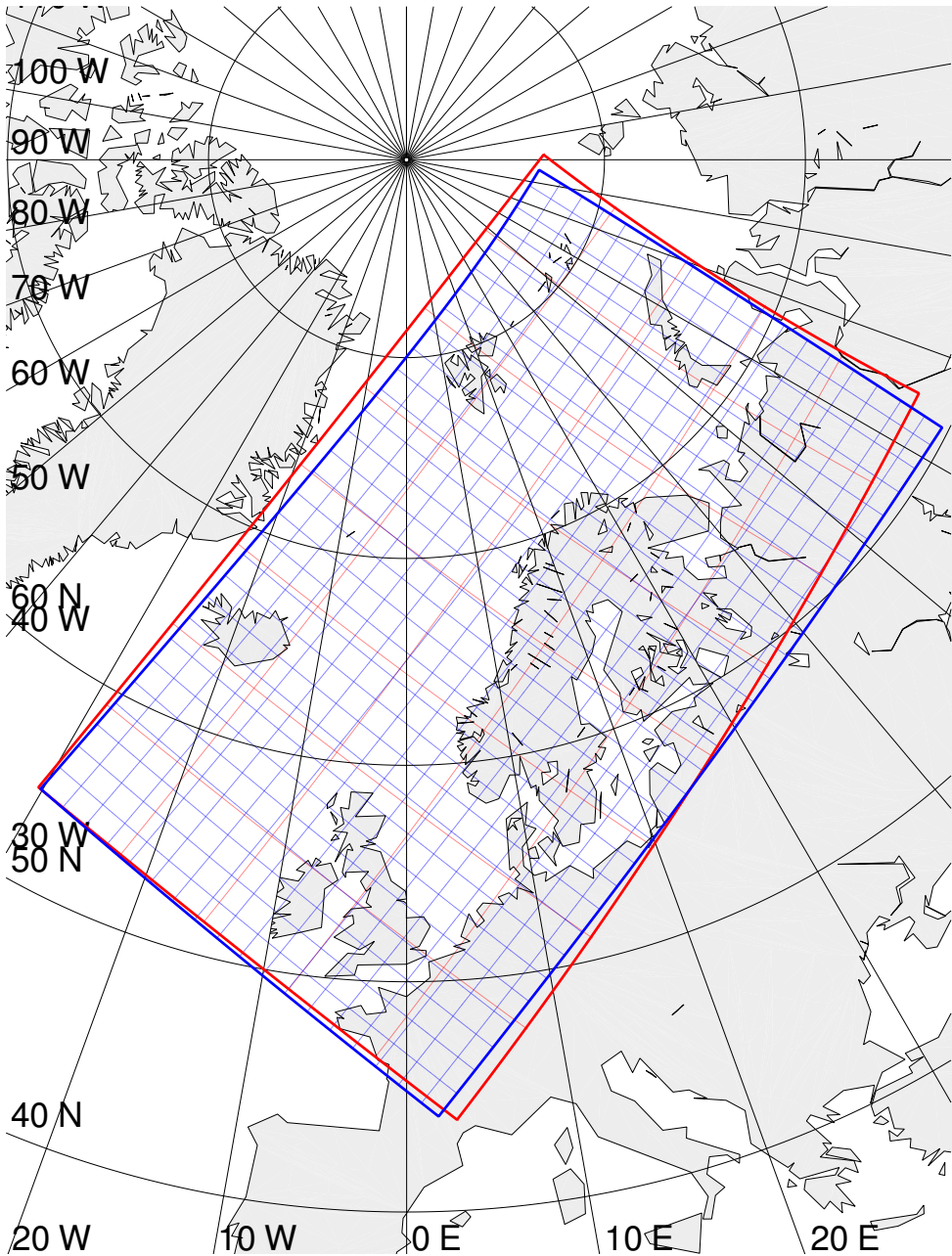


Figure 1.1: Figure showing the domain of NORA10EI in red and the domain of NORA3 in blue. Every 50th grid point is shown.

The 33-year period, 1989–2021, of NORA3 data, requires more than 200 TB of storage (6.2 TB per year). The hindcast has used 21.5 million CPU hours. This is approximately 125 times the NORA10EI consumption. The time step used in NORA3 has been 60 s. (In rare cases of instability problems it has been reduced to 30 s, but this shorter time step has been used for less than 300 cycles). The final NORA3 configuration was in 2018 installed at one of NSC’s supercomputers, `elvis.nsc.liu.se` (Elvis), in Linköping in Sweden. The configuration was later moved to a new supercomputer, `nebula.nsc.liu.se` (Nebula) in the beginning of 2019. Nebula is part of group of three supercomputers (Stratus, Cirrus and Nebula) used by the Meteorological co-operation on operational numerical weather prediction in the Nordic countries (MetCoOp, see *Müller et al.* 2017b). More details about Nebula are given in Table A.1.

# Chapter 2

## This study

### 2.1 Scientific background

Collaboration and sharing of scientific results has a long tradition in meteorology (Kalnay, 2003a) and started already with the international cooperation in part initiated by Vilhelm Bjerknes (Eliassen, 1982). In 1985, the HIRLAM consortium was established by the Nordic countries with the goal of providing short range regional NWP models and expertise to increase public safety ([hirlam.org](http://hirlam.org)). HIRLAM was the first consortium on limited area modelling in Europe. The collaboration between the Nordic countries was very successful and the HIRLAM consortium was gradually extended. In 2005 an agreement between the two consortia HIRLAM and ALADIN was signed “to provide the ALADIN and the HIRLAM Members with a state-of-the-art NWP-model for Short and Very Short Range Forecasting including Nowcasting, for both Research and Development activities and Operational usage” (<https://www.umr-cnrm.fr/aladin>). (ALADIN started as a collaboration between Météo-France and five Central and Eastern European countries.) Later “Limited Area modeling in Central Europe” (LACE) was also included in the collaboration and the consortium is now called “A Consortium for CONvection-scale modelling Research and Development” (ACCORD), the largest international weather prediction research consortium in the world. The goal of the ACCORD consortium is to “broaden and deepen the research collaboration on developing advanced high-resolution weather prediction capability for local areas. It will develop world-leading weather forecasting systems to provide the best possible support to society, based on knowledge leading research and pioneering super-computing technology” (Norman, 2021).

It is important to mention that the consortia, HIRLAM, HIRLAM-ALADIN and ACCORD, all have close ties to the European Centre for Medium-Range Weather Forecasts (ECMWF), one of the world’s leading meteorological centers for global forecasting.

In this PhD project I have taken advantage of the work carried out by the first two consortia as I have used the hydrostatic numerical weather prediction model, HIRLAM, (Uden *et al.* (2002)) and the convection-permitting non-hydrostatic (CP-NH) model, HARMONIE-AROME, (Bengtsson *et al.* (2017); Seity *et al.* (2011)). The two NWP models will be described in the next section.

### 2.1.1 HIRLAM

HIRLAM is the High-Resolution Limited Area Model (*Unden et al., 2002*), provided by the HIRLAM community. HIRLAM v. 6.4.2 was the operational version at MET Norway in 2006. HIRLAM is a hydrostatic model, and it solves the primitive equations by semi-implicit semi-Lagrangian discretization (*McDonald and Haugen, 1993*). It uses a hybrid (terrain-following and pressure-dependent) coordinate,  $\eta$ , in the vertical (*Laprise, 1992; Simmons and Burridge, 1981*) defined as

$$p(x, y, \eta, t) = A(\eta) + B(\eta)p_s(x, y, t). \quad (2.1)$$

Here  $p$  is the hydrostatic pressure, the subscript “s” denotes surface. The three-dimensional prognostic variables are the two horizontal wind components, temperature, specific humidity and cloud water. The geopotential and pressure are defined at half-levels, while wind, temperature, and specific humidity are defined at full levels. In the horizontal, an Arakawa C grid is employed (*Mesinger and Arakawa, 1976*). Here the wind components are staggered with respect to temperature, specific humidity and cloud water content. Vertical velocity is calculated diagnostically (see Appendix A.1). In our setup for NORA10EI (and NORA10 before that), HIRLAM was configured to run forecasts of nine hours four times a day. (Only the last six hours are kept.) The time step of the integrations is 240 s. NORA10EI runs on a rotated spherical grid with the South Pole positioned at 22° S, 40° W. The domain is resolved by 248 longitudinal grid points and 400 latitudinal grid points with 0.1° resolution. The model has 40 vertical levels, spaced more densely near the surface. Except for the very first cycle of the hindcast, the surface parameters are taken from the previous forecast at the beginning of every cycle, thus retaining the mesoscale features from the high resolution run, while in the upper atmosphere the model is forced with large-scale ERA-Interim fields (*Dee et al., 2011*) at the beginning of every cycle (6 hourly), following the method of *Yang (2005)*. HIRLAM runs with the “Soft TRAnSition Condensation” (STRACO) condensation scheme with convection based on *Kuo (1965, 1974)* and microphysics based on *Sundqvist (1993)*. Radiation follows the Savijärvi scheme (*Sass et al., 1994; Wyser et al., 1999*). HIRLAM runs the “Mosaic of tiles” land surface model (*Avisar and Pielke, 1989*), and distinguishes between five different surface types; sea/lake, ice, forest, low vegetation, and bare ground. Each grid square represent one or more of these surface types. For the three land surface types, “Interaction Soil Biosphere Atmosphere” (ISBA) surface layer physics (*Noilhan and Planton, 1989*) is used. The ISBA scheme divides the soil layers into two layers, with the first layer having a thickness of 1 cm and the second layer extending to a depth of 1 m. In these two layers, prognostic equations for temperature and soil water is calculated. Gravity wave drag is parameterized according to *Cordeneanu and Geleyn (1998); Rontu et al. (2002)*.

### 2.1.2 HARMONIE-AROME

Going below a spatial scale of 10 km requires the inclusion of nonhydrostatic effects (*Laprise, 1992*). This is taken care of in the HARMONIE-AROME model which is designed for resolutions of less than 3 km (*Termonia et al., 2018*). The dynamics of HARMONIE-AROME are described by *Bénard et al. (2010)*. The method is based

on *Bubnová et al.* (1995), but with a reformulation of the non-hydrostatic prognostic variables. The new pressure prognostic variable is defined as

$$\hat{q} = \ln \frac{p}{\pi}, \quad (2.2)$$

and the new vertical momentum prognostic variable is defined as

$$\mathbf{d} = -g \frac{p}{(\partial\pi/\partial\eta)R_a T} \frac{\partial w}{\partial\eta} + \frac{p}{(\partial\pi/\partial\eta)RT} \nabla\phi \cdot \left( \frac{\partial\mathbf{V}}{\partial\eta} \right). \quad (2.3)$$

Here,  $\hat{q}$  is the NH pressure deviation,  $p$  is the actual pressure and  $\pi$  is hydrostatic pressure,  $\mathbf{d}$  is the vertical momentum formulation,  $g = 9.80665 \text{ m s}^{-2}$  is the acceleration of gravity,  $\eta$  is the vertical coordinate, and  $R_a = 287$  is the gas constant for dry air.

The non-hydrostatic variables ( $\hat{q}$  and  $\mathbf{d}$ ) constitute together with ten other variables the set of prognostic quantities. These are the horizontal wind, temperature, specific water vapor content, the five hydrometeors rain, snow, graupel, cloud droplets and ice crystals, and the turbulent kinetic energy.

The model integrations use the Semi-Lagrangian (SL) advection scheme without horizontal staggering. Stable time integrations are assured through the stable-extrapolation two-time-level scheme (SETTLS) (*Hortal*, 2002). (The SETTLS scheme is described in Appendix A.3). HARMONIE-AROME is a spectral model and most of the prognostic variables have a spectral description based on a double Fourier decomposition (*ECMWF*, 2015).

The boundary forcing procedure is based on *Radnoti* (1995). The model domain is divided into a central area, an intermediate zone and an extension zone, and spline functions are used to make the fields periodic in the extension zone (*Termonia et al.*, 2018). (The method is described in Appendix A.3.)

Deep convection is assumed resolved by the model dynamics while shallow convection is parameterized as a sub-grid process. HARMONIE-AROME uses the boundary layer “Eddy Diffusivity Mass Flux” (EDMF-M) scheme with a dual mass flux framework (*de Rooy and Siebesma*, 2010; *Neggers et al.*, 2009; *Siebesma et al.*, 2007; *Soares et al.*, 2004). The EDMF-M scheme parameterizes the shallow convection and provides gradual transitions between the shallow convective cloud layer and the sub-cloud mixed layer. The eddy diffusivity approach parameterizes small eddies in the dry and stratus/stratocumulus boundary layers while the mass-flux approach allows non-local transport due to thermals (*Siebesma et al.*, 2007; *Soares et al.*, 2004). The framework is dual in the way that it represents both the dry updraft, but also the moist updraft (*Neggers et al.*, 2009) and soft triggering of moist convective flux takes place throughout the boundary layer. The reproduction of gradual transitions to and from shallow cumulus convection is included, and in this way integrates the representation of the turbulent mixed layer and the conditionally unstable cloud layer, which here is shown to suit the 3 km horizontal resolution grid used in NORA3 well.

The boundary layer moist mixing scheme is based on the “HARmonie with RAcmo TURbulence” (HARATU) turbulence scheme (*Lenderink and Holtslag*, 2004; *van Meijgaard et al.*, 2012), where the mixing length scale of the prognostic turbulent kinetic energy is diagnostically calculated based on the vertically integrated stability. Gravity wave drag is parameterized according to *Catry et al.* (2008).



For details of the equations used in the dynamical kernel of HARMONIE-AROME, see Appendix A.3 and a complete list of physical parameterizations is given in Appendix A.4. The model cycle proceeds following *Termonia et al.* (2018). First an inverse fast bi-Fourier transformation of the prognostic variables to grid point space is performed. Physical contributions are calculated in grid point space, and the tendencies of the variables are calculated. Explicit grid-point dynamics of the nonlinear terms are computed and added to the total tendencies of the variables. The spatially interpolated tendencies are then added to the model state. After the lateral boundary coupling, a fast bi-Fourier transformation takes the variables back to spectral space. Finally, the semi-implicit Helmholtz equation is solved in spectral space.

HAROMNIE-AROME performs well with high-resolution nonhydrostatic dynamics and the convection permitting of large scale convection, treating the five hydrometeors (rain, snow, graupel, cloud droplets and ice crystals) as prognostic variables (*Müller et al.*, 2017b). In particular, as shown by *Haakenstad and Breivik* (2022), precipitation is greatly improved in complex terrain.

### 2.1.3 The wave model WAM

WAM Cycle 4 (*Günther et al.*, 1992; *Komen et al.*, 1994; *Wamdi-Group*, 1988) was implemented on the same grid as the atmosphere model, nested inside a 50 km resolution WAM model covering most of the North Atlantic. A nesting procedure allowing arbitrary model orientation was used (*Breivik et al.*, 2009). The model runs with 15° directional bins and 25 logarithmically spaced frequency bins from 0.0420 to 0.4137 Hz. For the NORA3 wave hindcast (*Breivik et al.*, 2022), a recently developed version of WAM, Cycle 4.7, was utilized. The model employs a modified version of the wave physics proposed by *Arduin et al.* (2010) together with a modified Charnock parameter to reduce wave growth in strong winds and an obstruction scheme to handle fine-scale coastal features.

## 2.2 Scientific achievements

The hindcasts presented here are to our knowledge the only archives that comprehensively cover the atmospheric and wave conditions in the Norwegian Sea, the Barents Sea and the North Sea as well as the Norwegian mainland and Svalbard at very high resolution.

Scarcity of long reliable time series prevents assessment of the long-term probability of weather windows or threshold levels of wind and waves required in fine resolution both in space and time. A convection-permitting (CP) non-hydrostatic (NH) numerical weather prediction (NWP) model on 3 km resolution is a huge step forward in terms of model performance in complex topography, both for the coastline and in mountainous areas, compared to the coarser hydrostatic 10 km model. The high resolution CP-NH models are particularly useful for convection, nonlinear mountain wave modelling and flow patterns in complex terrain, but it turns out that the CP-NH model used here, does also improve the wind speed in synoptic wind storms, both over land and over sea.

The two hindcasts produced in the PhD project are called NORA10EI (*Haakenstad et al.*, 2020) and NORA3 (*Breivik et al.*, 2022; *Haakenstad and Breivik*, 2022; *Haak-*

*enstad et al.*, 2021). The first hindcast was generated using a hydrostatic NWP model with parameterized convection (NORA10EI). The second hindcast was produced using a non-hydrostatic NWP model where large-scale convection is permitted (NORA3).

The motivation to run NORA10EI was to investigate whether the gradually improving quality of the ECMWF analyses induces an artificial trend in the NORA10 hindcast. We therefore ran a hindcast with boundary and initial conditions that have errors that are statistically as stationary as we could get (by using the reanalysis ERA-Interim, *Dee et al.* 2011). The setup is otherwise identical to NORA10. This allowed us to evaluate the effect of the changing forcing on the resulting wind and wave fields of NORA10. We found that there is a very high degree of stationarity in the NORA10 error statistics, and that the changing forcing does not affect the model performance significantly.

The results in this study reveal that NORA10EI performs well in terms of wind in marine areas, and that it is not strictly necessary to go to higher resolution than 10 km to realistically model the mean marine wind conditions. However, by solving the non-hydrostatic equations, and including the hydrometeors as prognostic variables, also the feedback of small scale processes on the air flow are included in a consistent manner, (although this benefit is of course limited by the spatial resolution, which is still relatively coarse related to small scale features).

Close to the coast, the use of a model with higher resolution and a non-hydrostatic convection-permitting scheme yields great improvement in the wind field. The same is seen in mountainous regions. Also in large scale extremes do we find that the wind speed distribution in NORA3, both in the marine and terrestrial domain, compare better than the coarser hydrostatic NORA10EI integration. Mesoscale extremes such as polar lows are also better captured by NORA3 with more realistic and detailed structures. Finally, there is an exceptional improvement in the performance of daily precipitation by NORA3 compared to the hydrostatic runs in the whole terrestrial domain (*Haakenstad and Breivik*, 2022). The 2 m temperature is also improved in the CP-NH model. (The NORA10EI and NORA3 data are archived on MET Norway's publicly accessible Thredds server: <https://thredds.met.no>.)

## 2.3 Future perspectives and conclusions

We see great improvement in wind, precipitation and also temperature in the upgrade from a 10 km hindcast to a 3 km hindcast using the CP-NH HARMONIE-AROME model. These climatological fields can be used in dimensioning offshore and onshore installations, and in climate studies. However, it is always important to compare the model results to observations, since the results will have discrepancies related to inevitable model shortcomings (*de Rooy et al.*, 2022) and the difficulties of precisely capturing the initial or boundary conditions (*Degrauwe et al.*, 2012). The wave model WAM Cy 4.7, when run with the new reduction of the high-wind drag, also shows very good performance when forced with the winds from NORA3. The improvement is particularly pronounced in the coastal zone, where the higher-resolution winds together with the more detailed coastline allows much more detailed modelling of the wave field (*Breivik et al.*, 2022).

Some configurations will demand a grid of even finer resolution than NORA3 to realistically model the salient features of, e.g., the wind field in steep coastal terrain

(Christakos *et al.*, 2020). Running the HARMONIE-AROME model on higher resolution than 3 km has not been affordable in this project. With the stochastic behavior of the weather and wave field, showing great year-to-year differences, especially in the extremes, it was never an option to run only a few years with a higher resolution.

If affordable, the HARMONIE-AROME model could be run on even higher resolution, (recommended with the use of the “Horizontal Explicit Vertical Implicit” (HEVI) or split-explicit scheme (Lock *et al.*, 2014)). This could further improve modelling of local topographic effects. This has however not been feasible in this study, but could be possible in the future. (A 1.3 km resolution model setup for France is described by Brousseau *et al.* (2016), and in the Year of Polar Prediction (YOPP) project, a five days simulation was performed on 500 m horizontal resolution for the Svalbard Archipelago (Valkonen *et al.*, 2020) with promising results).

Large eddy simulation (LES) models (Maronga *et al.*, 2020) are also an alternative on metre scales, but with the present state-of-the-art these models and their slightly coarser relatives, the computational fluid dynamics models (see, e.g., OpenFOAM, Jasak *et al.* 2007), can only be run for small domains and short sequences with very limited atmospheric physics. As such, they are useful in combination with atmospheric models, but in the foreseeable future cannot be expected to replace them.

It would also be of interest to run with data assimilation, e.g., a three- or four-dimensional variational scheme (3D-VAR or 4D-VAR, see, e.g., Daley 1991; Kalnay 2003b). Using a 4D-VAR scheme, the integration would have been continuously corrected throughout the assimilation window. This could reduce differences in performance between forecast steps (Rabier *et al.*, 2000). However, the implementation of 4D-VAR will require considerable technical development (Rabier *et al.*, 2000). In the CARRA project, the HARMONIE-AROME model was used with a 3D-VAR scheme running three-hourly update sequences to produce a reanalysis covering an Arctic domain with 2.5 km resolution (Køltzow *et al.*, 2022; Yang *et al.*, 2020). However, the reanalysis was running without accounting for model, initial and lateral boundary condition errors. A common way to include this is to run an ensemble in which for example different parameterization schemes are used and/or small perturbations are added to the initial or boundary conditions (Frogner *et al.*, 2019). However, in an ensemble procedure it is necessary to have knowledge about the different errors affecting the forecasts, which is challenging. This subject is touched upon by Frogner *et al.* (2019b) but is here left for future studies.

Finally, the next obvious step for regional atmosphere-wave hindcasts is to couple the two models. This may have beneficial effects on both the wind field and the wave field. This has been done for a long time in the global forecast model of ECMWF (Janssen, 2004). Whether the impact will be important on a resolution of 3 km is an open question, but experiments are ongoing (Thomas *et al.*, 2021) at MET Norway where coupled atmosphere-wave forecasts are carried out experimentally. The results will give an indication of whether this approach is viable and affordable.

# Chapter 3

## Introduction to the papers

### **Paper I: NORA10EI: A revised regional atmosphere-wave hindcast for the North Sea, the Norwegian Sea and the Barents Sea**

*H. Haakenstad, Ø. Breivik, M. Reistad and O. J. Aarnes (2020), International Journal of Climatology, 40(10)*

Paper I investigates the outcome of different boundary forcings in the dynamical downscaling with the hydrostatic numerical weather prediction model HIRLAM (*Unden et al.*, 2002) and the wave model WAM (*Günther et al.*, 1992; *Komen et al.*, 1994). A 38-year hindcast, called the revised NORwegian hindcast Archive (NORA10EI), has been produced with forcing of the atmosphere and wave model from ERA-Interim (*Dee et al.*, 2011). This hindcast has been compared with its predecessor, the NORwegian hindcast Archive (NORA10, see *Reistad et al.* 2011). Both have a horizontal resolution of approximately 10 km and the same domain covering the North Sea the Norwegian Sea and the Barents Sea (see the red domain in Fig. 1.1). NORA10 is a long hindcast, extending back in time to September 1957 and is still regularly updated. This more than 60-year-long hindcast has been forced with different forcing products, first ERA-40 (*Uppala et al.*, 2005) until August 2002. From September 2002, ECMWF operational analyses were used because ERA-40 stopped in August 2002. The ECMWF operational analyses used after the ERA-40 period are neither fixed to one model configuration nor one fixed resolution, but rather consist of the daily analyses and forecasts archived over a number of different model updates. These updates involve improvements in data assimilation, dynamics and physics. This makes it important to assess the trend of the hindcast, and in particular whether these model updates to the host analysis have induced a spurious, unphysical trend. NORA10EI therefore has the exact same setup as NORA10, but instead uses ERA-Interim as its host reanalysis. This allows an evaluation of the stationarity of the NORA10 statistics. The results show only very small differences in the statistics and trends of the mean and upper percentiles of the 10-m wind speed of NORA10 compared with NORA10EI. NORA10EI performs slightly better than NORA10 in the ERA-40 period, since ERA-Interim outperforms ERA-40. By the same token, the operational ECMWF analyses outperform ERA-Interim and NORA10 thus performs slightly better than NORA10EI after 2006. The years 2002–2006 represent a transitional period where NORA10EI and NORA10 perform very similarly. In this period, NORA10 is forced with operational analyses of

high resolution, but with a model configuration which shows not the same performance as the model configuration of ERA-Interim, which is the operational cycle of 2006. However, despite the abrupt changes in forcing of NORA10 after August 2002, we do not see any statistically significant changes in the mean or in the upper percentiles of the 10-m wind speed of NORA10. In addition to the appraisal of NORA10's wind and wave performance, we also looked at trends in 10-m wind speed in four different domains; the southern (1) and northern (2) part of the North Sea, the main part of the Norwegian Sea (2) and the northern part (4) of the Norwegian Sea. While the reanalyses are affected by updates in the observation network (*Aarnes et al., 2015*), the hindcasts are in fact more robust because the impact of the assimilation scheme is dampened as the reanalyses provide only boundary and initial conditions for the high-resolution forecast, and the high-resolution forecasts are running without its own assimilation (see Fig. 2 and Table 5 in this paper). The results from the trend analysis do not show any significant trend in 10-m wind speed in NORA10EI, although the results indicate a weak negative trend in the mean and the 95 percentile in all the four domains, and also in the 99 percentile, except for the North Sea, domain 1 and 2, which shows a weak positive trend in the 99 percentile. (In the analysis, we used measurements from offshore installations. The handling of the measurements is described in Appendix A.5.)

## **Paper II: NORA3: A non-hydrostatic high-resolution hindcast of the North Sea, the Norwegian Sea, and the Barents Sea**

*H. Haakenstad, Ø. Breivik, B. R. Furevik, M. Reistad, P. Bohlinger and O. J. Aarnes (2021), Journal of Applied Meteorology and Climatology, 60(10)*

Paper II investigates the 10-m wind speed performance of the non-hydrostatic convection-permitting hindcast, NORA3. The hindcast represents a major upgrade compared to NORA10 as it uses the version of the non-hydrostatic numerical prediction model HARMONIE-AROME (*Bengtsson et al., 2017; Seity et al., 2011*) in operational use at MET Norway at the time when production started in the beginning of 2018. A relatively detailed description of the model configuration is given in the paper. In addition to a much finer grid with a horizontal resolution of 3 km, the model is also quite a lot more advanced than HIRLAM. It calculates the fully compressible Euler equations, using twelve prognostic three-dimensional variables where two of these variables are non-hydrostatic and related to pressure and vertical momentum. Five are hydrometeors, thus permitting convection. Its higher horizontal and vertical resolution and the shorter time step required alone make it almost 90 times as computationally demanding as NORA10. Added to this is the increased complexity of the physics. In total, HARMONIE-AROME-model is about 125 times more costly to run. The boundary and initial conditions are taken from ECMWF's most recent reanalysis, ERA5 (*Hersbach et al., 2020*). The validation of NORA3 is presented in the form of a general evaluation against reference and maritime stations with time series of mean error, mean absolute error and the activity ratio (the ratio between the standard deviation of the hindcast wind speed and the observations). After that a categorical validation in the form of the equitable threat score (ETS) score is presented for maritime, coastal, mountain and Arctic stations. The categorical validation is followed by a spatial comparison

between NORA3 and ERA5 and a look at the percentile performance. After that follows a study of the ability to capture and model polar lows, where one case is described in detail. The last section summarises the major wind storms in the hindcast period. In view of the far more realistic topography in NORA3, and the inherent potential for a much more realistic description of the three dimensional air flow in complex terrain, it is not surprising that NORA3 shows great improvement in mountainous areas and in the coastal zone, compared to ERA5 and NORA10. For maritime stations, NORA3 also performs very well. However, ERA5 displays higher correlation and lower mean absolute errors, despite a substantial negative bias, a trait also found in the earlier ECMWF reanalyses ERA-40 and ERA-Interim (*Haakenstad et al.*, 2020). The activity ratio is greatly improved in NORA3 compared to ERA5. This applies to all station classes, including the maritime stations. This means that NORA3 has the wind speed variability which best matches the observed variance. NORA3 also reproduces polar lows with much more detailed structures compared with NORA10 and ERA5. In the case presented in the paper, both NORA3 and ERA5 show a low-pressure track which roughly follows the observations. However, ERA5 shows too weak maximum winds without the same sharp structures found in NORA3. NORA3 also captures the characteristic small convective cells in the wake of the polar low, in good qualitative agreement with the satellite image found in the STARS database (*Furevik et al.*, 2015). These small convective cells are absent in ERA5 and NORA10, highlighting the added value of a convection-permitting model. (The influence of explicit deep convection is also pointed out by *Hallerstig et al.* (2021), where they found a more realistic convective cell representation compared with the parameterized deep convection case running ECMWF-IFS experimentally on 5 km resolution). The extra-tropical wind storms described in Section 3-d-2 shows that NORA3 also captures the maximum wind speed of wind storms better than NORA10 and ERA5. (Also in this analysis, measurements from offshore installations were used. For a closer look at the method, see Appendix A.5.

### **Paper III: NORA3 Part II: Precipitation and temperature statistics in complex terrain modeled with a non-hydrostatic model**

*H. Haakenstad and Ø. Breivik (2022), Submitted to Journal of Applied Meteorology and Climatology*

Paper III investigates the 2-m temperature and the daily precipitation performance of the NORA3 hindcast. The atmospheric three-dimensional state is archived with three-hourly resolution, whereas several surface and two-dimensional variables are archived with hourly resolution (in addition to wind at selected levels meant for studies of wind power generation, see *Solbrekke et al.* 2021). In addition, all the wave parameters from WAM are archived at hourly resolution. It is of interest to see how the 2-m temperature and the daily precipitation performs and compares to the reanalysis, ERA5. In a period with rapid climate change, precipitation extremes are a major concern (*IPCC-AR5 et al.*, 2014). Given NORA3's convection-permitting non-hydrostatic scheme and the use of the most recent ECMWF reanalysis for boundary and initial conditions, we expected to see an improvement in the performance of these variables, including a better representation of their extreme values. In the study we used daily precipitation from

NORA3 calculated as aggregated hourly values (taken at lead times 4 to 9 hours of the four daily forecast cycles starting at 00, 06, 12 and 18 UTC). Boundary and initial conditions were taken from lead times 7 to 18 hours from the two daily cycles of ERA5 (initialized at 06 and 18 UTC). The study shows much improved performance in daily precipitation and also in 2-m temperature of NORA3, compared to ERA5. The extremes of daily precipitation show very little bias up to the 99.9 percentile. In sum, the findings from the second paper and this paper, that NORA3 performs better than ERA5 in terms of 2-m temperature, daily precipitation and 10-m wind speed, demonstrates that NORA3 is well suited for studies of extreme events where complex coastlines and steep topography affect the passage of extratropical cyclones. By permitting deep convection, a more representative water cycle is achieved. The non-hydrostatic scheme also yields more realistic vertical accelerations, whereas the higher resolution and the more complex surface scheme (SURFEX, see *Masson et al. 2013*) generates more realistic flux exchange between the surface and the atmosphere. This all adds up to a more realistic climatology of wind, precipitation and temperature well suited for mesoscale analyses.

The main findings of the paper are that in terms of temperature, NORA3 and ERA5 in general show good agreement with observations, but an underestimation of the 2-m temperature is clear in both archives. The underestimation is greater in ERA5 than in NORA3, and both data sets show the strongest underestimation in spring. The ETS shows that NORA3 performs well for all temperatures above  $-10^{\circ}\text{C}$ , but is outperformed by ERA5 for very low temperatures (below  $-15^{\circ}\text{C}$ , typically below the first percentile). NORA3 has by far the best performance for the 99 percentile. NORA3 performs very well in terms of daily precipitation and has the highest correlation to the observed daily precipitation. NORA3 also shows the best scores of the 99 percentile, the 75 percentile, and the root mean square error for daily precipitation. It also has the best monthly mean value throughout the year, and the best ETS score over all precipitation categories.

#### **Paper IV: NORA3: A high-resolution wave hindcast for the North Sea, the Norwegian Sea and the Barents Sea with a modified Charnock coefficient for high wind situations**

*Ø. Breivik, A. Currasco, H. Haakenstad, M. Reistad, P. Bohlinger, O. J. Aarnes, B. R. Furevik, J.-R. Bidlot, J. Staneva, A. Behrens and H. Günther (2022), Journal of Geophysical Research: Oceans, 127(3), DOI: 10.1029/2021JC018196*

Due to the high sensitivity of wave growth in strong winds, Paper IV investigated a new modification of the Charnock parameter and with it a new approach to the determination of the roughness length over ocean waves. Charnock (*Charnock, 1955*) assumed a relationship between the wind stress and the roughness length itself

$$z_0 = \alpha u_*^2 / g. \quad (3.1)$$

Here,  $\alpha$  is a non-dimensional parameter, traditionally assumed constant, but here allowed to vary with the wind speed. In this study, a hindcast of the wave climate for the Norwegian Sea, the North Sea and the Arctic Ocean is presented, covering the years

---

1998 to 2020. The archive has been produced by running a third generation spectral wave model, WAM Cycle 4.7 (*ECMWF*, 2020; *Janssen*, 2004; *Komen et al.*, 1994; *Wamdi-Group*, 1988). Lower resolution wind fields from ERA5 have been used as forcing in the outer part of the domain, while high resolution winds from NORA3 have been used in the inner domain. Linear interpolation is performed in a limited transition zone inside the smaller area to achieve dynamical consistency in the wind forcing field. The growth of waves under extreme winds have been a topic of considerable interest over the past two decades (*Donelan et al.*, 2004; *Holthuijsen et al.*, 2012; *Powell et al.*, 2003; *Zweers et al.*, 2010). There is increasing evidence of a saturation and perhaps even a reduction of the drag under hurricane-strength winds. When waves are young and growing, the drag becomes large and in a stand-alone wave model, lacking the feedback with the atmospheric model which could have lowered the wind speed, the high drag can cause unrealistic wave growth. The problem is also present in coupled models of the atmosphere and the oceanic wave field, as excessive drag can lower the wind speed too much, yielding unrealistically weak wind fields in hurricane conditions. It was found by *Li et al.* (2021) that the implementation by *ECMWF* (2020) of a reduction of the Charnock parameter at high wind speeds gave wave growth in a coupled simulation that was in good agreement with observations in tropical cyclone LingLing. The new drag parameterization yields a significant bias reduction in strong winds in a two-year (2011–2012) twin experiment against a control run with the normal Charnock parameterization. The 23-year (uncoupled) wave hindcast (1998–2020) also shows very good performance compared against satellite and buoy measurements.





# **Chapter 4**

## **Scientific results**



# Paper I

## **NORA10EI: A revised regional atmosphere-wave hindcast for the North Sea, the Norwegian Sea and the Barents Sea.**

H. Haakenstad, Ø. Breivik, M. Reistad and O. J. Aarnes  
*International Journal of Climatology*, **40**(10), 2020



## RESEARCH ARTICLE

# NORA10EI: A revised regional atmosphere-wave hindcast for the North Sea, the Norwegian Sea and the Barents Sea

Hilde Haakenstad<sup>1,2</sup> | Øyvind Breivik<sup>1,2</sup>  | Magnar Reistad<sup>1</sup> | Ole J. Aarnes<sup>1</sup><sup>1</sup>Norwegian Meteorological Institute, Bergen, Norway<sup>2</sup>Geophysical Institute, University of Bergen, Bergen, Norway**Correspondence**Øyvind Breivik, Norwegian Meteorological Institute, Alleg 70, 5007 Bergen, Norway.  
Email: oyvind.breivik@met.no**Funding information**

ERA4CS, Grant/Award Number: WINDSURFER

**Abstract**

NORA10EI, a new atmosphere and wave hindcast for the Norwegian Sea, the North Sea and the Barents Sea is presented. The hindcast uses ERA-Interim as initial and boundary conditions and covers the period 1979–2017. The earlier NORA10 hindcast used ERA-40 as initial and boundary conditions before September 2002 and operational analyses from the European Centre for Medium-Range Weather Forecasts (ECMWF) in the continuation. This change in initial and boundary conditions may lead to non-stationarities in bias and random errors, and it is a question of some concern whether this also leads to spurious trends. We investigate this by comparing the two hindcasts. We find only minor differences in the statistics of means and upper percentiles, but somewhat larger differences in the extremes (100-year return values) of significant wave height and 10-m winds. Generally, NORA10EI outperforms NORA10 in the ERA-40 period (before September 2002) since ERA-Interim outperforms ERA-40. Conversely, NORA10 outperforms NORA10EI after 2006, since the operational ECMWF analyses here outperform ERA-Interim. Years 2002–2006 is a transition period with minor differences between the NORA10 and NORA10EI where the resolution of ERA-Interim is lower than that of the ECMWF analyses, but its physics are from a more recent model (2006). An important finding is that the regional hindcasts appear quite insensitive to changes in the host reanalysis with no statistically significant differences in mean and upper percentile trends of wind speed and wave height. A comparison of four polar low cases confirms that using ERA-Interim as host reanalysis yields a slightly better representation of evolution and intensity of polar lows than NORA10 in the ERA-40 period and the opposite after 2006.

**KEYWORDS**

North Sea, Norwegian Sea, regional hindcast, trend analysis, wave modelling

## 1 | INTRODUCTION

Regional downscaling of global reanalyses of the atmosphere and the wave field, known as hindcasts (a model

run without data assimilation but constrained by a reanalysis on the boundaries and as initial conditions), are a cheap and useful supplement to regional reanalyses as they are affordable on much higher lateral resolution

This is an open access article under the terms of the Creative Commons Attribution License, which permits use, distribution and reproduction in any medium, provided the original work is properly cited.

© 2019 The Authors. International Journal of Climatology published by John Wiley & Sons Ltd on behalf of the Royal Meteorological Society.

without the need for an expensive data assimilation system. Several high-quality regional hindcasts have been generated in recent years (e.g., the studies by Gaslikova and Weisse, 2006; Weisse and Günther, 2007 and Weisse and von Storch, 2010 for the North Sea and the NORA10 hindcast by Reistad *et al.*, 2011 to be investigated here). As waves are entirely forced by the wind, these studies perform well without assimilation of wave observations. Wave hindcasts are useful since the regional wave climate requires relatively high resolution to resolve topographical features that modify the wind field and obstruct the wave field. A number of regional (e.g., Bromirski *et al.*, 2013; Izaguirre *et al.*, 2013; Appendini *et al.*, 2014; Semedo *et al.*, 2015), basin-scale (Wang *et al.*, 2012) and global (Semedo *et al.*, 2011; Aarnes *et al.*, 2015; Meucci *et al.*, 2019) studies on wave climate variability and trends from hindcasts and reanalyses have recently been presented. Common to all of them is that they take their boundary conditions from global reanalyses.

The first global reanalyses were the ERA-15 reanalysis (Gibson *et al.*, 1997) developed at the European Centre for Medium-Range Weather Forecasts (ECMWF) and the 40-year reanalysis (since extended) developed at the National Centers for Environmental Prediction/National Center for Atmospheric Research (NCEP/NCAR) (Kalnay *et al.*, 1996). These were followed a few years later by the first coupled atmosphere-wave reanalysis, ERA-40 (Uppala *et al.*, 2005), developed at ECMWF.

After ERA-40 came a series of global atmospheric reanalyses, most notably the Japanese Reanalysis (JRA-25, Onogi *et al.*, 2007), the Climate and Forecast Reanalysis (CFSR, Saha *et al.*, 2010), the Modern Era Reanalysis (MERRA, Rienecker *et al.*, 2011), ERA-Interim (Dee *et al.*, 2011), and the updated version of CFSR (CFSv2, Saha *et al.*, 2014). Recently, century-long reanalyses have been produced at lower resolution, notably the 20th-century reanalysis, covering the period from 1871 to present (Compo *et al.*, 2011) and ERA20C, covering the period 1900–2010 (Hersbach *et al.*, 2015; Poli *et al.*, 2016). The latter was recently accompanied by CERA20C, a coupled atmosphere–ocean low-resolution reanalysis (Buizza *et al.*, 2018; Laloyaux, 2018).

ERA-Interim is continually updated but is not extended back beyond 1979. Compared with ERA-40, ERA-Interim has an improved hydrological cycle and better stratospheric circulation. Furthermore, in situ observations and satellite data are handled by four-dimensional variational data assimilation whereas ERA-40 employed a three-dimensional (3D) variational assimilation scheme (Dee *et al.*, 2011). Although now being replaced by the new modern-era reanalysis ERA-5 (Hersbach and Dee, 2016), ERA-Interim is still used extensively.

NORA10 (Reistad *et al.*, 2011) is a regional atmosphere and wave hindcast which employs ERA-40 on the boundaries and as initial conditions for the atmosphere, and spectra from a coarser wave model forced with ERA-40 winds for the wave field. NORA10 originally covered the same period as ERA-40, September 1957 to September 2002, but has since been extended to present time using operational analyses as boundary and initial conditions (Aarnes *et al.*, 2012). (This extension is referred to as the second period of NORA10). Although of high quality, this inconsistency in the boundary forcing has led to concerns about the stationarity of the statistical properties of the hindcast archive since model upgrades have inevitably led to improvements and thus a reduction of bias and random error in the boundary and initial conditions. The question of whether the intensity of storm systems has been affected by these gradual changes to the forcing is of particular interest. This would show up as spurious trends which could also be interpreted as a climate change signal and compromises extreme value estimation (Aarnes *et al.*, 2015). This question of how sensitive a regional hindcast is to its host analysis is of wider scientific interest, as reanalyses are often found to yield spurious trends due to increasing amounts of observations (of improving quality), see Aarnes *et al.* (2015) and Meucci *et al.* (2019).

In order to explore the stationarity issue, we have applied ERA-Interim on the boundaries of the NORA10 model domain and run the atmospheric model for the period 1979–2017. ERA-Interim was the best reanalysis available at the start of the NORA10EI production, and it is comparable in quality to the ECMWF analyses used for the early second period of the NORA10 hindcast.

The same wave model as was used for NORA10 was employed to produce wave fields for the period, where an outer wave model forced by ERA-Interim winds provided spectral wave boundary conditions to the inner model. With other things kept constant, we will thus investigate whether the change from ERA-40 to ECMWF analyses on the boundaries has led to spurious trends in mean and upper percentiles of the wind and wave field of NORA10.

This paper is organized as follows. A description of the new NORA10EI hindcast is presented in Section 2. A presentation of the general performance of NORA10EI follows in Section 3. Section 4 investigates median and upper percentiles of the wind speed at offshore wind-measuring stations. Section 5 assesses the performance of the wave model fields against offshore wave-measuring stations. The trends in wind speed are investigated in Section 6 and spatial wind patterns are presented in Section 7. A comparison of extreme value estimates from NORA10 and NORA10EI is presented in Section 8. The total impact of the transition to operational analyses on

NORA10 is discussed in Section 9 and the conclusions are summarized in Section 10. A short description of the usage of the offshore observations related to Section 4 is given in Appendix A1. Four polar low cases are presented in Appendix A2 (Figures A1–A8) where the relative merit of NORA10 v NORA10EI is considered, and the method used in trend analysis in Section 6 is presented in Appendix A3.

## 2 | MODEL SETUP

This hindcast study has deliberately been set up on the same model domain and with a configuration which closely matches that of NORA10. This is because we aim to investigate the sensitivity of a regional hindcast to host analysis forcing, and to what extent NORA10 is affected by the change in forcing data in 2002 where the transition from ERA-40 to ECMWF analyses takes place. The only exception to this is that the wind input to the wave model is hourly instead of 3 hr. This is not expected to have a major impact on the performance, except to give a slightly better representation of the upper percentiles.

The NORA10 atmosphere and wave hindcast (Reistad *et al.*, 2011) was based on an atmospheric downscaling of the global ERA-40 reanalysis (Uppala *et al.*, 2005). The wave model was set up in a nested configuration where ERA-40 10-m winds were used to force a 50-km resolution wave model covering the North Atlantic which provided boundary conditions for a 10-km wave model (see Breivik *et al.*, 2009 for details on the nesting scheme).

The NORA10EI atmospheric downscaling uses ERA-Interim as boundary and initial conditions but is otherwise, identical to NORA10. The High-Resolution Limited Area Model (HIRLAM, see Unden *et al.*, 2002) is run in four 9-hr forecast sequences every day. HIRLAM is initialized by a blending of the ERA-Interim reanalysis and the previous HIRLAM forecast, valid at the start time of the forecast. This allows small scale structures to develop freely in the forecast while the large-scale structures are being controlled by the large-scale forcing Yang (2005).

The model domain is a rotated spherical grid with the south pole positioned at 22° S, 40° W (see Figure 1). The domain is 248 × 400 grid points with 0.1° resolution. The vertical is resolved by 40 hybrid levels with variable spacing. Near the surface, the vertical coordinate closely follows the terrain and it gradually transforms with height toward a pressure coordinate at the top of the domain. The model equations are solved by a semi-implicit, semi-Lagrangian two-time level integration scheme and the time step is 240 s (Unden *et al.*, 2002). Sequences of 10-m wind fields from +3 to +8 hr lead time exhibit the lowest biases and random errors and were therefore chosen for the wave model forcing as well as the model-observation comparison presented in the following sections.

No changes were made to the wave model physics or the spectral or spatial resolution. The WAM Cycle 4 model physics is described by Günther *et al.* (1992); Komen *et al.* (1994). The ice coverage was updated every 10 days based on the ice concentration in the ERA-Interim reanalysis.

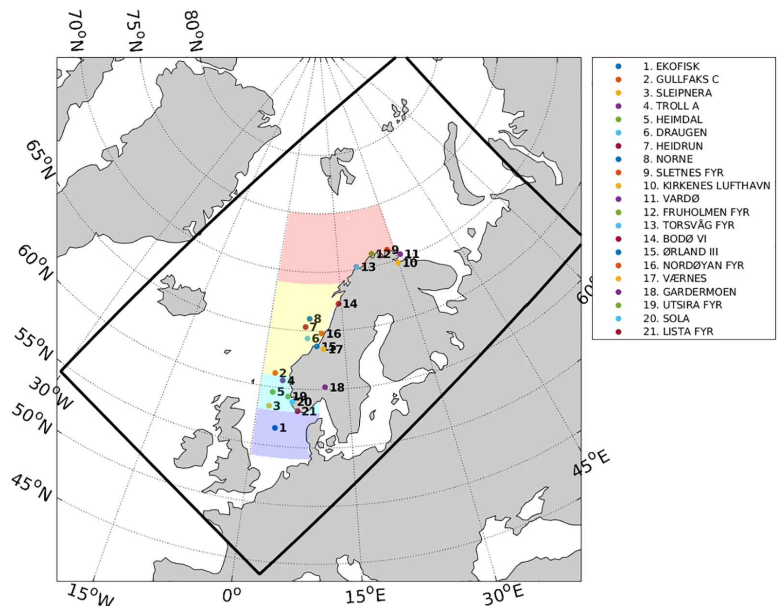


**FIGURE 1** Overview of the model domain with offshore and coastal stations. The domains used for trend analysis are coloured. The domains are numbered 1–4 from south to north



The model grid orientation and resolution are identical to the atmospheric grid. The two-dimensional spectrum is discretized with 24 directional bins ( $15^\circ$  resolution) and 25 logarithmically spaced frequency bins, ranging from 0.042 to 0.41 Hz in 10% increments.

### 3 | GENERAL PERFORMANCE OF NORA10EI

NORA10EI is compared against NORA10, the combined ERA-40 reanalysis/ECMWF analysis (hereafter referred to as EC), ERA-Interim and the more recent reanalysis ERA-5. Norwegian observations, retrieved from the climate database operated by the Norwegian Meteorological Institute, form the basis for the validation.<sup>1</sup> The observation locations are indicated in Figure 1, where the stations 1–8 are offshore and stations 9–21 are onshore. The offshore stations provide discontinuous measurements over the period investigated, 1979–2017, and will not be used in the performance appraisal. All the onshore stations have reliable and relatively continuous measurement series over this period where the requirement has been at least 60% coverage every month. Observations have been despiked by removing observations deviating by more than  $20 \text{ m}\cdot\text{s}^{-1}$  from the hindcasts or the reanalyses. All onshore stations are used in the assessment of the general performance of NORA10EI together with the two arctic stations, Jan Mayen and Hopen, which also meet the requirements.

The validation is based on a total of 753,403 wind measurements. Figure 2 compares the Weibull distribution (Zong, 2006) of these wind measurements against the Weibull distribution of the two hindcasts, NORA10EI, NORA10, and the three reanalyses, EC, ERA-Interim and ERA-5. All three reanalyses exhibit significant overestimation of the frequency of wind speed in the interval  $3\text{--}10 \text{ m}\cdot\text{s}^{-1}$  and an underestimation of wind speed above  $11 \text{ m}\cdot\text{s}^{-1}$ . The two hindcasts show the same pattern, but with less deviation from the observations. Most significant improvements from the reanalyses are seen for wind speeds between  $4$  and  $5 \text{ m}\cdot\text{s}^{-1}$  and for wind speeds higher than  $11 \text{ m}\cdot\text{s}^{-1}$ .

Figure 3 shows the general performance of the two hindcasts, NORA10EI and NORA10 together with the reanalyses EC, ERA-Interim and ERA-5, expressed by mean error (bias), root mean square error (RMSE) and the correlation with observations (panels a, b, and c, respectively).

The time series of the mean error (Figure 3a) shows that both the hindcasts and the host reanalyses primarily underestimate the wind speed, except for EC in the period 2006–2011. The hindcasts show shorter periods

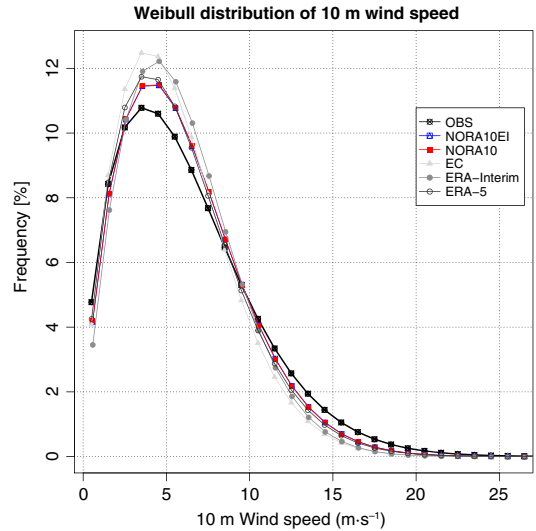


**FIGURE 2** Weibull distribution plot of 10 m wind speed for onshore measuring stations

with weak positive mean errors, however, the negative mean errors dominate the time series. The underestimation in wind speed is considerably smaller for NORA10EI and NORA10 than for EC and ERA-5, but very close to ERA-Interim up to 2002. From 2007 and forwards, NORA10 is the best performing of the hindcasts and the reanalyses, if we ignore the EC for the years 2012 and 2013. The performances of NORA10 and NORA10EI are also more stable, with smaller changes in mean error from year to year compared with the reanalyses. (The range interval in mean error is less than  $0.4 \text{ m}\cdot\text{s}^{-1}$  for the hindcasts, equal to  $0.4 \text{ m}\cdot\text{s}^{-1}$  for ERA-5,  $0.5 \text{ m}\cdot\text{s}^{-1}$  for ERA-Interim and  $1.2 \text{ m}\cdot\text{s}^{-1}$  for the EC.)

Before 2002, the underestimation is greatest in EC and smallest in NORA10EI. The transition from ERA-40 to ECMWF analysis in 2002 is clearly visible by the abrupt change from a strong underestimation of the wind speed before 2002 to a weak overestimation in the years 2006–2011.

This change in mean error in the EC time series has only a small impact on the NORA10 mean error, but the impact of changing the forcing of NORA10 is sufficient to cause a shift in the performance level. While NORA10EI outperforms NORA10 before 2002, NORA10 marginally outperforms NORA10EI in the second period of NORA10 (the mean error is reported for the period 2002–2017 in Table 1).

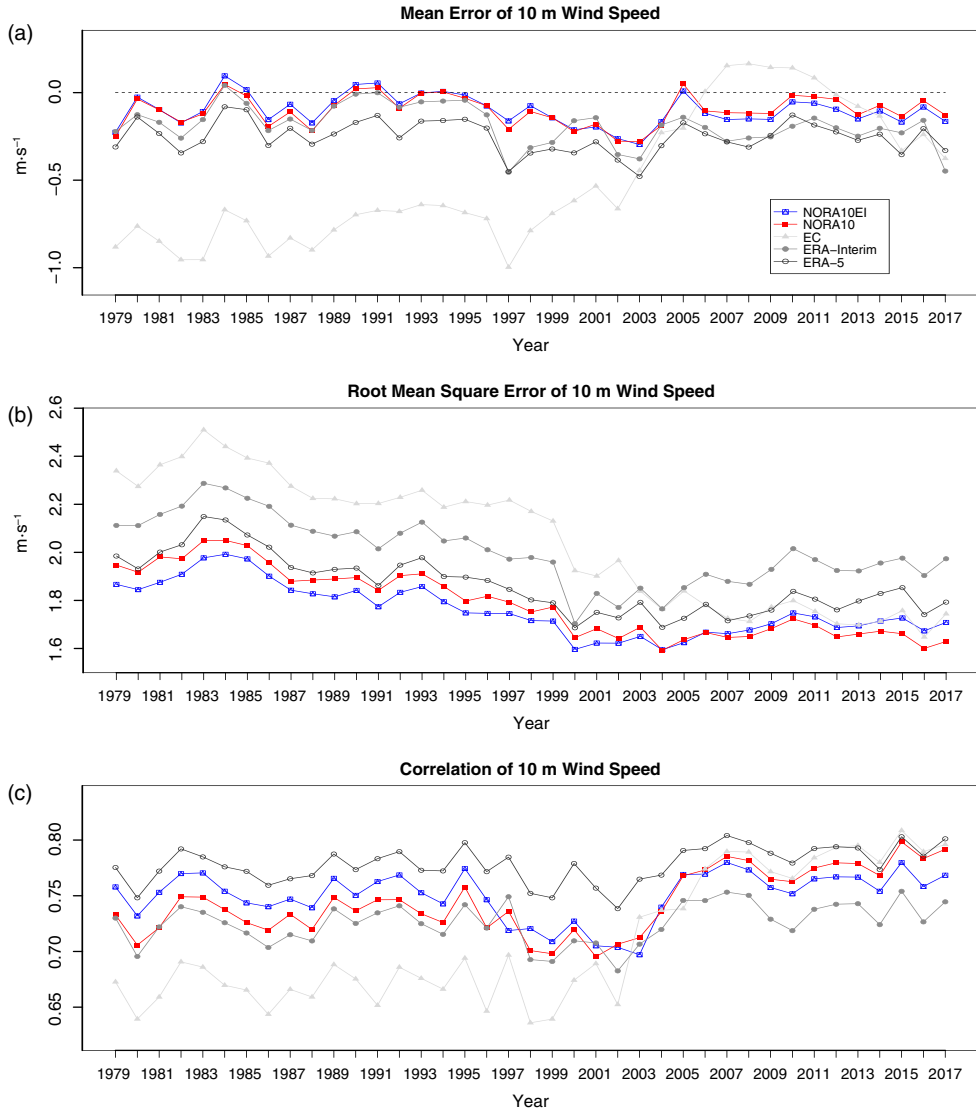


**FIGURE 3** General model wind speed performance expressed by mean error (a), root mean square error (b) and the correlation to the observations (c). EC (light grey) represents ERA-40 up to September 2002 and ECMWF analyses thereafter

The RMSE time series (Figure 3b) shows that NORAI0EI has the lowest RMSE in the period 1979–2002. The RMSE is almost the same for the two hindcast in the period 2004 to 2006, while NORAI10 outperforms NORAI0EI after 2006.

The decrease in RMSE over time for the host analyses (EC analysis and ERA-Interim, respectively) is almost uniformly in the period up to 2000, ignoring the first 5 years.

This trend is also found in the hindcasts and in ERA-5, however, the decrease is considerably weaker. From 2003 to 2005, the RMSE of ERA-Interim and the EC operational analyses are almost identical, while the EC operational analysis outperforms ERA-Interim from 2006 (the RMSE is reported for the period 2002–2017 in Table 2).

The time series of the correlation between the hindcasts and the observations and between the

Year	NORA10EI	NORA10	ERA-40/EC	ERA-interim	ERA-5
2002	-0.26	-0.28	-0.66	-0.35	-0.39
2003	-0.30	-0.28	-0.45	-0.38	-0.48
2004	-0.17	-0.19	-0.23	-0.19	-0.30
2005	0.01	0.05	-0.20	-0.14	-0.17
2006	-0.12	-0.10	0.01	-0.20	-0.24
2007	-0.15	-0.12	0.15	-0.28	-0.28
2008	-0.15	-0.12	0.17	-0.26	-0.31
2009	-0.15	-0.12	0.14	-0.25	-0.24
2010	-0.05	-0.02	0.14	-0.19	-0.13
2011	-0.06	-0.02	0.08	-0.15	-0.18
2012	-0.09	-0.04	-0.01	-0.20	-0.22
2013	-0.15	-0.13	-0.08	-0.25	-0.27
2014	-0.11	-0.07	-0.13	-0.20	-0.24
2015	-0.17	-0.14	-0.33	-0.23	-0.35
2016	-0.08	-0.05	-0.24	-0.16	-0.21
2017	-0.16	-0.13	-0.38	-0.45	-0.33

**TABLE 1** Mean error from 2002 to 2017 for the models NORA10EI, NORA10, ERA-40/EC, ERA-interim and ERA-5

Year	NORA10EI	NORA10	ERA-40/EC	ERA-interim	ERA-5
2002	1.62	1.64	1.97	1.77	1.73
2003	1.65	1.69	1.84	1.85	1.79
2004	1.60	1.59	1.76	1.77	1.69
2005	1.62	1.64	1.84	1.85	1.73
2006	1.67	1.67	1.78	1.91	1.78
2007	1.66	1.65	1.73	1.88	1.72
2008	1.68	1.65	1.71	1.87	1.74
2009	1.70	1.68	1.77	1.93	1.76
2010	1.75	1.72	1.80	2.02	1.84
2011	1.73	1.70	1.75	1.97	1.81
2012	1.69	1.65	1.70	1.93	1.76
2013	1.69	1.66	1.70	1.92	1.80
2014	1.72	1.67	1.71	1.96	1.83
2015	1.73	1.66	1.76	1.98	1.85
2016	1.67	1.60	1.65	1.90	1.74
2017	1.71	1.63	1.74	1.97	1.79

**TABLE 2** Root mean square error from 2002 to 2017 for the models NORA10EI, NORA10, ERA-40/EC, ERA-interim and ERA-5

reanalyses and the observations (Figure 3c) show that ERA-5 yields the highest correlation overall. However, ERA-5 is biased low in wind speed. NORA10EI is as expected surpassed by NORA10 in the last part of the period. EC outperforms ERA-Interim from 2006, as must be expected as it is built on the operational model version of the ECMWF Integrated Forecast System (IFS) that became operational in December 2006 (Cy31r2). Note, however, that EC analysis is very close in performance to

ERA-Interim even in the period 2003–2006, as its resolution is about 40 km in 2002 and thus much higher than the resolution of ERA-Interim (79 km).

Figure 3 and Tables 1–3 demonstrate the effect of increased resolution and improved model physics in the host analysis. In September 2002, the resolution of the host analysis to NORA10 was changed from approximately 125 km to about 40 km with the transition from ERA-40 to operational ECMWF analyses. The transition

**TABLE 3** Correlation coefficient from 2002 to 2017 for the models NORA10EI, NORA10, ERA-40/EC, ERA-interim and ERA-5

Year	NORA10EI	NORA10	ERA-40/EC	ERA-interim	ERA-5
2002	0.70	0.71	0.65	0.68	0.74
2003	0.70	0.71	0.73	0.71	0.77
2004	0.74	0.74	0.74	0.72	0.77
2005	0.77	0.77	0.74	0.75	0.79
2006	0.77	0.77	0.77	0.75	0.79
2007	0.78	0.79	0.79	0.75	0.80
2008	0.77	0.78	0.79	0.75	0.80
2009	0.76	0.77	0.77	0.73	0.79
2010	0.75	0.76	0.77	0.72	0.78
2011	0.77	0.77	0.78	0.74	0.79
2012	0.77	0.78	0.79	0.74	0.79
2013	0.77	0.78	0.80	0.74	0.79
2014	0.75	0.77	0.78	0.72	0.77
2015	0.78	0.80	0.81	0.75	0.80
2016	0.76	0.78	0.79	0.73	0.79
2017	0.77	0.79	0.80	0.75	0.80

also led to a cycle update from ERA-40's Cy23r4 to the operational Cy25r1.<sup>2</sup> Additional changes to the horizontal resolution of EC occurred in 2006, 2010 and 2016, when the resolution of ECMWF-IFS was refined to 25, 16 and 9 km. Increases in the vertical resolution took place in 2006 and 2013 to respectively 91 and 137 levels). Four polar low cases have been examined in Appendix A2 (see Figures A1–A8). Although the two hindcasts (NORA10 and NORA10EI) give quite similar results, the lows are somewhat better represented by NORA10EI in the period up to September 2002 (ERA-40 boundary conditions for NORA10), and conversely that NORA10 captures the polar lows better in the period after August 2002.

#### 4 | MEDIAN AND UPPER-PERCENTILE OFFSHORE WIND

Figure 4 shows the 50th (median), 95th and 99th percentiles of observed and modelled 10 m wind speed at offshore stations (stations 1–8 in Figure 1).

The offshore wind stations are very scarce in the early period, with just Ekofisk in operation between period 1980 and 1989. Gullfaks-C started reporting in October 1989, followed by Sleipner and Draugen in 1994 and Heidrun in 1995. Norne and Troll-A started reporting in 1998 and Heimdal in 2005. Offshore stations typically observe winds at heights between 30 and 130 m. The observations are here reduced to 10 m height by using the NORSOK profile defined in Appendix A1.

The median observed wind speed (Figure 4a) ranges from 7.5 to 9.1 m s<sup>-1</sup>. The first two decades show higher median wind speeds relative to the last part of the period. The median percentile wind speed of NORA10EI ranges from 7.3 to 9.0 m s<sup>-1</sup>. NORA10EI does also show the highest values in the first 20 years (1979–1998), and somewhat lower values during the last part of the period. This is in agreement with the observations. NORA10 shows slightly higher median wind speeds (ranging from 7.4 to 9.2 m s<sup>-1</sup>), however, both NORA10EI and NORA10 match the observations well.

EC exhibits a lower range (6.7–8.4 m s<sup>-1</sup>) for the median wind speed. The trend is also opposite to what is observed with the highest values in the last decade of the period, caused by the change from ERA-40 to operational EC analyses in 2002. ERA-Interim has somewhat higher values than EC (ranging from 6.9 to 8.8 m s<sup>-1</sup>) and is closer to the observations. The ERA-Interim trends are also similar to the observations, that is, the highest values during the first two decades and somewhat weaker winds during the last part of the period. ERA-5 displays a relatively similar range (7.0–8.6 m s<sup>-1</sup>).

The 95th percentile observed wind speed varies between 15.2 and 19.8 m s<sup>-1</sup>. NORA10EI underestimates the 95th percentile (with a range 14.4–17.3 m s<sup>-1</sup>). The underestimation is quite strong in the beginning of the period but is strongly reduced from 1998, probably caused by increased confidence in the measuring data with the take in of NORNE and TROLL-A. NORA10 exhibits a slightly smaller range in 95th percentiles than NORA10EI,

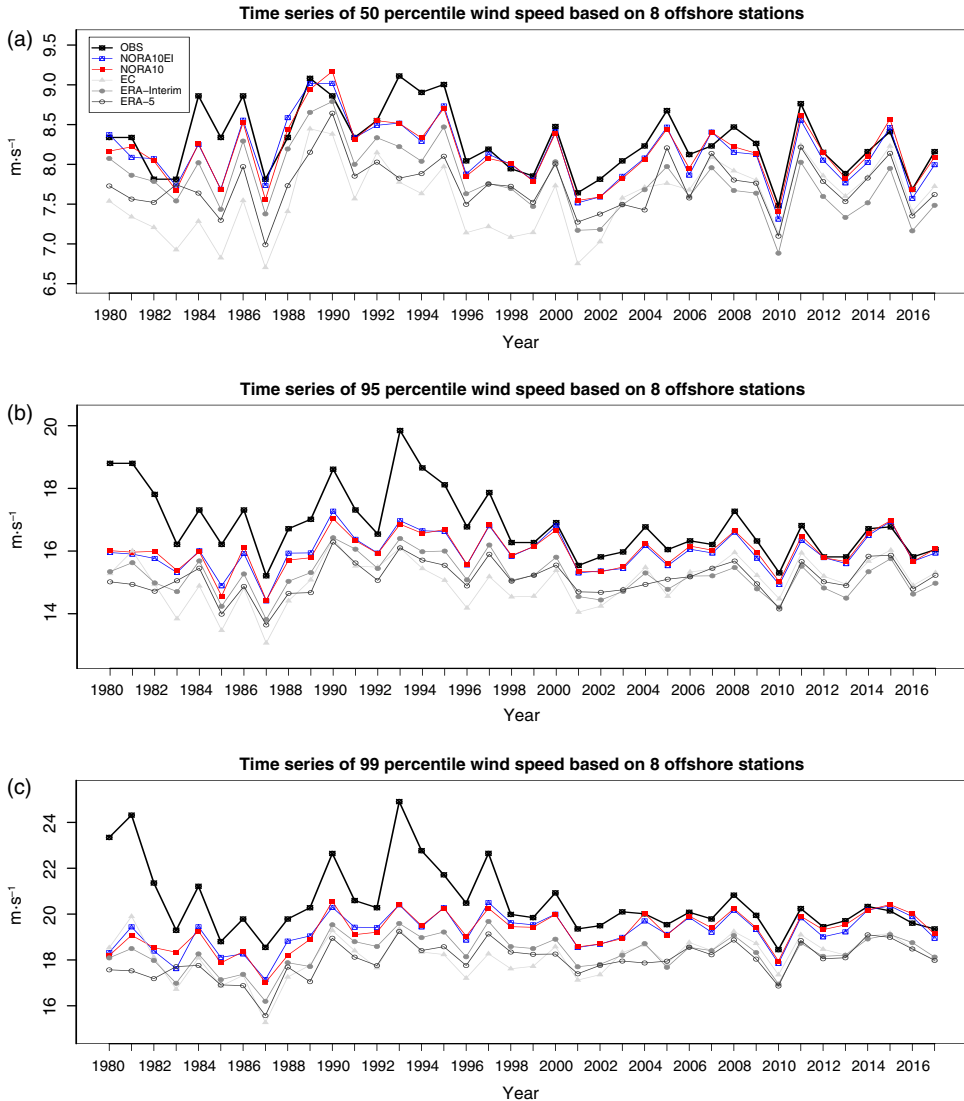


**FIGURE 4** Offshore stations, 50th (a), 95th (b) and 99th (c) percentiles of 10-m wind speed ( $\text{m}\cdot\text{s}^{-1}$ )

but the differences are very small. Among the reanalyses, ERA-Interim performs the best in terms of 95th percentile wind speed, closely followed by ERA-5.

The 99th percentile observed wind speed ranges from  $18.5$  to  $24.9 \text{ m}\cdot\text{s}^{-1}$ . NORA10EI and NORA10 both fit the 99th percentile observations in the last part of the period, but underestimate in the first part of the period. The range of NORA10EI is  $17.1$ – $20.5 \text{ m}\cdot\text{s}^{-1}$  and NORA10 displays almost exactly the same range. It is however a

question of how credible the observed percentiles in the beginning of the period are, as there are very few observations in the first two decades (see Figure 5).

A general observation from inspection of Figure 3 is that the NORA10 mean error (panel a) and RMSE (panel b) exhibit a weak, decreasing trend, with NORA10 outperforming NORA10EI after 2006. This suggests a small spurious trend in wind speed for NORA10, but, as can be seen from Figure 4, the effect is rather weak.

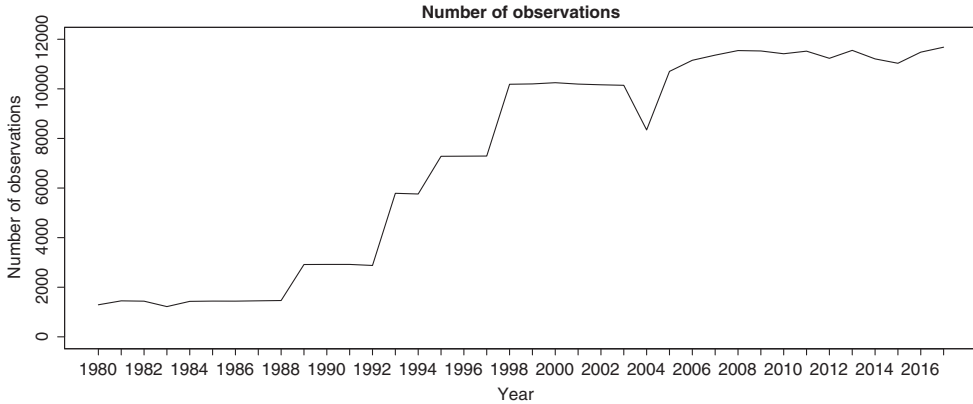


**FIGURE 5** Yearly number of observations at offshore stations

**FIGURE 6** Scatter plot (left panel) and quantile-quantile (QQ) plot of 10 m wind speed (right panel) of NORA10EI (blue) and NORA10 (red) against observations from eight offshore stations. The slightly smaller RMSE of NORA10EI is visible in the left panel as smaller spread, but the quantiles (right panel) overlap almost exactly

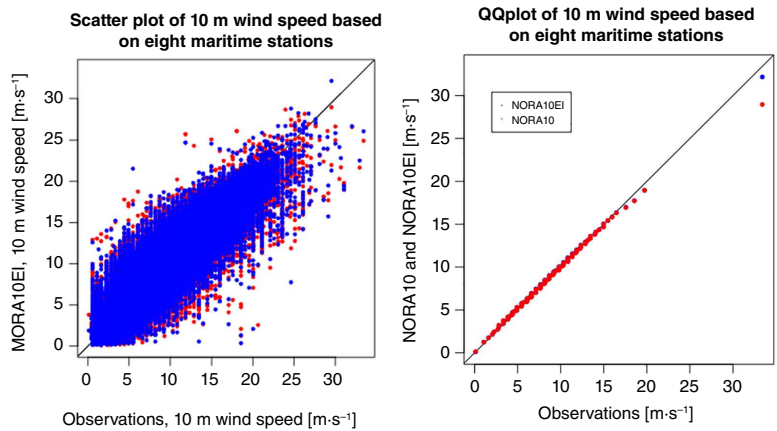


Figure 6 shows the quantile-quantile (QQ) comparison of 10-m wind speed and the associated scatter plot based on the eight maritime stations 1–8 in Figure 1. It is clear that the wind speed distributions of NORA10EI and NORA10 are very similar and very close to the observed distribution with NORA10EI showing a slightly better match against the highest observed wind speeds. The slightly lower RMSE of NORA10EI is evident in the slightly smaller spread seen in Figure 6b), but the quantiles very nearly coincide.

## 5 | OFFSHORE WAVE MEASUREMENTS

The wave model fields have been compared against wave observations of significant wave height,  $H_s$ , from a number

of offshore platforms in Tables 4 and 5. The performance of NORA10EI is generally slightly better than for NORA10 before 2002, and slightly poorer after 2006, in agreement with the results presented above for the 10-m wind speed. This is illustrated in Figures 7 and 8. The differences are small, and the comparison with observations in generally good. There are no big differences between the two, but NORA10 (red) tends to yield slightly higher  $H_s$  after 2006. This tendency is particularly evident in Figure 8 (Draugen field, location 6 in Figure 1), where the 99th percentile (panel b) deviates by as much as 5% toward the end of the period. Ekofisk in the central North Sea (location 1 in Figure 1) exhibits a similar, but weaker, pattern (Figure 7b). The main reason is the small increase in mean wind speed due to higher resolution in EC analyses compared to the early period which is forced with ERA-40, as seen in the trend analysis (Section 6).

**TABLE 4** Observed and modelled significant wave height at offshore stations in the Barents Sea and the eastern Norwegian Sea

Location		<i>N</i>	Mean	<i>SD</i>	MAD	RMSD	Corr.	<i>P</i> <sub>90</sub>	<i>P</i> <sub>95</sub>	<i>P</i> <sub>99</sub>	<i>P</i> <sub>99,9</sub>
Barents Sea 1978–1998	Obs.	58,637	2.31	1.32				4.1	4.9	6.7	9.2
	NORA10		2.33	1.36	0.34	0.49	0.935	4.2	5.0	6.9	9.3
	NORA10EI		2.35	1.37	0.34	0.47	0.939	4.2	5.0	7.0	9.3
Barents Sea 2007–2015	Obs.	36,003	2.36	1.33				4.1	5.0	6.9	9.1
	NORA10		2.38	1.32	0.32	0.44	0.944	4.2	5.0	6.9	8.9
	NORA10EI		2.33	1.31	0.34	0.47	0.937	4.1	4.9	6.8	8.7
Barents Sea 2007–2015	Obs. 1-hr	108,064	2.36	1.33				4.1	5.0	6.9	9.1
	NORA10EI 1-hr		2.34	1.31	0.34	0.47	0.937	4.1	4.9	6.8	8.8
Haltenbanken 1980–1988	Obs.	12,195	2.68	1.60				4.9	5.9	8.0	10.5
	NORA10		2.57	1.59	0.34	0.47	0.959	4.8	5.8	7.8	10.3
	NORA10EI		2.60	1.61	0.33	0.46	0.960	4.8	5.9	7.9	10.3
Heidrun 1996–2005	Obs.	24,814	2.63	1.50				4.7	5.5	7.4	9.5
	NORA10		2.72	1.61	0.47	0.65	0.917	4.9	5.9	8.1	10.3
	NORA10EI		2.75	1.65	0.48	0.66	0.929	4.9	6.0	8.3	10.7
Heidrun 2006–2017	Obs.	34,170	2.59	1.52				4.7	5.5	7.2	9.8
	NORA10		2.78	1.62	0.45	0.62	0.932	5.0	5.9	8.1	11.1
	NORA10EI		2.75	1.62	0.46	0.63	0.928	4.9	5.9	8.0	11.1
Draugen 1995–2005	Obs.	24,104	2.61	1.65				4.9	5.9	7.8	9.6
	NORA10		2.66	1.61	0.41	0.56	0.941	4.8	5.9	8.1	10.2
	NORA10EI		2.70	1.63	0.42	0.57	0.940	4.9	6.0	8.2	10.7
Draugen 2006–2017	Obs.	30,912	2.69	1.61				4.9	5.9	7.6	9.9
	NORA10		2.81	1.62	0.40	0.54	0.946	5.0	6.0	8.1	10.8
	NORA10EI		2.79	1.62	0.42	0.57	0.941	5.0	6.0	8.0	10.7

**TABLE 5** Observed and modelled significant wave height at Norwegian offshore stations in the North Sea

Location		<i>N</i>	Mean	<i>SD</i>	MAD	RMSD	Corr.	<i>P</i> <sub>90</sub>	<i>P</i> <sub>95</sub>	<i>P</i> <sub>99</sub>	<i>P</i> <sub>99,9</sub>
Gullfaks 1990–2005	Obs.	38,911	2.69	1.53				4.8	5.7	7.3	9.8
	NORA10		2.76	1.58	0.35	0.49	0.952	4.9	5.9	7.7	10.2
	NORA10EI		2.79	1.60	0.35	0.50	0.953	5.0	6.0	7.8	10.4
Gullfaks 2006–2017	Obs.	30,549	2.79	1.57				4.9	5.8	7.6	9.7
	NORA10		2.84	1.60	0.35	0.47	0.956	5.0	5.9	8.0	10.8
	NORA10EI		2.81	1.59	0.35	0.48	0.954	4.9	5.9	8.0	10.8
Ekofisk 1980–2005	Obs.	67,527	2.07	1.26				3.8	4.5	6.1	8.5
	NORA10		2.07	1.30	0.27	0.41	0.949	3.9	4.6	6.2	8.5
	NORA10EI		2.11	1.32	0.28	0.42	0.948	3.9	4.7	6.3	8.7
Ekofisk 2006–2017	Obs.	29,396	1.98	1.27				3.6	4.4	6.1	8.3
	NORA10		2.09	1.31	0.26	0.37	0.962	3.9	4.7	6.4	9.1
	NORA10EI		2.07	1.31	0.26	0.38	0.958	3.8	4.7	6.4	9.1

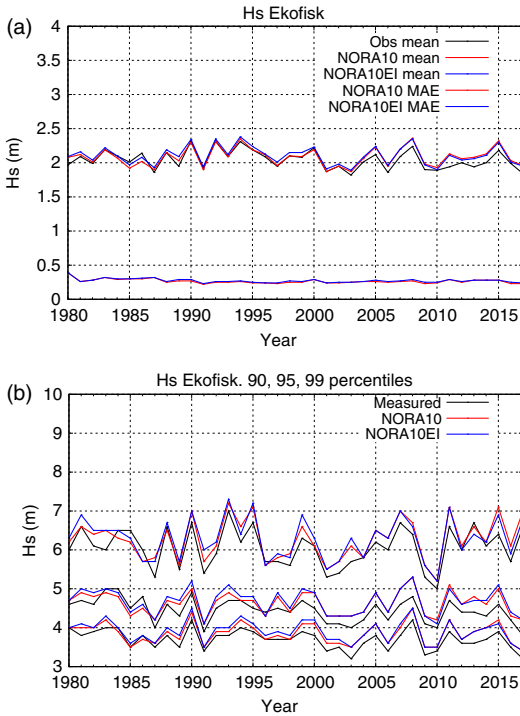


**FIGURE 7** (a) Time series of the annual mean significant wave height and the mean absolute error at Ekofisk in the Central North Sea (location 1 in Figure 1). (b) Time series of the 90th, 95th and 99th percentiles of significant wave height

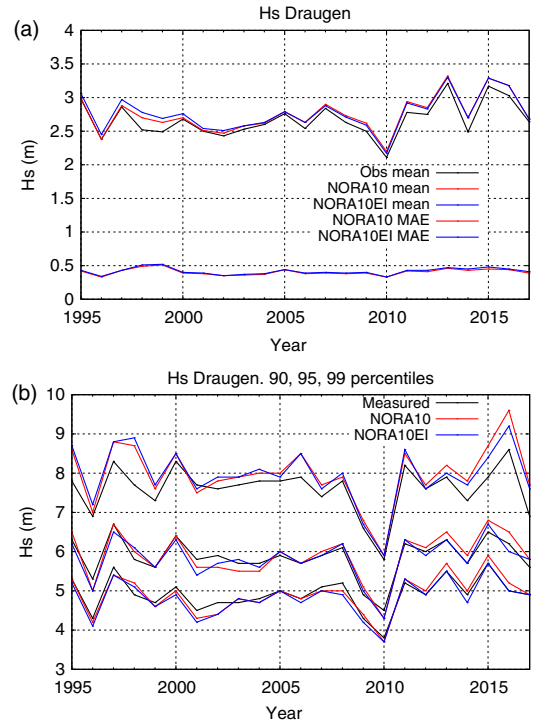


**FIGURE 8** (a) Time series of the annual mean significant wave height and the mean absolute error at Draugen in the eastern Norwegian Sea (location 6 in Figure 1). (b) Time series of the 90th, 95th and 99th percentiles of significant wave height

## 6 | TRENDS IN MARINE WIND CLIMATE

It is generally difficult to estimate trends from reanalyses as updates to the observation network can lead to spurious trends, even with no changes to the model setup or to the assimilation scheme. ERA-Interim is no exception, as Aarnes *et al.* (2015) demonstrated. It is however clear that the trends found in the downscaled hindcast are somewhat more robust than those of the reanalysis itself. This is because the impact of the assimilation scheme is significantly weakened when the reanalysis is employed as a host analysis providing boundary and initial conditions for short-range forecasts with no assimilation. We do not see strong evidence of spurious trends throughout the model period, but the mean error is slightly more stationary for NORA10EI than for NORA10 (see upper panel, Figure 3, where the wind speed bias for all quality-controlled stations is shown). The RMSE (panel b) is also more stationary for NORA10EI than NORA10, and the

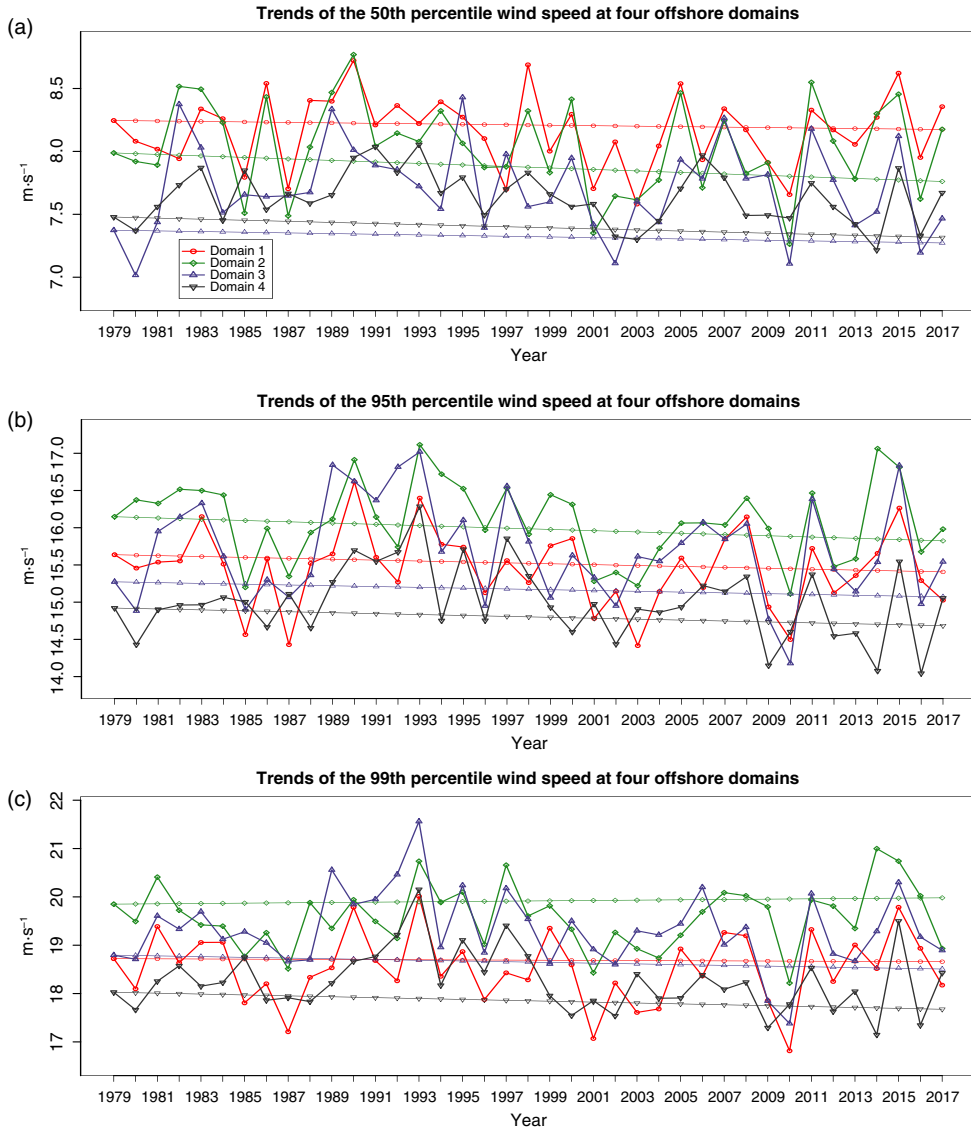
correlation (panel c) is significantly higher near the beginning of the period for NORA10EI compared to NORA10. These differences are however small and in the open ocean even smaller (see Figure 4).

Figure 9 shows the median and the 95th and 99th percentiles 10-m wind speed from NORA10EI at four offshore domains (shown in Figure 1) with trends calculated using Sen's slope (see Appendix A3).

Figure 9 shows that Domain 1 has typically the highest median wind speed, but among the lowest 99th percentile wind speeds. Domain 4 has typically the lowest values of both median and upper percentiles. Domain 2 has the strongest wind speeds with  $19.6 \text{ m}\cdot\text{s}^{-1}$  in mean of the 99th percentile wind speed compared to  $19.3 \text{ m}\cdot\text{s}^{-1}$  for Domain 3.

The trend of the median and the 95th percentile wind speed is negative for all domains (see Table 6, NORA10EI). The values range between  $-0.008$  (Domain 3) to  $-0.067 \text{ m}\cdot\text{s}^{-1} \text{ decade}^{-1}$  (Domain 2) for the 50th percentile and  $-0.029$  (Domain 1) to  $-0.087 \text{ m}\cdot\text{s}^{-1} \text{ decade}^{-1}$  (Domain 4) for the 95th percentile.





**FIGURE 9** NORA10EI time series of the trend in 50th (a), 95th (b) and 99th (c) percentile 10 m wind speed at the four different offshore domains shown in Figure 1

The 99th percentile shows a decreasing trend for Domains 3 and 4 and an increasing trend for Domains 1 and 2. The signs of the trends are also in agreement with Figures 10b and 11b, which are discussed in Section 7. The decreasing trends of the 99th percentile are  $-0.067 \text{ m}\cdot\text{s}^{-1} \text{ decade}^{-1}$  for Domain 3 and  $-0.128 \text{ m}\cdot\text{s}^{-1} \text{ decade}^{-1}$  for Domain 4. The increasing trends of the 99th percentile are  $+0.020 \text{ m}\cdot\text{s}^{-1} \text{ decade}^{-1}$  for Domain 1 and  $+0.075 \text{ m}\cdot\text{s}^{-1}$

$\text{decade}^{-1}$  for Domain 2. Both the decreasing trends and the increasing trends are small and none of the NORA10EI trends are statistically significant at 95% confidence level.

Table 6 summarizes the trends for NORA10, ERA-Interim and ERA-40/EC. While a weak negative trend dominates in NORA10EI, NORA10 shows a balance between weak positive and weak negative trends.

**TABLE 6** A 10-m wind speed trend estimates based on Sen's slope and the statistically significant threshold

Domain	Trend in 50th percentile wind speed (m s <sup>-1</sup> decade <sup>-1</sup> ) With significance threshold (%)	Trend in 95th percentile wind speed (m s <sup>-1</sup> decade <sup>-1</sup> ) With significance threshold (%)	Trend in 99th percentile wind speed (m s <sup>-1</sup> decade <sup>-1</sup> ) With significance threshold (%)
<b>NORA10EI</b>			
Domain 1	-0.032 <i>43.6</i>	-0.029 <i>70.6</i>	+0.020 <i>88.0</i>
Domain 2	-0.067 <i>25.8</i>	-0.101 <i>29.1</i>	+0.075 <i>49.7</i>
Domain 3	-0.008 <i>92.0</i>	-0.058 <i>61.5</i>	-0.067 <i>54.6</i>
Domain 4	-0.044 <i>18.3</i>	-0.087 <i>32.7</i>	-0.128 <i>15.9</i>
<b>NORA10</b>			
Domain 1	+0.029 <i>43.9</i>	-0.015 <i>84.7</i>	+0.076 <i>49.8</i>
Domain 2	-0.004 <i>96.1</i>	+0.112 <i>24.6</i>	-0.008 <i>92.3</i>
Domain 3	+0.018 <i>71.7</i>	-0.017 <i>92.3</i>	+0.026 <i>82.8</i>
Domain 4	+0.019 <i>54.5</i>	-0.035 <i>54.5</i>	+0.051 <i>59.5</i>
<b>ERA-interim</b>			
Domain 1	-0.018 <i>54.5</i>	-0.123 <i>14.0</i>	-0.059 <i>59.5</i>
Domain 2	-0.068 <i>17.5</i>	-0.132 <i>8.2</i>	-0.101 <i>27.6</i>
Domain 3	-0.044 <i>56.1</i>	-0.077 <i>45.3</i>	-0.095 <i>32.1</i>
Domain 4	-0.043 <i>18.3</i>	-0.055 <i>38.4</i>	-0.094 <i>29.8</i>
<b>ERA40/EC</b>			
Domain 1	+0.270 <i>0.0</i>	+0.033 <i>62.8</i>	-0.044 <i>73.5</i>
Domain 2	+0.354 <i>0.0</i>	+0.331 <i>0.0</i>	+0.395 <i>0.0</i>
Domain 3	+0.343 <i>0.0</i>	+0.401 <i>0.0</i>	+0.380 <i>0.5</i>
Domain 4	+0.256 <i>0.0</i>	+0.302 <i>0.0</i>	+0.299 <i>0.0</i>

Note: Note that the combined trend estimates for ERA-40 and ECMWF analyses are included here for reference as they represent that boundary forcing for NORA10. Significance threshold values are given as italic.

Unsurprisingly, the transition from ERA-40 to EC analyses shows a relatively strong positive trend for all the domains and for all the three percentiles investigated, except for the 99th percentile trend for Domain 1. Finally, ERA-Interim shows uniformly negative trends.

The slightly stronger positive trends (and weaker negative trends) in NORA10 compared to NORA10EI are mainly caused by the change in boundary conditions from ERA-40 to ECMWF operational analyses in September 2002. Note that these trends are all weak and in fact not statistically significant. Interestingly, the relatively minor differences seen between NORA10 and NORA10EI demonstrate that the hindcasts are quite insensitive to resolution changes in the host analysis. This is also in accordance with Davis (2014) who showed that little error can be clearly ascribed to the lateral boundary conditions with a proper choice of domain.

## 7 | SPATIAL WIND PATTERNS

Figure 10 shows the mean wind speed in the two periods related to the two different forcing periods of NORA10, 1979–2002 and 2002–2017. The general picture shows decreasing wind speed from west to east between Iceland and Great Britain, and from north to south in the North sea and from south to north in the Norwegian Sea and the Greenland Sea. This pattern reflects the synoptic-scale picture with frequent low-pressure systems moving eastward over the Atlantic and weakening as the systems approach land and when they travel northward into the Barents Sea. This pattern is clearly visible in both periods. The mean wind speed ranges from 4 to 10 m·s<sup>-1</sup> over the ocean. Figure 10b) shows the difference between the two periods for NORA10EI and for NORA10. Except for the Arctic region, NORA10EI exhibits only minor differences between the two periods. NORA10 shows weakly

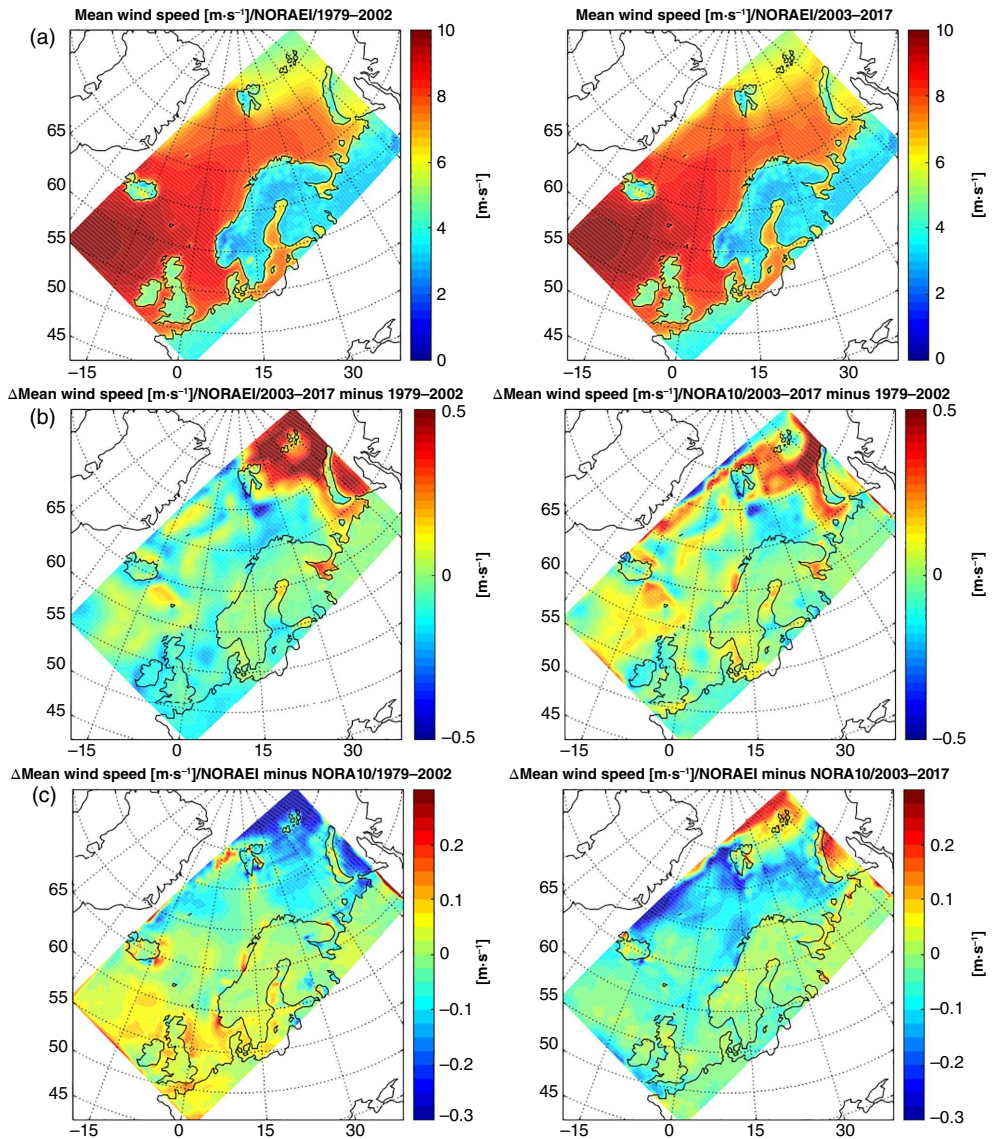


**FIGURE 10** Map of mean wind speed in (a) NORA10EI (left) in the first (1979–2002) and (right) second period (2003–2017), (b) the difference between the second and first period in NORA10EI (left) and NORA10 (right), and (c) the difference between NORA10EI (left) and NORA10 (right) in the first and the second period

increasing wind speed in large parts of the domain. Common to the two hindcasts is an increase in wind speed south and south-east of Iceland, and in the Greenland Sea. The difference in wind speed between the two periods also agrees quite well with the trend analysis performed in Section 6. Because of the lack of reliable long-term measurements for the Arctic, we will not focus on

the Arctic area here. However, due to receding sea ice cover, we expect considerable changes in wind speed and waves in this area (Aarnes *et al.*, 2017; Waseda *et al.*, 2018; Morim *et al.*, 2019). Figure 10c) shows the difference between NORA10EI and NORA10 in the first and the second period. In the first period, the wind speed is stronger in NORA10EI in the southern part of the

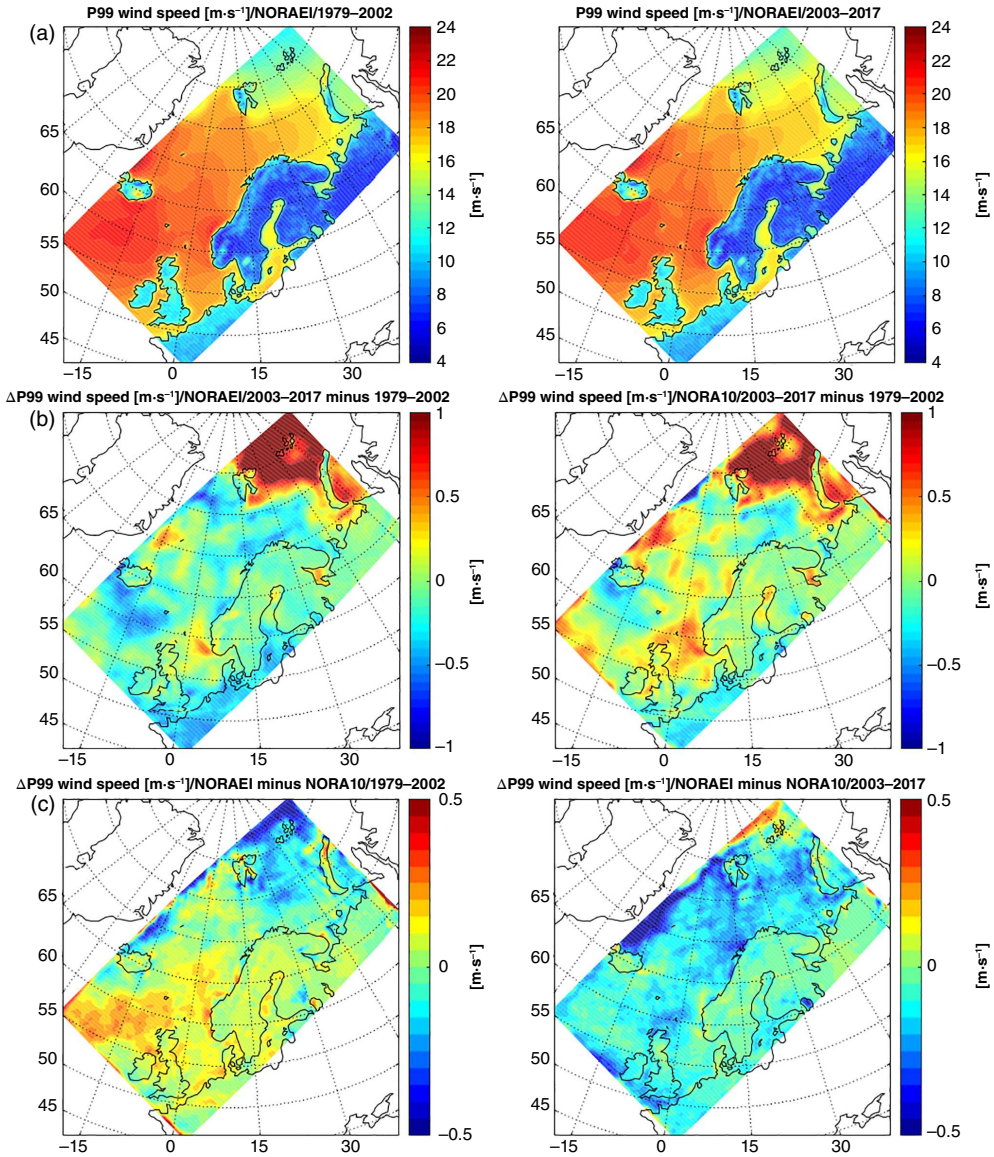


**FIGURE 11** Map of the 99th percentile wind speed (a) NORAEI (left) in the first (1979–2002) and (right) second period (2003–2017), (b) the difference between the second and first period in NORAEI (left) and NORAEI (right), and (c) the difference between NORAEI (left) and NORAEI (right) in the first and the second period

domain, and weaker in the northern part of the domain. In the second period, the two models are more equal and the differences are mostly limited to different inflow at the boundaries. NORAEI shows stronger inflow between 65° and 80°N, but NORAEI still has stronger wind speed over the sea ice north of 80°N.

Figure 11 shows the 99th percentile wind speed. It is clear that the upper percentiles exhibit the same spatial pattern as the mean values in Figure 10, but with values ranging from 13 to above 20  $\text{m}\cdot\text{s}^{-1}$  over the ocean. Figure 11b) shows the difference between the two periods for NORAEI and for NORAEI.

While NORA10 showed an increase in mean wind speed over large parts of the ocean, which was not visible in NORA10EI, NORA10EI shows an increase up to  $0.5 \text{ m s}^{-1}$  offshore from western Norway. NORA10EI also shows an increase in wind speed over the northern part of Great Britain and a strong increase north of Svalbard. NORA10 shows the same pattern, however, with even stronger increase in wind speed in the southern part of the domain. Figure 11c) shows the difference between the 99th percentile of NORA10EI and NORA10 in the first and the second period. NORA10EI has higher 99th percentile wind speeds in the southern domain in the first period and weaker wind speeds than NORA10 in the second period, as can be expected based on the differences between their host analyses.

## 8 | EXTREME VALUE ESTIMATES OF WIND SPEED AND SIGNIFICANT WAVE HEIGHT

The comparison of trends in mean and upper percentile wind speed and significant wave height suggest that the differences are small, and that the impact of the transition in boundary forcing used in NORA10 has had negligible impact on the overall statistics. As a further test of this, we compare the return value estimates from annual maxima of wind speed and significant wave height in NORA10 and NORA10EI.

The procedure follows that outlined by Aarnes *et al.* (2012) where a generalized extreme value (GEV) distribution is fitted to annual (block) maxima (see Coles, 2001, pp 45–51). The GEV distribution is an asymptotic limit

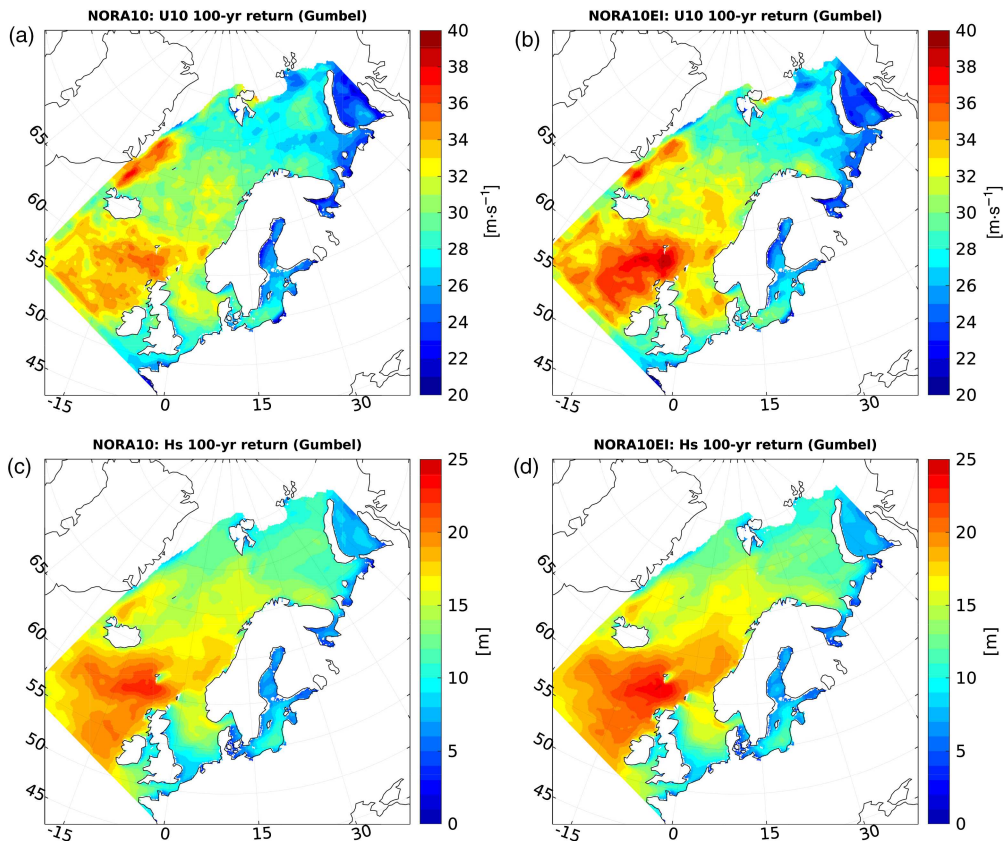


**FIGURE 12** Map of 100 year return values of 10 m wind speed (upper panels) and significant wave height (lower panels). The NORA10 return value estimates are shown on the left (a) and (c) for the period 1979–2017. The corresponding estimates for NORA10EI are found on the right (b) and (d). The NORA10EI estimates are higher than the NORA10 estimates, particularly in wind speed (up to  $5 \text{ m s}^{-1}$  difference), and considerably less in significant wave height

for a distribution of blocked maxima  $M_n = \max\{X_1, X_2, \dots, X_n\}$ . Following Coles (2001), the cumulative distribution function (CDF) of the block maxima formed from a random sequence of independent variables can be written

$$G(z) = \exp \left\{ - \left[ 1 + \xi \left( \frac{z - \mu_n}{\sigma_n} \right) \right]^{-1/\xi} \right\}, \quad (1)$$

where  $\sigma_n$  is the scale parameter,  $\mu_n$  is known as the location parameter, and  $\xi$  is the so-called shape parameter. The GEV distribution contains as special cases the Fréchet ( $\xi > 0$ ), Gumbel ( $\xi = 0$ ) and reversed Weibull ( $\xi < 0$ ) distributions. In the following analysis, we use the Gumbel distribution, fitted using a maximum likelihood method (Coles, 2001). This has the desired effect of creating smoother spatial return value estimates than the full GEV, making it easier to compare the two datasets.

Figure 12 contrasts the 100-year return value estimates for  $U_{10}$  and  $H_s$ . For consistency, the NORA10 estimates (a) and (c) are based on the same period as NORA10EI (b) and (d), that is, 1979–2017. It is clear that NORA10EI yield somewhat higher return values than NORA10, both for  $U_{10}$  and  $H_s$ , especially in the region south of Iceland and north-west of Scotland. Here, the 100-year return value for wind speed increase from 35 to 40  $\text{m}\cdot\text{s}^{-1}$  between the Faroe islands and Scotland. This gives a slight increase in 100-year return estimates of the significant wave height from 22 to 24 m in the same region. Although these changes are not dramatic, it shows that using EC analysis to force NORA10 has not led to particularly high return estimates, rather the opposite. It is however important to note that the return values are based on just 29 years, which is considered a short period for extreme value analysis, and represents a much smaller data set than other recent extreme value estimates of wind speed and significant wave height (Breivik *et al.*, 2013, 2014; Meucci *et al.*, 2018). This means that the impact of individual storms becomes large (Aarnes *et al.*, 2012).

## 9 | DISCUSSION

This study was motivated by the question of non-stationarity in NORA10 at the changeover from using ERA-40 to using ECMWF analyses as initial and boundary conditions. The results show that the stationarity issue is of negligible importance, although we do see a decreasing bias and RMSE and increasing correlation with wind observations in the second part of NORA10 (Figure 3).

The maps in Figure 10 reveal a larger negative wind speed bias in NORA10 compared with NORA10EI in the

first period (1979–2002) in the North Sea and the Norwegian Sea, but a better match in the second period (2003–2017). This explains the weak positive trends in NORA10 which are not reproduced by NORA10EI. However, over most parts of the oceans, the two hindcasts show a large degree of similarity despite differences in boundary and initial conditions. Since the two hindcasts employ the same numerical weather prediction model at the identical horizontal and vertical resolutions, the only differences stem from the boundary and surface forcing.

The weak trends in wind speed in NORA10EI are in agreement with other studies for northwestern Europe and the North-eastern Atlantic (Ciavola *et al.*, 2011; Cusack, 2013; Feser *et al.*, 2015; Minola *et al.*, 2016).

## 10 | CONCLUSIONS AND FURTHER WORK

The NORA10EI hindcast is generally found to be in close agreement with NORA10. This study, and the generation of the NORA10EI hindcast, was in part motivated by a need to test the impact of an abrupt change in the forcing fields in the NORA10 hindcast as it is extensively used for extreme value analysis and climatological studies of wind and wave height in the North Sea, the Norwegian Sea and the Barents Sea (Aarnes *et al.*, 2012; Furevik and Haakenstad, 2012; Bruserud and Haver, 2016), but more generally to look for the impact of host analysis on regional hindcasts. We find a slight reduction in the mean wind speed trend compared with NORA10, and as expected the bias and RMSE are more stationary. This does not appear to have a major impact on the upper percentiles, although, and the two hindcasts are in close agreement with each other for the offshore locations analysed. The representation of polar lows was qualitatively found to be slightly better in NORA10EI in the period before September 2002 (the host reanalysis ERA-Interim is superior to ERA-40). The difference is again small, and it is clear that a better host model and higher resolution of the hindcast itself is required before a proper representation of polar lows can be expected. Improved reanalyses are now available, in particular the new ERA-5 (Hersbach and Dee, 2016), and work is now underway to assess the required resolution for the next generation hindcast archive. The AROME atmospheric model (Seity *et al.*, 2011) is one candidate to be tested with non-hydrostatic physics and a resolution of the order of 3 km.

## ACKNOWLEDGMENTS

This study was carried out with support from the ERA4CS WINDSURFER project and the Norwegian Climate Service Centre (KSS). The hindcast archive was

made possible with computational resources provided by NOTUR, <http://www.sigma2.no>, on the Vilje national supercomputing facility. The Norwegian Deepwater Programme and later Equinor ASA funded the development of the NORA10 archive. MR, OJA and ØB acknowledge the Research Council of Norway for funding through the ExWaMar project (grant no 256466).

## ORCID

Øyvind Breivik  <https://orcid.org/0000-0002-2900-8458>

## ENDNOTES

<sup>1</sup> <https://frost.met.no>, last accessed October 2019.

<sup>2</sup> <https://www.ecmwf.int/en/forecasts/documentation-and-support/changes-ecmwf-model>

<sup>3</sup> <https://projects.met.no/stars/>

## REFERENCES

- Aarnes, O.J., Abdalla, S., Bidlot, J.-R. and Breivik, Ø. (2015) Marine wind and wave height trends at different ERA-interim forecast ranges. *Journal of Climate*, 28, 819–837. <https://doi.org/10.1175/JCLI-D-14-00470.1>.
- Aarnes, O.J., Breivik, Ø. and Reistad, M. (2012) Wave extremes in the Northeast Atlantic. *Journal of Climate*, 25, 1529–1543. <https://doi.org/10.1175/JCLI-D-11-00132.1>.
- Aarnes, O.J., et al. (2017) Projected changes in significant wave height towards the end of the 21st century: Northeast Atlantic. *Journal of Geophysical Research, Oceans*, 122, 3394–3403. <https://doi.org/10.1002/2016JC012521>.
- Appendini, C.M., Torres-Freyermuth, A., Salles, P., López-González, J. and Mendoza, E.T. (2014) Wave climate and trends for the gulf of Mexico: a 30-yr wave hindcast. *Journal of Climate*, 27, 1619–1632. <https://doi.org/10.1175/JCLI-D-13-00206.1>.
- Breivik, Ø., Aarnes, O., Abadalla, S., Bidlot, J.-R. and Janssen, P. (2014) Wind and wave extremes over the world oceans from very large ensembles. *Geophysical Research Letters*, 41(14), 5122–5131. <https://doi.org/10.1002/2014GL060997>.
- Breivik, Ø., Aarnes, O.J., Bidlot, J.-R., Carrasco, A. and Saetra, Ø. (2013) Wave extremes in the Northeast Atlantic from ensemble forecasts. *Journal of Climate*, 26, 7525–7540. arXiv:1304.1354, doi:10/mpf.
- Breivik, Ø., Gusdal, Y., Furevik, B.R., Aarnes, O.J. and Reistad, M. (2009) Nearshore wave forecasting and hindcasting by dynamical and statistical downscaling. *Journal of Marine Systems*, 78 (2), S235–S243.
- Bromirski, P.D., Cayan, D.R., Helly, J. and Wittmann, P. (2013) Wave power variability and trends across the North Pacific. *Journal of Geophysical Research Oceans*, 118(12), 6329–6348. <https://doi.org/10.1002/2013JC009189>.
- Bruserud, K. and Haver, S. (2016) Comparison of wave and current measurements to NORA10 and NoNoCur hindcast data in the northern North Sea. *Ocean Dynamics*, 66(6), 823–838. <https://doi.org/10.1007/s10236-016-0953-z>.
- Buizza, R., Bronnimann, S., Haimberger, L., Laloyaux, P., Martin, M.J., Fuentes, M., et al. (2018) The EU-FP7 ERA-CLIM2 project contribution to advancing science and production of earth system climate reanalyses. *Bulletin of the American Meteorological Society*, 99(5), 1003–1014. <https://doi.org/10.1175/BAMS-D-17-0199.1>.
- Ciavola, P., Ferreira, O., Haerens, P., Koningsveld, M.V., Armaroli, C. and Lequeux, Q. (2011) Storm impacts along European coastlines. Part 1: the joint effort of the MICORE and ConHaz projects. *Environmental Science & Policy*, 14(7), 912–923. <https://doi.org/10.1016/j.envsci.2011.05.011>.
- Coles, S. (2001) *An Introduction to Statistical Modeling of Extreme Values*. Berlin, Germany: Springer Verlag, p. 210.
- Compo, G.P., Whitaker, J.S., Sardeshmukh, P.D., Matsui, N., Allan, R.J., Yin, X., et al. (2011) The twentieth century reanalysis project. *Quarterly Journal of the Royal Meteorological Society*, 137(654), 1–28. <https://doi.org/10.1002/qj.776>.
- Cusack, S. (2013) A 101 year record of windstorms in the Netherlands. *Climatic Change*, 116, 693–704. <https://doi.org/10.1007/s10584-012-0527-0>.
- Davis, T. (2014) Lateral boundary conditions for limited area models. *Quarterly Journal of the Royal Meteorological Society*, 140, 185–196.
- Dee, D., Uppala, M., Simmons, A.J., Berrisford, P., Poli, P., Kobayashi, S., Andrae, U., et al. (2011) The ERA-interim reanalysis: configuration and performance of the data assimilation system. *Quarterly Journal of the Royal Meteorological Society*, 137(656), 553–597. <https://doi.org/10.1002/qj.828>.
- Douglas, M.W., Shapiro, M.A., Fedor, L.S. and Saukkonen, L. (1995) Research aircraft observations of a polar low at the East Greenland ice edge. *Monthly Weather Review*, 123, 5–15.
- Feser, F., Barcikowska, M., Krueger, O., Schenk, F., Weisse, R. and Xia, L. (2015) Storminess over the North Atlantic and north-western Europe—a review. *Quarterly Journal of the Royal Meteorological Society*, 141, 350–382. <https://doi.org/10.1002/qj.2364>.
- Furevik, B.R. and Haakenstad, H. (2012) Near-surface marine wind profiles from rawinsonde and NORA10 hindcast. *Journal of Geophysical Research*, 117(D23), 14. <https://doi.org/10.1029/2012JD018523>.
- Gaslikova, L. and Weisse, R. (2006) Estimating near-shore wave statistics from regional hindcasts using downscaling techniques. *Ocean Dynamics*, 56(1), 26–35.
- Gibson, J., Kallberg, P., Uppala, S., Hernandez-Carrascal, A., Nomura, A., Serrano, E., 1997: ERA Description In ECMWF ERA-15 Project Report Series, No. 1. Tech. rep., European Centre for Medium-Range Weather Forecasting, ECMWF Shinfield, Reading, UK.
- Günther, H., Hasselmann, S., and Janssen, P. A. E. M., 1992: Wamodel Cycle 4 (revised version). Tech. Rep. 4, Deutsches KlimaRechenZentrum, Hamburg, Germany.
- Haakenstad, H., Reistad, M., Haugen, J., and Breivik, Ø., 2012: Update of the NORA10 hindcast archive for 2011 and a study of polar low cases with the WRF model. Research Report 12/2012, The Norwegian Meteorological Institute, Oslo, Norway, 69 pp.
- Hersbach, H. and Dee, D. (2016) ERA5 reanalysis is in production. *ECMWF Newsletter*, 147, 7.
- Hersbach, H., Peubey, C., Simmons, A., Berrisford, P., Poli, P. and Dee, D. (2015) ERA-20CM: a twentieth-century atmospheric model ensemble. *Quarterly Journal of the Royal Meteorological Society*, 141(691), 2350–2375. <https://doi.org/10.1002/qj.2528>.

- Hsu, E.A.M., Meindl, E.A. and Gilhousen, D.B. (1994) Determining the power-law wind-profile exponent under near-neutral stability conditions at sea. *Journal of Applied Meteorology*, 33, 757–765.
- Izaguirre, C., Méndez, F.J., Espejo, A., Losada, I.J. and Reguero, B. G. (2013) Extreme wave climate changes in Central-South America. *Climatic Change*, 119(2), 277–290. <https://doi.org/10.1007/s10584-013-0712-9>.
- Kalnay, E., Kanamitsu, M., Kistler, R., Collins, W., Deaven, D., Gandin, L., Iredell, M., Saha, S., White, G., Woollen, J., Zhu, Y., Chelliah, M., Ebisuzaki, W., Higgins, W., Janowiak, J., Mo, K.C., Ropelewski, C., Wang, J., Leetmaa, A., Reynolds, R., Jenne, R., and Joseph, D. 1996: The NCEP/NCAR 40-year reanalysis project. *Bulletin of American Meteorological Society*, 77, 437–472, doi:10/fg6f9.
- Kendall, M.G. (1975) *Rank Correlation Methods*. London, UK: Griffin.
- Komen, G.J., Cavaleri, L., Donelan, M., Hasselmann, K., Hasselmann, S. and Janssen, P.A.E.M. (1994) *Dynamics and Modelling of Ocean Waves*. Cambridge: Cambridge University Press 532 pp.
- Laloyaux, P., and Coauthors, 2018: CERA-20C: a coupled reanalysis of the twentieth century. *Journal of Advances in Modeling Earth Systems*, 10(5), 1172–1195. <https://doi.org/10.1029/2018MS001273>.
- Mann, H. (1945) Nonparametric tests against trend. *Econometrica*, 13, 245–259.
- Meucci, A., Young, I.R., Aarnes, O.J. and Breivik, Ø. (2019) Comparison of wind speed and wave height trends from twentieth century models and satellite altimeters. *Journal of Climate*, 33, 611–624. <https://doi.org/10.1175/JCLI-D-19-0540.1>.
- Meucci, A., Young, I.R. and Breivik, Ø. (2018) Wind and wave extremes from atmosphere and wave model ensembles. *Journal of Climate*, 31(21), 8819–8842. <https://doi.org/10.1175/JCLI-D-18-0217.1>.
- Minola, L., Azorin-Molina, C. and Chen, D. (2016) Homogenization and assessment of observed near-surface wind speed trends across Sweden, 1956–2013. *Journal of Climate*, 29, 7397–7415.
- Morim, J., et al. (2019) Robustness and uncertainties in global multivariate wind-wave climate projections. *Nature Climate Change*, 9, 711–718. <https://doi.org/10.1038/s41558-019-0542-5>.
- NORSOK, 2007: NORSOK standard: Action and action effects, N-003. Tech. rep., Standard Norge, Postboks 242, 1326 Lysaker.
- Onogi, K., et al. (2007) The JRA-25 reanalysis. *Journal of the Meteorological Society of Japan*, 85(3), 369–432. <https://doi.org/10.2151/jmsj.85.369>.
- Poli, P., Hersbach, H., Dee, D.P., Berrisford, P., Simmons, A.J., Vitart, F., Laloyaux, P., Tan, D.G.H., et al. (2016) ERA-20C: an atmospheric reanalysis of the twentieth century. *Journal of Climate*, 29(11), 4083–4097. <https://doi.org/10.1175/JCLI-D-15-0556.1>.
- Rasmussen, E.A. and Turner, J. (2003) *Polar Lows: Mesoscale Weather Systems in the Polar Regions*. Cambridge: Cambridge University Press.
- Reistad, M., Breivik, Ø., Haakenstad, H., Aarnes, O.J., Furevik, B.R. and Bidlot, J.-R. (2011) A high-resolution hindcast of wind and waves for the North Sea, the Norwegian Sea, and the Barents Sea. *Journal of Geophysical Research*, 116, 18, C05 019 doi:10/fmnr2m.
- Rienecker, M.M., et al. (2011) MERRA: NASA's modern-era retrospective analysis for research and applications. *Journal of Climate*, 24 (14), 3624–3648. <https://doi.org/10.1175/JCLI-D-11-00015.1>.
- Saha, S., et al. (2010) The NCEP climate forecast system reanalysis. *Bulletin of American Meteorological Society*, 91(8), 1015–1057. <https://doi.org/10.1175/2010Bams3001.1>.
- Saha, S., et al. (2014) The NCEP climate forecast system version 2. *Journal of Climate*, 27, 2185–2208. <https://doi.org/10.1175/JCLI-D-12-00823.1>.
- Seity, Y., Brousseau, P., Malardel, S., Hello, G., Benard, P., Bouttier, F., Lac, C. and Masson, V. (2011) The AROME-France convective-scale operational model. *Monthly Weather Review*, 139(3), 976–991. <https://doi.org/10.1175/2010MWR3425.1>.
- Semedo, A., Sušelj, K., Rutgersson, A. and Sterl, A. (2011) A global view on the wind sea and swell climate and variability from ERA-40. *Journal of Climate*, 24(5), 1461–1479. <https://doi.org/10.1175/2010JCLI3718.1>.
- Semedo, A., Vettor, R., Breivik, Ø., Sterl, A., Reistad, M., Soares, C. G. and Lima, D.C.A. (2015) The Wind Sea and swell waves climate in the Nordic seas. *Ocean Dynamics*, 65(2), 223–240. <https://doi.org/10.1007/s10236-014-0788-4>.
- Sen, P. (1968) Estimates of the regression coefficient based on Kendall's tau. *Journal of the American Statistical Association*, 63, 1379–1389.
- Theil, H. (1950) A rank-invariant method of linear and polynomial regression analysis. I, II and III. *Proceedings of the Royal Netherlands Academy of Sciences*, 53, 386–392 521–525, 1397–1412.
- Uden, P., et al. 2002. Hirlam-5 scientific documentation. Tech. Rep. GKSS 97/E/46, SMHI, SMHI, SE-601 76 Norrköping, Sweden.
- Uppala, S., P. Kållberg, A. Simmons, and Coauthors, 2005: The ERA-40 re-analysis. *Quarterly Journal of the Royal Meteorological Society*, 131, 2961–3012. <https://doi.org/10.1256/qj.04.176>.
- Wang, X., Y. Feng, and V. Swail, 2012: North Atlantic wave height trends as reconstructed from the 20th century reanalysis. *Geophysical Research Letters*, 39, L18 705, 6. <https://doi.org/10.1029/2012GL053381>.
- Waseda, T., Webb, A., Sato, K., Inoue, J., Kohout, A., Penrose, B. and Penrose, S. (2018) Correlated increase of High Ocean waves and winds in the ice-free waters of the Arctic Ocean. *Scientific Reports*, 8(4489), 9. <https://doi.org/10.1038/s41598-018-22500-9>.
- Weisse, R. and Günther, H. (2007) Wave climate and long-term changes for the southern North Sea obtained from a high-resolution hindcast 1958–2002. *Ocean Dynamics*, 57(3), 161–172. <https://doi.org/10.1007/s10236-006-0094-x>.
- Weisse, R. and von Storch, H. (2010) *Marine Climate and Climate Change: Storms, Wind Waves and Storm Surges*. Berlin, Germany: Springer Science & Business Media, p. 219.
- Yang, X. (2005) Background blending using an incremental spatial filter. *Hirlam Newsletter*, 49, 3–11.
- Zong, Z. (Ed.). (2006) *Information-Theoretic Methods for Estimating of Complicated Probability Distributions*. Amsterdam, Netherlands: Elsevier Science, p. 298.

**How to cite this article:** Haakenstad H, Breivik Ø, Reistad M, Aarnes OJ. NORA10EI: A revised regional atmosphere-wave hindcast for the North Sea, the Norwegian Sea and the Barents Sea. *Int J Climatol*. 2020;40:4347–4373. <https://doi.org/10.1002/joc.6458>



## APPENDIX

### Offshore observations

Among the observation locations indicated in Figure 1, the stations 1–8 are offshore stations. Offshore stations typically observe winds at heights between 30 and 130 m. This adds uncertainty to the comparison to modelled 10-m wind speed. Observations in the North Sea and the Norwegian Sea are usually reduced to 10 m height along a power-law profile (Furevik and Haakenstad, 2012),

$$U(z) = U_{10} \left( \frac{z}{z_r} \right)^\alpha, \quad (\text{A1})$$

where  $U_{10}$  is the wind speed at the reference height  $z_r = 10$  m, and  $z$  is the observation height. It is customary to assume  $\alpha = 0.13$ , but it typically varies between 0.08 and 0.14 (Hsu *et al.*, 1994), and  $\alpha = 0.08$  is normally a better fit over the ocean (Furevik and Haakenstad, 2012). We have instead chosen the NORSOK profile (NORSOK, 2007),

$$U(z) = U_{10} \left( 1 + C \ln \frac{z}{z_r} \right) \quad (\text{A2})$$

where  $C = 5.73 \times 10^{-2} (1 + 0.15 U_{10})^{1/2}$ , as it was found by Furevik and Haakenstad (2012) to give a better match than the power law profile (A1). It is however more expensive as it involves a third-order polynomial which requires an iterative root-finding procedure for the reduction to 10 m height.

### Polar lows

It is of interest to qualitatively explore the development of polar lows in the two data sets to further assess the impact of changing the boundary conditions from ERA-40 to ERA-Interim. Polar lows are short-lived (less than 48 hr) meso-scale cyclones that are hard for numerical weather prediction models to capture (Rasmussen and Turner, 2003). It is known that NORA10 tends to underestimate the intensity of polar lows in the ERA-40 period (up to September 2002), and the lows typically do not continue to develop from one cycle to another (Haakenstad *et al.*, 2012). We will therefore first investigate if NORA10EI has an improved representation of polar lows compared to NORA10 forced by ERA-40 (before September 2002), and if the opposite is the case after August 2002.

Here, we have chosen to study four polar lows which evolve differently in NORA10 and NORA10EI. Two of the polar lows occur in the Barents Sea and two in the Norwegian Sea.

### ERA-40 period: Polar low case 1 (January 12, 2002)

Figure A1 shows the track of the January 12, 2002 Barents Sea polar low and the NOAA image of the cloud signature. The polar low was first observed in position 74°N and 28°E. It moved south-east and dissolved after 15 hr hitting Novaya Zemlya. Figure A2 shows the evolution of the mean sea level pressure field in NORA10 and in NORA10EI and near-surface wind speed exceeding 14 m·s<sup>-1</sup> from NORA10EI. The polar low is well

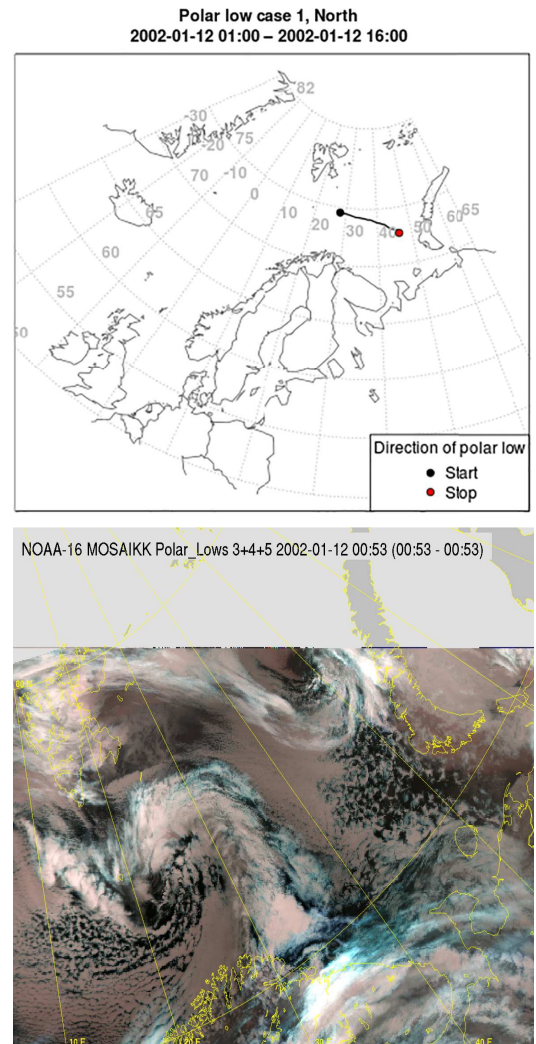


**FIGURE A1** Track and NOAA-image of polar low January 12, 2002. Source: STARS database

represented in NORA10EI. The cyclone has a mean sea level pressure of 980 hPa in the first-time step which decreases to 976 hPa after 13 hr. The maximum wind

speed increases from  $18 \text{ m}\cdot\text{s}^{-1}$  in the first-time step to  $24 \text{ m}\cdot\text{s}^{-1}$  after 13 hr. NORA10 does not produce a cyclone until 5 hr later than observed and has a minimum mean

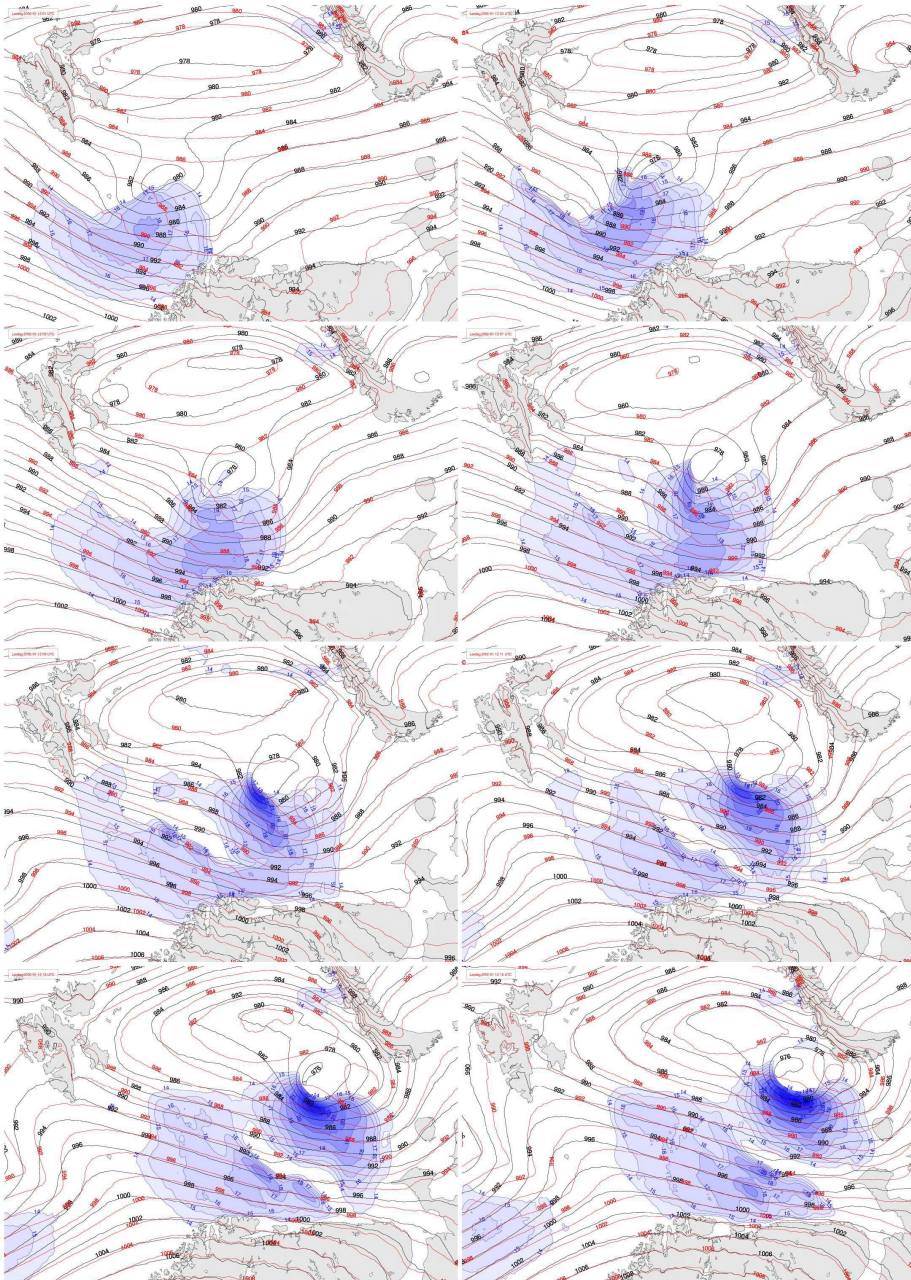


**FIGURE A2** Polar low case January 12, 2002. Mean sea level pressure from NORA10EI (black) and NORA10 (red) and wind speed exceeding  $14 \text{ m}\cdot\text{s}^{-1}$  from NORA10EI (blue)

sea level pressure of 982 hPa. Maximum wind speed in NORA10 is  $16 \text{ m}\cdot\text{s}^{-1}$ . The conclusion from this polar low is that NORA10EI reproduces the polar low very well, while NORA10 shows a too late and too weak evolution.

#### ERA-40 period: Polar low case 2 (March 9, 2002)

Figure A3 shows the track of the March 9, 2002 Jan Mayen polar low and the NOAA-image of the cloud signature. The cloud image shows a characteristic comma-shaped pattern which suggests a typical wave cyclone near occlusion (Douglas *et al.*, 1995). The polar low was first observed just south of Jan Mayen with the vortex position  $70^\circ\text{N}$  and  $5^\circ\text{W}$  at 11 UTC, 9 March 2002. The polar low moved southward to the final observed position  $65.5^\circ\text{N}$  and  $1.5^\circ\text{W}$  22 hr later. Figure A4 shows the evolution of the mean sea level pressure field in NORA10 and in NORA10EI together with the near-surface wind speed exceeding  $14 \text{ m}\cdot\text{s}^{-1}$  from NORA10EI. The polar low occurs in the rear of a synoptic scale cyclone hitting Trøndelag at the time step when the polar low was first observed. The polar low is not a fully developed vortex in neither NORA10 nor NORA10EI in the first-time step, but shows up in NORA10EI as a cyclone 6 hr later than first observed and last for the rest of the observed period. NORA10 shows a polar low 8 hr later than first observed and this polar low does only last for 3 hr. According to these two situations, NORA10EI shows an improved representation of the polar lows compared to NORA10.

#### After ERA-40: Polar low case 3 (January 7, 2009)

The third polar low investigated, occurred in the Barents Sea 7 January 2009 and lasted for 7 hr. SAR winds of above  $25 \text{ m}\cdot\text{s}^{-1}$  were observed in the Barents Sea and part of the coast of Finnmark. At Banak airport located sheltered in the innermost part of the Porsanger fjord, wind speed of  $13 \text{ m}\cdot\text{s}^{-1}$  and wind gust of  $17 \text{ m}\cdot\text{s}^{-1}$  were observed. Figure A5 shows the track of the polar low and the NOAA image of the cloud signature. Figure A6 shows the evolution of the mean sea level pressure field in NORA10 and in NORA10EI and near-surface wind speed exceeding  $14 \text{ m}\cdot\text{s}^{-1}$  from NORA10. The location of the polar low is the same in NORA10 and NORA10EI. The location fits quite well with the observed polar low, but is somewhat too far east of the observed one. The polar low is fully developed in NORA10 at 04:00 UTC and in NORA10EI 1 hr later. NORA10 shows a maximum wind speed of  $26 \text{ m}\cdot\text{s}^{-1}$  which last for the whole period of the polar low. This wind speed values fits the SAR

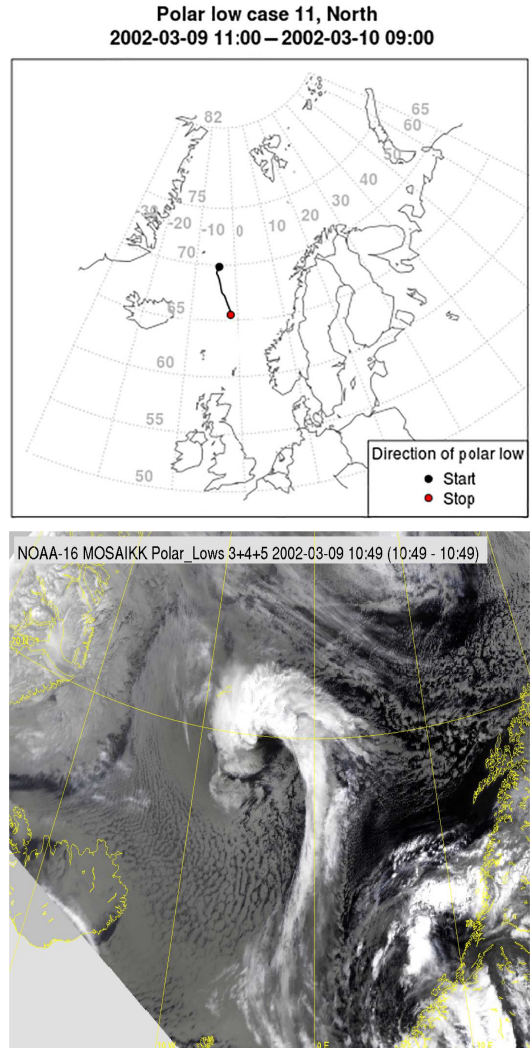


**FIGURE A3** Track and NOAA-image of polar low March 9, 2002. Source: STARS database

observations. NORA10EI shows somewhat lower wind speed and reaches  $26 \text{ m}\cdot\text{s}^{-1}$  at just one-time step (2009-01-07 08:00).

#### After ERA-40: Polar low case 3 (7 January 2009)

The fourth polar low appeared in the Norwegian Sea at 18:00 UTC 26 February 2009 and lasted until 11:00 UTC 27 February. The Stars database<sup>3</sup> describes the polar low

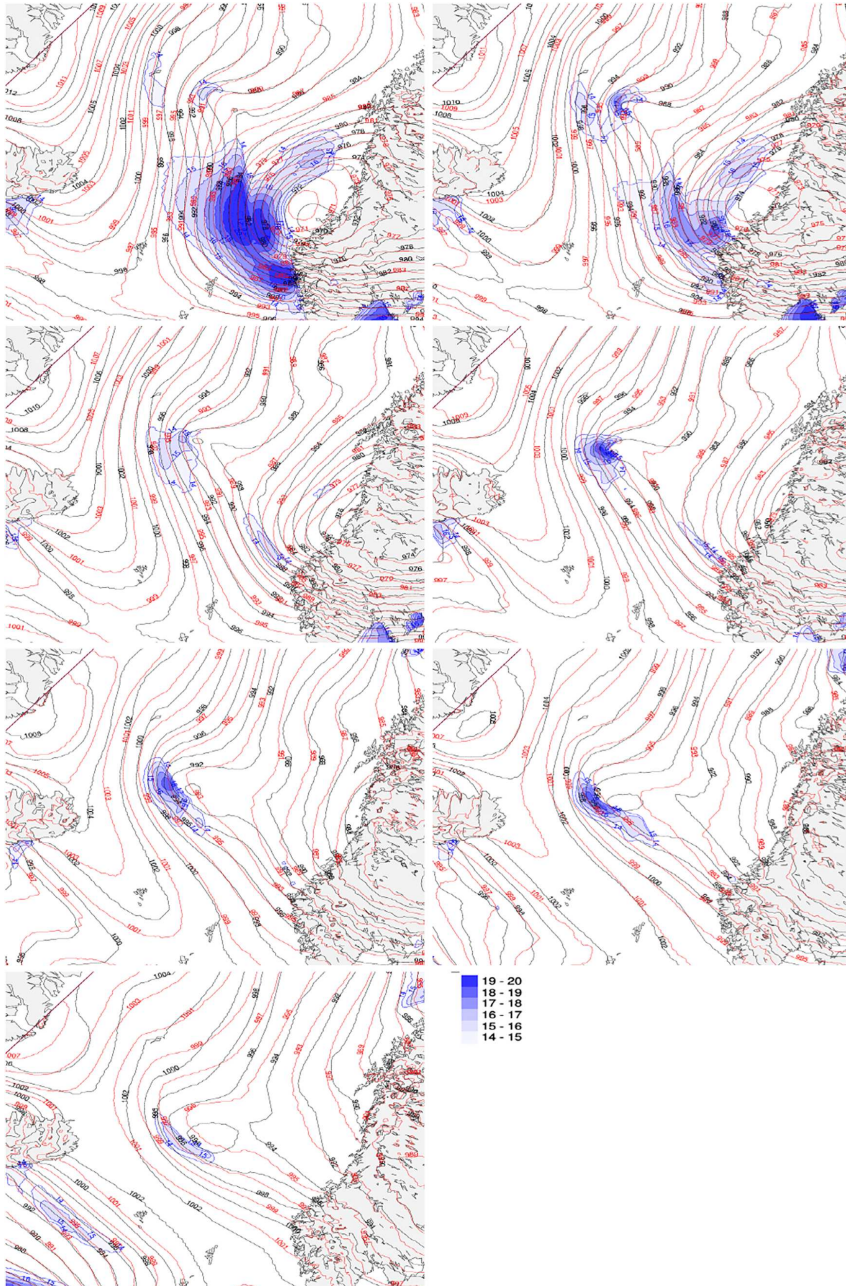


**FIGURE A4** Polar low case March 9, 2002. Mean sea level pressure from NORA10EI (black) and NORA10 (red) and wind speed exceeding  $14 \text{ m s}^{-1}$  from NORA10EI (blue)

as a classic version formed off the coast of Troms with a cold-air outbreak and a strong cold upper trough as precursors to the polar low. Southwest of the main low, a

secondary, less intense centre formed. An inversion layer north east of the northern centre was broken by heating from air above the sea surface, intensifying the polar low.

**Polar low case 39, North**  
2009-01-07 03:00 – 2009-01-07 10:00

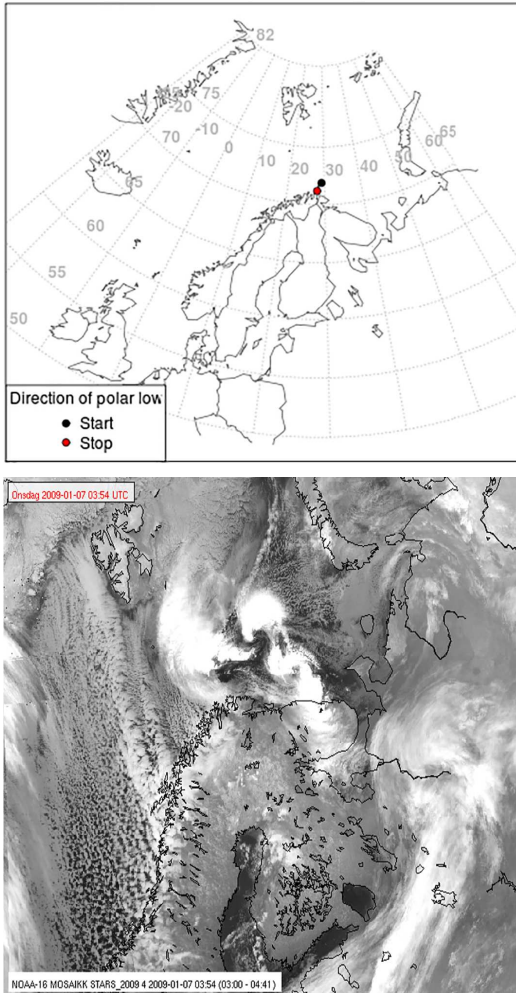


**FIGURE A5** Track and NOAA-image of polar low January 7, 2009. Source: STARS database

The low made landfall at the coast of the Nordland in northern Norway with a maximum observed wind speed of  $23 \text{ m}\cdot\text{s}^{-1}$ . Wind gusts up to  $28 \text{ m}\cdot\text{s}^{-1}$  were observed. Figure A7 shows the track of the polar low and the NOAA-image of the cloud signature. Figure A8 shows that a polar low off the coast of Troms in northern Norway with a minimum mean sea level pressure of 989 hPa is present in both NORA10 and NORA10EI. However, the low is more extensive in NORA10 compared to

NORA10EI. NORA10 shows the overall deepest mean sea level pressure throughout the lifetime of the low. NORA10 wind speed reached  $24 \text{ m}\cdot\text{s}^{-1}$  at 02:00 UTC February 27, 2009, comparable, but slightly stronger than the NORA10EI wind speed ( $23 \text{ m}\cdot\text{s}^{-1}$ ). The maximum wind speeds in the models occur offshore and becomes strongly weakened before landfall.

Although no firm conclusions can be drawn from these four case studies, it seems clear that the polar lows are better represented by NORA10EI in the period up to September 2002 when ERA-40 was used as boundary conditions for NORA10, and conversely that NORA10 captures the polar lows better in the period after August 2002.

### Trend analysis

The non-parametric Mann–Kendall (Mann, 1945; Kendall, 1975) and Sen's (Theil, 1950; Sen, 1968) method were used in the trend analysis of the 50th, 95th and 99th percentile wind speed in Section 6. The Mann–Kendall trend test is a frequently used test for monotonic trend in a time series based on Kendall rank correlation. The Mann–Kendall test statistic or score  $S$  is calculated as

$$S = \sum_{i=1}^{n-1} \sum_{j=i+1}^n \text{sgn}(x_j - x_i) \quad (\text{A3})$$

where  $n$  is the length of the time series,  $x$  is the data values in the time series, and  $\text{sgn}$  is the sign function;

$$\text{sgn}(x_j - x_i) = \begin{cases} +1, & \text{if } x_j - x_i > 0 \\ 0, & \text{if } x_j - x_i = 0 \\ -1, & \text{if } x_j - x_i < 0. \end{cases} \quad (\text{A4})$$

The variance is calculated as

$$\text{var}(S) = \frac{n(n-1)(2n+5) - \sum_{i=1}^m t_i(t_i-1)(2t_i+5)}{18} \quad (\text{A5})$$

where data having the same value in the sample, have been tied up in groups.  $m$  is the number of tied groups and  $t_i$  is the number of ties of extent  $i$ . With the requirement of a sample size which is greater than 10, the standard normal test statistic  $Z_s$  is computed as

$$Z_s = \begin{cases} \frac{S-1}{\sqrt{\text{var}(S)}}, & \text{if } S > 0 \\ 0, & \text{if } S = 0 \\ \frac{S+1}{\sqrt{\text{var}(S)}}, & \text{if } S < 0. \end{cases} \quad (\text{A6})$$

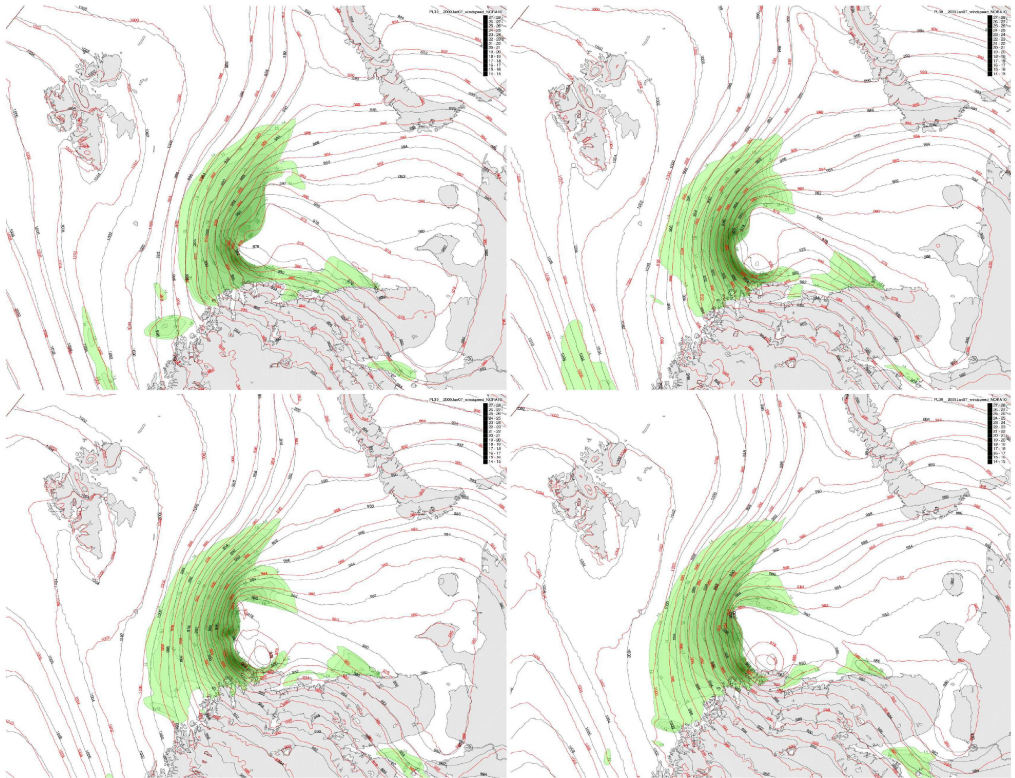


**FIGURE A6** Polar low case January 7, 2009. Mean sea level pressure from NORA10EI (black) and NORA10 (red) and wind speed exceeding  $14 \text{ m s}^{-1}$  from NORA10 (green)

If  $Z_s$  is positive, the trend is increasing and opposite, if  $Z_s$  is negative the trend is decreasing. The trend test is done at significance level  $\alpha = 0.1$ . Sen's slope is used to determine the strength of the trend, calculated as the median of the slopes in the time series,

$$Q_i = \text{median} \left( \frac{x_j - x_k}{j - k} \right). \tag{A7}$$

**Polar low case 44, North**  
2009-02-26 18:00 – 2009-02-27 11:00

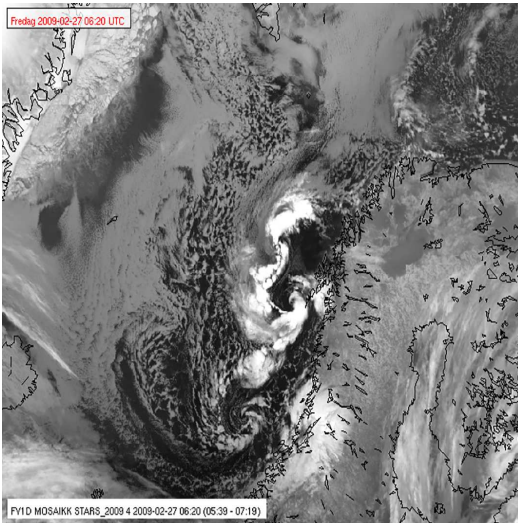
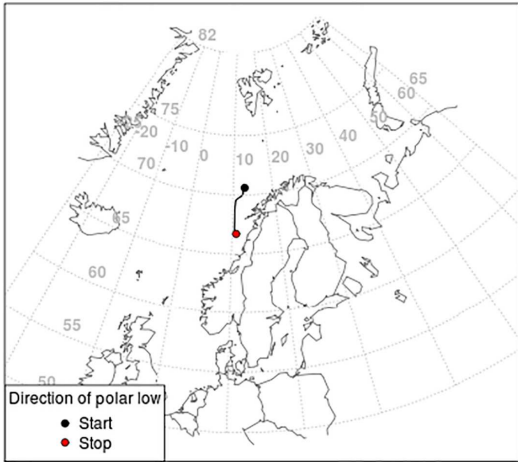
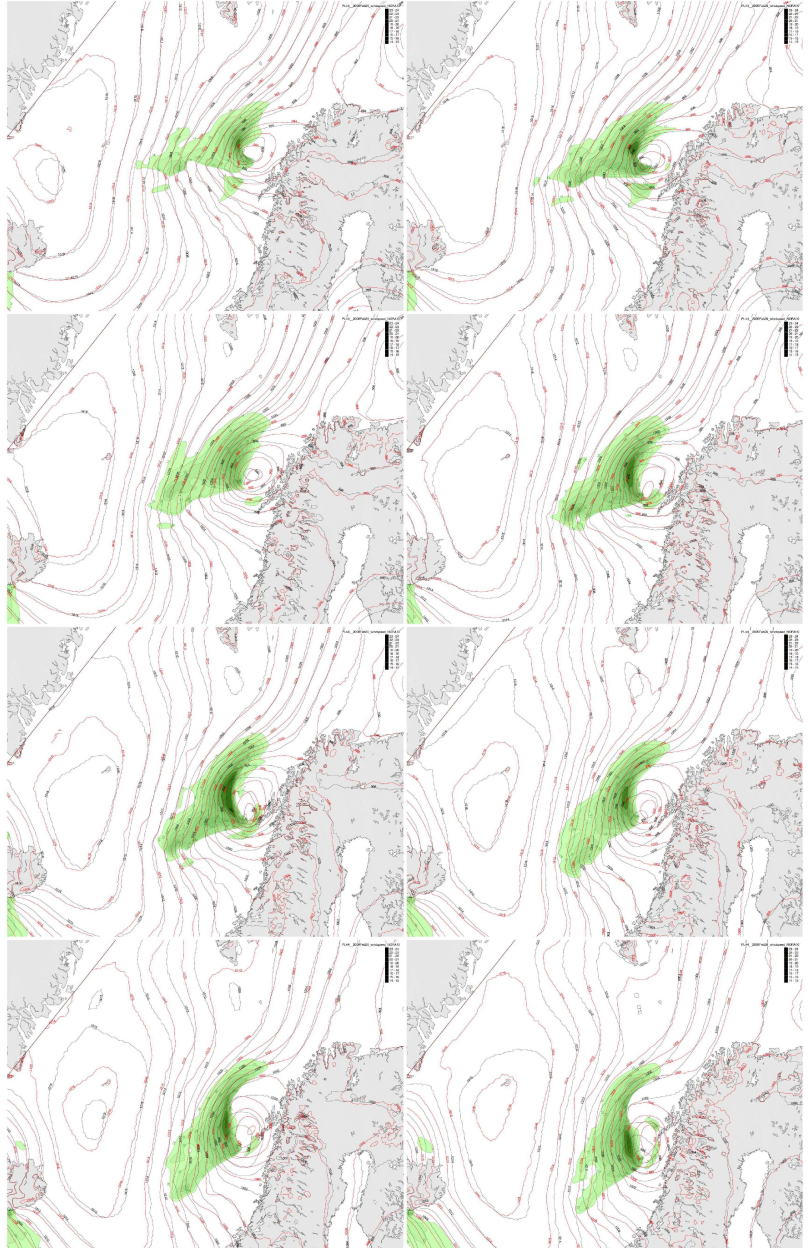


**FIGURE A7** Track and NOAA-image of polar low February 26, 2009. Source: STARS database

**FIGURE A8** Polar low case 26 and February 27, 2009. Mean sea level pressure from NORA10EI (black) and NORA10 (red) and wind speed exceeding  $14 \text{ m s}^{-1}$  from NORA10 (green)







# Paper II

## **NORA3: A nonhydrostatic high-resolution hindcast of the North Sea, the Norwegian Sea, and the Barents Sea**

H. Haakenstad and Ø. Breivik and B. R. Furevik and M. Reistad and P. Bohlinger and O J. Aarnes

*Journal of applied meteorology and climatology*, **60**(10), 2021



## 🔗 NORA3: A Nonhydrostatic High-Resolution Hindcast of the North Sea, the Norwegian Sea, and the Barents Sea

HILDE HAAKENSTAD,<sup>a,b</sup> ØYVIND BREIVIK,<sup>a,b</sup> BIRGITTE R. FUREVIK,<sup>a,b</sup> MAGNAR REISTAD,<sup>a</sup>  
PATRIK BOHLINGER,<sup>a</sup> AND OLE JOHAN AARNES<sup>a</sup>

<sup>a</sup> Norwegian Meteorological Institute, Oslo, Norway

<sup>b</sup> Geophysical Institute, University of Bergen, Bergen, Norway

(Manuscript received 18 February 2021, in final form 25 June 2021)

**ABSTRACT:** The 3-km Norwegian Reanalysis (NORA3) is a 15-yr mesoscale-permitting atmospheric hindcast of the North Sea, the Norwegian Sea, and the Barents Sea. With a horizontal resolution of 3 km, the nonhydrostatic numerical weather prediction model HARMONIE-AROME runs explicitly resolved deep convection and yields hindcast fields that realistically downscale the ERA5 reanalysis. The wind field is much improved relative to its host analysis, in particular in mountainous areas and along the improved grid-resolving coastlines. NORA3 also performs much better than the earlier hydrostatic 10-km Norwegian Hindcast Archive (NORA10) in complex terrain. NORA3 recreates the detailed structures of mesoscale cyclones with sharp gradients in wind and with clear frontal structures, which are particularly important when modeling polar lows. In extratropical windstorms, NORA3 exhibits significantly higher maximum wind speeds and compares much better to observed maximum wind than do NORA10 and ERA5. The activity of the model is much more realistic than that of NORA10 and ERA5, both over the ocean and in complex terrain.

**SIGNIFICANCE STATEMENT:** The 3-km Norwegian Reanalysis (NORA3) hindcast offers the first kilometer-scale climatological description produced with nonhydrostatic model physics of the North Sea, the Norwegian Sea, and the Barents Sea. With a horizontal resolution of 3 km, the nonhydrostatic numerical weather prediction model resolves deep convection and yields hourly hindcast fields (2004–18) that realistically downscale the recent ERA5 reanalysis. The wind field is greatly improved relative to its host analysis, in particular in mountainous areas and along the improved grid-resolving coastlines. NORA3 also performs much better than the earlier hydrostatic 10-km Norwegian Hindcast Archive (NORA10) in complex terrain. NORA3 is also better at reproducing the detailed structures of polar lows and comes closer to the maximum wind observed in extratropical windstorms than do NORA10 and ERA5.

**KEYWORDS:** Arctic; North Atlantic Ocean; Wind; Climatology; Storm environments; Nonhydrostatic models; Reanalysis data; Coastal meteorology; Mountain meteorology; Orographic effects; Wind effects

### 1. Introduction

High-resolution atmospheric hindcast archives are essential to assessing the detailed wind climate in the coastal zone and in complex terrain. They also provide forcing for nearshore wave hindcasts (Gaslikova and Weisse 2006; Breivik et al. 2009; Christakos et al. 2020a,b). Although global atmospheric reanalyses with sophisticated data assimilation systems yield the best possible overall accounts of past synoptic weather situations, their resolution is too coarse to adequately resolve mesoscale features. The latest reanalysis from the European Centre for Medium-Range Weather Forecasts (ECMWF), ERA5, has a horizontal resolution of 31 km (Hersbach et al. 2020) and a vertical resolution of 137 levels. Other recent reanalyses, such as MERRA (Rienecker et al. 2011) and the NCEP Climate Forecast System Reanalysis (CFSR; Saha et al.

2010) and its updated version 2, CFSRv2 (Saha et al. 2014), as well as the older ECMWF analyses ERA-40 (Uppala et al. 2005) and ERA-Interim (Dee et al. 2011), have horizontal resolutions ranging from about 50 km to 1.5°. The resolution of such global reanalyses is generally so coarse that winds in extratropical systems tend to be biased toward lower values (Hodges et al. 2011). This makes them unsuitable for studies of mesoscale phenomena, both marine and terrestrial [see Moore et al. (2015) and Moore et al. (2016) for a detailed account of the impact of resolution on the topographic flow in complex terrain]. Mesoscale polar lows (Rasmussen and Turner 2003; Førre et al. 2011) are not even properly modeled at a resolution of 10 km (Reistad et al. 2011; Haakenstad et al. 2020). It is also evident that extremes will be biased toward lower values in global reanalyses, whether these are related to synoptic or mesoscale systems (Breivik et al. 2013, 2014; Breivik and Aarnes 2017; Meucci et al. 2018; Takbash et al. 2019).

From a practical point of view, extreme value estimates and other statistics of marine wind and wave climate are crucial for the assessment of safe shipping (Bitner-Gregersen et al. 2018), wind energy assessment (Furevik and Haakenstad 2012) and construction of coastal and offshore structures (Donelan and Magnusson 2017; Gramstad et al. 2018). It is therefore important that biases in the upper percentiles of hindcasts and

🔗 Denotes content that is immediately available upon publication as open access.

Breivik's ORCID: 0000-0002-2900-8458.

Corresponding author: Øyvind Breivik, oyvind.breivik@met.no

DOI: 10.1175/JAMC-D-21-0029.1

© 2021 American Meteorological Society. For information regarding reuse of this content and general copyright information, consult the [AMS Copyright Policy](#) ([www.ametsoc.org/PUBSReuseLicenses](http://www.ametsoc.org/PUBSReuseLicenses)).

reanalyses used for extreme value estimation are properly accounted for.

Long-term historical archives of extremes are also important for gauging changes in marine wind and wave climate, even if trends are notoriously difficult to assess from reanalyses (Aarnes et al. 2015; Meucci et al. 2020). While there is a growing consensus that an increase in wind speed and wave height is likely in the southern extratropics under a warmer climate (Morim et al. 2019), it is still unclear how the wind climate in the northern extratropics will change in the future (Shimura et al. 2016; Aarnes et al. 2017; Bricheno and Wolf 2018; Catto et al. 2019; Morim et al. 2017).

The model performance in this hindcast study is measured primarily in terms of surface wind speed. This has a practical motivation, because the 10-m wind is the single most important parameter for marine and coastal climate and is the only atmospheric variable to directly affect a wave model.

Covering the North Sea, the Norwegian Sea, and the Barents Sea, the nonhydrostatic (NH) convection-permitting numerical weather prediction (NWP) model, HIRLAM-ALADIN Research on Mesoscale Operational NWP in Euromed—Applications of Research to Operations at Mesoscale (HARMONIE-AROME) has been set up on a 3-km horizontal resolution grid with 65 vertical levels. ERA5 reanalysis fields (Hersbach et al. 2020) provided the initial and boundary conditions. In addition, a surface analysis was performed to refine the initial conditions of each integration cycle. Utilizing a high-resolution nonhydrostatic NWP model such as HARMONIE-AROME allows modeling of atmospheric features having comparable scales in the vertical and horizontal dimension. Thunderstorms, squall lines, and orographically induced gravity waves are examples of features requiring the full nonhydrostatic equations to be modeled realistically.

This article is organized as follows: The HARMONIE-AROME model setup and its ERA5 boundary conditions are presented in section 2. Results from the 15-yr hindcast integration are presented and its performance in coastal, maritime, and mountain regions assessed in section 3. Section 4 discusses the findings and the applicability of the archive for estimates of mean and extreme wind climatology.

## 2. Model setup

The nonhydrostatic convection-permitting numerical weather prediction model HARMONIE-AROME, Cy 40h1.2, is used in the downscaling of the ERA5 reanalyses. AROME takes its adiabatic part from the nonhydrostatic ALADIN model (Bubnová et al. 1995; ALADIN International Team 1997; Bénard et al. 2010) and its physical parameterizations from Meso-NH (Lafore et al. 1998). The AROME model has been running operationally as the national short range model by Météo-France since December 2008. The fundamentals of AROME are described by Seity et al. (2011) and Brousseau et al. (2016). The HARMONIE-AROME version is developed and maintained as part of the shared ALADIN-HIRLAM system (Bengtsson et al. 2017). The HARMONIE-AROME became operational for the Nordic Meteorological Cooperation on Operational Numerical Weather Prediction (MetCoOp)

domain in 2013 (Müller et al. 2017b) and an extended version (AROME-Arctic) is also running operationally for the Arctic domain (Müller et al. 2017a). The changes introduced in Cycle 40 relative to the earlier Cycle 38 are described by HIRLAM Consortium (2016).

Here, we have set up a 3-km horizontal resolution domain that covers the Norwegian Sea, the North Sea, the Barents Sea, and the Baltic Sea ( $900 \times 1500$  grid points, see Fig. 1). The model runs on a Lambert conformal conic grid with its central meridian at  $42^\circ\text{W}$ . The latitude of its projection origin and standard parallel is  $66.3^\circ\text{N}$ . The use of 3-km grid resolution is coarser than the AROME-based operational models, which typically run at 2.5-km-or-higher resolution. The 3-km Norwegian Reanalysis (NORA3) grid could be on the limit for which deep convection should be partly parameterized as a subgrid process in addition to the permitted deep convection. Too-low resolution could potentially cause unrealistic precipitation (Deng and Stauffer 2006). An upper resolution limit of 2.5 km has been recommended by several studies (Gerard et al. 2009; Malardel 2013; Yano et al. 2018). Here we have chosen 3 km as an affordable compromise that allows us to cover the entire Norwegian Sea. Although this is slightly coarser than what is commonly used, we find that the performance is comparable to that of the operational 2.5-km model domain (see the appendix).

In NORA3, the HARMONIE-AROME runs have been organized as a sequence of short prognostic runs (see appendix Table A1 and Fig. A2). The nonhydrostatic fully compressible Euler equations are discretized by a semi-Lagrangian (SL) advection scheme without horizontal staggering. The stable extrapolation two-time-level scheme (SETTLS; see Hortal 2002) is applied to ensure stable integration. In the first time steps, a limit on the three-dimensional divergence is applied to avoid problems when initializing from a lower-resolution host model (Bengtsson et al. 2017).

### a. The nonhydrostatic model formulation

The evolution equations use a terrain-following pressure-based vertical  $\sigma$  coordinate (Simmons and Burridge 1981; Laprise 1992) on 65 levels (similar to the operational model; Müller et al. 2017b) with the lowest level at 12 m and the uppermost level at 10 hPa. The time step is 60 s. The model comprises 12 three-dimensional prognostic variables; five hydrometeors (rain, snow, graupel, cloud droplets, and ice crystals), horizontal wind, temperature, specific water vapor content, and turbulent kinetic energy. In addition to these 10 prognostic variables are two nonhydrostatic variables related to pressure and vertical momentum (see Bénard et al. 2010).

### b. Surface analysis

Surface fields are taken from the previous forecast of NORA3 but adjusted to applicable observations through a surface analysis that is a combination of Code d'Analyse Nécessaire à ARPEGE pour ses Rejets et son Initialization (CANARI; see Giard and Bazile 2000; Le Moigne et al. 2012; Taillefer 2002) and Surface Externalisée (SURFEX; Masson et al. 2013) (CANARI-OI-Main). In CANARI-OI-Main, the

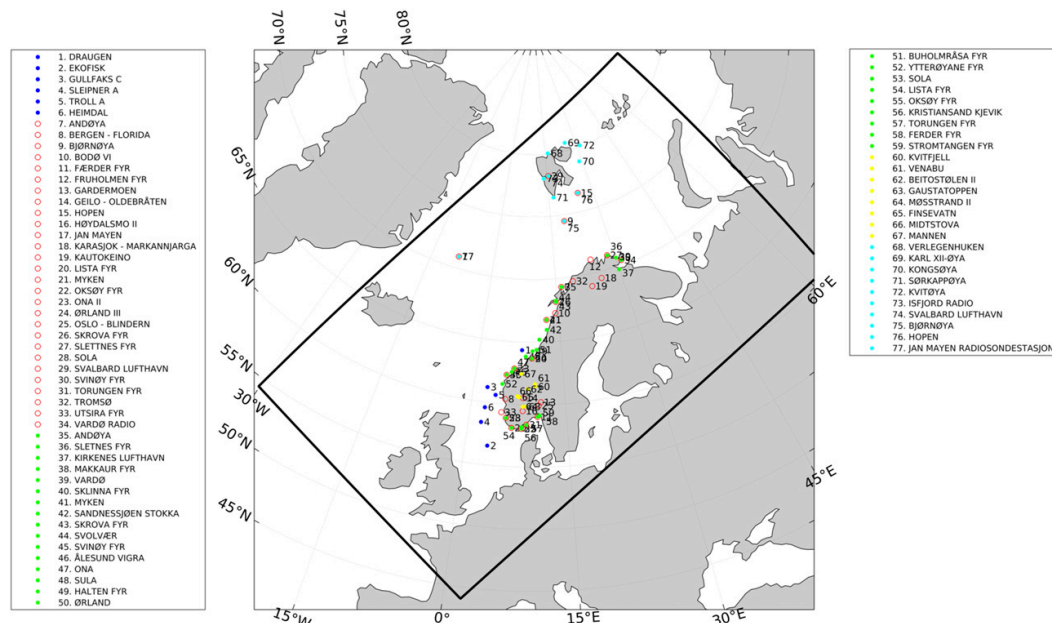


FIG. 1. Map showing the NOR3 domain and location of observation stations. Blue dots indicate maritime stations, red open circles are reference stations, green dots are coastal stations, yellow dots are mountain stations, and light-blue dots are Arctic stations.

analysis increment is calculated using an optimum interpolation method (Daley 1991). The method starts with a general initialization and continues with a quality control that selects pertinent observations before the analysis of the different fields is performed. The formulation of the optimum interpolation is

$$\mathbf{x}_a = \mathbf{x}_g + \mathbf{P}\mathbf{H}^T(\mathbf{O} + \mathbf{H}\mathbf{P}\mathbf{H}^T)^{-1}(\mathbf{H}\mathbf{x}_g - \mathbf{y}). \quad (1)$$

Here,  $\mathbf{x} \in R^n$  is the state vector of the atmosphere (all prognostic variables in all grid points  $n$ ),  $\mathbf{y} \in R^m$  is the observation vector of length  $m$ ,  $\mathbf{O} \in R^{m \times m}$  is the variance-covariance matrix of the observation errors (assumed to be diagonal),  $\mathbf{P} \in R^{n \times n}$  is the variance-covariance matrix of the model errors (first-guess errors), and  $\mathbf{H}$  is the observation operator, which here is supposed to be linear (Taillefer 2002). Subscripts “a” and “g” denote analysis and first guess, respectively. Soil moisture and soil temperature are corrected in the Interactions between Soil, Biosphere, and Atmosphere (ISBA) land surface model running within the surface module (SURFEX; see below) using the updated information from the screen-level observation output from CANARI.

c. Physical parameterizations

HARMONIE-AROME uses microphysics that is a three-class ice parameterization of cloud ice, snow, and a combination of graupel and hail (ICE3; Pinty and Jabouille 1998; Lascaux et al. 2006). The microphysics also comprises water vapor, cloud liquid water, and rain. The microphysics runs with the option “OCND2,” which improves clouds in cold

conditions (Müller et al. 2017b). Rainprod activation is parameterized by the Kogan autoconversion (Khairoutdinov and Kogan 2000). Shallow convection is parameterized in the eddy diffusivity mass flux (EDMF-M) scheme (Siebesma et al. 2003, 2007; de Rooy and Siebesma 2008, 2010). Turbulence is represented in the HARMONIE with RACMO Turbulence (HARATU) parameterization (van Meijgaard et al. 2012; Lenderink and Holtslag 2004). HARATU uses a prognostic equation for the turbulent kinetic energy combined with a diagnostic length scale. HARATU distinguishes between stable condition and near-neutral to convective conditions. For radiation, the Rapid Radiative Transfer Model (RRTM) (Mlawer et al. 1997) is used for longwave radiation, while shortwave runs the ECMWF operational shortwave (SW) scheme (ECMWF 1989). Aerosols and ozone are based on monthly climatologies.

d. Land and ocean surface processes

The land and ocean surface module used in HARMONIE-AROME is the comprehensive SURFEX model (Masson et al. 2013), consisting of four different models that represent nature, lakes and rivers, urban regions, and sea as different tiles. Exchanges of meteorological and radiative fields connect the atmospheric model and the SURFEX model. Each surface grid cell receives basic atmospheric fields, the air temperature, specific humidity, the horizontal wind components, pressure, total precipitation, and longwave radiation as well as the shortwave direct and diffuse radiation. SURFEX then computes the averaged fluxes for momentum and sensible and

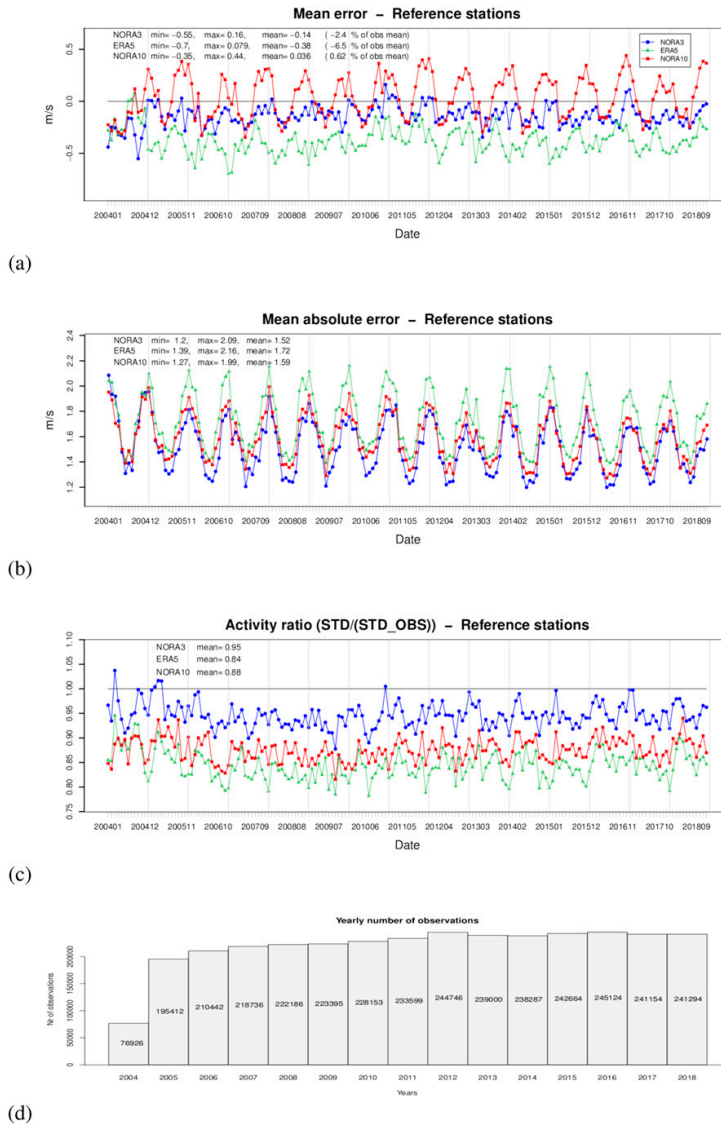


FIG. 2. Time series of NORA3 (blue), NORA10 (red), and ERA5 (green) (a) mean error, (b) MAE, and (c) the AR. (d) The yearly number of observations used in the validation. All statistics were computed for the period 2004–18.

latent heat that serve as lower boundary conditions for the atmospheric radiation and turbulent schemes (Le Moigne et al. 2012).

The sea surface and the atmosphere are connected through the Unified Multicampaigns Estimates (ECUME) scheme (Weill et al. 2003; Belamari 2005; Belamari and Pirani 2007). ECUME is a bulk parameterization scheme with neutral transfer coefficients at 10 m estimated from a multicampaign

calibration derived from the AUTOFLUX Linked Base for Atmospheric Transfer at the Ocean Surface (ALBATROS) database, which collected data from different flux measurement campaigns (Weill et al. 2003). Sea surface roughness is parameterized as (Smith 1988)

$$z_0 = \frac{\alpha u_*^2}{g} + \frac{\beta \nu}{u_*}, \tag{2}$$

TABLE 1. Reference stations' 10-m wind speed statistics (2004–18). The best performance (in comparison with the observed 10-m wind speed) is marked in boldface type.

	Jan	Feb	Mar	Apr	May	Jun	Jul	Aug	Sep	Oct	Nov	Dec
	<i>Monthly mean values</i>											
Obs ( $m s^{-1}$ )	6.84	6.43	6.23	5.54	5.24	5.03	4.71	4.71	5.54	6.08	6.49	6.73
NORA3 ( $m s^{-1}$ )	<b>6.76</b>	<b>6.38</b>	6.13	5.40	<b>5.03</b>	<b>4.82</b>	4.53	4.56	5.38	<b>5.92</b>	<b>6.36</b>	<b>6.67</b>
ERA5 ( $m s^{-1}$ )	6.40	6.00	5.76	5.10	4.79	4.59	4.35	4.41	5.30	5.78	6.11	6.34
NORA10 ( $m s^{-1}$ )	7.07	6.60	<b>6.24</b>	<b>5.44</b>	5.02	4.82	<b>4.56</b>	<b>4.67</b>	<b>5.65</b>	6.31	6.72	7.00
	<i>Deviation from obs</i>											
NORA3 (%)	<b>-1.2</b>	<b>-0.8</b>	-1.5	-2.4	<b>-3.9</b>	<b>-4.1</b>	-3.8	-3.2	-2.9	<b>-2.6</b>	<b>-2.0</b>	<b>-0.8</b>
ERA5 (%)	-6.4	-6.8	-7.5	-8.0	-8.5	-8.7	-7.7	-6.5	-4.4	-4.9	-5.7	-5.7
NORA10 (%)	3.3	2.6	<b>0.2</b>	<b>-1.8</b>	-4.1	-4.2	<b>-3.3</b>	<b>-0.9</b>	<b>2.1</b>	3.7	3.7	4.0

where  $\alpha$  is the Charnock constant (here  $\alpha$  is assumed to take the value 0.011; see Charnock 1955). Furthermore,  $\beta$  is a numerical constant,  $g$  is the gravitational acceleration, and  $\nu$  is the kinematic viscosity coefficient. The ECUME scheme is summarized in appendix Table A2.

Surface types are extracted from the ECOCLIMAP2 database (Faroux et al. 2013). ECOCLIMAP2 is a 1-km-resolution database based on satellite information. Surface topography is

defined by Global Multi-Resolution Terrain Elevation Data 2010 (GMTED2010; Danielson and Gesch 2011).

*e. Forcing data*

ERA5 (Hersbach et al. 2020) is the newest reanalysis from ECMWF. It is produced as part of the Copernicus Climate Change Service (C3S). ERA5 is based on the Integrated Forecasting System (IFS) Cy41r2. The horizontal resolution of

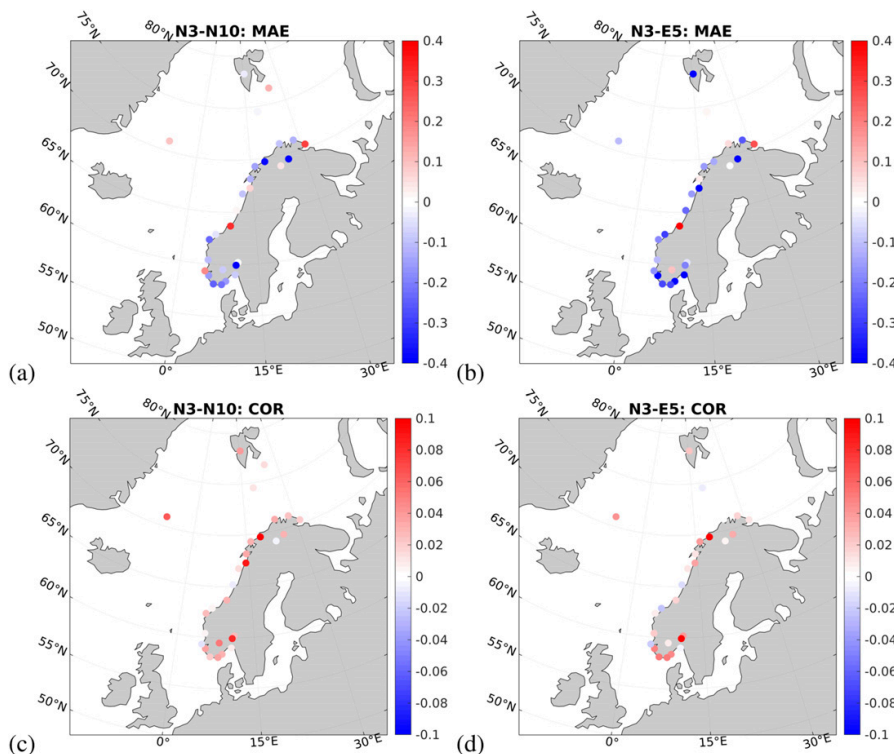


FIG. 3. Difference [(a) NORA3 – NORA10; (b) NORA3 – ERA5] of MAEs on reference stations (blue when NORA3 has lower MAE). Also shown is a comparison of Pearson's correlation coefficient (red when NORA3 scores higher); (c) NORA3 – NORA10; (d) NORA3 – ERA5. All statistics were computed for the period 2004–18.



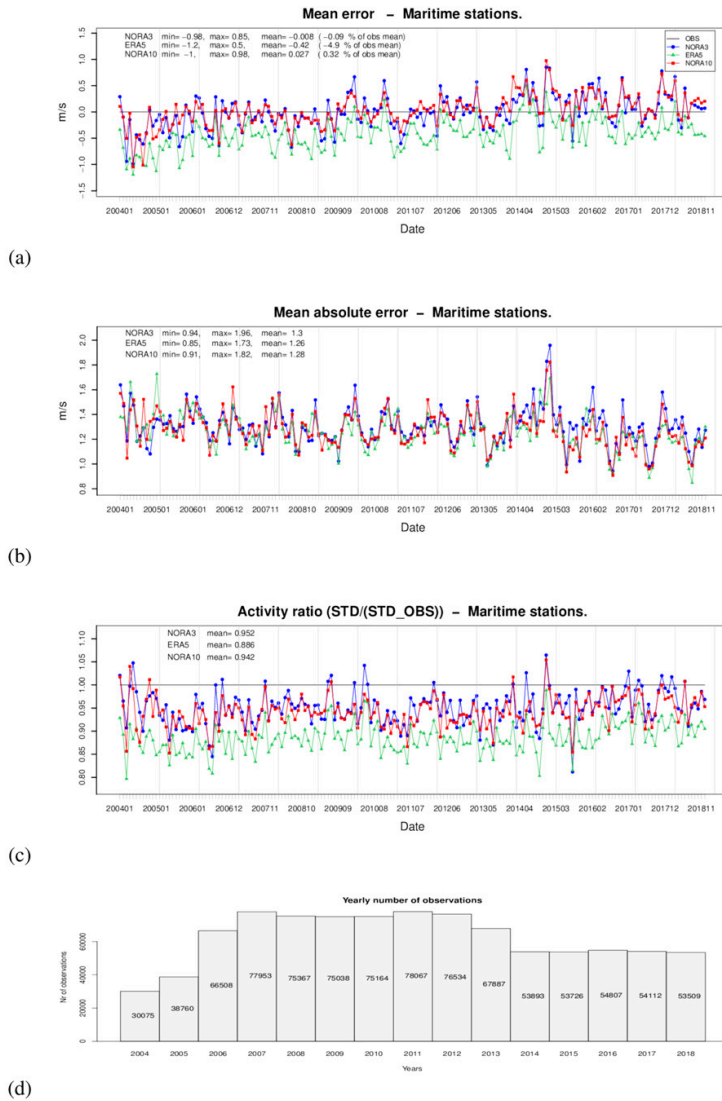


FIG. 4. As in Fig. 2, but for the maritime stations.

ERA5 is 31 km. ERA5 has been shown (Hersbach et al. 2020) to provide considerably better wind, temperature, humidity, and precipitation fields than the earlier, coarser (79 km), ERA-Interim reanalysis (Dee et al. 2011). Its performance over the open ocean is generally considered to be very good (Rivas and Stoffelen 2019). Renfrew et al. (2021) also note that ERA5 performs well in terms of wind and turbulent fluxes over the open ocean but found that its performance in the marginal ice zone is significantly poorer. They attributed the difference in quality to excessively smooth sea ice distribution in the surface boundary conditions.

Here we start each prognostic run from an initialized model state built from an analyzed surface field and a simple upper-air blending with ERA5 fields. Upper-air temperature, specific humidity, and the zonal and meridional wind components are taken from ERA5 and interpolated to the high-resolution grid. The remaining upper-air prognostic variables are taken from the first guess, that is, the last forecast valid at the start of the new forecast (see Fig. A3). Observations used by the surface analysis are all land and sea surface measurements retrieved from ECMWF’s Meteorological Archival and Retrieval System (MARS).

TABLE 2. Maritime stations' 10-m wind speed statistics (2004–18). The best performance (in comparison with the observed 10-m wind speed) is marked in boldface type.

	Jan	Feb	Mar	Apr	May	Jun	Jul	Aug	Sep	Oct	Nov	Dec
	<i>Monthly mean values</i>											
Obs ( $m s^{-1}$ )	10.82	9.81	8.98	7.81	7.28	6.66	6.80	7.08	8.56	9.50	9.98	10.24
NORA3 ( $m s^{-1}$ )	<b>10.91</b>	<b>9.94</b>	<b>9.03</b>	7.76	7.15	6.71	<b>6.64</b>	<b>6.98</b>	8.48	<b>9.49</b>	<b>10.10</b>	<b>10.35</b>
ERA5 ( $m s^{-1}$ )	10.31	9.45	8.59	7.42	6.88	6.41	6.38	6.69	8.11	9.04	9.61	9.81
NORA10 ( $m s^{-1}$ )	10.93	9.95	9.08	<b>7.82</b>	<b>7.18</b>	<b>6.66</b>	<b>6.64</b>	<b>6.98</b>	<b>8.54</b>	9.59	10.15	10.40
	<i>Deviation from obs</i>											
NORA3 (%)	<b>0.8</b>	<b>1.3</b>	<b>0.5</b>	-0.7	-1.8	0.9	<b>-2.3</b>	<b>-1.3</b>	-0.9	<b>-0.1</b>	<b>1.3</b>	<b>1.1</b>
ERA5 (%)	-4.8	-3.7	-4.4	-4.9	-5.5	-3.8	-6.2	-5.5	-5.3	-4.8	-3.7	-4.2
NORA10 (%)	0.95	1.4	1.1	<b>0.1</b>	<b>-1.4</b>	<b>0.1</b>	<b>-2.3</b>	<b>-1.3</b>	<b>-0.3</b>	1.0	1.7	1.6

3. Results

a. General performance of NORA3

The surface wind speed of NORA3 is compared with a range of quality-assured offshore (maritime) and land-based observing

stations retrieved from the Norwegian Meteorological Institute (<https://www.met.no/en> and <https://frost.met.no/index.html>).

A comparison with the earlier 10-km Norwegian Hindcast Archive (NORA10; see [Reistad et al. 2011](#); [Furevik and Haakenstad 2012](#)) and the host analysis ERA5

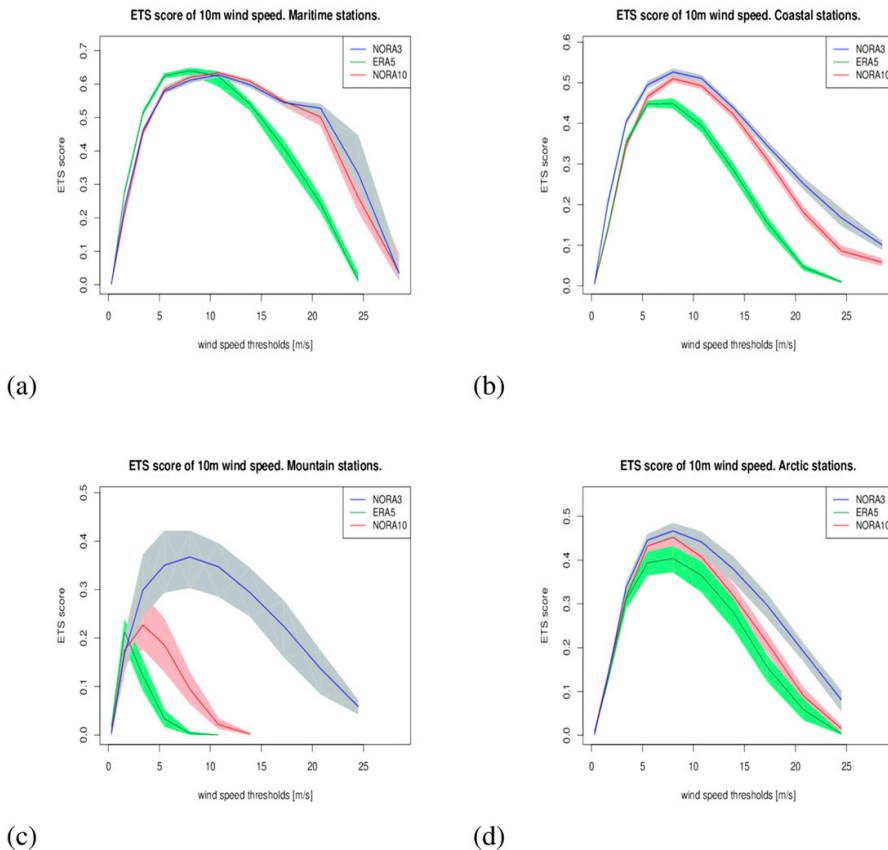


FIG. 5. ETS for (a) maritime, (b) coastal, (c) mountain, and (d) Arctic stations. Statistics were computed for the period 2004–18 for the three first categories and for 2010–18 for the Arctic stations. All panels include 95% confidence limits based on a nonparametric bootstrap procedure.

(Hersbach et al. 2020) is also performed. We have excluded observations from locations where the model topography differs by more than 200 m from the actual station height in either of the three datasets. The observation stations that are used are shown in Fig. 1.

Three statistical measures are used repeatedly in the following: (i) the mean error (or bias), (ii) the mean absolute error (MAE; see Wilks 2006, 279–281), and (iii) the model activity ratio (AR). The latter is the ratio of the modeled standard deviation (std) over the observed standard deviation of the 10-m wind speed and is a convenient way to compare the variability of observed and modeled quantities:

$$AR = \frac{\text{std}U_m}{\text{std}U_o}. \quad (3)$$

In addition to the validation metrics listed above, we use Pearson's correlation coefficient (Press et al. 2007, 745–747) and the equitable threat score (ETS). The latter is otherwise known as the Gilbert skill score (Gandin and Murphy 1992; Wilks 2006). The ETS is a categorical score; that is, it classifies a hit or miss, determined by a threshold value, in our case the values of the wind speed. It is defined as

$$ETS = \frac{a - a_r}{a + b + c - a_r}, \quad (4)$$

where  $a$  is the number of observed events that are correctly forecast (hits),  $b$  is the number of forecast events for which the event was not observed (false alarms),  $c$  is the number of events observed but not forecast (misses), and  $d$  is the number of events that were not observed and (correctly) not forecast (correct negatives). The number of hits due to random forecasts is

$$a_r = (a + b)(a + c)/n. \quad (5)$$

Here,  $n = a + b + c + d$  is the total potential number of events, whether or not they occurred (were observed). The ETS has a range from  $-1/3$  to 1, where 1 is a perfect score and 0 denotes no skill (Wilks 2006). The score is sensitive to the climatological probabilities of the events, making it useful also in rare-event situations.

### 1) VALIDATION AGAINST REFERENCE STATIONS

The reference validation uses hourly measurements from a set of quality-assured stations shown in Fig. 1 (marked with red open circles) and described in Table A3 denoted with category reference station (RS). The reference stations are found in one or more of the following databases: the Regional Basic Synoptic Network (RBSN), Regional Basic Climatological Network (RBCN), Reference Climatological Station (RCS), and Global Climate Observing System Surface Network (GSN). The stations consist mostly of land-based observations from the Norwegian mainland and Spitsbergen as well as Bear Island, Jan Mayen Island, and Hopen Island. The comparison between the model results and the observations is handled by bilinear interpolation of the model results to the observation positions. Although the stations are quality assured, some measurements can be spurious. Therefore, all observations

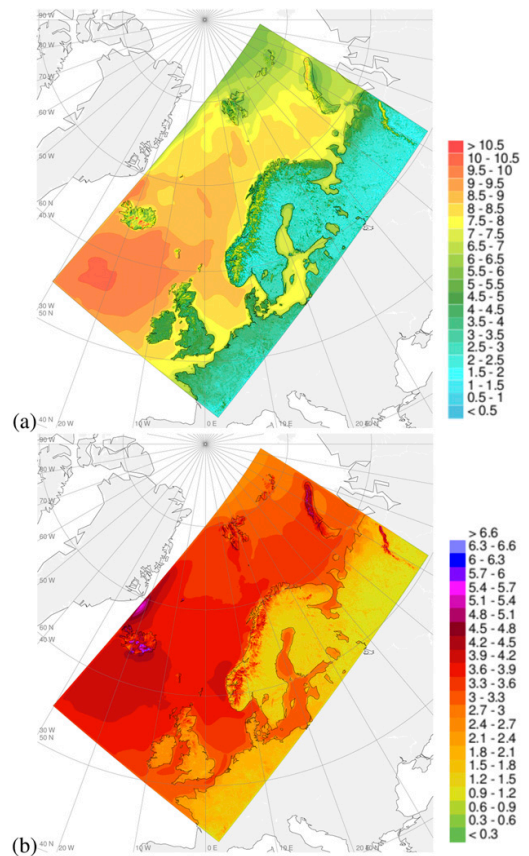


FIG. 6. The NOR3 10-m wind speed ( $\text{m s}^{-1}$ ) (a) average and (b) standard deviation for the period 2004–18.

deviating by more than  $20 \text{ m s}^{-1}$  from the model results are rejected from the validation.

The time series of 10-m wind speed bias, mean absolute error, and activity ratio of all three datasets (NORA3, NORA10, and ERA5) are shown for the period 2004–18 in Fig. 2 (observation count is shown in Fig. 2d). There is a marked reduction in the annual cycle of the mean wind error (bias) in NORA3 (blue) when compared with NORA10 (red), with considerably less overestimation of the wind speed during fall [September–January (SON)] and winter [December–February (DJF)] and less underestimation during spring [March–May (MAM)] and summer [June–August (JJA)] (see also Table 1 for monthly mean values).

A negative year-round bias in ERA5 (green) of about  $-0.38 \text{ m s}^{-1}$  is found. The activity ratio of NORA3 is significantly better than both NORA10 and ERA5. An overview of the performance of NORA3 in terms of MAE and correlation on the reference stations is given in Fig. 3. The MAE is mostly lower than NORA10 (Fig. 3a). The improvement over ERA5 (Fig. 3b) is somewhat stronger, although in both cases there are

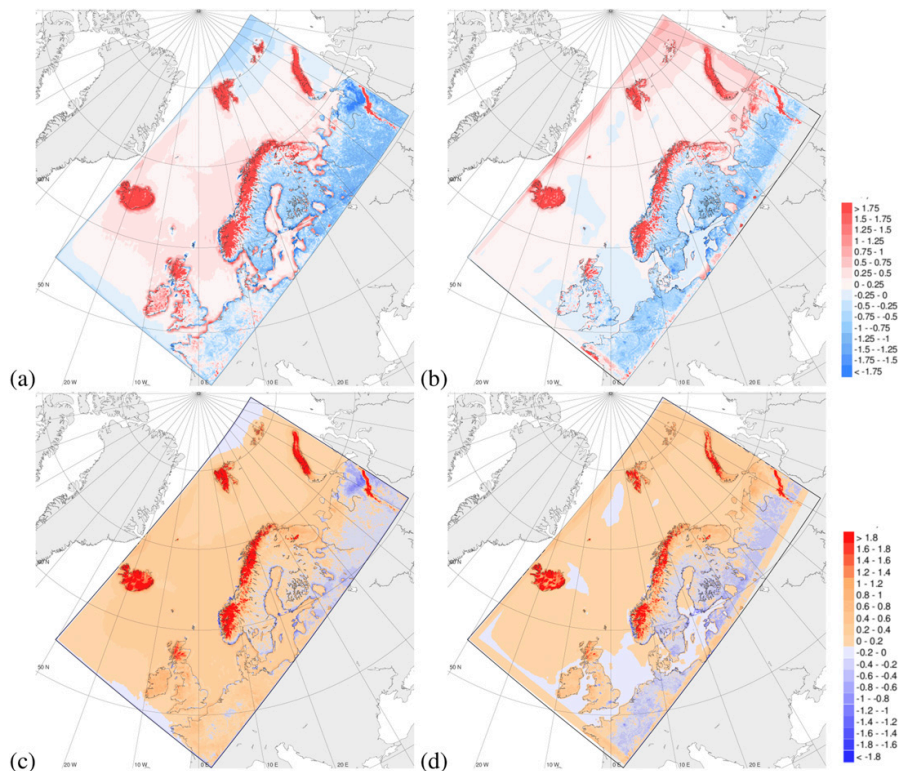


FIG. 7. The difference in annual mean 10-m wind speed ( $\text{m s}^{-1}$ ) for (a) NORA3 – ERA5 and (b) NORA3 – NORA10. Also shown is the difference in 10-m wind speed standard deviation (c) NORA3 – ERA5 and (d) NORA3 – NORA10. All panels show statistics for the period 2004–18.

exceptions. The correlation (lower panels) is also generally higher, and again the improvement over ERA5 (Fig. 3d) is stronger than over NORA10 (Fig. 3c). This is unsurprising, as the stations that make up the reference list are in most cases located in complex terrain, which is not well resolved by ERA5.

2) VALIDATION AGAINST MARITIME STATIONS

We have chosen a subset of offshore stations [see Fig. 1 (marked with blue dots) and the category maritime station (MR) in Table A3] that have nearly continuous measurements during the validation period, 2004–18, and where accurate information about the sensor height is available. The stations are located in the North Sea and the Norwegian Sea between 56.54°N and 64.35°N (marked with dark blue dots in Fig. 1) and cover a central part of the maritime NORA3 domain. The stations measure wind speed at heights between 71 and 141 m. The wind observations are reduced to 10-m height following the NORSOK wind profile (NORSOK 2007; Andersen and Løvseth 2006; Haakenstad et al. 2020). NORSOK is in common use in the Norwegian offshore community and was chosen based on a comparison of four different wind profiles (not shown) using high-quality wind speed measurements at

different heights from the German FINO1 offshore platform, located in the southern North Sea (at 54.015°N, 6.604°E). For brevity, the 10-m values will hereinafter be referred to as the observed values.

Figure 4a shows the monthly values of mean error in 10-m wind speed for NORA3, ERA5 and NORA10 (observation count is shown in Fig. 4d). NORA3 has a negligible long-term average mean error. However, it varies from mainly negative values in the start of the period to more positive values in the end of the period 2004–18. For the period with the best observation coverage (2006–13), NORA3 has an average mean

TABLE 3. Percentiles of 10-m wind speed for maritime stations (2004–18). The best performance (in comparison with the observed 10-m wind speed) is marked in boldface type.

	50	75	90	95	98	99	Max value
Obs	8.22	11.59	14.79	16.69	18.86	20.38	28.76
NORA3	<b>8.24</b>	<b>11.48</b>	14.53	16.35	18.51	<b>20.01</b>	<b>28.80</b>
ERA5	7.87	10.90	13.78	15.45	17.26	18.44	24.71
NORA10	8.24	11.47	<b>14.60</b>	<b>16.48</b>	<b>18.56</b>	19.98	27.48

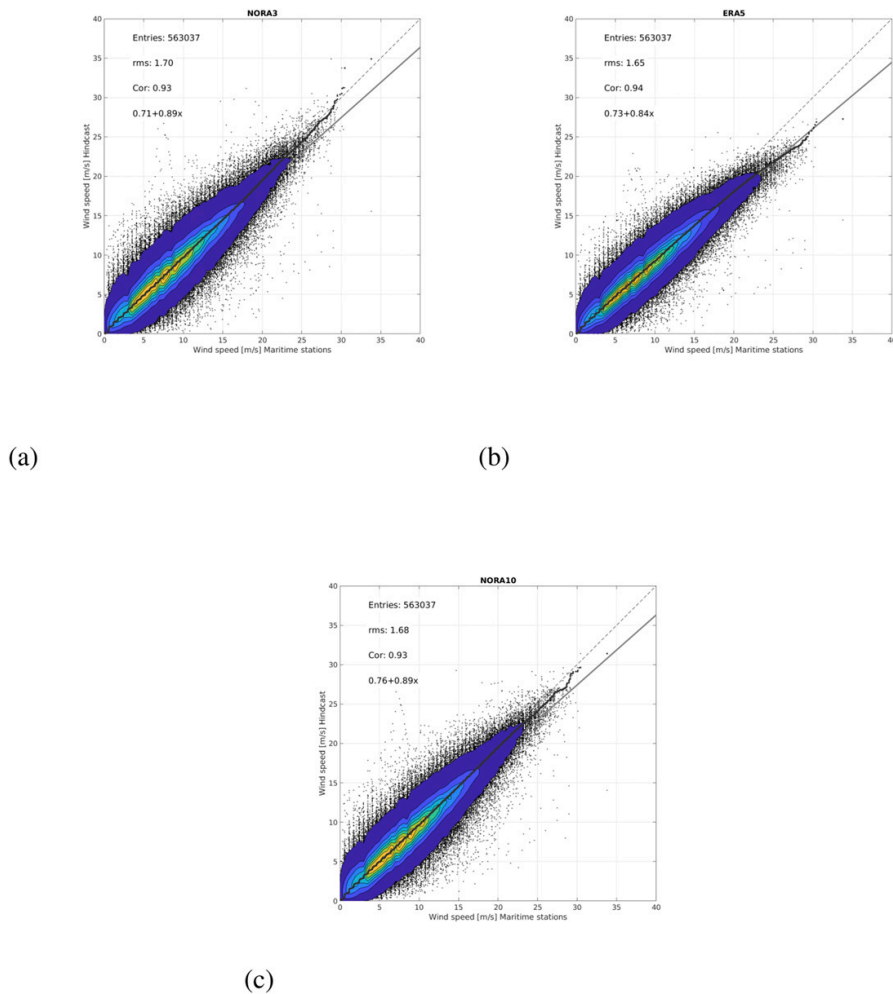


FIG. 8. Combined scatter and Q-Q plots of (a) NORA3, (b) ERA5, and (c) NORA10 vs maritime wind observations (period 2004–18).

error of  $-0.06 \text{ m s}^{-1}$ , as compared with  $-0.04$  and  $-0.45 \text{ m s}^{-1}$  for NORA10 and ERA5, respectively. In the same period, the mean absolute error is  $1.29 \text{ m s}^{-1}$  for NORA3 and NORA10 and  $1.26 \text{ m s}^{-1}$  for ERA5 (see Fig. 4b). Figure 4c shows that NORA3 has a slightly better activity ratio than NORA10 and significantly better activity ratio than ERA5.

Table 2 summarizes the monthly mean values of the observations, NORA3, ERA5, and NORA10 and the relative differences of the model values in comparison with the observations. The relative differences become more sensitive during summertime and all the model values show a maximum relative underestimation in July. ERA5 shows the greatest underestimation of  $-6.2\%$  while the value is  $-2.3\%$  for NORA3 and NORA10. NORA3 shows a maximum overestimation of

$1.3\%$  in November and February, and ERA5 underestimates the wind speed throughout the year.

### 3) CATEGORICAL VALIDATION

Figure 5 shows the ETS performance of NORA3, ERA5, and NORA10 for four different station classes: maritime, coastal, mountain, and Arctic stations. The stations are shown by, respectively, blue, green, yellow, and turquoise dots in Fig. 1. (All of the stations are also listed in Table A3.) For the Arctic stations, the instruments were upgraded in the period 2010–15; therefore, the years 2004–09 have been excluded from the Arctic ETS validation. The other station categories operate with the period 2004–18. All ETS estimates are shown with 90% confidence limits taken from 1000 nonparametric bootstrap estimates of the ETS.

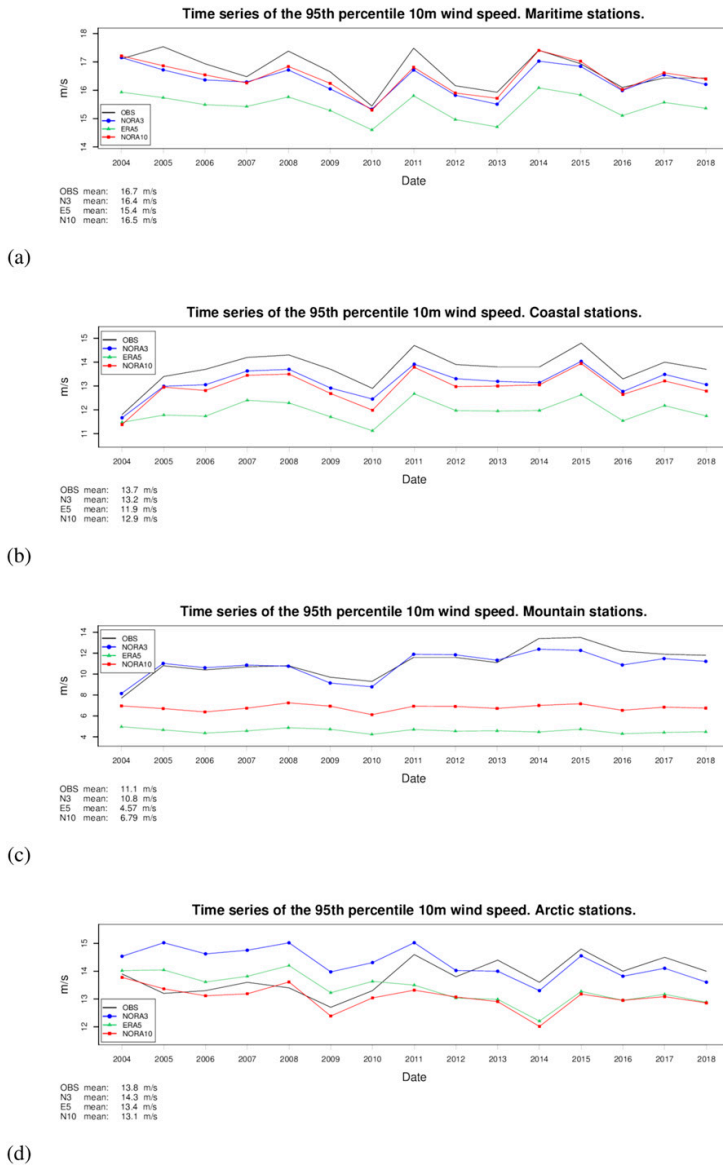


FIG. 9. Time series of the 95th-percentile 10-m wind speed for (a) maritime, (b) coastal, (c) mountain, and (d) Arctic stations. Observations are in black, NORA3 is in blue, ERA5 is in green, and NORA10 is in red. The mean value of the 95th percentile for the whole time period (2004–18) is shown at the lower left of the panels.

The best ETS is found for maritime stations with a maximum score of 0.64 by ERA5 for the wind speed category  $8 \text{ m s}^{-1}$  (fresh breeze). NORA3 has an ETS of 0.61 for this threshold but surpasses ERA5 for higher wind speed thresholds and has a score of 0.63 for strong breeze,  $10.8 \text{ m s}^{-1}$ , which is identical to

the NORA10 ETS. NORA10 and NORA3 have almost the same performance up to gale force ( $17.2 \text{ m s}^{-1}$ ). Above that, NORA3 performs better. At the coastal stations (Fig. 5b), NORA3 outperforms ERA5 and NORA10 for all categories of wind speeds. At mountain stations (Fig. 5c), NORA3 far

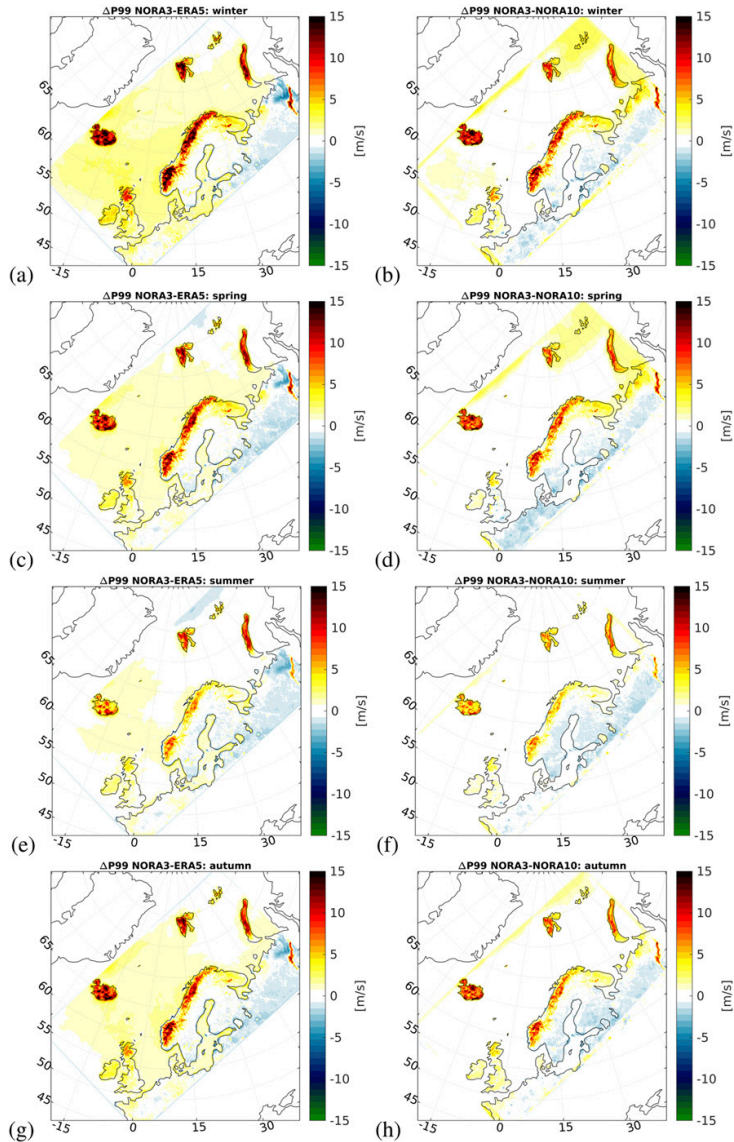


FIG. 10. The 99th-percentile wind field difference (left) between NORA3 and ERA5 and (right) between NORA3 and NORA10 for the period 2004–18 for (a),(b) DJF; (c),(d) MAM; (e),(f) JJA; and (g),(h) SON.

outperforms both ERA5 and NORA10 for all thresholds of wind speed above light breeze. NORA3, although better than NORA10 and ERA5, has a lower ETS at the mountain stations when compared with the other station classes. This highlights the difficulties of correctly modeling mountainous terrain. For Arctic stations (Fig. 5d), NORA3 again clearly outperforms ERA5 and NORA10 above  $3.3 \text{ m s}^{-1}$ , but its performance is

weaker than for the maritime and coastal stations for the same reasons as mentioned for the mountain stations.

#### b. Spatial comparison between NORA3 and ERA5

The activity (standard deviation of the wind speed) is shown in Fig. 6b, and the difference in activity is shown in Fig. 7. As can be seen, the activity of NORA3 is much higher than ERA5

TABLE 4. Polar lows where the identification number (ID), center position (CLON and CLAT) and wind speed observations are taken from Rojo et al. (2019). The maximum 10-m wind speeds for the different polar low events are shown for NORA3, ERA5, and NORA10 in the last three columns. The best performance (in comparison with the maximum observed 10-m wind speed) is marked in boldface type.

No.	ID	Date	CLON	CLAT	Obs	Obs gust	NORA3	ERA5	NORA10
1	78	0900 UTC 22 Dec 2006	12.0	72.1	25.3	32.1	20.4	17.5	<b>20.6</b>
2	79	0900 UTC 26 Dec 2006	22.0	72.8	25.8	33.2	<b>19.2</b>	16.1	17.8
3	82	0900 UTC 26 Jan 2007	14.5	69.5	26.8	—	28.5	20.4	<b>25.6</b>
4	104	1500 UTC 19 Nov 2008	15.0	69.9	29.0	—	<b>20.0</b>	18.0	17.0
5	105	0900 UTC 20 Nov 2008	7.5	68.0	32.6	38.9	<b>28.2</b>	24.6	27.1
6	108	0900 UTC 7 Jan 2009	33.0	72.5	25.8	33.7	<b>25.5</b>	20.3	24.5
7	122	2100 UTC 30 Jan 2010	4.0	60.5	20.0	—	<b>20.9</b>	17.5	18.9
8	149	0900 UTC 7 Feb 2011	1.0	66.0	21.6	—	<b>19.2</b>	15.1	15.6
9	151	0300 UTC 11 Mar 2011	0.0	68.2	24.7	—	<b>21.1</b>	19.5	18.6
10	160	0300 UTC 28 Nov 2011	11.5	67.0	30.0	37.9	<b>24.2</b>	18.6	22.2
11	161	1500 UTC 6 Dec 2011	3.0	59.8	26.3	35.8	<b>21.4</b>	17.1	18.7
12	162	1200 UTC 27 Dec 2011	7.0	71.3	21.6	31.6	32.8	<b>23.3</b>	26.8
13	173	0900 UTC 1 Feb 2013	10.5	66.5	21.1	—	<b>21.5</b>	19.0	19.3
14	196	0900 UTC 24 Nov 2013	21.5	71.7	21.6	—	24.3	18.3	<b>22.6</b>
15	198	0900 UTC 30 Nov 2013	45.0	71.8	21.0	—	24.6	<b>20.3</b>	24.5
16	219	1500 UTC 26 Dec 2015	29.0	71.7	31.1	37.4	<b>30.9</b>	23.2	29.0
17	227	0300 UTC 9 Dec 2016	31.5	70.8	30.0	37.9	<b>26.9</b>	22.6	26.7
18	230	0300 UTC 20 Jan 2017	36.0	76.5	24.7	36.8	30.7	<b>24.1</b>	27.5
19	240	1500 UTC 22 Nov 2017	−12.5	57.5	22.6	—	29.9	<b>21.0</b>	26.0

in mountainous regions. This can probably to a large degree be explained by the more detailed topography of NORA3 and the impact of nonhydrostatic vertical accelerations.

### c. Wind speed, upper-percentile statistics

The median and upper percentiles of the wind speed at offshore stations are summarized in Table 3. NORA3 has the closest fit to the median, the 75th-, and the 99th-percentile wind speed (Fig. 8). NORA10 also shows very good performance, with the best fit to the 90th–98th percentiles. The ERA5 wind speed is again found to be biased low, but its root-mean-square error (RMSE) is very low, and the correlation with the maritime observations is indeed slightly higher than for NORA3.

Figure 9 shows the time series of the 95th percentiles of 10-m wind speed for NORA3, ERA5 and NORA10 at maritime stations (Fig. 9a), coastal (Fig. 9b), mountain (Fig. 9c) as well as the Arctic stations (Fig. 9d). NORA3 and NORA10 both perform very well at the upper percentiles at maritime stations, with no significant differences between them, while ERA5 underestimates the 95th percentile by  $1.4 \text{ m s}^{-1}$ . NORA3 scores slightly better than NORA10 at the coastal stations (Fig. 9b) but much better at the mountain stations (Fig. 9c). The Arctic stations exhibit a shift in behavior after 2010 resulting from an increase in observation stations (see Fig. A3). After 2011, NORA3 shows very good agreement with the observations.

Figure 10 shows the seasonal (DJF, MAM, JJA, and SON) difference in 99th-percentile 10-m wind speed between NORA3 and ERA5 (Figs. 10a,c,e,g), and between NORA3 and NORA10 (Figs. 10b,d,f,h). The ERA5 wind speed is found to be consistently weaker than NORA3 throughout the maritime domain, but differences in mountainous terrain are much larger because of the lower resolution of ERA5. The 99th percentile of ERA5 is typically  $2 \text{ m s}^{-1}$  lower than NORA3. NORA10 also displays a field

with weaker gradients than NORA3 and a broader low pressure track across the area between Iceland and the British Isles. It is also clear from comparing Figs. 10a,e,i that the winter (DJF) fields of NORA3 exhibit markedly stronger winds near the Norwegian west coast.

### d. Polar lows and windstorms

#### 1) POLAR LOWS

Rojo et al. (2019) lists a number of polar low events over the Nordic seas tracked using Advanced Very High Resolution Radiometer (AVHRR) imagery. We have investigated all polar lows listed by Rojo et al. (2019) that have a minimum mean sea level pressure value below 980 hPa within the model domain in the period 2004–18. We retrieved the maximum 10-m wind speed within an area extending  $0.6^\circ$  north and south and  $6^\circ$  east and west around the observed polar low center from NORA3, ERA5, and NORA10. Table 4 shows that NORA3 has a maximum wind speed value closest to the observed value in 12 of 19 cases. NORA10 performs best in three of the cases, and ERA5 has the most optimal value in four of the cases.

As an illustration of the differences between the two hindcast archives and the ERA5 reanalysis, we have investigated a short-lived but intense polar low that developed east of Bear Island. The polar low was first detected at 0300 UTC 7 January 2009. The low caused severe damage when making landfall in the northernmost part of Finnmark (Magerøya and Honningsvåg). The polar low is described as a multiple, baroclinic, convergence low with a reversed shear in the database for Surface Temperature and Altimeter Synergy for Improved Forecasting of Polar Lows (STARS, see <https://projects.met.no/stars/>; Furevik et al. 2015). The low was also investigated by Haakenstad et al. (2020).

The initial situation (0300 UTC 7 January 2009) is shown in Fig. 11. An upper-level low is situated ahead of the polar low,



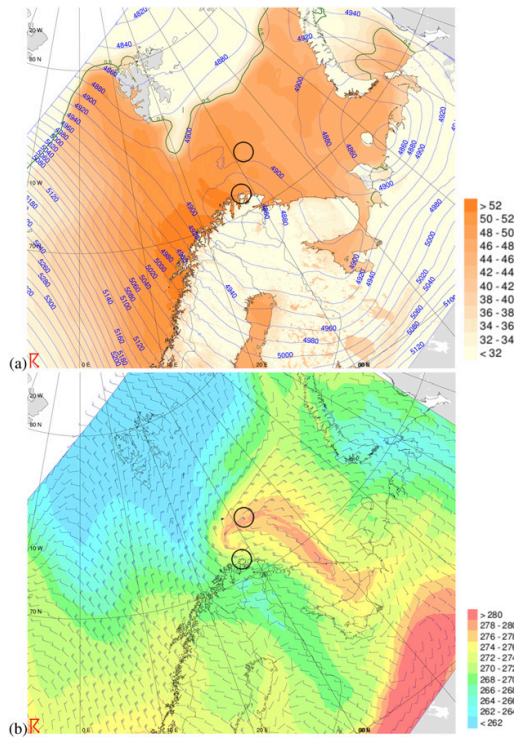


FIG. 11. The NOR3 atmospheric situation at 0300 UTC 7 Jan 2009. (a) The difference between sea surface temperature and the temperature (K) at the 500-hPa level is indicated by orange colors, and the ice edge is indicated in dark green. Blue contour lines show the height of the 500-hPa level. (b) The equivalent potential temperature (K) at 850 hPa and 10-m wind speed, where a large feather on the barb is 10 kt, a small feather is 5 kt, and triangles indicate 50 kt ( $1 \text{ kt} = 0.5 \text{ m s}^{-1}$ ). In (a) and (b), the start position and end position of the polar low are shown by the circles, with the northernmost circle being the start position. (The positions are taken from the STARS database).

over Finnmark in northern Norway (see Fig. 11a), indicating a reversed shear and a typical baroclinically driven initial condition for the formation of the polar low (Reed and Duncan 1987). The ice edge stretches southward east of the Svalbard Archipelago, and open water is present on the western side. This shape of the sea ice edge favors the formation of a downstream convergence zone conducive to mesoscale cyclone development (Sergeev et al. 2018). There is a large temperature difference (49–51 K) between the sea surface and the 500-hPa surface [also documented in the STARS database (Furevik et al. 2015)] and thus also a large atmospheric heat potential. The difference is well above the commonly cited threshold of 43 K (Zahn and von Storch 2008), above which there is thought to be a 25% chance of developing a polar low. The temperature difference  $T_{\text{sea}} - T_{500}$  modeled by NOR3 mirrors closely the observed situation described in the STARS database, and it is likely that the polar low was intensified by

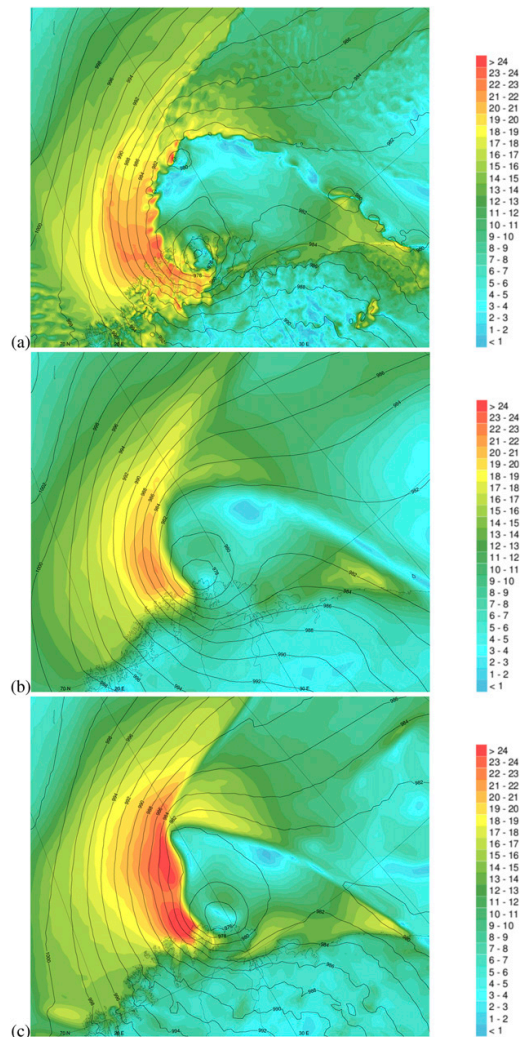


FIG. 12. Polar low at 0900 UTC 7 Jan 2009, showing 10-m wind speed (shading) and MSLP (contours) from (a) NOR3, (b) ERA5, and (c) NOR3.

convective and diabatic processes. Figure 11b shows NOR3's 850-hPa equivalent potential temperature. A sharp gradient is visible along the ice edge. A cold-air outbreak is evident from the extended sea ice east of Svalbard with prevailing northerly wind transporting stably stratified, dry cold air from the Arctic over warmer water, creating a shallow, secondary baroclinic layer. Figure 12 compares NOR3, ERA5, and NOR3 10-m wind speed (Fig. 12a) and MSLP fields (Fig. 12b) at the mature stage (0900 UTC 7 January 2009). The maximum wind speed value at 0900 UTC is  $26 \text{ m s}^{-1}$  in NOR3,  $22 \text{ m s}^{-1}$  in ERA5, and  $26 \text{ m s}^{-1}$  in NOR3. The NOR3 maximum of

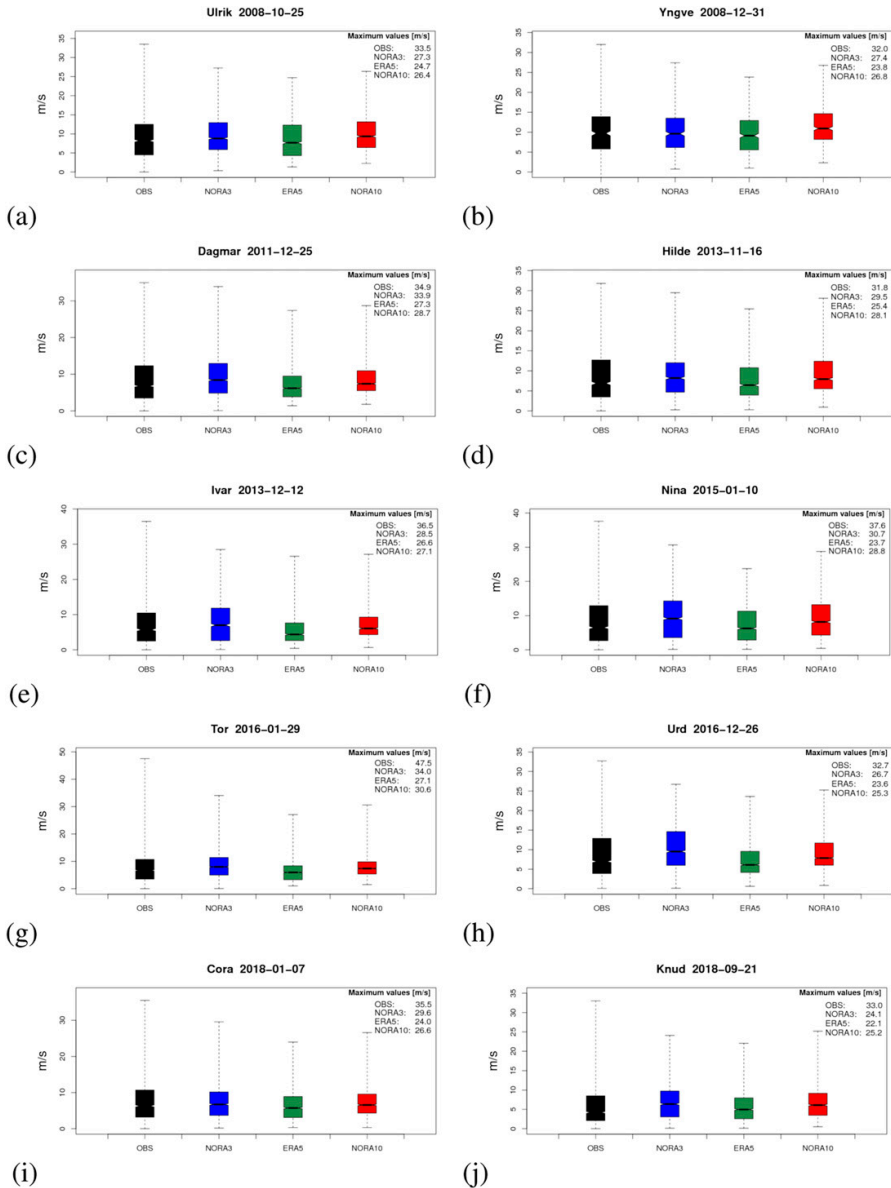


FIG. 13. Wind speed statistics from observations, NORA3, NORA10, and ERA5 for named windstorms during the period 2008–18. The boxes show the 25th and 75th percentiles and the median. The whiskers show the maximum and minimum values. Stations from counties affected by each windstorm are included (this list deviates from the list shown in Fig. 1 and includes only quality-assured observation stations acquired by the Norwegian Meteorological Institute).

26 m s<sup>-1</sup> occurs on the trailing arm in the position 72°51'N, 29°02'E and is far away from the coast, as opposed to the low. NORA3 also shows much more fine structure in the wind field with small-scale convective cells and close similarity to the satellite image [cf. with Fig. 7a of Furevik et al.

of 23 m s<sup>-1</sup> in the location of landfall on the western side of the low. NORA3 also shows much more fine structure in the wind field with small-scale convective cells and close similarity to the satellite image [cf. with Fig. 7a of Furevik et al.

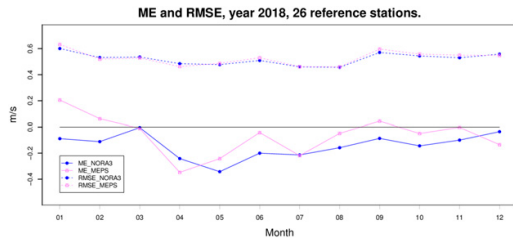


FIG. A1. A comparison between MEPS and NORA3 in terms of mean error and root-mean-square error.

(2015)]. Such convective cells are obviously not present in the fields from NORA10 and ERA5 because they are the result of the convection-permitting nonhydrostatic dynamics of the HARMONIE-AROME model. The polar low centers of NORA3 and ERA5 agree well with the tracked polar low in the STARS database, whereas NORA10 puts the center too far to the northeast.

2) WINDSTORMS

The maximum winds of NORA3, ERA5, and NORA10 during the 10 most important (named) windstorms to hit the

Norwegian mainland in the period 2009–18 have been investigated. All quality-assured observations from the databases of the Norwegian Meteorological Institute (<https://www.met.no/en> and <https://frost.met.no/index.html>) from the affected counties have been compared with collocated wind speeds from NORA3, ERA5, and NORA10. The results are shown as boxplots in Fig. 13. The maximum wind speed (upper whiskers; see also the statistics in the individual panels) is consistently higher (and closer to the observed maximum) in NORA3 than in ERA5. This is also the case with respect to NORA10 except for one case, *Knud* (Fig. 13j), where NORA3 underestimates the maximum wind speed by 18%. We also note that NORA3’s wind speed interquartile distance, a measure of the spread, is closer to the observed interquartile distance. This suggests that not only are the windstorm maxima better modeled, but the spatial variability is also more realistic.

4. Discussion and concluding remarks

NORA3 represents the most detailed hindcast study performed to date for the Norwegian Sea, the North Sea, and the Barents Sea. We find a clear improvement when compared with ERA5 in the representation of near-surface winds over the open ocean (cf. Fig. 4), but an even greater improvement in

TABLE A1. Model configuration.

Domain	The domain covers the North Sea, the Norwegian Sea, and the Barents Sea; the grid is a Lambert conformal conic grid, with 900 longitudinal × 1500 latitudinal grid points; the central meridian = 42.0°W, the central latitude = 66.3°N, and the reference parallel = 66.3°N
Horizontal resolution	3 km
No. of vertical levels	65
Coupling model	ERA5 (IFS Cycle 41r2, horizontal resolution 31 km, and 137 vertical levels)
Initialization method	No initial digital filtering
Coupling frequency	6 hourly
Integration hours	0000, 0600, 1200, and 1800 UTC
Forecast range	9 h
Surface analysis	CANARI
Background	OI-Main
Observations	Land surface: synoptic (SYNOP) and METAR; Sea surface: ships (SHIP), drifting buoys (DRIBU), and buoys (BUOYS) (retrieved from the MARS database)
Dynamics	Nonhydrostatic, convection permitting; solves the fully compressible Euler equations
Discretization	Two-time-level, semi-implicit, semi-Lagrangian discretization using SETTLS; A-grid; linear
Time step	60 s
Microphysics	ICE3 (Pinty and Jabouille 1998; Lascaux et al. 2006) combined with the OCND2 scheme (Müller et al. 2017b) and Kogan autoconversion (Khairoutdinov and Kogan 2000)
Surface	SURFEX (Le Moigne et al. 2012; Masson et al. 2013) Land surface model: ISBA-3L (Boone et al. 1999) Inland water: prognostic variables are kept constant, and the roughness length is defined by the Charnock relation $z_0 = 0.015u_*^2/g$ Sea surface: ECUME (see Table A3) Sea ice: SICE (Batra et al. 2018) Urban areas: Town energy budget scheme
Convection	EDMF-M (Siebesma et al. 2003; Soares et al. 2004; Siebesma et al. 2007; de Rooy and Siebesma 2010)
Turbulence	HARATU (van Meijgaard et al. 2012; Lenderink and Holtslag 2004)
Radiation	Longwave: RRTM (Mlawer et al. 1997) Shortwave: ECMWF operational SW scheme (ECMWF 1989)
Aerosols and ozone	Monthly climatologies
Physiography	ECOCLIMAP, version 2
Computing platform	The Nebula cluster of the National Supercomputer Centre, located in Linköping

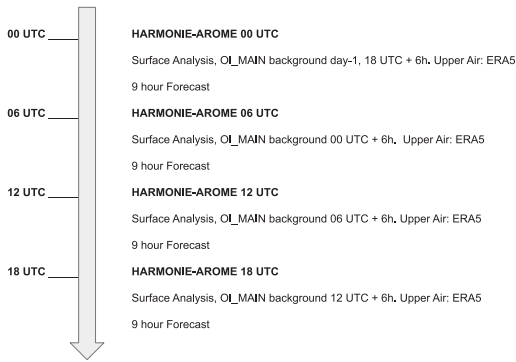


FIG. A2. The NORA3 hindcast production cycle. Four consecutive and partly overlapping 9-hourly forecast cycles with HARMONIE-AROME are shown. Each cycle starts with a surface analysis and upper-air blending of ERA5 fields. A 9-h forecast is then run, of which time steps at 4–9 h are concatenated onto the previous cycle to form a continuous hindcast archive.

mountainous and coastal terrain (see Fig. 5). NORA3’s activity ratio is considerably better than both NORA10 and ERA5. Although NORA10 has only marginally lower mean absolute error for maritime stations and ERA5 in fact exhibits slightly higher correlation than NORA3, the fact that the activity ratio is better in NORA3 means that the wind climate is more realistically modeled by the nonhydrostatic model, even over the open ocean (see Fig. 4). This is also the case for spatial variations, which is seen in the wind field of the polar low. Over land, this becomes much more evident (Fig. 2), and the large annual variations in bias seen in NORA10 are absent. The mean absolute error is also much smaller, and the activity ratio remains closer to unity than for both NORA10 and ERA5.

In the Arctic, NORA3 also shows an improvement of upper-percentile wind speed relative to ERA5 and also to NORA10 (Fig. 5). Müller et al. (2017a) showed that AROME-Arctic adds value to the representation of the surface parameters

relative to ECMWF’s forecast and reanalysis model systems, a finding that is in agreement with our results. The study by Koltzow et al. (2019) also found the operational AROME-Arctic model to have good performance around Svalbard. Further work will also look at the performance of the model setup in terms of extreme rainfall in the steep topography over Svalbard and the Norwegian mainland.

The NORA3 hindcast archive will be used as forcing for high-resolution coastal wave hindcast integrations as well as for extreme value analyses of wind climate. It has thus been important to assess its ability to represent the surface wind field across a range of statistics, from its correlation, bias, and activity to its representation of upper-percentile wind speed and from open ocean conditions to complex coastal terrain. Its performance is generally good, and the improvement over the host analysis is naturally particularly strong in the coastal zone and in mountainous terrain. However, it is clear that there are limits to the performance that can be achieved with stand-alone atmospheric hindcast integrations. A natural extension of such a modeling effort would be to conduct a full three-dimensional or four-dimensional variational data assimilation to achieve a complete reanalysis on a similar resolution. This is, however, very costly [cf. the ongoing effort to create the Copernicus Arctic Regional Reanalysis (CARRA) funded by the Copernicus Climate Change Service]. Another possible extension is to incorporate a wave model into a coupled atmosphere–wave hindcast to account for the feedback between the sea surface roughness controlled by the wave field (Janssen 1989, 1991). This feedback has been shown to be important on larger scales (Janssen et al. 2004), but on the spatial and temporal scales considered here, its impact on the climatology is not expected to be big. It would, however, be a natural next step to attempt a coupled atmosphere–wave hindcast integration on a similar spatial scale (2–4 km).

The hindcast has been shown to represent the upper percentiles of wind speed much better than the host analysis ERA5, and also better than the older hindcast NORA10. This suggests that the new hindcast should be suitable for extreme value analyses. Topographic effects are much better resolved than in the coarser (hydrostatic) NORA10 hindcast and the

TABLE A2. The ECUME (Le Moigne et al. 2012) scheme.

Roughness length	$z_0 = (\alpha u_*^2/g) + (\beta v/u_*)$ (Smith 1988), where $\alpha = 0.011$ and $\beta = 0.11$
Stability functions	Modified Businger functions $\psi_m$ and $\psi_h$ that depend on the Monin–Obukhov parameter $\zeta = z/L$ Stable cases ( $\zeta \geq 0$ ): $\psi_m = \psi_h = -\Gamma\zeta$ , where $\Gamma = 7$ Unstable cases ( $\zeta < 0$ ): $\psi_m = (1-f)\psi_{mK} + f\psi_{mC}$ and $\psi_h = (1-f)\psi_{hK} + f\psi_{hC}$ , where $f = \zeta^2/(1 + \zeta^2)$ , $\psi_{mK} = 2 \ln\left(\frac{1+x}{2}\right) + \ln\left(\frac{1+x^2}{2}\right) - 2 \arctan x + \frac{\pi}{2}$ , with $x = (1 - 16\zeta)^{1/4}$ ( $K$ denotes Kansas), $\psi_{hK} = 2 \ln\left(\frac{1+x}{2}\right)$ , $\psi_{mC} = \frac{3}{2} \ln\left(\frac{y^2 + y + 1}{3}\right) - \sqrt{3} \arctan\left(\frac{2y+1}{\sqrt{3}}\right) + \frac{\pi}{\sqrt{3}}$ , with $y = (1 - 12.87\zeta)^{1/3}$ ( $C$ denotes convective), and $\psi_{hC} = \frac{3}{2} \ln\left(\frac{y^2 + y + 1}{3}\right) - \sqrt{3} \arctan\left(\frac{2y+1}{\sqrt{3}}\right) + \frac{\pi}{\sqrt{3}}$
Sea surface drag	$\tau_{\text{sea}} = -\rho_a C_D U^2 + \tau_p$ (Fairall et al. 1996)
Sea surface heat flux	$H_{\text{sea}} = \rho_a c_p C_H U(\theta_s - \theta_a) + H_p$ (Gosnell et al. 1995)
Sea surface latent heat flux	$LE_{\text{sea}} = \rho_a \mathcal{L}_v C_E U(q_s - q_a) + LE_{\text{Webb}}$ , where $LE_{\text{Webb}}$ is an adjustment due to air density variations as the humidity varies with evaporation
$C_D$	Neutral stability 10-m drag coefficient

TABLE A3. Station list (ID = identifier; WIGOS is the WMO Integrated Global Observing System). Abbreviations are as follows: Categories (Cat): maritime stations (MR), reference stations (RS), coastal stations (CS), mountain stations (MO), and Arctic stations (AS). Station holder (Stn holder): The Norwegian Meteorological Institute (MET), ConocoPhillips (CP), High Mountain Research Station (HMRS), AVINOR (a state-owned limited company that operates most of the civil airports in Norway), Stiftung Alfred-Wegener-Institut Für Polar- und Meeresforschung (AWI), University of Oslo (UiO), and Norwegian Water Resources and Energy Directorate (NVE). Name: airport (AP) and lighthouse (LH).

ID	Name	Height (m)	Stn holder	WIGOS ID	WMO ID	Lon	Lat	Cat
SN87110	Andøya	10	MET; AVINOR	0-20000-0-01010	1010	16.131	69.307	RS; CS
SN23550	Beitostølen II	965	MET	0-20000-0-01365	1365	8.923	61.251	MO
SN50540	Bergen-Florida	12	MET	0-20000-0-01317	1317	5.333	60.383	RS
SN99710	Bjørnøya	16	MET	0-20000-0-01028	1028	18.998	74.504	RS; AS
SN82290	Bodø VI	11	MET; AVINOR	0-20000-0-01152	1152	14.364	67.267	RS
SN71990	Buholmråsa LH	18	MET	0-20000-0-01259	1259	10.455	64.4013	CS
SN76925	Draugen	76	OKEA AS	0-578-0-76925	1202	7.779	64.352	MR
SN76920	Ekofisk	114	CP	0-20000-0-01400	1400	3.224	56.543	MR
SN25830	Fansevatn	1210	HMRS; MET	0-20000-0-01350	1350	7.527	60.594	MO
SN94500	Fruholmen LH	13	MET	0-20000-0-01055	1055	23.982	71.094	RS
SN27500	Færder LH	6	MET	0-20000-0-01482	1482	10.524	59.027	RS; CS
SN4780	Gardermoen	202	AVINOR	0-20000-0-01384	1384	11.080	60.207	RS
SN31970	Gaustatoppen	1804	MET	0-20000-0-01461	1461	8.656	59.850	MO
SN76923	Gullfaks C	141	EQUINOR ASA	0-20000-0-01300	1300	2.269	61.204	MR
SN71850	Halten LH	16	MET	0-20000-0-01240	1240	9.405	64.173	CS
SN76932	Hemdald	71	EQUINOR ASA	0-578-0-76932	1404	2.227	59.574	MR
SN99720	Hopen	6	MET	0-20000-0-01062	1062	25.013	76.510	RS; AS
SN32890	Høydalsmo II	560	MET	0-20000-0-01447	1447	8.199	59.497	RS
SN99790	Isfjord Radio	7	MET	0-744-0-99790	1013	13.619	78.063	AS
SN99950	Jan Mayen	10	MET	0-20000-0-01001	1001	-8.669	70.939	RS; AS
SN97251	Karasjok-Mar.	131	MET	0-20000-0-01065	1065	25.502	69.464	RS
SN99935	Karl XII-Øya	5	MET	0-20000-0-01009	1009	25.005	80.652	AS
SN93700	Kautokeino	307	MET	0-20000-0-01047	1047	23.034	68.997	RS
SN99370	Kirkenes AP	89	AVINOR	0-20000-0-01089	1089	29.898	69.726	CS
SN39040	Kjevik	12	MET	0-20000-0-01452	1452	8.077	58.200	CS
SN99740	Kongsøya	20	MET; UiO	0-20000-0-01016	1016	28.888	78.907	AS
SN13160	Kvitfjell	1030	MET	0-20000-0-01375	1375	10.128	61.465	MO
SN99938	Kvitøya	10	MET	0-20000-0-01011	1011	31.459	80.104	AS
SN42160	Lista LH	14	MET	0-20000-0-01427	1427	6.568	58.109	RS; CS
SN98400	Makkaur LH	9	MET	0-20000-0-01092	1092	30.07	70.706	CS
SN61410	Mannen	1294	NVE	0-20000-0-01220	1220	7.770	62.460	MO
SN53530	Midtstova	1162	BANE NOR	0-20000-0-01346	1346	7.276	60.656	MO
SN80610	Myken	17	MET	0-20000-0-01115	1115	12.486	66.763	RS; CS
SN31620	Møsstrand II	977	MET	0-20000-0-01450	1450	8.179	59.840	MO
SN39100	Oksøy LH	9	MET	0-20000-0-01448	1448	8.053	58.073	RS; CS
SN62480	Ona II	20	MET	0-20000-0-01212	1212	6.538	62.859	RS; CS
SN18700	Oslo-Blindern	94	MET	0-20000-0-01492	1492	10.720	59.942	RS
SN76750	Sandnessjøen LH	17	AVINOR	0-20000-0-01116	1116	12.478	65.964	CS
SN75550	Sklinna LH	23	MET	0-20000-0-01102	1102	10.997	65.202	RS; CS
SN85380	Skrova LH	14	MET	0-20000-0-01160	1160	14.649	68.154	RS; CS
SN76926	Sleipner A	135	EQUINOR ASA	0-578-0-76926	1402	1.909	58.371	MR
SN96400	Slettnes LH	8	MET	0-20000-0-01078	1078	28.217	71.089	RS; CS
SN44560	Sola	7	AVINOR; MET	0-20000-0-01415	1415	5.637	58.884	RS; CS
SN17000	Strømtangen LH	10	MET.NO	0-20000-0-01495	1495	10.829	59.151	CS
SN65940	Sula	5	MET.NO	0-20000-0-01228	1228	8.467	63.847	CS
SN99840	Svalbard AP	28	AVINOR; MET	0-20000-0-01008	1008	15.502	78.245	RS; AS
SN59800	Svinøy LH	38	MET	0-20000-0-01205	1205	5.268	62.329	RS; CS
SN85450	Svolvær AP	9	AVINOR	0-20000-0-01161	1161	14.669	68.245	CS
SN99752	Sørkappøya	10	MET.NO	0-20000-0-01020	1020	16.543	76.473	AS
SN36200	Torungen LH	12	MET	0-20000-0-01465	1465	8.789	58.399	RS; CS
SN76931	Troll A	92	EQUINOR ASA	0-20000-0-01309	1309	3.719	60.644	MR
SN90450	Tromsø	100	MET	0-20000-0-01026	1026	18.937	69.654	RS
SN47300	Utsira LH	55	MET	0-20000-0-01403	1403	4.872	59.307	RS

TABLE A3. (Continued)

ID	Name	Height (m)	Stn holder	WIGOS ID	WMO ID	Lon	Lat	Cat
SN98550	Vardø Radio	10	MET	0-20000-0-01098	1098	31.096	70.371	RS; CS
SN13420	Venabu	930	MET	0-20000-0-01380	1380	10.108	61.651	MO
SN99927	Verlegenuken	8	MET	0-20000-0-01002	1002	16.243	80.056	AS
SN60990	Vigra	22	AVINOR	0-20000-0-01210	1210	6.115	62.5617	CS
SN57770	Ytterøyane LH	26	MET	0-20000-0-01304	1304	4.682	61.572	CS
SN71550	Ørland III	10	MET	0-20000-0-01241	1241	9.611	63.705	RS; CS

host analysis, ERA5. This is particularly important in fjord systems, where the wind field is dominated by local effects (Christakos et al. 2020a,b).

**Acknowledgments.** This study was carried out with support from the ERA4CS WINDSURFER project and the Norwegian Climate Service Centre (KSS). We gratefully acknowledge the support from Equinor ASA who have cofunded the development of the NORA3 archive. Authors Reistad, Aarnes, and Breivik gratefully acknowledge the Research Council of Norway for funding through the ExWaMar project (Grant 256466). Authors Furevik and Haakenstad are grateful for funding from the Norwegian Public Roads Administration through the project “E39 Coastal Highway Route.”

**Data availability statement.** The data will be archived on The Norwegian Meteorological Institute’s publicly accessible Thredds server (<https://thredds.met.no>). Quality-assured offshore (maritime)

and land-based observing stations used in this study are retrieved from the Norwegian Meteorological Institute (<https://www.met.no/en> and <https://frost.met.no/index.html>).

APPENDIX

**Details of the Model Performance, Model Configuration, and Observation Network**

*a. A comparison of NORA3 and the short-range ensemble forecast system for the Nordic countries*

To investigate how the performance of NORA3 is affected by the choice of 3-km resolution, we have compared the NORA3 10-m wind speed at the reference stations on the Norwegian mainland in 2018 with the operational short-range ensemble prediction system (MEPS) forecasts (Müller et al. 2017b). MEPS runs the 2.5-km HARMONIE-AROME model with full 3DVAR assimilation. The assimilation will favor the operational forecasts, and deviations from the MEPS results must be expected. The comparison (Fig. A1) has been performed by using the 10-m wind speed at 6-h lead time for both models. It is clear from Fig. A1 that the differences are marginal, both in terms of mean error and RMSE.

*b. Model configuration*

The model setup is outlined in Table A1, and the sequence of 9-hourly forecast cycles is shown in Fig A2. The ECUME scheme is outlined in Table A2.

*c. Observing stations*

All observing stations are listed in Table A3. The annual number of coastal, mountain, and Arctic observations are shown in Fig. A3. The reason why there are so few observations in 2004 for all station categories is that only observations with the strictest quality (Kjelland 2005) have been used in the validation, and before 2005 there were only a few observations that fulfilled this requirement.

REFERENCES

Aarnes, O. J., S. Abdalla, J.-R. Bidlot, and Ø. Breivik, 2015: Marine wind and wave height trends at different ERA-Interim forecast ranges. *J. Climate*, **28**, 819–837, <https://doi.org/10.1175/JCLI-D-14-00470.1>.  
 —, and Coauthors, 2017: Projected changes in significant wave height towards the end of the 21st century: Northeast Atlantic. *J. Geophys. Res. Oceans*, **122**, 3394–3403, <https://doi.org/10.1002/2016JC012521>.

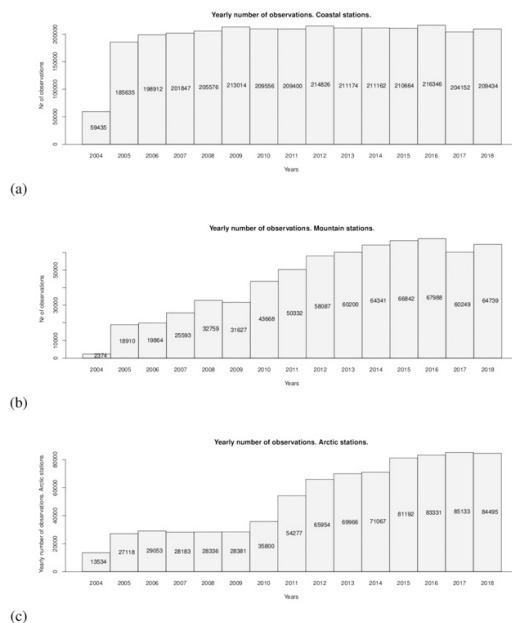


FIG. A3. Observation count: (a) coastal, (b) mountain, and (c) Arctic stations.

- ALADIN International Team, 1997: The ALADIN project: Mesoscale modelling seen as basic tool for weather forecasting and atmospheric research. *WMO Bull.*, **46**, 317–324.
- Andersen, O. J., and J. Løvseth, 2006: The Frøya database and maritime boundary layer wind description. *Mar. Structures*, **19**, 173–192, <https://doi.org/10.1016/j.marstruc.2006.07.003>.
- Batrak, Y., E. Kourzeneva, and M. Homleid, 2018: Implementation of a simple thermodynamic sea ice scheme, SICE version 1.0-38h1, within the ALADIN–HIRLAM numerical weather prediction system version 38h1. *Geosci. Model Dev.*, **11**, 3347–3368, <https://doi.org/10.5194/gmd-11-3347-2018>.
- Belamari, S., 2005: Report on uncertainty estimates of an optimal bulk formulation for surface turbulent fluxes. Marine Environment and Security for the European Area—Integrated Project Tech. Rep., 29 pp.
- , and A. Pirani, 2007: Validation of the optimal heat and momentum fluxes using the ORCA2-LIM global ocean-ice model. Marine Environment and Security for the European Area—Integrated Project Tech. Rep., 88 pp.
- Bénard, P., J. Vivoda, J. Mašek, P. Smolíková, K. Yessad, C. Smith, R. Brozková, and J.-F. Geleyn, 2010: Dynamical kernel of the Aladin–NH spectral limited-area model: Revised formulation and sensitivity experiments. *Quart. J. Roy. Meteor. Soc.*, **136**, 155–169, <https://doi.org/10.1002/qj.522>.
- Bengtsson, L., and Coauthors, 2017: The HARMONIE–AROME model configuration in the ALADIN–HIRLAM NWP system. *Mon. Wea. Rev.*, **145**, 1919–1935, <https://doi.org/10.1175/MWR-D-16-0417.1>.
- Bitner-Gregersen, E., and Coauthors, 2018: Climate change and safe design of ship structures. *Ocean Eng.*, **149**, 226–237, <https://doi.org/10.1016/j.oceaneng.2017.12.023>.
- Boone, A., J. C. Calvet, and J. Noilhan, 1999: Inclusion of a third soil layer in a land surface scheme using the force-restore method. *J. Appl. Meteor.*, **38**, 1611–1630, [https://doi.org/10.1175/1520-0450\(1999\)038<1611:IOATSL>2.0.CO;2](https://doi.org/10.1175/1520-0450(1999)038<1611:IOATSL>2.0.CO;2).
- Breivik, Ø., and O. J. Aarnes, 2017: Efficient bootstrap estimates for tail statistics. *Nat. Hazards Earth Syst. Sci.*, **17**, 357–366, <https://doi.org/10.5194/nhess-17-357-2017>.
- , Y. Gusdal, B. R. Furevik, O. J. Aarnes, and M. Reistad, 2009: Nearshore wave forecasting and hindcasting by dynamical and statistical downscaling. *J. Mar. Syst.*, **78**, S235–S243, <https://doi.org/10.1016/j.jmarsys.2009.01.025>.
- , O. J. Aarnes, J.-R. Bidlot, A. Carrasco, and Ø. Setra, 2013: Wave extremes in the northeast Atlantic from ensemble forecasts. *J. Climate*, **26**, 7525–7540, <https://doi.org/10.1175/JCLI-D-12-00738.1>.
- , O. Aarnes, S. Abadalla, J.-R. Bidlot, and P. Janssen, 2014: Wind and wave extremes over the world oceans from very large ensembles. *Geophys. Res. Lett.*, **41**, 5122–5131, <https://doi.org/10.1002/2014GL060997>.
- Bricheno, L. M., and J. Wolf, 2018: Future wave conditions of Europe, in response to high-end climate change scenarios. *J. Geophys. Res. Oceans*, **123**, 8762–8791, <https://doi.org/10.1029/2018JC013866>.
- Brousseau, P., Y. Seity, D. Ricard, and J. Léger, 2016: Improvement of the forecast of convective activity from the AROME-France system. *Quart. J. Roy. Meteor. Soc.*, **142**, 2231–2243, <https://doi.org/10.1002/qj.2822>.
- Bubnová, R., G. Hello, P. Bénard, and J.-F. Geleyn, 1995: Integration of the fully elastic equations cast in the hydrostatic pressure terrain-following coordinate in the framework of the ARPEGE/Aladin NWP system. *Mon. Wea. Rev.*, **123**, 515–535, [https://doi.org/10.1175/1520-0493\(1995\)123<0515:IOTFEE>2.0.CO;2](https://doi.org/10.1175/1520-0493(1995)123<0515:IOTFEE>2.0.CO;2).
- Catto, J. L., and Coauthors, 2019: The future of midlatitude cyclones. *Curr. Climate Change Rep.*, **5**, 407–420, <https://doi.org/10.1007/s40641-019-00149-4>.
- Charnock, H., 1955: Wind stress on a water surface. *Quart. J. Roy. Meteor. Soc.*, **81**, 639–640, <https://doi.org/10.1002/qj.49708135027>.
- Christakos, K., J.-V. Björkqvist, L. Tuomi, B. R. Furevik, and Ø. Breivik, 2020a: Modelling wave growth in narrow fetch geometries: The white-capping and wind input formulations. *Ocean Modell.*, **157**, 101730, <https://doi.org/10.1016/j.ocemod.2020.101730>.
- , B. R. Furevik, O. J. Aarnes, Ø. Breivik, L. Tuomi, and Ø. Byrkjedal, 2020b: The importance of wind forcing in fjord wave modelling. *Ocean Dyn.*, **70**, 57–75, <https://doi.org/10.1007/s10236-019-01323-w>.
- Daley, R., 1991: *Atmospheric Data Analysis*. Atmospheric and Space Science Series, Vol. 2, Cambridge University Press, 460 pp.
- Danielson, J., and D. Gesch, 2011: Global multi-resolution terrain elevation data 2010 (GMTED2010). U.S. Geological Survey Tech. Rep. 2011-1073, 26 pp., <https://pubs.usgs.gov/of/2011/1073/pdf/of2011-1073.pdf>.
- Dee, D. P., and Coauthors, 2011: The ERA-Interim reanalysis: Configuration and performance of the data assimilation system. *Quart. J. Roy. Meteor. Soc.*, **137**, 553–597, <https://doi.org/10.1002/qj.828>.
- Deng, A., and D. R. Stauffer, 2006: On improving 4-km mesoscale model simulations. *J. Appl. Meteor. Climatol.*, **45**, 361–381, <https://doi.org/10.1175/JAM2341.1>.
- de Rooy, W. C., and A. P. Siebesma, 2008: A simple parameterization for detrainment in shallow cumulus. *Mon. Wea. Rev.*, **136**, 560–576, <https://doi.org/10.1175/2007MWR2201.1>.
- , and —, 2010: Analytical expressions for entrainment and detrainment in cumulus convection. *Quart. J. Roy. Meteor. Soc.*, **136**, 1216–1227, <https://doi.org/10.1002/qj.640>.
- Donelan, M. A., and A. K. Magnusson, 2017: The making of the Andrea wave and other rogues. *Sci. Rep.*, **7**, 44124, <https://doi.org/10.1038/srep44124>.
- ECMWF, 1989: ECMWF forecast model: Physical parameterization. ECMWF Res. Manual RM-3, 154 pp.
- Fairall, C. W., E. F. Bradley, D. P. Rogers, J. B. Edson, and G. S. Young, 1996: Bulk parameterization of air-sea fluxes for Tropical Ocean-Global Atmosphere Coupled-Ocean Atmosphere Response Experiment. *J. Geophys. Res.*, **101**, 3747–3764, <https://doi.org/10.1029/95JC03205>.
- Faroux, S., A. T. K. Tchuente, J. L. Roujean, V. Masson, E. Martin, and P. Le Moigne, 2013: ECOCLIMAP-II/Europe: A twofold database of ecosystems and surface parameters at 1 km resolution based on satellite information for use in land surface, meteorological and climate models. *Geosci. Model Dev.*, **6**, 563–582, <https://doi.org/10.5194/gmd-6-563-2013>.
- Føre, I., J. Kristjánsson, Ø. Setra, Ø. Breivik, B. Røsting, and M. Shapiro, 2011: The full life cycle of a polar low over the Norwegian Sea probed by three research aircraft flights. *Quart. J. Roy. Meteor. Soc.*, **137**, 1659–1673, <https://doi.org/10.1002/qj.825>.
- Furevik, B. R., and H. Haakenstad, 2012: Near-surface marine wind profiles from rawinsonde and NORA10 hindcast. *J. Geophys. Res.*, **117**, D23106, <https://doi.org/10.1029/2012JD018523>.
- , H. Schyberg, G. Noer, F. Tveter, and J. Röhrs, 2015: ASAR and ASCAT in polar low situations. *J. Atmos. Oceanic Technol.*, **32**, 783–792, <https://doi.org/10.1175/JTECH-D-14-00154.1>.
- Gandin, L. S., and A. H. Murphy, 1992: Equitable skill scores for categorical forecasts. *Mon. Wea. Rev.*, **120**, 361–370, [https://doi.org/10.1175/1520-0493\(1992\)120<0361:ESSFCF>2.0.CO;2](https://doi.org/10.1175/1520-0493(1992)120<0361:ESSFCF>2.0.CO;2).

- Gaslikova, L., and R. Weisse, 2006: Estimating near-shore wave statistics from regional hindcasts using downscaling techniques. *Ocean Dyn.*, **56**, 26–35, <https://doi.org/10.1007/s10236-005-0041-2>.
- Gerard, L., J.-M. Piriou, R. Brozkova, J.-F. Geleyn, and D. Banciu, 2009: Cloud and precipitation parameterization in a meso-gamma-scale operational weather prediction model. *Mon. Wea. Rev.*, **137**, 3960–3977, <https://doi.org/10.1175/2009MWR2750.1>.
- Giard, D., and E. Bazile, 2000: Implementation of a new assimilation scheme for soil and surface variables in a global NWP model. *Mon. Wea. Rev.*, **128**, 997–1015, [https://doi.org/10.1175/1520-0493\(2000\)128<0997:IOANAS>2.0.CO;2](https://doi.org/10.1175/1520-0493(2000)128<0997:IOANAS>2.0.CO;2).
- Gosnell, R. C., C. Fairall, and P. J. Webster, 1995: The sensible heat of rainfall in the tropical ocean. *J. Geophys. Res.*, **100**, 18 437–18 442, <https://doi.org/10.1029/95JC01833>.
- Gramstad, O., E. Bitner-Gregersen, Ø. Breivik, A. K. Magnusson, M. Reistad, and O. J. Aarnes, 2018: Analysis of rogue waves in North-Sea in-situ surface wave data. *Proc. 37th Int. Conf. on Ocean, Offshore and Arctic Engineering*, Madrid, Spain, ASME, V003T02A005, <https://doi.org/10.1115/OMAE2018-77858>.
- Haakenstad, H., Ø. Breivik, M. Reistad, and O. J. Aarnes, 2020: NORA10EI: A revised regional atmosphere-wave hindcast for the North Sea, the Norwegian Sea and the Barents Sea. *Int. J. Climatol.*, **40**, 4347–4373, <https://doi.org/10.1002/joc.6458>.
- Hersbach, H., and Coauthors, 2020: The ERA5 global reanalysis. *Quart. J. Roy. Meteor. Soc.*, **146**, 1999–2049, <https://doi.org/10.1002/qj.3803>.
- HIRLAM Consortium, 2016: Quality assessment of Harmonic Cycle 40 for use in operational Hirlam systems. KNMI Note, 22 pp.
- Hodges, K., R. Lee, and L. Bengtsson, 2011: A comparison of extratropical cyclones in recent reanalyses ERA-Interim, NASA MERRA, NCEP CFSR, and JRA-25. *J. Climate*, **24**, 4888–4906, <https://doi.org/10.1175/2011JCLI4097.1>.
- Hortal, M., 2002: The development and testing of a new two-time-level semi-Lagrangian scheme (SETTLs) in the ECMWF forecast model. *Quart. J. Roy. Meteor. Soc.*, **128**, 1671–1687, <https://doi.org/10.1002/qj.200212858314>.
- Janssen, P., 1989: Wave-induced stress and the drag of air flow over sea waves. *J. Phys. Oceanogr.*, **19**, 745–754, [https://doi.org/10.1175/1520-0485\(1989\)019<0745:WISAATD>2.0.CO;2](https://doi.org/10.1175/1520-0485(1989)019<0745:WISAATD>2.0.CO;2).
- , 1991: Quasi-linear theory of wind-wave generation applied to wave forecasting. *J. Phys. Oceanogr.*, **21**, 1631–1642, [https://doi.org/10.1175/1520-0485\(1991\)021<1631:QLTOWW>2.0.CO;2](https://doi.org/10.1175/1520-0485(1991)021<1631:QLTOWW>2.0.CO;2).
- , O. Sætra, C. Wettre, H. Hersbach, and J. Bidlot, 2004: Impact of the sea state on the atmosphere and ocean. *Ann. Hydrogr.*, **772**, 143–157.
- Khairoutdinov, M., and Y. Kogan, 2000: A new cloud physics parameterization in a large-eddy simulation model of marine stratocumulus. *Mon. Wea. Rev.*, **128**, 229–243, [https://doi.org/10.1175/1520-0493\(2000\)128<0229:ANCPPI>2.0.CO;2](https://doi.org/10.1175/1520-0493(2000)128<0229:ANCPPI>2.0.CO;2).
- Kjelland, G., 2005: KVALOBS—The quality assurance system of Norwegian Meteorological Institute observations. WMO Instruments and Observing Methods Rep. 82, WMO/TD-1265, 5 pp., [https://library.wmo.int/doc\\_num.php?explnum\\_id=9293](https://library.wmo.int/doc_num.php?explnum_id=9293).
- Költzow, M., B. Casati, T. Haiden, and T. Valkonen, 2019: An NWP model intercomparison of surface weather parameters in the European Arctic during the Year of Polar Prediction Special Observing Period Northern Hemisphere 1. *Wea. Forecasting*, **34**, 959–983, <https://doi.org/10.1175/WAF-D-19-0003.1>.
- Lafore, L., and Coauthors, 1998: The Meso-NH Atmospheric Simulation System. Part I: Adiabatic formulation and control simulations. *Ann. Geophys.*, **16**, 90–109, <https://doi.org/10.1007/s00585-997-0090-6>.
- Laprise, R., 1992: The Euler equations of motion with hydrostatic pressure as an independent variable. *Mon. Wea. Rev.*, **120**, 197–207, [https://doi.org/10.1175/1520-0493\(1992\)120<0197:TEEOMW>2.0.CO;2](https://doi.org/10.1175/1520-0493(1992)120<0197:TEEOMW>2.0.CO;2).
- Lascaux, F., E. Richard, and J.-P. Pinty, 2006: Numerical simulations of three different MAP IOPs and the associated microphysical processes. *Quart. J. Roy. Meteor. Soc.*, **132**, 1907–1926, <https://doi.org/10.1256/qj.05.197>.
- Le Moigne, P., and Coauthors, 2012: SURFEX scientific documentation. CNRM/GAME Météo-France/CNRS Sci. Doc., 237 pp., [https://www.umr-cnrm.fr/surfex/IMG/pdf/surfex\\_scidoc\\_v2-2.pdf](https://www.umr-cnrm.fr/surfex/IMG/pdf/surfex_scidoc_v2-2.pdf).
- Lenderink, G., and A. A. Holtslag, 2004: An updated length-scale formulation for turbulent mixing in clear and cloudy boundary layers. *Quart. J. Roy. Meteor. Soc.*, **130**, 3405–3427, <https://doi.org/10.1256/qj.03.117>.
- Malardel, S., 2013: Physics/dynamics coupling at very high resolution: Permitted versus parametrized convection. *ECMWF Seminar on Numerical Methods for Atmosphere and Ocean Modelling*, Reading, United Kingdom, ECMWF, 83–98, <https://www.ecmwf.int/node/10948>.
- Masson, V., and Coauthors, 2013: The SURFEXv7.2 land and ocean surface platform for coupled or offline simulation of earth surface variables and fluxes. *Geosci. Model Dev.*, **6**, 929–960, <https://doi.org/10.5194/gmd-6-929-2013>.
- Meucci, A., I. R. Young, and Ø. Breivik, 2018: Wind and wave extremes from atmosphere and wave model ensembles. *J. Climate*, **31**, 8819–8842, <https://doi.org/10.1175/JCLI-D-18-0217.1>.
- , —, O. J. Aarnes, and Ø. Breivik, 2020: Comparison of wind speed and wave height trends from twentieth century models and satellite altimeters. *J. Climate*, **33**, 611–624, <https://doi.org/10.1175/JCLI-D-19-0540.1>.
- Mlawer, E. J., S. J. Taubman, P. D. Brown, M. J. Iacono, and S. A. Clough, 1997: Radiative transfer for inhomogeneous atmospheres: RRTM, a validated correlated-k model for the longwave. *J. Geophys. Res.*, **102**, 16 663–16 682, <https://doi.org/10.1029/97JD00237>.
- Moore, G. W. K., I. A. Renfrew, B. E. Harden, and S. H. Mernild, 2015: The impact of resolution on the representation of Greenland barrier winds and katabatic flows. *Geophys. Res. Lett.*, **42**, 3011–3018, <https://doi.org/10.1002/2015GL063550>.
- , D. H. Bromwich, A. B. Wilson, I. Renfrew, and L. Bai, 2016: Arctic system reanalysis improvements in topographically forced winds near Greenland. *Quart. J. Roy. Meteor. Soc.*, **142**, 2033–2045, <https://doi.org/10.1002/qj.2798>.
- Morim, J., and Coauthors, 2019: Robustness and uncertainties in global multivariate wind-wave climate projections. *Nat. Climate Change*, **9**, 711–718, <https://doi.org/10.1038/s41558-019-0542-5>.
- Müller, M., Y. Batrak, J. Kristiansen, M. A. Ø. Koltzow, and G. Noer, 2017a: Characteristics of a convective-scale weather forecasting system for the European Arctic. *Mon. Wea. Rev.*, **145**, 4771–4787, <https://doi.org/10.1175/MWR-D-17-0194.1>.
- , and Coauthors, 2017b: AROME-MetCoOp: A Nordic convective-scale operational weather prediction model. *Wea. Forecasting*, **32**, 609–627, <https://doi.org/10.1175/WAF-D-16-0099.1>.
- NORSOK, 2007: NORSOK standard N-003: Action and action effects. Standards Norway Doc., 57 pp.
- Pinty, J.-P., and P. Jabouille, 1998: A mixed-phase cloud parameterization for use in a mesoscale non-hydrostatic model:



- Simulation of a squall line and of orographic precipitation. Preprints, *Conf. on Cloud Physics*, Everett, WA, Amer. Meteor. Soc., 217–220.
- Press, W. H., S. A. Teukolsky, W. T. Vetterling, and B. P. Flannery, 2007: *Numerical Recipes in C*. 3rd ed. Cambridge University Press, 1235 pp.
- Rasmussen, E. A., and J. Turner, 2003: *Polar Lows: Mesoscale Weather Systems in the Polar Regions*. Cambridge University Press, 612 pp.
- Reed, R. J., and C. N. Duncan, 1987: Baroclinic instability as a mechanism for the serial development of polar lows: A case study. *Tellus*, **39A**, 376–384, <https://doi.org/10.1111/j.1600-0870.1987.tb00314.x>.
- Reistad, M., Ø. Breivik, H. Haakenstad, O. J. Aarnes, B. R. Furevik, and J.-R. Bidlot, 2011: A high-resolution hindcast of wind and waves for the North Sea, the Norwegian Sea, and the Barents Sea. *J. Geophys. Res.*, **116**, C05019, <https://doi.org/10.1029/2010JC006402>.
- Renfrew, I. A., and Coauthors, 2021: An evaluation of surface meteorology and fluxes over the Iceland and Greenland Seas in ERA5 reanalysis: The impact of sea ice distribution. *Quart. J. Roy. Meteor. Soc.*, **147**, 691–712, <https://doi.org/10.1002/qj.3941>.
- Rienecker, M. M., and Coauthors, 2011: MERRA: NASA's Modern-Era Retrospective Analysis for Research and Applications. *J. Climate*, **24**, 3624–2648, <https://doi.org/10.1175/JCLI-D-11-00015.1>.
- Rivas, M. B., and A. Stoffelen, 2019: Characterizing ERA-Interim and ERA5 surface wind biases using ASCAT. *Ocean Sci.*, **15**, 831–852, <https://doi.org/10.5194/os-15-831-2019>.
- Royo, M., G. Noer, and C. Claud, 2019: Polar low tracks in the Norwegian Sea and the Barents Sea from 1999 until 2019. PANGAEA, accessed 11 March 2021, <https://doi.org/10.1594/PANGAEA.903058>.
- Saha, S., and Coauthors, 2010: The NCEP Climate Forecast System Reanalysis. *Bull. Amer. Meteor. Soc.*, **91**, 1015–1057, <https://doi.org/10.1175/2010BAMS3001.1>.
- , and Coauthors, 2014: The NCEP Climate Forecast System version 2. *J. Climate*, **27**, 2185–2208, <https://doi.org/10.1175/JCLI-D-12-00823.1>.
- Seity, Y., P. Brousseau, S. Malardel, G. Hello, P. Benard, F. Bouttier, C. Lac, and V. Masson, 2011: The AROME-France convective-scale operational model. *Mon. Wea. Rev.*, **139**, 976–991, <https://doi.org/10.1175/2010MWR3425.1>.
- Sergeev, D., I. A. Renfrew, and T. Spengler, 2018: Modification of polar low development by orography and sea ice. *Mon. Wea. Rev.*, **146**, 3325–3341, <https://doi.org/10.1175/MWR-D-18-0086.1>.
- Shimura, T., N. Mori, and M. A. Hemer, 2016: Variability and future decreases in winter wave heights in the western North Pacific. *Geophys. Res. Lett.*, **43**, 2716–2722, <https://doi.org/10.1002/2016GL067924>.
- Siebesma, A. P., and Coauthors, 2003: A large eddy simulation intercomparison study of shallow cumulus convection. *J. Atmos. Sci.*, **60**, 1201–1219, [https://doi.org/10.1175/1520-0469\(2003\)60<1201:ALESIS>2.0.CO;2](https://doi.org/10.1175/1520-0469(2003)60<1201:ALESIS>2.0.CO;2).
- , P. M. Soares, and J. Teixeira, 2007: A combined eddy-diffusivity mass-flux approach for the convective boundary layer. *J. Atmos. Sci.*, **64**, 1230–1248, <https://doi.org/10.1175/JAS3888.1>.
- Simmons, A., and D. Burridge, 1981: An energy and angular-momentum conserving vertical finite-difference scheme and hybrid vertical coordinates. *Mon. Wea. Rev.*, **109**, 758–766, [https://doi.org/10.1175/1520-0493\(1981\)109<0758:AEAAMC>2.0.CO;2](https://doi.org/10.1175/1520-0493(1981)109<0758:AEAAMC>2.0.CO;2).
- Smith, S. D., 1988: Coefficients for sea surface wind stress, heat flux, and wind profiles as a function of wind speed and temperature. *J. Geophys. Res.*, **93**, 15 467–15 472, <https://doi.org/10.1029/JC093iC12p15467>.
- Soares, P., P. Miranda, A. Siebesma, and J. Teixeira, 2004: An eddy-diffusivity mass-flux parameterization for dry and shallow cumulus convection. *Quart. J. Roy. Meteor. Soc.*, **130**, 3365–3383, <https://doi.org/10.1256/qj.03.223>.
- Taillefer, F., 2002: CANARI. CNRM/GMAP Tech. Doc., 55 pp., [http://www.umr-cnrm.fr/gmapdoc/IMG/ps/canari\\_doc\\_cy25t1.ps](http://www.umr-cnrm.fr/gmapdoc/IMG/ps/canari_doc_cy25t1.ps).
- Takbashi, A., I. Young, and Ø. Breivik, 2019: Global wind speed and wave height extremes derived from long-duration satellite records. *J. Climate*, **32**, 109–126, <https://doi.org/10.1175/JCLI-D-18-0520.1>.
- Uppala, S. M., and Coauthors, 2005: The ERA-40 Re-Analysis. *Quart. J. Roy. Meteor. Soc.*, **131**, 2961–3012, <https://doi.org/10.1256/qj.04.176>.
- van Meijgaard, E., L. H. van Ulft, G. Lenderink, S. D. Roode, E. L. Wipfler, R. Boers, and R. van Timmermans, 2012: Refinement and application of a regional atmospheric model for climate scenario calculations of western Europe. KVR Rep. 054/12, 44 pp., [http://climexp.knmi.nl/publications/FinalReport\\_KvR-CS06.pdf](http://climexp.knmi.nl/publications/FinalReport_KvR-CS06.pdf).
- Weill, A., and Coauthors, 2003: Toward a better determination of turbulent air–sea fluxes from several experiments. *J. Climate*, **16**, 600–618, [https://doi.org/10.1175/1520-0442\(2003\)016<0600:TABDOT>2.0.CO;2](https://doi.org/10.1175/1520-0442(2003)016<0600:TABDOT>2.0.CO;2).
- Wilks, D. S., 2006: *Statistical Methods in the Atmospheric Sciences*. 2nd ed. Academic Press, 627 pp.
- Yano, J.-I., and Coauthors, 2018: Scientific challenges of convective-scale numerical weather prediction. *Bull. Amer. Meteor. Soc.*, **99**, 699–710, <https://doi.org/10.1175/BAMS-D-17-0125.1>.
- Zahn, M., and H. von Storch, 2008: A long-term climatology of North Atlantic polar lows. *Geophys. Res. Lett.*, **35**, L22702, <https://doi.org/10.1029/2008GL035769>.





# Paper IV

## **The impact of a reduced high-wind Charnock parameter on wave growth with application to the North Sea, the Norwegian Sea and the Arctic Ocean**

Ø. Breivik and A. Carrasco and H. Haakenstad and O. J. Aarnes and A. Behrens and J.-R. Bidlot and J.-V. Björkqvist and P. Bohlinger and B. R. Furevik and J. Staneva and M. Reistad *Journal of Geophysical Research: Oceans*, Accepted 2022-03-10



## Key Points:

- A semiempirical parameterization for high-wind drag (above  $30 \text{ m s}^{-1}$ ) is implemented in WAM
- A 2-year comparison against a control run shows significant bias reduction in strong winds
- A 23-year wave hindcast shows very good performance compared to satellite and buoy measurements

## Correspondence to:

Ø. Breivik,  
[oyvind.breivik@met.no](mailto:oyvind.breivik@met.no)




## Citation:

Breivik, Ø., Carrasco, A., Haakenstad, H., Aarnes, O. J., Behrens, A., Bidlot, J.-R., et al. (2022). The impact of a reduced high-wind Charnock parameter on wave growth with application to the North Sea, the Norwegian Sea, and the Arctic Ocean. *Journal of Geophysical Research: Oceans*, 127, e2021JC018196. <https://doi.org/10.1029/2021JC018196>

Received 29 OCT 2021

Accepted 9 MAR 2022

## The Impact of a Reduced High-Wind Charnock Parameter on Wave Growth With Application to the North Sea, the Norwegian Sea, and the Arctic Ocean

Øyvind Breivik<sup>1,2</sup> , Ana Carrasco<sup>1</sup> , Hilde Haakenstad<sup>1,2</sup>, Ole Johan Aarnes<sup>1</sup> , Arno Behrens<sup>3</sup> , Jean-Raymond Bidlot<sup>4</sup>, Jan-Victor Björkqvist<sup>1,5</sup> , Patrik Bohlinger<sup>1</sup> , Birgitte R. Furevik<sup>1,2</sup>, Joanna Staneva<sup>3</sup>, and Magnar Reistad<sup>1</sup> 

<sup>1</sup>Norwegian Meteorological Institute, Oslo, Norway, <sup>2</sup>University of Bergen, Bergen, Norway, <sup>3</sup>Helmholtz-Zentrum Hereon, Geesthacht, Germany, <sup>4</sup>European Centre for Medium-Range Weather Forecasts, Reading, UK, <sup>5</sup>Finnish Meteorological Institute, Helsinki, Finland

**Abstract** As atmospheric models move to higher resolution and resolve smaller scales, the maximum modeled wind speed also tends to increase. Wave models tuned to coarser wind fields tend to overestimate the wave growth under strong winds. A recently developed semiempirical parameterization of the Charnock parameter, which controls the roughness length over surface waves, substantially reduces the aerodynamic drag of waves in high winds (above a threshold of  $30 \text{ m s}^{-1}$ ). Here, we apply the formulation in a recent version of the wave model WAM (Cycle 4.7), which uses a modified version of the physics parameterizations by Ardhuin et al. (2010, <https://doi.org/10.1175/2010jpo4324.1>) as well as subgrid obstructions for better performance around complex topography. The new Charnock formulation is tested with wind forcing from NORA3, a recently completed nonhydrostatic atmospheric downscaling of the global reanalysis ERA5 for the North Sea, the Norwegian Sea and the Barents Sea. Such high-resolution atmospheric model integrations tend to have stronger (and more realistic) upper-percentile winds than what is typically found in coarser atmospheric models. A 2-year comparison (2011–2012) of a control run against the run with the modified Charnock parameter shows a dramatic reduction of the wave height bias in high-wind cases. The added computational cost of the new physics and the reduction of the Charnock parameter compared to the earlier WAM physics is modest (14%). A longer (1998–2020) hindcast integration with the new Charnock parameter is found to compare well against in situ and altimeter wave measurements both for intermediate and high sea states.

**Plain Language Summary** Wave models are sensitive to strong winds, and as the atmospheric models have increased in resolution, the strength of the winds has also increased as small-scale features of synoptic storms become more realistically modeled. Here, we investigate the behavior of a bespoke version of the wave model WAM, where we have modified how waves grow in strong winds. More specifically, we have modified the so-called Charnock parameter, which determines how rough the sea surface gets as the wind picks up. By making the sea surface smoother under strong winds, we reduce the growth of the waves under hurricane conditions in a manner which appears to be in line with recent studies of the behavior of the sea surface in very strong winds. The results match our observations very well over a wide range of conditions throughout the model domain and show a clear improvement over a control experiment with the same wave model without a modified Charnock parameter. Finally, a detailed wave hindcast, or sea state archive, for the Norwegian Sea, North Sea and the Arctic Ocean covering the period 1998–2020 is presented where this modified Charnock parameter is employed. The results compare well against observations.

### 1. Introduction

Third generation spectral wave models (Booij et al., 1999; ECMWF, 2020; Hasselmann et al., 1988; Janssen, 2004; Komen et al., 1994; Tolman, 1991; Wavewatch III Development Group, 2019) balance the energy and momentum flux from the wind field against the dissipation due to wave breaking (Janssen, 2004) as well as the nonlinear transfer of energy within the wave spectrum. Modern wave models tend to perform well in terms of integrated wave parameters such as significant wave height, mean wave period and mean wave direction as long as the quality of the wind field is high (see, e.g., Hersbach et al., 2020). It is however not clear whether wave models also perform well under very strong winds (Du et al., 2017; Jensen et al., 2006), and it is known that the wind input

© 2022. The Authors.

This is an open access article under the terms of the [Creative Commons Attribution-NonCommercial-NoDerivs License](https://creativecommons.org/licenses/by/4.0/), which permits use and distribution in any medium, provided the original work is properly cited, the use is non-commercial and no modifications or adaptations are made.

source term based on conservation of momentum in the boundary layer first proposed by Janssen (1989) tends to overestimate the drag at high winds (Du et al., 2017; Jensen et al., 2006).

The growth of waves under extratropical wind storms and tropical cyclones has been the topic of several studies in the past two decades (S. S. Chen et al., 2013; Donelan et al., 2004; Powell et al., 2003; Zweers et al., 2010). Wave growth is controlled by the aerodynamic roughness of the surface, that is, the drag that is felt by the wind. There is increasing evidence from theoretical (Makin, 2005), laboratory (Curcic & Haus, 2020; Donelan et al., 2004) and field studies (Donelan, 2018; Holthuijsen et al., 2012; Powell et al., 2003) that the roughness (and thus the drag) starts to level off or even drop (Powell et al., 2003) at very high wind speeds. The exact threshold where the drag will start to level off remains unclear, with Curcic and Haus (2020), in a recent revisit of the drag saturation rate measured by Donelan et al. (2004), suggesting that it may start as low as around  $20 \text{ m s}^{-1}$  (see also Bi et al., 2015). Other studies (see the overview in Figure 6 by Holthuijsen et al., 2012) report a leveling off from around  $30 \text{ m s}^{-1}$  (Zweers et al., 2010).

As the resolution of atmospheric models continues to increase and the models increasingly include nonhydrostatic physics, the intensity of the strongest wind storms modeled also increases. This does not mean that the winds are overestimated, merely that high-resolution nonhydrostatic atmosphere models capture small-scale features that cannot be resolved by coarser models (Haakenstad et al., 2021). Since wave models have hitherto not realistically modeled the reduction in drag under the strongest winds (Du et al., 2017), this tendency for coarser, hydrostatic atmospheric models to produce too weak winds may have been partly compensated by the wind input source term in the wave model. Thus, how wave models parameterize wave growth under high winds becomes increasingly important as forecast systems, both coupled and uncoupled, move toward higher resolution. That is the topic of this paper.

There are several semiempirical approaches to reducing the momentum flux to the wave field under strong winds. A parameterization for the direct reduction of the drag coefficient was proposed by Holthuijsen et al. (2012). As summarized by Du et al. (2017), other approaches include capping the limit on the ratio between the wind speed and the friction velocity (Jensen et al., 2006) and setting a limit on the roughness length (Arduin et al., 2010). A spectral sheltering to reduce the high-frequency wave growth in the presence of longer waves was formulated by Banner and Morison (2010), following work by G. Chen and Belcher (2000). The impact of limiting the maximum steepness of short waves was reported by Magnusson et al. (2019). In addition, the Charnock parameter itself (Charnock, 1955; Janssen, 1989) can be modified for strong winds, thus directly controlling the wave growth by limiting the surface roughness. This is an approach somewhat similar to the cap on the roughness length introduced by Arduin et al. (2010). This modification of the Charnock parameter is specifically investigated in this paper.

This article is laid out as follows. We first present in Section 2 the relevant details of the wind input source term as implemented in the WAM Cycle 4.7 wave model, a recent version of the open-source WAM model (Günther et al., 1992; Hasselmann et al., 1988; Komen et al., 1994). In Section 3, we present a recently proposed semiempirical reduction of the Charnock parameter at high winds (ECMWF, 2020; Li et al., 2021). Section 4 presents a comparison of two wave model runs, one with a reduced Charnock parameter at high winds and a control run with no reduction, covering a 2-year period. Section 5 presents a 23-year (uncoupled) wave hindcast where we have applied the new Charnock parameter to a WAM domain forced with high-resolution winds (3 km) from the recent NORA3 atmospheric hindcast (Haakenstad et al., 2021), hereafter referred to as the NORA3 wave hindcast or simply NORA3 WAM. Finally, in Section 6, we summarize our findings and draw some conclusions regarding the usefulness of implementing a reduced-drag parameterization for high-resolution forecast and hindcast systems, both coupled and uncoupled.

## 2. The Wind Input Source Term in WAM Cycle 4.7

The WAM wave model (Günther et al., 1992; Hasselmann et al., 1988; Komen et al., 1994) has in recent years undergone major code restructuring as it has been made openly accessible through the EU project MyWave (Behrens et al., 2013). WAM Cycle 4.7 contains model physics that is similar to what is described by Arduin et al. (2010) and often referred to as “Source term package 4” (ST4), but with some differences indicated below. The implementation of the source terms is taken from a recent version of the wave model component (ECWAM

Cycle 47R1, see ECMWF, (2020) of the Integrated Forecast System (IFS) operated by the European Centre for Medium-Range Weather Forecasts (ECMWF).

The air-side stress,  $\tau_a$  [Pa], is supported almost entirely by the roughness of the oceanic wave field itself (Janssen, 1989, 1991). There must thus exist a relationship between the wind stress and the roughness length  $z_0$  of a water surface with waves, as Charnock (1955) showed,

$$z_0 = \alpha u_*^2 / g. \quad (1)$$

Here,  $\alpha$  is a dimensionless coefficient known as the Charnock parameter and  $g = 9.81 \text{ m s}^{-2}$  is the gravitational acceleration. The friction velocity  $u_*$  relates to the air-side stress  $\tau_a$  as

$$u_* \equiv \sqrt{\tau_a / \rho_a} \quad (2)$$

with  $\rho_a$ , the atmospheric density, assumed here to be constantly  $1.225 \text{ kg m}^{-3}$ . The dimensionless drag coefficient  $C_d$  is a bulk parameter as it relates an atmospheric state variable (the wind speed) at a specific height ( $z = 10 \text{ m}$ ) to a momentum flux,

$$\tau_a = \rho_a u_*^2 = \rho_a C_d U_{10}^2. \quad (3)$$

The drag coefficient has been the subject of many studies over the years, and we refer the reader to Edson et al. (2013) for a thorough overview of the drag coefficient parameterizations currently in use. The drag is related to the roughness length, Equation 1, through the logarithmic wind profile, which itself can be derived from a dimensional argument that in a constant-flux layer near the surface (see, for example, Stull, 1988) there is no divergence of momentum and hence no change in wind speed with time. The wind profile must thus be logarithmic,

$$U(z) = \frac{u_*}{\kappa} \ln((z + z_0) / z_0), \quad z > z_0. \quad (4)$$

Here,  $\kappa \approx 0.4$  is von Kármán's constant. This eventually leads to the relation between the drag coefficient and the roughness length,

$$C_d = \frac{\kappa^2}{\ln^2((z + z_0) / z_0)}. \quad (5)$$

We will now start with the observation, made by Janssen (1989, 1991), that the Charnock parameter  $\alpha$  in Equation 1 is not a constant, but is in fact a function of the sea state,

$$\alpha = \frac{\hat{\alpha}}{\sqrt{1 - \tau_{in} / \tau_a}}. \quad (6)$$

Here,  $\tau_{in}$  is the momentum flux to the wave field and is directly related to wave growth and  $\hat{\alpha}$  is a parameter which, as was noted already by Janssen (1989), is controlled by the shortest gravity-capillary waves. It is commonly taken to be a constant and henceforth referred to as the minimum Charnock parameter since it represents the lowest value that  $\alpha$  can attain. Due to Cycle 47R1 of the ECWMF WAM model (ECWAM, see ECMWF, 2020), it has been kept at  $\hat{\alpha} = \hat{\alpha}_0 = 0.0065$ .

It is clear that when waves absorb a sizable amount of the momentum (when they grow quickly), the denominator in Equation 6 becomes small, making the Charnock parameter large. This means that in strong winds, where waves are young and growing, the drag will become large. This has dramatic consequences for the wave growth in standalone wave models with no feedback to the atmospheric model, but also for coupled systems, such as the IFS, where too much drag lowers the near-surface wind speed excessively in storm conditions (J.-R. Bidlot et al., 2020; Li et al., 2021; Pineau-Guillou et al., 2020).

The wave growth is controlled by the wind input term  $S_{in}$ . The form used here is based on the formulation presented as Equation 19 by Ardhuin et al. (2010). We repeat it here for convenience,

$$S_{in} = \frac{\rho_a \beta_{\max}}{\rho_w \kappa^2} e^Z Z^4 \left[ \frac{u_*}{c} \right]^2 \max(\cos(\theta - \phi), 0)^p \sigma F(k, \theta). \quad (7)$$



Here,  $F(k, \theta)$  [ $\text{m}^3 \text{rad}^{-1}$ ] is the wave variance density in wavenumber ( $k$ )-direction ( $\theta$ ) space,  $\phi$  is the wind direction,  $\beta_{\max}$  is a constant nondimensional growth parameter and

$$Z = \ln(kz_1) + \kappa / [\cos(\theta - \phi)(u_* / c + z_a)] \quad (8)$$

is an effective wave age with  $c$  being the phase speed,  $\sigma$  being the intrinsic circular frequency [ $\text{rad s}^{-1}$ ] and  $z_a$  being a dimensionless wave age tuning parameter that shifts the growth curve. The directional spread is controlled by the power  $p$ , a tunable constant which is commonly (and here) set to 2. Higher powers give a more narrowly directed wind input.

It is important to note that Ardhuin et al. (2010) already introduced a cap on the surface roughness in the form

$$z_0 = \min(\alpha_0 u_*^2 / g, z_{0,\max}) \quad (9)$$

which in turn is used to calculate

$$z_1 = \frac{z_0}{\sqrt{1 - \tau_{\text{in}} / \tau}}. \quad (10)$$

Ardhuin et al. (2010) mention that imposing  $z_{0,\max} = 0.0015$  corresponds to capping the drag coefficient at  $C_D = 2.5 \times 10^{-3}$ . It is thus clear that adjusting  $\beta_{\max}$  and  $z_{0,\max}$  allows some freedom in tuning a wave model to an atmospheric model, but they will not allow a reduction of the roughness length above a certain wind speed threshold. It is also important to note that  $z_{0,\max}$  is not always active (i.e., it is set to 1). This is the case for the TEST471 tuning, considered the best option for global wind fields (see Table 2.6 by Wavewatch III Development Group, 2019). We have not used the  $z_{0,\max}$  parameter in our WAM implementation.

A further tuning parameter introduced by Ardhuin et al. (2010) is a wavenumber-dependent sheltering effect where  $u_*^2$  in Equation 7 is replaced by

$$\left(u_*^2\right)_i = u_*^2(\cos \phi, \sin \phi) - \tau_{\text{shelter}} \frac{\rho_w}{\rho_a} g \int_0^{2\pi} \int_0^k \frac{k'}{\omega} S_{\text{in}}(\cos \theta, \sin \theta) dk' d\theta. \quad (11)$$

Here,  $\omega = 2\pi f$  [ $\text{rad s}^{-1}$ ] is the circular frequency (identical to the intrinsic frequency  $\sigma$  in the absence of currents) and  $\rho_w$  is the density of sea water, assumed here to be constantly  $1,000 \text{ kg m}^{-3}$ . Note also that the equation is applied in the vector form with  $\phi$  being the wind direction and subscript  $i$  indicating  $x$  and  $y$  components. This sheltering effect also yields somewhat weaker growth in high-wind situations. The sheltering coefficient can vary between 0 and 1. Here we use a rather modest sheltering with  $\tau_{\text{shelter}} = 0.25$ .

ECWAM Cycle 47R1 and WAM Cycle 4.7 also impose a maximum steepness for the high-frequency part of the spectrum (ECMWF, 2020; Magnusson et al., 2019) by demanding the spectrum be limited to

$$F(f, \theta) = \min(F, F_{\max}). \quad (12)$$

Here,

$$F_{\max} = \frac{\alpha_{\max}}{\pi} g^2 (2\pi)^{-4} f^{-5} \quad (13)$$

is the Phillips spectrum (Phillips, 1958) with an omnidirectional normalizing constant  $(2\pi)^{-4}$  and the linear frequency  $f = \omega/2\pi$ . This maximum steepness is a plausible limiting mechanism for the roughness length in high-wind situations as short waves should start to break as they get steeper than what the Phillips spectrum dictates. We have set  $\alpha_{\max} = 0.031$  in accordance with ECWAM (ECMWF, 2020).

### 3. A Semiempirical Reduction of the Charnock Parameter in High-Wind Regimes

The drag coefficient (for wind at  $z = 10 \text{ m}$ ) can be seen from Equation 5 to be related to the roughness length of the sea surface as

$$z_0 = (10 + z_0) \exp\left(-\kappa / \sqrt{C_d}\right) \approx 10 \exp\left(-\kappa / \sqrt{C_d}\right). \quad (14)$$

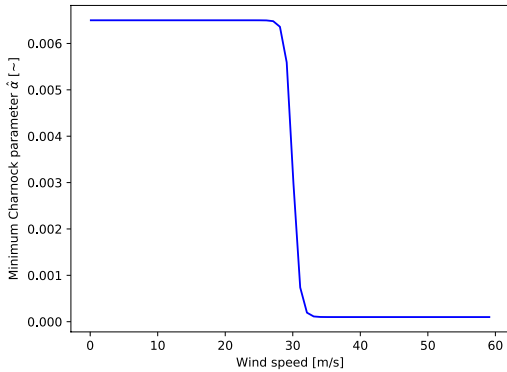


**Figure 1.** The tan h formulation, see Equation 15, of the high-wind reduction of the minimum Charnock parameter  $\hat{\alpha}$  plotted for a threshold wind speed  $U_{th} = 30.0 \text{ m s}^{-1}$  and a transition range  $\sigma_U = 1.0 \text{ m s}^{-1}$  drag coefficient.

Since the wave growth depends on the momentum flux, it is closely linked to the drag coefficient, see Equation 3. For varying wave ages  $c/u_a$ , the ratio  $\tau_{in}/\tau_a$  in Equation 6 will also vary. The roughness is controlled by both long and short waves. The roughness of long waves is controlled by the denominator in Equation 6. A young sea will tend to have high ratios since the wave growth is rapid. This in turn leads to a small denominator in Equation 6 and high Charnock values. This is the impact of the long (resolved) waves on the surface roughness. As mentioned before, it is clear that the wave growth will be stronger for a young wind sea than for an older wind sea, and for really strong winds, approaching  $30 \text{ m s}^{-1}$ , the sea state is always young as such strong winds are rarely sustained over long periods (Li et al., 2021). If the roughness does indeed go down for very high winds, it seems reasonable to attempt to adjust  $\hat{\alpha}$  since, as Janssen (1989) pointed out, this parameter represents the roughness due to the shortest (unresolved) waves of the  $f^{-5}$  Phillips tail, as shown in Equation 13. In essence, this will allow us to control the roughness of the shortest waves for different wind regimes.

Li et al. (2021), employing the recent implementation from ECWAM (ECMWF, 2020), tested the following minimum Charnock parameterization for typhoon Lingling in a coupled atmosphere-wave model run,

$$\hat{\alpha} = \hat{\alpha}_- + 0.5(\hat{\alpha}_0 - \hat{\alpha}_-) \left( 1 - \tanh \left[ (U_{10} - U_{th}) / \sigma_U \right] \right). \quad (15)$$

Here,  $\hat{\alpha}_0 = 0.0065$  and corresponds to the previously constant  $\hat{\alpha}$  in Equation 6 while  $\hat{\alpha}_- = 0.0001$  is the value that  $\hat{\alpha}$  asymptotes toward at very high wind speeds. We employ the same parameterization with some minor adjustments. The optimum threshold wind speed  $U_{th}$  and the transition range  $\sigma_U$  over which the transition should take place are not well known. At one extreme Bi et al. (2015) found that the drag coefficient starts to level off between  $18$  and  $27 \text{ m s}^{-1}$ , while Zwers et al. (2010) found the drag coefficient to peak around  $27 \text{ m s}^{-1}$ . Others have reported even higher wind speeds for the leveling off (Holthuijsen et al., 2012; Makin, 2005; Powell et al., 2003). After having tested a range of thresholds between  $28$  and  $33 \text{ m s}^{-1}$  (not shown), we chose  $U_{th} = 30 \text{ m s}^{-1}$ , whereas Li et al. (2021) chose  $U_{th} = 28 \text{ m s}^{-1}$ . We set the transition range  $\sigma_U = 1 \text{ m s}^{-1}$  in accordance with ECMWF (2020) and Li et al. (2021). The minimum Charnock parameter now takes the functional form shown in Figure 1.

#### 4. The Impact of a Modified Charnock Parameter on the Sea State in High-Wind Situations

A modified wave model WAM Cycle 4.7 with source terms based on the physics described by Ardhuin et al. (2010) (see Section 2) was set up on a 3-km resolution pan-Arctic domain (see Figure 2). In a subregion that covers the North Sea, the Norwegian Sea and the Barents Sea, high-resolution (3 km) surface winds from the NORA3 atmospheric hindcast were used as forcing (Haakenstad et al., 2021). Lower resolution (approx. 31 km) surface winds from ERA5 (Hersbach et al., 2020), the latest ECMWF reanalysis, were used in the outer part of the domain, interpolated to a 3-km grid. A linear interpolation was made over a transition zone of 20 grid points inside the boundaries of the smaller domain. The NORA3 high resolution fields were produced by downscaling ERA5 using the nonhydrostatic convection-permitting atmospheric model, HARMONIE-AROME Cy40h1.2 (see Bengtsson et al., 2017; Seity et al., 2011). NORA3 includes a surface analysis scheme and is reinitialized from ERA5 every 6 hours (see Haakenstad et al., 2021), making the two wind fields dynamically consistent.

The WAM model was set up with 30 frequencies logarithmically spanning the range  $0.0345\text{--}0.5476 \text{ Hz}$  and 24 directional bins. WAM was forced with hourly 10 m neutral winds calculated from the NORA3 hindcast and ERA5 as described above, daily ice concentration fields from the ARC-MFC physical reanalysis system of the Copernicus Marine Service (CMEMS), and wave spectra from ERA5 at the boundaries. The model was run in a shallow-water mode, that is, with the full linear dispersion relation, but without depth refraction and bottom-induced breaking. We set  $\beta_{max} = 1.28$  after having tested a range from 1.25 to 1.42 (not shown).

Two wave model runs covering the period 2011–2012 were carried out. The reference run without modifications to the Charnock parameter is denoted CTRL and ALT is the run with a reduced minimum Charnock parameter

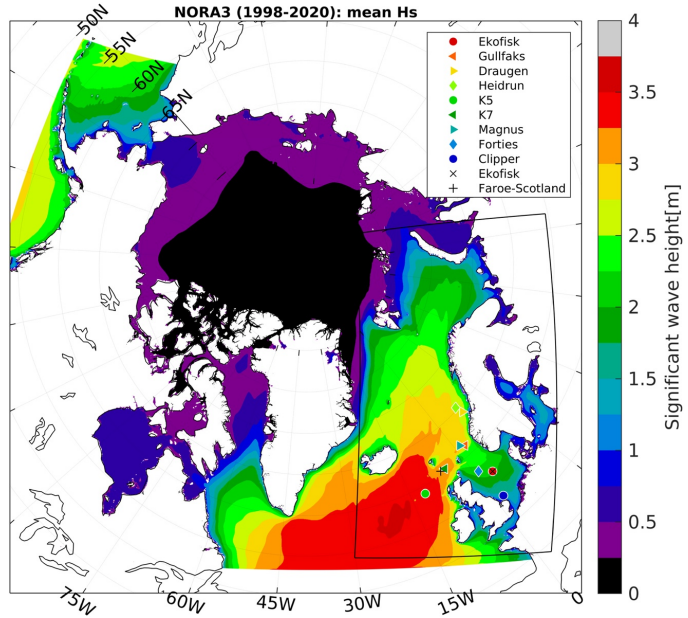


**Figure 2.** Outline of the WAM model domain with the NORA3 subdomain outlined (black box). The average significant wave height over the period 1998–2020 is shown together with the in situ wave measurement locations. The two locations used for the computation of the drag coefficient and roughness length in Figure 3 are indicated with “x” and “+” for Ekofisk and Faroe-Scotland, respectively.

above  $30 \text{ m s}^{-1}$ . We have compared the two wave model runs against buoy and platform measurements in locations indicated in Figure 2. See Table 1 for an overview of the parameter settings used in the CTRL run. In the ALT run, the settings are the same, except for the introduction of the reduced minimum Charnock parameter following Equation 15.

To investigate the impact of the reduction of the Charnock parameter, we have compared the drag coefficient and the sea surface roughness in two locations over the period 2011–2012 (Figure 3). The first location is in the region between the Faroe Islands and Scotland ( $60.51^\circ\text{N}$ ,  $006.02^\circ\text{W}$ , and marked as “+” just west of K7 in Figure 2). This is an area dominated by synoptic low pressures advancing from the North Atlantic. The fetch in the south-westerly direction is very long. The second location is a grid point near Ekofisk in the central North Sea ( $56.48^\circ\text{N}$ ,  $003.19^\circ\text{E}$ , see Figure 2), where the fetch is shorter, except in northerly wind. The impact on the drag coefficient, Equation 5, is complex, as it depends on the wave-induced momentum flux  $\tau_{in}$ , see Equation 6, and the full history

of the wind forcing. Although Equation 15 modifies the Charnock parameter significantly only for winds approaching the threshold (here  $30 \text{ m s}^{-1}$ , see Figure 1), the modeled sea state is also affected at weaker winds. This is because, as the wind is decaying, the sea state, and the roughness length, remain high. Thus, the “memory” of waves having already seen higher winds is visible below the threshold. This is also referred to as “old sea” (Hell et al., 2021). It is thus clear that if stronger winds have been encountered at some point “up-wave”, the effect will also be seen at winds well below the threshold. In fact, the reduction in the drag coefficient (Figure 3, Panel a) in the ALT run starts to taper off already at  $25 \text{ m s}^{-1}$  at the Ekofisk location in the central North Sea (compare the red and the blue curves), whereas in the Faroe-Scotland region the divergence appears at slightly higher wind speeds. This is probably because sea states in the North Sea area are generally

**Table 1**  
Summary of WAM Settings Used in the CTRL Run

Parameter	Value
Minimum Charnock parameter $\hat{\alpha}$	0.0065
Normalized wind input parameter $\beta_{\max}$	1.28
Wave age tuning parameter $\tau_{\alpha}$	0.008
Sheltering coefficient $\tau_{\text{shelter}}$	0.25
Maximum spectral steepness parameter $\alpha_{\max}$	0.031

*Note.* The ALT run has identical settings plus a modification of the minimum Charnock parameter.

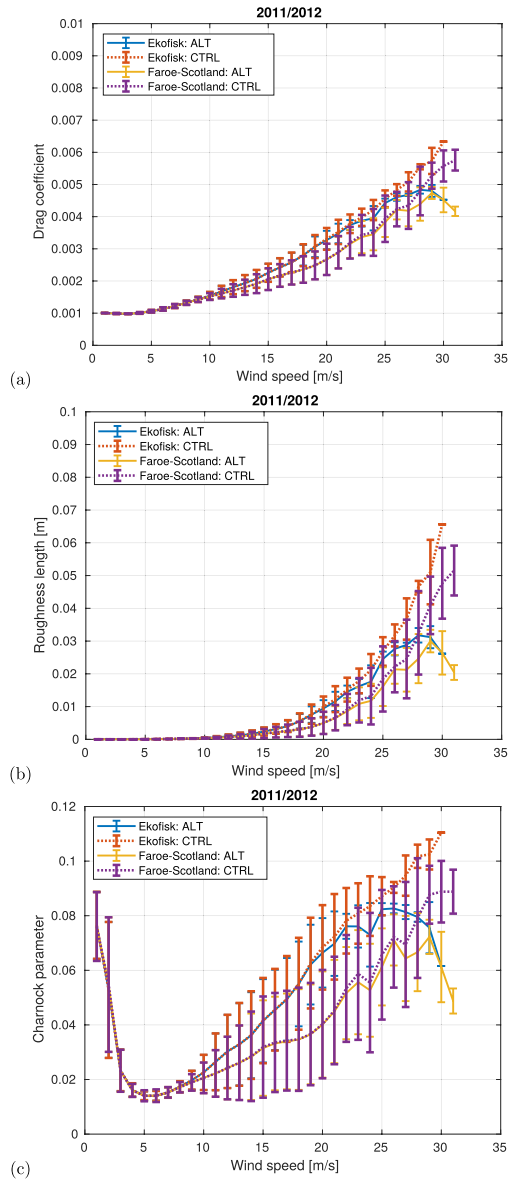


**Figure 3.** Drag coefficient  $C_D$  (panel a), roughness length  $z_0$  [m] (panel b) and Charnock parameter (panel c) binned at  $1 \text{ m s}^{-1}$  resolution and averaged over 2011–2012 for the ALT and CTRL runs. Two locations, the Faroe-Scotland channel and Ekofisk in the central North Sea are shown (locations indicated in Figure 2). Vertical bars represent the standard deviation in each bin.

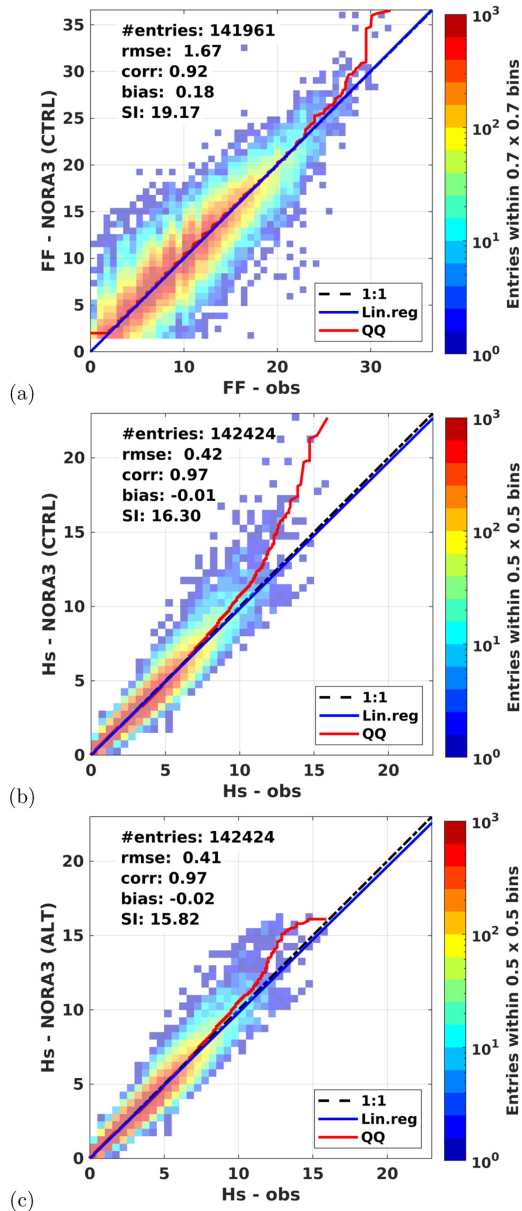


**Figure 4.** Aggregate scatter density histograms and quantiles (red line) of all in situ observations in the nine observation locations in Figure 2 (x-axis) versus NORA3 (y-axis) are shown. Panel (a) Comparison of  $U_{10}$  [ $\text{m s}^{-1}$ ] wind speed (referred to as FF in the meteorological convention). Panel (b) Significant wave height of CTRL run and  $H_s$  [m] against observations in locations shown in Figure 2, 2011–2012. Panel (c) Same as panel b for ALT run. The number of data points (entries), correlation (cor), bias and regression slope (blue line) are provided in the legend. Quantiles are shown in red. There is a marked reduction in the bias for wave heights above 12 m.

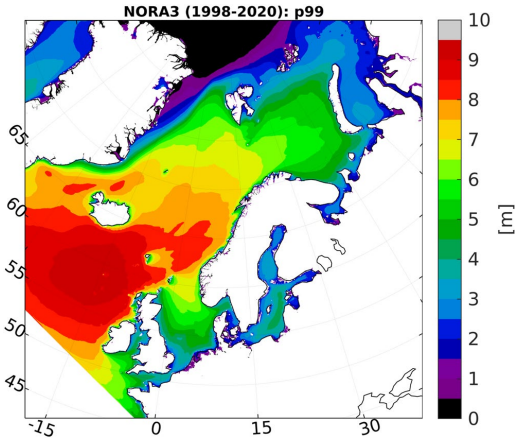


Figure 5. NORA3 WAM 99 percentile statistics (1998–2020) of  $H_s$  [m].

younger than in the North Atlantic (also evident from the fact that the drag coefficient is on average lower in the Faroe-Scotland region for high winds). The surface roughness length,  $z_0$  (panel b), undergoes a similar flattening and subsequent decrease above wind speeds of  $25 \text{ m s}^{-1}$ . The drag (and the Charnock parameter, panel c) of the CTRL run is quite high (but more or less in line with what is found by Li et al., 2021 for their coupled model) and higher than what is found for coupled systems such as the ECMWF CY41R1 (see, e.g., Figure 9 by Pineau-Guillou et al., 2018). The drag in the CTRL run is also higher than what is typically found in measurement campaigns (Donelan et al., 2004; Edson et al., 2013; Holthuijsen et al., 2012).

The wind speed in situ measurements (locations shown in Figure 2) are reduced to 10-m height and compared to the NORA3 hindcast in the upper panel of Figure 4 together with a quantile-quantile comparison. The two wave model runs are presented in the lower panels. It is evident that the wave growth in the CTRL run (with no modification of the Charnock parameter, see panel b) becomes excessive above 10-m significant wave height. In contrast, the ALT run exhibits a much smaller bias above 10-m significant wave height. It is also clear that the wave field, even for nearly unbiased winds (see the wind comparison for locations K7, Forties, Magnus, and Gullfaks in Figure A1, Appendix A), is improved in the ALT run (see Figure A2).

It is particularly interesting to note that there is a small improvement in the

Forties location, even though the wind speed rarely exceeds  $25 \text{ m s}^{-1}$ . This must again be related to the memory effect of a sea state that has seen stronger winds, although here presumably in the upwind (“up-wave”) fetch of the Forties location.

## 5. NORA3: A 23-Year Hindcast Archive

A 23-year wave hindcast covering the period 1998–2020 with settings identical to the ALT run (2011–2012) presented in Section 4 is presented here (see Appendix D for a list of output parameters and locations of 2-D spectra). The inner domain is the North Sea, the Norwegian Sea and the Barents Sea. The resolution, as described above, is 3 km, which coincides with the spatial resolution of the NORA3 atmospheric hindcast (Haakenstad et al., 2021). The outer part of the domain (forced with ERA5 winds) covers the same domain as the Arctic operational wave forecast model of the Copernicus Marine Service (CMEMS). Boundary spectra are taken from ERA5. Our investigation of the model performance is confined to the inner domain.

Figure 5 presents the 99th percentile significant wave height for the entire period (1998–2020). The mean (Figure 2) and upper percentiles in the open ocean are very similar (see Appendix C) but a little weaker than those of the coarser (10 km resolution) NORA10 archive (Reistad et al., 2011). Only in the central North Sea do we see systematic differences in the upper percentiles due to the fact that NORA10 is run in deep-water mode (i.e., no depth-dependent dispersion and refraction). Differences in resolution naturally lead to quite substantial differences in nearshore regions with complex topography where NORA3 is able to resolve more of the coastline and islands and is also able to account for subgrid obstructions (see Appendix B).

Figure 6 compares the wind speed observations from selected offshore locations against NORA3. Pineau-Guillou et al. (2018) found that Jason-2 altimeter measurements of wind speed were biased high compared to buoy measurements in the North Sea and the Norwegian Sea (see their Figure 4), but tended to yield similar winds to the platform measurements in the North Sea. Our comparison of Sentinel-3A/B, Jason-3 and HaiYang-2B altimeter wind measurements against NORA3 (Figure 7b) suggest on the other hand that the strongest satellite winds are biased a little low compared to the in situ (buoys and platforms) measurements (Figure 6).

Haakenstad et al. (2021) showed that the 10-m wind at offshore platforms in the North Sea and the Norwegian Sea were in very close agreement with NORA3, and in fact were biased slightly high compared to NORA3 (see their Figure 9). This was confirmed in the study by Solbrekke et al. (2021), who investigated the performance of NORA3 against the FINO-1 wind mast and a number of offshore platforms in the North Sea and the Norwegian

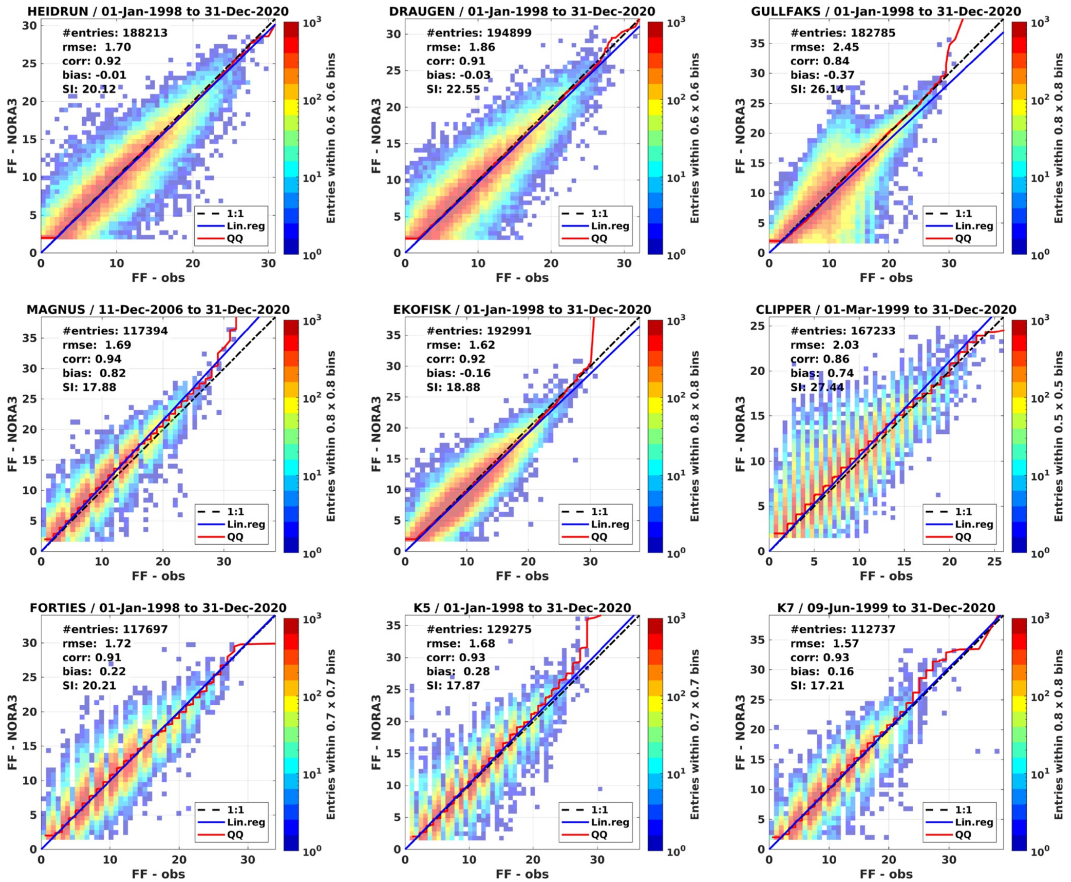


**Figure 6.** Scatter density histograms and quantiles (red line) of in situ  $U_{10}$  [m s<sup>-1</sup>] observations (x-axis) versus NORA3 (y-axis). Station and validation period is presented in the title, while the number of corresponding data (entries), correlation (cor), bias and regression slope (blue line) are provided in the legend. Quantiles are shown in red.

Sea. The differences between NORA3 and in situ measurements appear to be a little larger in the North Atlantic (see K5 and K7), where we see a slight overestimation of the wind speed above 20 m s<sup>-1</sup> for NORA3. We thus cannot rule out that there is a small tendency for a positive upper-percentile bias in the wind speed even if it is not evident in most of the in situ measurements.

The significant wave height corresponds well to in situ and altimeter measurements all the way up to 14 m (see Figures 7a and 8). The exceptions are Draugen, Gullfaks and Heidrun, which are known to have radar instruments that are biased low at high wave heights (see the comparison against the NORA10EI hindcast by Haakenstad et al., 2020). The significant wave period (zero-crossing period),  $T_s$ , shown in Figure 9, shows generally good agreement, with correlations in the range 0.82–0.91, but with a small negative bias. This bias is to be expected, since wave buoys have a cutoff frequency of about 0.5 Hz, whereas ECWAM and WAM Cycle 4.7 add an  $f^{-5}$  spectral tail (ECMWF, 2020). The performance is good throughout the range of wave periods, but certain extreme swell periods are not well captured in the North Atlantic (see location K7).

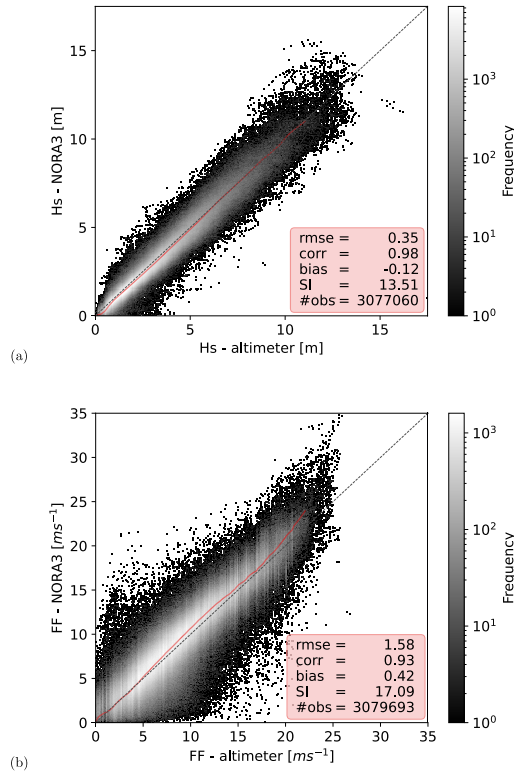


**Figure 7.** Panel (a) Scatter density histograms and quantiles (red line) of altimeter measurements (x axis) of significant wave height  $H_s$  [m] (Sentinel-3A/B, Jason-3, CFOSAT and HaiYang-2B) versus NORA3 WAM (y axis). Panel (b) Altimeter 10-m wind speed (same satellites as panel a, but without CFOSAT) versus NORA3. All measurements are collocated with model values within the NORA3 WAM subdomain during 2020. The collocation method is described in detail by Böhlinger et al. (2019). The applied temporal and spatial constraints for the collocation are 30 min and 6 km, respectively. Note that the frequency color scale is logarithmic with outliers plotted as black dots. Quantiles (up to the 99th percentile) are shown in red.

## 6. Discussion and Concluding Remarks

The wave model WAM Cycle 4.7 has been used to produce a 23-year hindcast forced with wind fields blended from ERA5 and NORA3. The results show good performance in terms of  $H_s$  when the minimum Charnock parameter is reduced above  $30 \text{ m s}^{-1}$ . Its performance is comparable to, or better, than that of the earlier hindcasts, NORA10 and NORA10EI (Haakenstad et al., 2020; Reistad et al., 2011).

Accounting for the smoothing of the sea surface by a reduced Charnock parameter is physically motivated but strongly parameterized. Implementation details will therefore naturally differ depending on the models used and on the degree of coupling between the models. When applied to the uncoupled NORA3 wave hindcast, the approach yielded results in good agreement with available observations, with only a small upper-percentile bias in the wave heights (Figure 7, top panel, Figure 8). For coupled systems, the impact may be even greater, as the near-surface winds respond to a smoother surface by speeding up. This is indeed partly the motivation for the introduction of the modified Charnock parameter in the ECWAM component of ECMWF's IFS (ECMWF, 2020).

There is virtually no added computational cost associated with the reduction of the Charnock parameter. WAM Cycle 4.7 has also been found to perform well compared against the earlier WAM Cycle 4.5, which used the older WAM physics (J. Bidlot et al., 2007). The added cost of introducing the new wave model physics based on



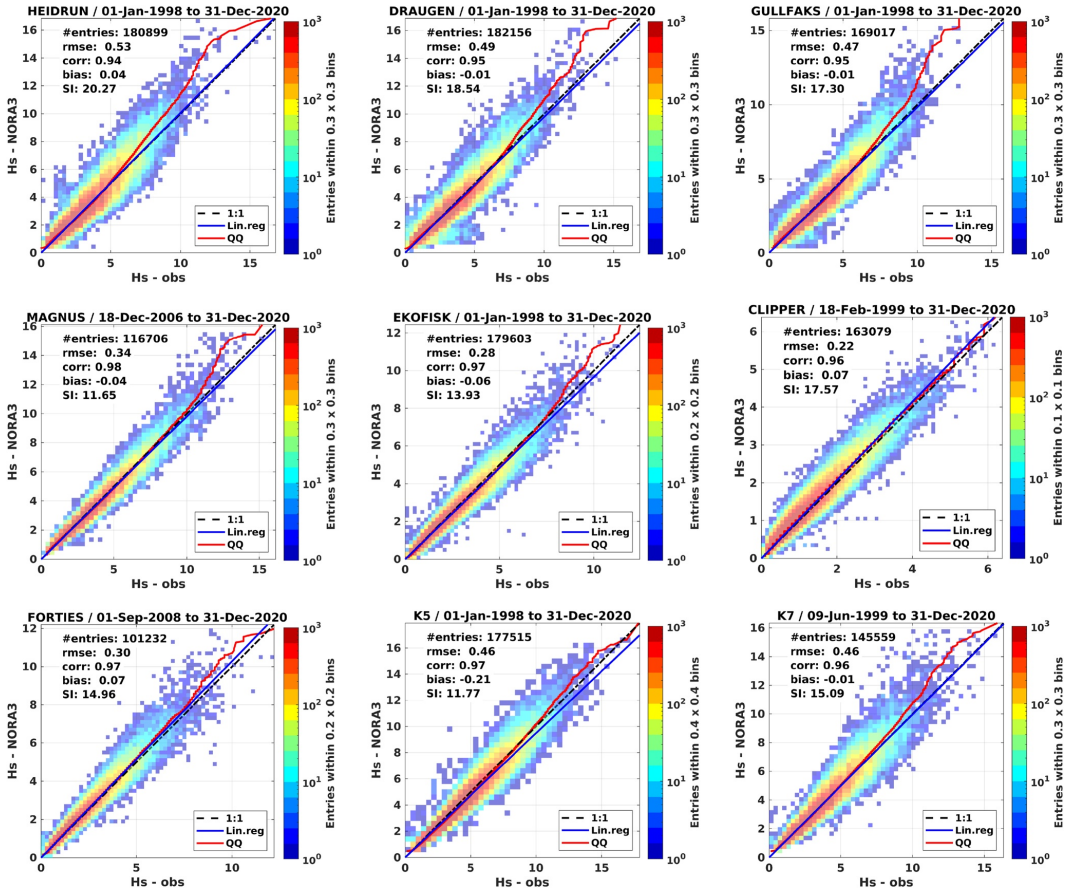


**Figure 8.** Scatter density histograms and quantiles (red line) of in situ  $H_s$  [m] observations (x-axis) versus NORA3 WAM (y-axis). Station and validation period is presented in the title, while the number of corresponding data (entries), correlation (cor), bias and regression slope (blue line) are provided in the legend. Quantiles are shown in red up to the maximum value.

Arduin et al. (2010) is also modest (of the order of 14%, and as source terms are local in physical space, this ratio changes only if the number of frequency and direction bins is changed). Our implementation does not include the cumulative breaking term in the whitecap dissipation presented by Arduin et al. (2010) as it has been found to be very expensive yet having only marginal impact on the sea state (ECMWF, 2020). The implementation, even though we have only tested a standalone wave model here, is efficient enough to be well suited for inclusion in a coupled forecast system, as was shown by Li et al. (2021) for WAM Cycle 4.7 as well as in the ECMWF ECWAM model (ECMWF, 2020), from which WAM Cycle 4.7 has taken its new model physics.

As (nonhydrostatic) atmospheric models move toward higher horizontal resolution, the upper percentiles of the wind distribution become stronger but not necessarily too strong. Traditionally, wave models have been tuned to lower winds and their validity must be reconsidered at very high winds. Controlling the wave growth at hurricane-strength winds thus serves the dual purpose of tuning the wave model to stronger winds in a way consistent with observations, and controlling for possible high-wind biases in the atmospheric model. The results appear satisfactory, with small upper-percentile biases against in situ and satellite altimeter wave height measurements

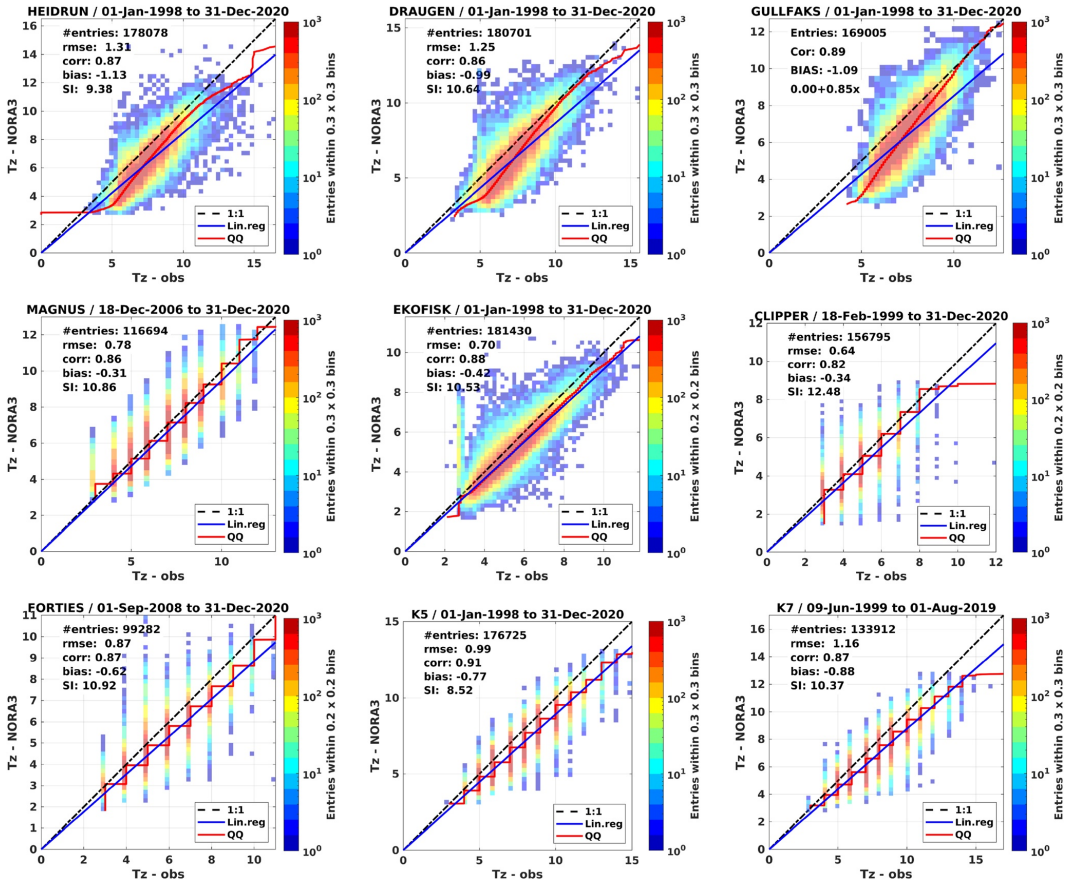


**Figure 9.** Scatter density histograms and quantiles (red line) of in situ observations of the zero-crossing wave period  $T_z$  [s] (x-axis) versus NORA3 WAM (y-axis). Station and validation period is presented in the title, while the number of corresponding data (entries), correlation (cor), bias and regression slope (blue line) are provided in the legend. Quantiles are shown in red up to the maximum value.

(Figures A2 and 7a). It is also possible that even when assuming perfect tuning of the wave model, the weak winds typically present in coarser atmospheric models have failed to reveal the deficiencies in the physics since so few high-wind cases have previously appeared. It is quite reasonable to think that too strong wave growth has compensated for weak winds in coarser atmospheric models. The CTRL experiment (Section 4, see also Figure A2) shows that the impact of the (nearly unbiased) winds in NORA3 is significant as  $H_s$  exceeds 10 m and starts to become really excessive near 15 m. It is also clear that the response of an uncoupled system such as NORA3 will be different from that of coupled atmosphere-wave models (ECMWF, 2020; Li et al., 2021) where the wind field will adjust to the sea surface roughness and where the Charnock parameter is exchanged, yielding identical roughness for the atmosphere and the wave model (van Nieuwkoop et al., 2015).

The current high-resolution hindcast also addresses another challenge for high-resolution basin-scale wave models, namely to realistically represent coastal features and open-ocean conditions at the same time. These two regimes are very different (Cavaleri et al., 2018) with strong gradients in winds (Christakos et al., 2021) adding to the complexity in nearshore regions. In our implementation in WAM, we try to reconcile these competing needs by pragmatically employing a simple formulation for the reduction of the minimum Charnock parameter, Equa-

tion 15, and by introducing subgrid obstructions for complex coastlines (see Appendix B). It is however clear that more work is needed to further explore the nonlinear processes of short gravity-capillary waves on the wave growth in strong winds (Janssen & Bidlot, 2021), and the simple reduction of the minimum Charnock parameter is clearly a simplification of the response of the sea surface to hurricane strength winds.

We have shown that including the saturation of the drag can be used to achieve accurate results with low cost in an uncoupled model. It is however clear that further studies into the air-sea momentum balance will require the use of two-way (atmosphere-wave) or even three-way (atmosphere-wave-ocean) coupled models.

### Appendix A: Comparison of CTRL and ALT Hindcast Performance at Selected Offshore and Open Ocean Buoy Locations (2011–2012)

The 10-m wind speed measurements for all nine locations shown in Figure 2 are compared to the NORA3 wind speed in Figure A1. The NORA3 performance is generally found to be good, which is in accordance with what is found by Haakenstad et al. (2021) and Solbrekke et al. (2021), but the uppermost percentiles of K5 and K7

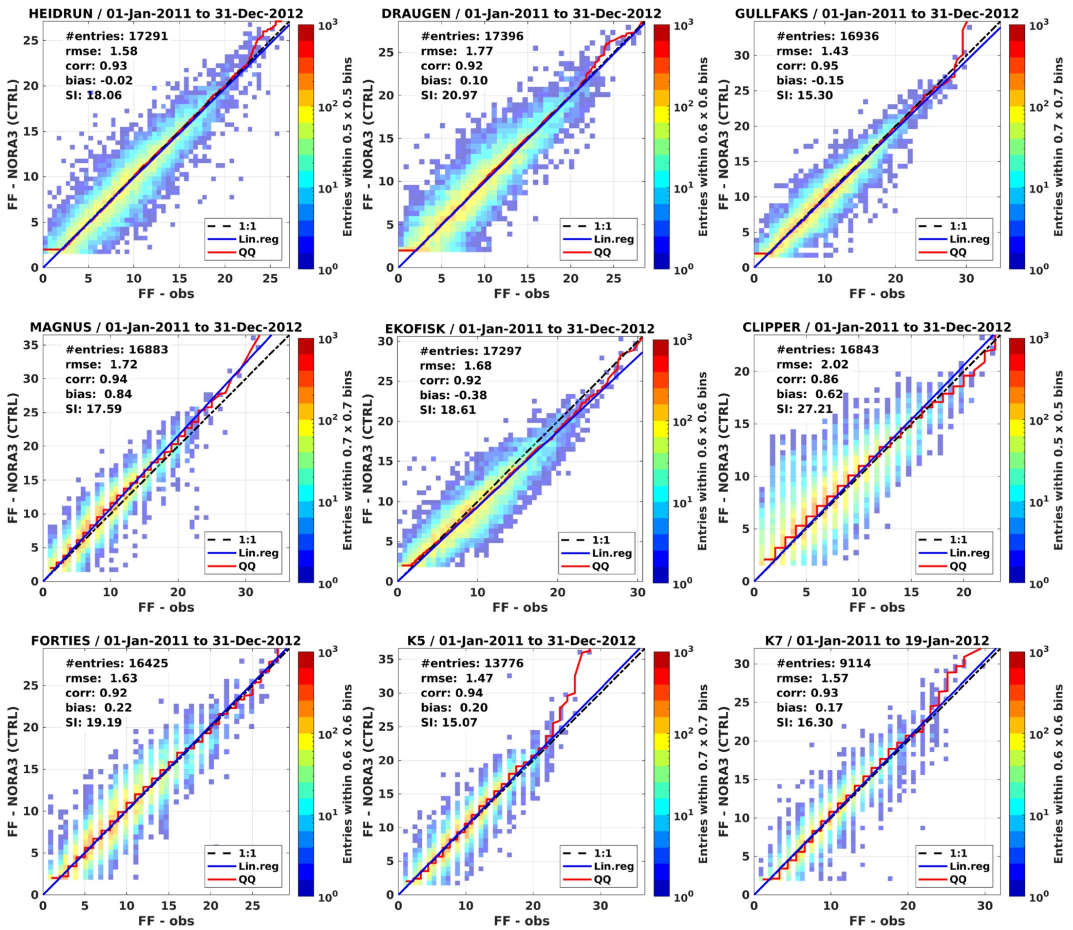


Figure A1. Comparison of  $U_{10}$  [ $m\ s^{-1}$ ], observations (x-axis) versus NORA3 (y-axis), 2011–2012. Quantiles are shown in red up to the maximum value.

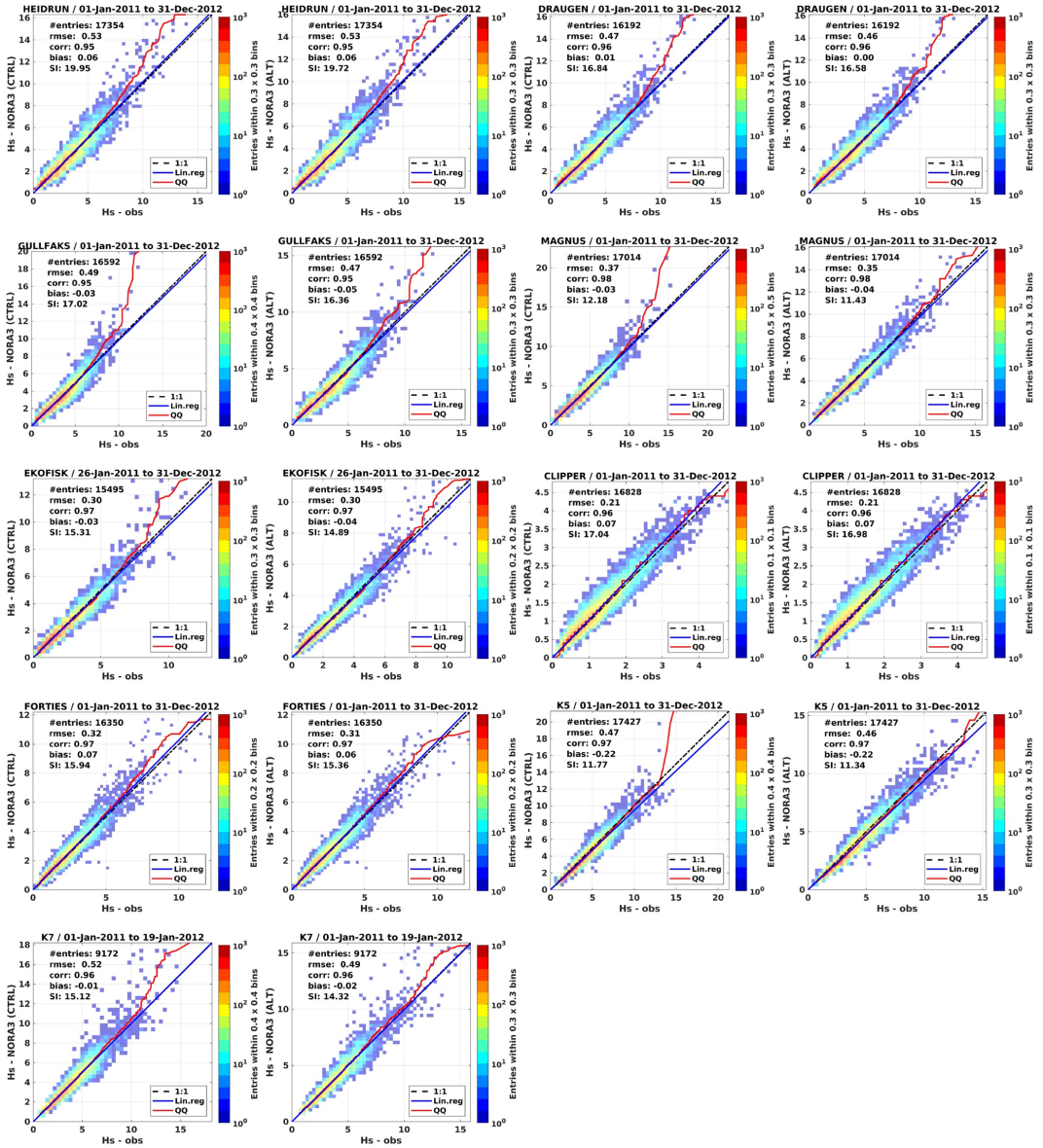
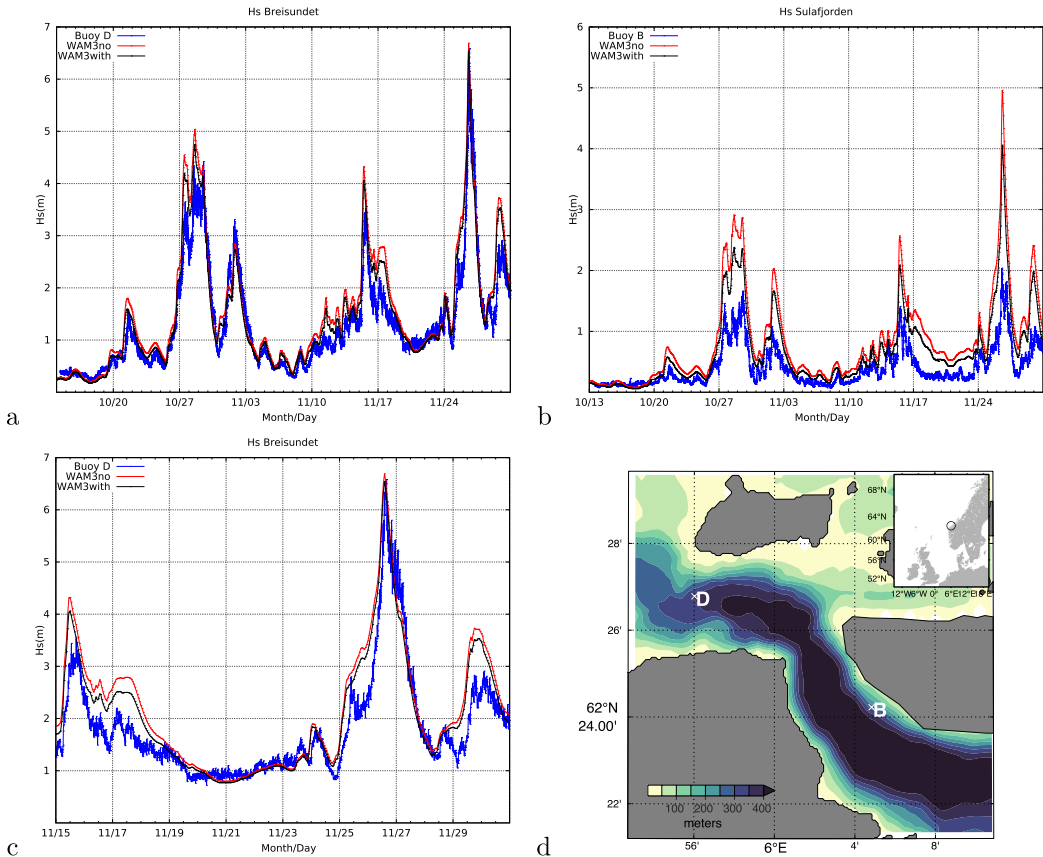


Figure A2. Comparison of  $H_s$  [m], observations (x-axis) versus model (y-axis); CTRL (columns 1 and 3) and ALT (columns 2 and 4), 2011–2012. Quantiles are shown in red up to the maximum value.

in the North Atlantic are biased a little high. The performance of the CTRL and ALT integrations in terms of significant wave height (2011–2012) is shown in Figure A2. Their aggregate performance is shown in Figure 4. It is clear that in most locations the upper percentiles in ALT compare better with observations than the reference run (CTRL) with no reduction in the drag coefficient. The exception is Clipper which, located close to the east coast of England in the shallow southern North Sea, rarely exceeds a wave height of 5 m.

### Appendix B: Subgrid Obstructions

The Norwegian coastline is extremely complex (Adams, 1979, pp 199–200), and many of its islands, fjords and promontories are not captured even at 3-km resolution. Interpolating from a more detailed topographic database can also introduce spurious features in the grid, such as the closing of narrow inlets or the appearance of unrealistically large islands. We therefore implemented a subgrid scheme to increase the usefulness of the hindcast for coastal applications. This scheme (Tuomi et al., 2014) uses information from a high-resolution topography to reduce the energy that propagates through partially land-covered grid points. The depth data for the 3-km grid were calculated as the mean of 25 grid points from a 600 m resolution bathymetric grid calculated from the



**Figure B1.** WAM with and without subgrid obstructions. Panel (a) Comparison against buoy D in Breisundet. Panel (b) Buoy B further into the fjord shows a larger damping with the subgrid obstructions than the outer buoy. Panel (c) Buoy D, close-up of the storm event on 26 November 2016. The NOR3 WAM run with subgrid obstructions is shown in black and the run without obstructions in red, and the observations in blue. Panel (d) Map of the Breisundet-Sulafjord area with buoys B and D marked on top of the bathymetry [m]. An inset shows Sulafjord's location on the Norwegian coast.

EMODNET topographic database (EMODnet Bathymetry Consortium, 2018). The land-sea mask, using a 50% threshold for land, was then constructed by the method Tuomi et al. (2014) developed for the Finnish Archipelago Sea. The method is designed to better account for small islands that are spread out over several coarser grid points and therefore may not be detected by simply applying a threshold to each grid point individually. We chose a relatively high threshold because a lower one (e.g., 30%) can close some of the narrow passages in the fjords. Depths less than 10 m were set as land in the final coarse grid. The method also determined compatible obstruction grids for the coarse sea-points. Finally, adding the subgrid obstructions to the model run is a standard part in WAM Cycle 4.7, where they are accounted for in the transport equation following Tolman (2003).

Nearshore observations are scarce along the coast of Norway with the notable exception of the wave measurement program operated by the Norwegian Public Roads Administration for the E39 fjord crossing project along the western coast of Norway. The results from two buoys in the Breisundet and Sulafjord area near Ålesund are shown in Figure B1 for a period covering October and November 2016. See Christakos et al. (2020, 2021) for a detailed account of the observation campaign. Although the differences are mostly modest, it is clear that there is a reduction in the wave height of 10–20 cm in the ALT (hindcast) run with obstructions (black curve, see Panels a, b, and c), compared with the run without obstructions but with all other settings equal to the ALT run (red curve) on the Breisundet buoy (marked “D” in Panel d). This has a beneficial impact on the model bias. Panel b shows that buoy “B” located further into the fjord exhibits greater damping in the run with obstructions (up to 1 m difference), but the outer buoy (Panels a and c) also experiences some damping due to subgrid obstructions at the mouth of the fjord system.

### Appendix C: Comparison Against NORA10 $H_s$

The earlier NORA10 hindcast archive (Aarnes et al., 2012; Reistad et al., 2011) covers approximately the same geographical area as the inner domain of NORA3. Due to its extensive use in extreme value analysis (Aarnes et al., 2012; Breivik et al., 2013; Vanem, 2014) and more generally for mapping the wave climatology of the region (Bruserud & Haver, 2016; Semedo et al., 2015), it is of interest to compare the two hindcast archives for the same period (1998–2020). NORA3 has a slightly weaker annual mean  $H_s$  (see Figure C1, panel a), but the differences in the open ocean are of the order of 20 cm. The 99th percentile shows larger differences, as must be expected, but again the differences are small, with most open-ocean regions exhibiting differences of the order of  $\pm 0.25$  m. In the North Sea NORA3 is about 0.6 m lower than NORA10 at the 99th percentile but with very small differences for the annual mean (Panel a). This is partly due to the lack of shallow-water physics in NORA10, which causes the model to overestimate the highest waves in shallow areas. The effect is particularly evident in the shallowest areas in the German Bight. Another effect is the coarser resolution of NORA10, which leads to differences in the shadow between islands. This is particularly evident off the tip of Cornwall and along the west coast of Scotland. Differences in ice extent is the cause of the large differences north of Svalbard and east of Novaya Zemlya.

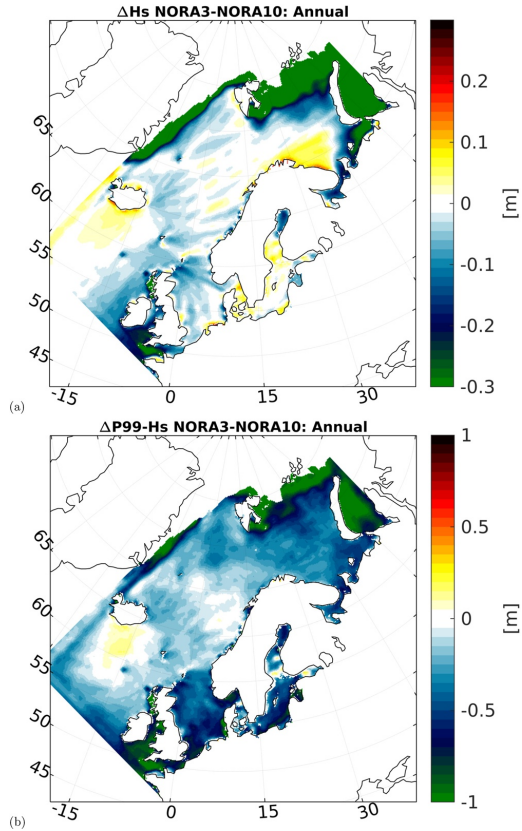


**Figure C1.** Difference between NORA3 and NORA10  $H_s$  for the period 1998–2020. Panel (a) Difference in annual average  $H_s$  (NORA3-NORA10). Panel (b) Difference in 99th percentile  $H_s$ . Note the difference in the color scale.

#### Appendix D: List of Output Parameters in the NORA3 WAM Wave Hindcast

Table D1 shows a truncated output of the contents of the NetCDF files with integrated output parameters from the NORA3 WAM hindcast. All parameters are stored with hourly resolution. In addition, the 2-D spectra from selected grid points at about  $0.25^\circ$  resolution are archived every hour, with higher spatial resolution along the coast of Norway (see Figure D1).

**Table D1**

List of Integrated Output Parameters From NORA3 WAM

```

dimensions:
    time = UNLIMITED // (24 currently)
    rlat = 1995
    rlon = 2379
variables:
    rlat: "rotated latitude"; rlat:units = "degrees"
    rlon: "rotated longitude"; rlon:units = "degrees"
    ff: "Wind speed"; ff:units = "m/s"
    dd: "Wind direction"; dd:units = "degrees"
    FV: "friction velocity"; FV:units = "m/s"
    DC: "drag coefficient"; DC:units = "1"
    hs: "Total significant wave height"; hs:units = "m"
    tp: "Total peak period"; tp:units = "s"
    tmp: "Total mean period"; tmp:units = "s"
    tm1: "Total m1-period"; tm1:units = "s"
    tm2: "Total m2-period"; tm2:units = "s"
    thq: "Total mean wave direction"; thq:units = "degrees"
    hs_sea: "Sea significant wave height"; hs_sea:units = "m"
    tp_sea: "Sea peak period"; tp_sea:units = "s"
    tmp_sea: "Sea mean period"; tmp_sea:units = "s"
    tm1_sea: "Sea m1-period"; tm1_sea:units = "s"
    thq_sea: "Sea mean wave direction"; thq_sea:units = "degrees"
    SIC: "sea ice concentration"; SIC:units = "1"
    hs_swell: "Swell significant wave height"; hs_swell:units = "m"
    tp_swell: "Swell peak period"; tp_swell:units = "s"
    thq_swell: "Swell mean wave direction"; thq_swell:units = "degrees"
    mHs: "expected maximum wave height"; mHs:units = "m"
    mwp: "expected wave period"; mwp:units = "s"
    fpI: "interpolated peak frequency"; fpI:units = "s"
    Pdir: "peak direction"; Pdir:units = "degrees"
    fshs: "first swell significant wave height"; fshs:units = "m"
    fstm1: "first swell mean period"; fstm1:units = "s"
    fsdir: "first swell direction"; fsdir:units = "degrees"
    sshs: "second swell significant wave height"; sshs:units = "m"
    sstm1: "second swell mean period"; sstm1:units = "s"
    ssdir: "second swell direction"; ssdir:units = "degrees"
    tshs: "third swell significant wave height"; tshs:units = "m"
    tstm1: "third swell mean period"; tstm1:units = "m/s"
    tsdir: "third swell direction"; tsdir:units = "degrees"
    SIT: "sea_ice_thickness"; SIT:units = "m"
    utrs: "x-comp Stokes drift transport"; utrs:units = "m^2/s"
    sdx: "x-comp. Stokes drift"; sdx:units = "m/s"
    sdy: "y-comp. Stokes drift"; sdy:units = "m/s"
    phioc: "normalized energy flux to ocean"; phioc:units = "W/m^2"
    phiaw: "normalized energy flux from wind to waves"; phiaw:units = "W/m^2"
    tauocx: "x-comp. normalized momentum flux into ocean"; tauocx:units = "Pa"
    tauocy: "y-comp. normalized momentum flux into ocean"; tauocy:units = "Pa"
    phibot: "energy flux from waves to bottom"; phibot:units = "W/m^2"
    taubot_x: "x-comp. momentum flux from waves into bottom"; taubot_x:units = "Pa"
    taubot_y: "y-comp. momentum flux from waves into bottom"; taubot_y:units = "Pa"
    vtrs: "y-comp Stokes drift transport"; vtrs:units = "m^2/s"
    projection_ob_tran:grid_north_pole_longitude = 140.0
    projection_ob_tran:grid_north_pole_latitude = 25.0
    projection_ob_tran:earth_radius = 6371000.0
    projection_ob_tran:proj4 = "+proj=ob_tran +o_proj=longlat +lon_0=-40 +o_lat_p=25 +R=6.371e+06 +no_defs"
    latitude:units = "degrees_north"
    longitude:units = "degrees_east"
    model_depth: "water depth"; model_depth:units = "m"

```



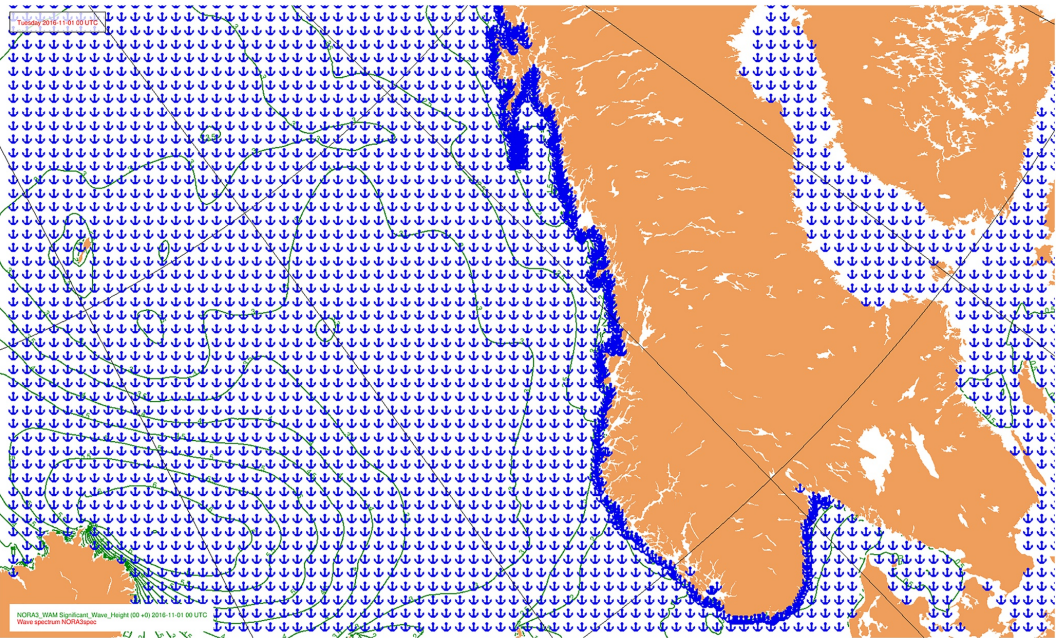


**Figure D1.** Excerpt of the NORA3 WAM model domain showing the typical resolution of the spectral grid. 2-D spectra (marked as blue anchors) are archived hourly with a resolution of about  $0.25^\circ$  except along the coast of Norway where the resolution is higher.

#### Acknowledgments

Thanks go to the editor and the two anonymous reviewers whose constructive comments helped us improve the article. JRB, JS and ØB are grateful for support from Mercator Ocean and CMEMS through the WaveFlow Service Evolution 2 project, which helped facilitate the implementation of the new physics (Ardhuin et al., 2010) implemented in ECWAM into the open-source WAM Cycle 4.7 and later in WAM Cycle 6. AC, PB and ØB are grateful for support from Mercator Ocean and CMEMS through the ARC-MFC contract. This paper also serves as a documentation of the ARC-MFC hindcast archive product, ARCTIC\_MULTITYEAR\_WAV\_002\_013. HH and ØB gratefully acknowledge the support from ERA4CS through the WINDSURFER project. We are also grateful to Equinor ASA for their continued financial support of the NORA3 hindcast archive as well as the previous NORA10 and NORA10EI archives. We also gratefully acknowledge the Norwegian Public Roads Administration for the long-standing collaboration and their financial support of our research on the Coastal Highway E39 project. We also acknowledge support from the Research Council of Norway through the Stormrisk project (Grant No. 300608).

#### Data Availability Statement

The NORA3 wave hindcast is archived and openly available on the THREDDS server of the Norwegian Meteorological Institute: <https://thredds.met.no/thredds/projects/windsurfer.html>. The atmospheric hindcast (Haakenstad et al., 2021) is also openly available and archived here: <https://thredds.met.no/thredds/catalog/nora3/catalog.html>. The latest version (Cycle 6) of the open-source WAM model (including the subgrid option, but without the reduced high-wind drag option) can be found here: <https://github.com/mywave/WAM>.

#### References

- Aarnes, O. J., Breivik, Ø., & Reistad, M. (2012). Wave extremes in the northeast Atlantic. *Journal of Climate*, 25, 1529–1543. <https://doi.org/10.1175/jcli-d-11-00132.1>
- Adams, D. (1979). *The Hitchhiker's guide to the galaxy: Volume one in the trilogy of five*. Pan.
- Ardhuin, F., Rogers, E., Babanin, A. V., Filipot, J.-F., Magne, R., Roland, A., et al. (2010). Semiempirical dissipation source functions for ocean waves. Part I: Definition, calibration, and validation. *Journal of Physical Oceanography*, 40(9), 1917–1941. <https://doi.org/10.1175/2010JPO4324.1>
- Banner, M. L., & Morison, R. P. (2010). Refined source terms in wind wave models with explicit wave breaking prediction. Part I: Model framework and validation against field data. *Ocean Modelling*, 33, 177–189. <https://doi.org/10.1016/j.ocemod.2010.01.002>
- Behrens, A., Staneva, J., Saetra, Ø., & Janssen, P. (2013). *Documentation of a web based source code library for WAM (Tech. Rep.)*. Helmholtz-Zentrum Geestacht. Retrieved from [http://met-xpprod.customer.enonic.io/sokeresultat/\\_attachment/inlinel/c1fdc351-1109-47fc-9d9e-65c9f31eac6b:b52dfc2b5953103564a339bb290b83c66b1315f6/MyWave\\_Report\\_D1.1.pdf](http://met-xpprod.customer.enonic.io/sokeresultat/_attachment/inlinel/c1fdc351-1109-47fc-9d9e-65c9f31eac6b:b52dfc2b5953103564a339bb290b83c66b1315f6/MyWave_Report_D1.1.pdf)
- Bengtsson, L., Andrae, U., Aspelien, T., Batrak, Y., Calvo, J., de Rooy, W., et al. (2017). The HARMONIE-AROME model configuration in the ALADIN-HIRLAM NWP system. *Monthly Weather Review*, 145(5), 1919–1935. <https://doi.org/10.1175/MWR-D-16-0417.1>
- Bi, X., Gao, Z., Liu, Y., Liu, F., Song, Q., Huang, J., et al. (2015). Observed drag coefficients in high winds in the near offshore of the South China Sea. *Journal of Geophysical Research: Atmospheres*, 120(13), 6444–6459. <https://doi.org/10.1002/2015JD023172>
- Bidlot, J., Janssen, P., & Abdalla, S. (2007). *A revised formulation of ocean wave dissipation and its model impact (ECMWF Technical Memorandum No. 509)*. European Centre for Medium-Range Weather Forecasts.
- Bidlot, J.-R., Prates, F., Ribas, R., Mueller-Quintino, A., Crepulja, M., & Vitart, F. (2020). *Enhancing tropical cyclone wind forecasts* (Vol. 164). ECMWF newsletter/European Centre for Medium-Range Weather Forecasts.
- Bohlinger, P., Breivik, Ø., Economou, T., & Müller, M. (2019). A novel approach to computing super observations for probabilistic wave model validation. *Ocean Modelling*. <https://doi.org/10.1016/j.ocemod.2019.101404>

- Booi, N., Ris, R. C., & Holthuijsen, L. H. (1999). A third-generation wave model for coastal regions 1. Model description and validation. *Journal of Geophysical Research*, 104(C4), 7649–7666. <https://doi.org/10.1029/98JC02622>
- Breivik, Ø., Aarnes, O. J., Bidlot, J.-R., Carrasco, A., & Saetra, Ø. (2013). Wave extremes in the northeast Atlantic from ensemble forecasts. *Journal of Climate*, 26, 7525–7540. arXiv:1304.1354. <https://doi.org/10.1175/jcli-d-12-00738.1>
- Bruserud, K., & Haver, S. (2016). Comparison of wave and current measurements to NORA10 and NoNoCur hindcast data in the northern North Sea. *Ocean Dynamics*, 66(6), 823–838. (14th wave special issue). <https://doi.org/10.1007/s10236-016-0953-z>
- Cavaleri, L., Abdalla, S., Benetazzo, A., Bertotti, L., Bidlot, J.-R., Breivik, Ø., et al. (2018). Wave modelling in coastal and inner seas. *Progress in Oceanography*, 167, 164–233. <https://doi.org/10.1016/j.pocean.2018.03.010>
- Charnock, H. (1955). Wind stress on a water surface. *Quarterly Journal of the Royal Meteorological Society*, 81(350), 639–640. <https://doi.org/10.1002/qj.49708135027>
- Chen, G., & Belcher, S. E. (2000). Effects of long waves on wind-generated waves. *Journal of Physical Oceanography*, 30(9), 2246–2256. [https://doi.org/10.1175/1520-0485\(2000\)030<2246:eolwov>2.0.co;2](https://doi.org/10.1175/1520-0485(2000)030<2246:eolwov>2.0.co;2)
- Chen, S. S., Zhao, W., Donelan, M. A., & Tolman, H. L. (2013). Directional wind-wave coupling in fully coupled atmosphere-wave-ocean models: Results from CBLAST-hurricane. *Journal of the Atmospheric Sciences*, 70(10), 3198–3215. <https://doi.org/10.1175/JAS-D-12-0157.1>
- Christakos, K., Björkqvist, J.-V., Tuomi, L., Furevik, B. R., & Breivik, Ø. (2021). Modelling wave growth in narrow fetch geometries: The white-capping and wind input formulations. *Ocean Modelling*, 157, 101730. <https://doi.org/10.1016/j.ocemod.2020.101730>
- Christakos, K., Furevik, B. R., Aarnes, O. J., Breivik, Ø., Tuomi, L., & Byrkjedal, Ø. (2020). The importance of wind forcing in fjord wave modelling. *Ocean Dynamics*, 70(1), 57–75. <https://doi.org/10.1007/s10236-019-01323-w>
- Curcic, M., & Haus, B. K. (2020). Revised estimates of ocean surface drag in strong winds. *Geophysical Research Letters*, 47(10), e2020GL087647. <https://doi.org/10.1029/2020GL087647>
- Donelan, M. A. (2018). On the decrease of the oceanic drag coefficient in high winds. *Journal of Geophysical Research: Oceans*, 123(2), 1485–1501. <https://doi.org/10.1002/2017JC013394>
- Donelan, M. A., Haus, B. K., Reul, N., Plant, W. J., Stiassnie, M., Graber, H. C., et al. (2004). On the limiting aerodynamic roughness of the ocean in very strong winds. *Geophysical Research Letters*, 31, L18306. <https://doi.org/10.1029/2004GL019460>
- Du, J., Bolaños, R., & Guo Larsén, X. (2017). The use of a wave boundary layer model in SWAN. *Journal of Geophysical Research: Oceans*, 122(1), 42–62. <https://doi.org/10.1002/2016JC012104>
- ECMWF. (2020). *IFS documentation CY43r1, Part VII: ECMWF wave model (ECMWF model documentation)*. European Centre for Medium-Range Weather Forecasts.
- Edson, J., Jampana, V., Weller, R., Bignor, S., Plueddemann, A., Fairall, C., et al. (2013). On the exchange of momentum over the open ocean. *Journal of Physical Oceanography*, 43, 1589–1610. <https://doi.org/10.1175/JPO-D-12-0173.1>
- EMODnet Bathymetry Consortium. (2018). *EMODnet digital bathymetry (DTM) 2018*. <https://doi.org/10.12770/18ff0d48-b203-4a65-94a9-5fd8b0ec35f6>
- Günther, H., Hasselmann, S., & Janssen, P. A. E. M. (1992). *Wamodell Cycle 4 (revised version) (tech. Rep. No. 4)*. Deutsches KlimaRechenZentrum.
- Haakenstad, H., Breivik, Ø., Furevik, B., Reistad, M., Bohlinger, P., & Aarnes, O. J. (2021). NORA3: A nonhydrostatic high-resolution hindcast of the North Sea, the Norwegian Sea, and the Barents Sea. *Journal of Applied Meteorology and Climatology*. Accepted for publication in <https://doi.org/10.1175/JAMC-D-21-0029.1>
- Haakenstad, H., Breivik, Ø., Reistad, M., & Aarnes, O. J. (2020). NORA10EI: A revised regional atmosphere-wave hindcast for the North Sea, the Norwegian Sea and the Barents Sea. *International Journal of Climatology*, 40(10), 4347–4373. <https://doi.org/10.1002/joc.6458>
- Hasselmann, S., Hasselmann, K., Bauer, E., Janssen, P. A. E. M., Komen, G. J., Bertotti, L., et al. (1988). The WAM model—A third generation ocean wave prediction model. *Journal of Physical Oceanography*, 18, 1775–1810. <https://doi.org/10.1016/bbs3r>
- Hell, M. C., Ayet, A., & Chapron, B. (2021). Swell generation under extra-tropical storms. *Journal of Geophysical Research: Oceans*, 126(9), e2021JC017637. <https://doi.org/10.1029/2021JC017637>
- Hersbach, H., Bell, B., Berrisford, P., Hirahara, S., Horányi, A., Muñoz-Sabater, J., et al. (2020). The ERA5 global reanalysis. *Quarterly Journal of the Royal Meteorological Society*, 146. <https://doi.org/10.1002/qj.3803>
- Holthuijsen, L. H., Powell, M. D., & Pietrzak, J. D. (2012). Wind and waves in extreme hurricanes. *Journal of Geophysical Research*, 117(C9). <https://doi.org/10.1029/2012JC007983>
- Janssen, P. (1989). Wave-induced stress and the drag of air flow over sea waves. *Journal of Physical Oceanography*, 19(6), 745–754. [https://doi.org/10.1175/1520-0485\(1989\)019<0745:wisatd>2.0.co;2](https://doi.org/10.1175/1520-0485(1989)019<0745:wisatd>2.0.co;2)
- Janssen, P. (1991). Quasi-linear theory of wind-wave generation applied to wave forecasting. *Journal of Physical Oceanography*, 21(11), 1631–1642. [https://doi.org/10.1175/1520-0485\(1991\)021<1631:qctoww>2.0.co;2](https://doi.org/10.1175/1520-0485(1991)021<1631:qctoww>2.0.co;2)
- Janssen, P. (2004). *The interaction of ocean waves and wind*. Cambridge University Press.
- Janssen, P., & Bidlot, J. (2021). *On the consequences of nonlinearity and gravity-capillary waves on wind-wave interaction (ECMWF Technical Memorandum No. 882)*. European Centre for Medium-Range Weather Forecasts.
- Jensen, R., Cardone, V., & Cox, A. (2006). Performance of third generation wave models in extreme hurricanes. In *Proceedings of the 9th international workshop on wave hindcasting and forecasting and coastal hazard symposium* (p. 23).
- Komen, G. J., Cavaleri, L., Donelan, M., Hasselmann, K., Hasselmann, S., & Janssen, P. A. E. M. (1994). *Dynamics and modelling of ocean waves*. Cambridge University Press.
- Li, D., Staneva, J., Bidlot, J. R., Grayek, S., Zhu, Y., & Yin, B. (2021). Improving regional model skills during typhoon events: A case study for super typhoon lingling over the northwest Pacific ocean. *Frontiers in Marine Science*, 8, 42. <https://doi.org/10.3389/fmars.2021.613913>
- Magnusson, L., Bidlot, J.-R., Bonavita, M., Brown, A. R., Browne, P. A., Chiara, G. D., et al. (2019). ECMWF activities for improved hurricane forecasts. *Bulletin of the American Meteorological Society*, 100(3), 445–458. <https://doi.org/10.1175/BAMS-D-18-0044.1>
- Makin, V. K. (2005). A note on the drag of the sea surface at hurricane winds. *Boundary-Layer Meteorology*, 115, 169–176. <https://doi.org/10.1007/s10546-004-3647-x>
- Phillips, O. M. (1958). The equilibrium range in the spectrum of wind-generated waves. *Journal of Fluid Mechanics*, 4, 426–434. <https://doi.org/10.1017/S0022112058000550>
- Pineau-Guillou, L., Ardhuin, F., Bouin, M.-N., Redelsperger, J.-L., Chapron, B., Bidlot, J.-R., & Quilfen, Y. (2018). Strong winds in a coupled wave-atmosphere model during a North Atlantic storm event: Evaluation against observations. *Quarterly Journal of the Royal Meteorological Society*, 144(711), 317–332. <https://doi.org/10.1002/qj.3205>
- Pineau-Guillou, L., Bouin, M.-N., Ardhuin, F., Lyard, F., Bidlot, J.-R., & Chapron, B. (2020). Impact of wave-dependent stress on storm surge simulations in the North Sea: Ocean model evaluation against in situ and satellite observations. *Ocean Modelling*, 154, 101694. <https://doi.org/10.1016/j.ocemod.2020.101694>

- Powell, M., Vickery, P., & Reinhold, T. (2003). Reduced drag coefficient for high wind speeds in tropical cyclones. *Nature*, *422*, 279–283. <https://doi.org/10.1038/nature01481>
- Reistad, M., Breivik, Ø., Haakenstad, H., Aarnes, O. J., Furevik, B. R., & Bidlot, J.-R. (2011). A high-resolution hindcast of wind and waves for the North Sea, the Norwegian Sea, and the Barents Sea. *Journal of Geophysical Research*, *116*, 18C05019. arXiv:1111.0770. <https://doi.org/10.1029/2010jc006402>
- Seity, Y., Brousseau, P., Malardel, S., Hello, G., Bénard, P., Bouttier, F., et al. (2011). The AROME-France convective-scale operational model. *Monthly Weather Review*, *139*(3), 976–991. <https://doi.org/10.1175/2010MWR3425.1>
- Semedo, A., Vettor, R., Breivik, Ø., Sterl, A., Reistad, M., Soares, C. G., & Lima, D. C. A. (2015). The wind sea and swell waves climate in the nordic seas. *Ocean Dynamics*, *65*(2), 223–240. (13th wave special issue). <https://doi.org/10.1007/s10236-014-0788-4>
- Solbrekke, I. M., Sorteberg, A., & Haakenstad, H. (2021). The 3 km Norwegian reanalysis (NORA3) – A validation of offshore wind resources in the North Sea and the Norwegian Sea. *Wind Energy Science*, *6*(6), 1501–1519. <https://doi.org/10.5194/wes-6-1501-2021>
- Stull, R. B. (1988). *An introduction to boundary layer meteorology*. Kluwer.
- Tolman, H. L. (1991). A third-generation model for wind waves on slowly varying, unsteady, and inhomogeneous depths and currents. *Journal of Physical Oceanography*, *21*(6), 782–797. [https://doi.org/10.1175/1520-0485\(1991\)021<0782:atgmfw>2.0.co;2](https://doi.org/10.1175/1520-0485(1991)021<0782:atgmfw>2.0.co;2)
- Tolman, H. L. (2003). Treatment of unresolved islands and ice in wind wave models. *Ocean Modelling*, *5*(3), 219–231. [https://doi.org/10.1016/S1463-5003\(02\)00040-9](https://doi.org/10.1016/S1463-5003(02)00040-9)
- Wavewatch III Development Group. (2019). *User manual and system documentation of WAVEWATCH III version 6.07* (Tech. Rep. No. 333). MMAB/NCEP/NOAA.
- Tuomi, L., Pettersson, H., Fortelius, C., Tikka, K., Björkqvist, J.-V., & Kahma, K. K. (2014). Wave modelling in archipelagos. *Coastal Engineering*, *83*, 205–220. <https://doi.org/10.1016/j.coastaleng.2013.10.011>
- Vanem, E. (2014). Spatiotemporal analysis of NORA10 data of significant wave height. *Ocean Dynamics*, *64*(6), 879–893. (13th wave special issue). <https://doi.org/10.1007/s10236-014-0729-2>
- van Nieuwkoop, J., Baas, P., Caires, S., & Groeneweg, J. (2015). On the consistency of the drag between air and water in meteorological, hydrodynamic and wave models. *Ocean Dynamics*, *65*(7), 989–1000. <https://doi.org/10.1007/s10236-015-0849-3>
- Zweers, N. C., Makin, V. K., de Vries, J. W., & Burgers, G. (2010). A sea drag relation for hurricane wind speeds. *Geophysical Research Letters*, *37*(21). <https://doi.org/10.1029/2010GL045002>



# Appendix A

## Appendix

### A.1 Technical details of the supercomputer Nebula

Compute nodes	136 (124 thin, 12 fat)
Total number of cores	4,352
Estimated max. power	ca 55 kW
Fast network	Intel OmniPath 100 Gbit/s with 48-port leaf and spine switches
Global storage	IBM Spectrum Scale GPFS-based storage appliance
Server model	Intel HNS2600BPB with Intel H2204XXLRE 2U/4-node chassis
CPUs	2x Intel Xeon Gold model 6130 at 2.1 GHz (16 cores each)
L2/L3 cache	1 MiB/core L2 cache, 44 MiB per socket L3 cache
Memory (thin)	96 GiB DDR4 2666 Mhz dual rank memory
Memory (fat)	384 GiB DDR4 2666 Mhz dual rank memory
Disk (thin)	240 GiB SSD (Intel DC S4500)
Disk (fat)	960 GiB SSD (Intel DC S4500)

Table A.1: System details of the supercomputer *nebula.nsc.liu.se*. (<https://www.nsc.liu.se/systems/nebula/>)

Details about the supercomputer Nebula are given in A.1. The supercomputer, elvis, is retired and information about the computer is not posted here.

## A.2 Calculation of vertical velocity in the hydrostatic model HIRLAM

The vertical velocity ( $\dot{s}$ ) is in HIRLAM calculated diagnostically with the method by *McDonald and Haugen* (1993), *Gustafsson and McDonald* (1996), and *Uden et al.* (2002)

$$(\dot{s})_{k+1/2}^{n+1/2} = -B_{k+1/2} \left( \frac{\partial \ln p_s}{\partial t} \right)^{n+1/2} - \frac{1}{p_s} \left[ \sum_{j=1}^k \nabla_H \cdot [(\mathbf{v}_H)_j \Delta p_j] \right]^{n+1/2} \quad (\text{A.1})$$

where

$$\left( \frac{\partial \ln p_s}{\partial t} \right)^{n+1/2} = -\frac{1}{p_s} \sum_{j=1}^N \nabla_H \cdot [(\mathbf{v}_H)_j \Delta p_j] \quad (\text{A.2})$$

where  $p_s$  is surface pressure,  $B$  is from Eq. (2.1). The total number of levels in the vertical is  $N$ , and  $k = 1, 2, \dots, N$ . The vertical velocity is defined on half levels ( $k + 1/2$ ), and the vertical velocity is needed at times  $n + 1/2$ . (The terms on the right hand side of Eq. (A.2) are extrapolated to the time  $n + 1/2$  using the extrapolation  $f^{n+1/2} = (1/2)(3f^n - f^{n-1})$ .)

## A.3 The fully compressible Euler equations and other relevant information

The atmospheric flow can be described by the physical laws of conservation of momentum, mass and energy (*Stull*, 1988). The technique of solving the evolution equations in numerical weather prediction models has progressed through a long series of pioneering works, starting with the first endeavor by *Richardson* (1922), “Weather prediction by numerical process”, to the complex calculation of convection-permitting non-hydrostatic models in the recent decades. In the beginning of the 1980s, *Robert* (1981, 1982) suggested the semi-Lagrangian (SL) method for handling advection together with a semi-implicit (SI) method for solving the gravitational oscillation. The semi-Lagrangian method allows computational stability for much longer time steps with much higher Courant-Friedrichs-Lewy (CFL) values than what the Euler method can handle. Among the first to implement the SI-SL method in limited area models were *McDonald and Haugen* (1992), using a two-time-level  $\sigma$ -coordinate scheme, and later with a hybrid vertical coordinate (*McDonald and Haugen*, 1993). *Tanguay et al.* (1990) transferred the SI-SL methodology for the hydrostatic primitive equations to the non-hydrostatic case, and *Laprise* (1992) introduced the hybrid pressure-terrain coordinate in the fully compressible Euler equations (EE). This is among several other pioneering work that make up the framework for the equations cast in the HARMONIE-AROME model, which was first taken from the ALADIN-NH dynamical core *Bubnová et al.* (1995), and later revised by *Bénaud et al.* (2010).

The semi-Lagrangian method can be presented as (*Hortal*, 2002)

$$\frac{dX}{dt} = \frac{\partial X}{\partial t} + A(X) = L + N \quad (\text{A.3})$$

where  $X$  is a random prognostic variable, and  $\partial X/\partial t$  is the local derivative and  $A$  is the advection of  $X$ . The right hand side is divided into a linearized part,  $L$ , and the remainder,  $N$ , which denotes nonlinear terms (*Caya and Laprise, 1999*).

The HARMONIE-AROME model uses the two-time-level scheme, called Stable Extrapolation Two-Time Level Scheme (SETTLS) (*Hortal, 2002*) to discretize the SL equations. The SETTLS method solves the evolution equation by expanding a Taylor series around the departure point (D) of the semi-Lagrangian trajectory (*Hortal, 2002*),

$$\mathbf{R}_A^{t+\Delta t} \approx \mathbf{R}_D^t + \Delta t \cdot \mathbf{V}_D^t + \frac{\Delta t^2}{2} \cdot \left[ \frac{d\mathbf{V}}{dt} \right]_{\text{average}}. \quad (\text{A.4})$$

Here,  $\mathbf{R}$  is the position vector of an air parcel and  $\mathbf{V}$  is the velocity of that air parcel. D denotes the departure point at the present time step,  $t$ , for the air parcel that will arrive at grid point A at time  $t + \Delta t$ . With this method, the trajectory is allowed to follow a curved line. Further, no extrapolation of the wind in the first-order term ( $\Delta t \cdot \mathbf{V}_D^t$ ) is needed, while the second-order term  $\frac{\Delta t^2}{2} \cdot \left[ \frac{d\mathbf{V}}{dt} \right]_{\text{average}}$  is achieved through stable time extrapolation from the previous time step (*Hortal, 2002*);

$$\left[ \frac{d\mathbf{V}}{dt} \right]_{\text{average}} \approx \left[ \frac{d\mathbf{V}}{dt} \right]^{t-\frac{\Delta t}{2}} \approx \frac{\mathbf{V}_A^t - \mathbf{V}_D^{t-\Delta t}}{\Delta t}. \quad (\text{A.5})$$

The fully compressible Euler Equation (EE) system is expressed in *Bénard et al. (2010)* and used by the HARMONIE-AROME model. It operates with the hybrid (terrain, pressure) coordinate,  $\eta$  which is derived from the hydrostatic-pressure (*Laprise, 1992*).

$$\pi(x, y, \eta, t) = A(\eta) + B(\eta)\pi_s(x, y, t) \quad (\text{A.6})$$

where  $\pi_s$  is the surface hydrostatic pressure and  $\eta$  varies between 0 and 1.

With the non-hydrostatic variables  $\hat{q}, \mathbf{d}$  defined in 2.2 and 2.3, the EE system is as follows.

1. The conservation of horizontal momentum (*Bénard et al., 2010*)

$$\frac{d\mathbf{V}}{dt} + \frac{RT}{p} \nabla p + \frac{1}{m} \frac{\partial p}{\partial \eta} \nabla \phi = \mathbf{F}_v, \quad (\text{A.7})$$

where  $\mathbf{V}$  is the horizontal wind vector and  $\mathbf{F}_v$  represents the contribution from external forces,  $m = \partial \pi / \partial \eta$ ,  $R$  is the thermodynamic constant for moist air,  $T$  is temperature and  $p$  is actual pressure.  $\phi$  is defined as  $\phi = \phi_s + \int_{\eta}^1 \frac{mRT}{p}$ .

2. The conservation of vertical momentum (*Bénard et al., 2010*)

$$\begin{aligned} \frac{d\mathbf{d}}{dt} + g^2 \frac{p}{mR_a T} \frac{\partial}{\partial \eta} \left( \frac{1}{m} \frac{\partial (p - \pi)}{\partial \eta} \right) - g \frac{p}{mR_a T} \frac{\partial \mathbf{V}}{\partial \eta} \cdot \nabla_w - \mathbf{d}(\nabla \cdot \mathbf{V} - D_3) \\ = -g \frac{p}{mR_a T} \frac{\partial F_w}{\partial \eta} \end{aligned} \quad (\text{A.8})$$

where  $D_3$  is

$$D_3 = \nabla \cdot \mathbf{V} + \frac{1}{m} \frac{p}{RT} \nabla \phi \cdot \frac{\partial \mathbf{V}}{\partial \eta} + \frac{R_a}{R} \mathbf{d}.$$

In addition to this prognostic equation for vertical momentum, a prognostic equation for the vertical velocity,  $w$ , is also used to overcome the explicit handling of the non-linear terms. Transformation between the two variables is taken place at the start and the end of the explicit computations (*Bénard et al.*, 2010).

3. The conservation of heat (the thermodynamic energy equation) (*Bénard et al.*, 2010)

$$\frac{dT}{dt} + \frac{RT}{c_v} D_3 = \frac{Q}{c_v}, \quad (\text{A.9})$$

where  $Q$  represents heat sources and  $c_v$  is the constant-volume specific heat capacity for moist air.

4. The prognostic equation for the non-hydrostatic deviation from hydrostatic pressure (*Bénard et al.*, 2010)

$$\frac{d\hat{q}}{dt} + \frac{c_p}{c_v} D_3 + \frac{\hat{\pi}}{\pi} = \frac{Q}{c_v T}, \quad (\text{A.10})$$

where  $c_p$  is the constant-pressure specific heat capacity for moist air.

5. The continuity equation (*Bénard et al.*, 2010)

$$\frac{\partial \pi_s}{\partial t} + \int_0^1 \nabla \cdot (m \mathbf{V}) d\eta = 0. \quad (\text{A.11})$$

Integrating the continuity equation in the vertical through the depth of the atmosphere gives the equation for the surface hydrostatic pressure tendency (*Bénard et al.*, 2010),

$$\frac{\partial \pi_s}{\partial t} + \nabla \cdot \int_0^1 m \mathbf{V} d\eta = 0. \quad (\text{A.12})$$

In the same way, integrating from the top to the current level gives the pseudo-vertical advection velocity in  $\eta$  coordinates (*Bénard et al.*, 2010),

$$m\dot{\eta} = B(\eta) \int_0^1 \nabla \cdot (m \mathbf{V}) d\eta - \int_0^\eta \nabla \cdot (m \mathbf{V}) d\eta. \quad (\text{A.13})$$

Solving the equation system with respect to  $\mathbf{d}$  gives the following structure equation (*Bénard et al.*, 2010),

$$\left[ -\frac{1}{c_*^2} \frac{\partial^4}{\partial t^4} + \frac{\partial^2}{\partial t^2} \left( \nabla^2 + \frac{\Lambda^*}{r_s H_*^2} \right) + \frac{N_*^2}{r_s} \nabla^2 \right] \mathbf{d} = 0, \quad (\text{A.14})$$

where  $c_*^2 = (c_{pa}/c_{va})R_a T^*$ ,  $r_s = (T_e^*/T^*)$ ,  $H_* = (R_a T^*/g)$ ,  $N_*^2 = g^2/(c_{pa} T^*)$ . The operator  $\Lambda^*$  is a spatial linear operator defined by  $\Lambda^* X = \partial^*(\partial^* + 1)X$  and  $T^*, T_e^*$  are



semi-implicit-reference temperatures and  $c_p$ ,  $c_{pa}$  are constant-pressure specific heat capacity of moist and dry air  $c_v$ ,  $c_{va}$  are constant-volume specific heat capacity of moist and dry air.

In addition to the prognostic equations mention above, HARMONIE-AROME also operates with prognostic equations for the hydrometeors following the semi-Lagrangian scheme for horizontal advection and *Bouteloup et al. (2011)* for vertical advection and sedimentation.

The boundary relaxation scheme follows *Radnoti (1995)* and *Termonia et al. (2018)*. The boundary relaxation model state,  $\mathbf{X}$ , is (*Termonia et al., 2018*)

$$\mathbf{X} = \alpha_b \mathbf{X}_G + (1 - \alpha_b) \left(1 - \frac{\Delta t}{2} \Lambda\right) \mathbf{X}_H, \quad (\text{A.15})$$

where  $\mathbf{X}_G$  is the model state after interpolated tendencies have been added,  $\mathbf{X}_H$  is the host model fields,  $\Lambda$  is the linear operator for the semi-implicit scheme, and  $\alpha_b$  is given by (*Termonia et al., 2018*)

$$\alpha_b(z_n) = 1 - (r + 1)z_n^r + rz_n^{r+1}. \quad (\text{A.16})$$

Here,  $z_n$  is the normalized distance from the boundary of the center zone to the border of the intermediate zone,  $r$  is used to tune  $\alpha_b$ , and is set to 2.16 for wind and temperature, and to 5.52 for water vapor.

## A.4 HARMONIE-AROME configuration in NORA3

Host model	ERA5
Physiography	ECOCLIMAP, v.2
Orography	GMTED2010
Microphysics	ICE3 OCND2 Kogan autoconversion
Turbulence	HARATU
Radiation	Longwave, RRTM ECMWF operational SW scheme
Convection	EDMF-M
Surface modeling	SURFEX
Number of patches	1
ISBA-Scheme	3-Layer ISBA
Grid type	Linear
Surface Boundary Layer	No multilayer scheme

Table A.2: The configuration of HARMONIE-AROME in NORA3.

The configuration of HARMONIE-AROME in NORA3 is provided in Table A.2 and is as follows. NORA3 uses the ERA5 (*Hersbach et al., 2020*) reanalysis as its host model. The ECOCLIMAP, v.2 (*Faroux et al., 2013*) physiography is used, and GMTED2010 orography. The schemes ICE3 (*Lascaux et al., 2006; Pinty and Jabouille, 1998*), OCND2 (*Müller et al., 2017b*) and Kogan autoconversion (*Khairoutdinov and Kogan, 2000*) is used in the microphysics.

The cloud microphysics uses a Kessler scheme for warm processes and the three-class ice scheme (ICE3) for cold processes (*Pinty and Jabouille, 1998*). Vapor, cloud water, rain, cloud ice, snow and graupel are prognostic variables. The OCND2-modifications to the scheme involves separating the liquid-phase processes which are fast processes from the far slower ice-phase processes. It also involves a reduction of the speed of the sublimation of ice particles, and it also consider the less optical thickness ice phase clouds compared to the water and mixed-phase clouds (*Müller et al., 2017b*).

The HARATU (*Lenderink and Holtslag, 2004; van Meijgaard et al., 2012*) turbulence parameterization is used. Regarding radiation, the RRTM (*Mlawer et al., 1997*) scheme is used for longwave radiation and ECMWF operational short wave (*ECMWF, 1989*) is used. The convection scheme is the EDMF-M scheme (*de Rooy and Siebesma, 2010; Neggers et al., 2009; Siebesma et al., 2003, 2007; Soares et al., 2004*). The surface model is the SURFEX (*Masson et al., 2013*).

## A.5 The choice of the NORSOK wind profile

In the first, second and fourth paper, we used measurements from offshore installations. Since offshore measurements are performed at different sensor heights, it is necessary to reduce the measurements to 10 m before they are used for validation. Sensor heights are typically between 30 and 150 m above sea level, where the wind profile is less affected by surface friction, but more influenced by baroclinicity, stability and inversion capping when approaching the boundary layer height (*Gryning et al., 2007*). In the Frost database (<https://frost.met.no>), the wind speed has been reduced to 10 m with a standard procedure using the power law with a coefficient which is too high and not recommended to be used in maritime conditions (*Furevik and Haakenstad, 2012*). To evaluate different wind profile methods, we used FINO-1 as a test station where wind speed in 100m and 40m are available. (The FINO-1 measurements is available from the Bundesministerium für Umwelt, Federal Ministry for the Environment, Nature Conservation and Nuclear Safety, Germany). Different profile-methods have been applied to the measurements in 100m in order to estimate the value in 40 m and compare to the observed values in 40m. The wind profiles investigated are the NORSOK profile (*Andersen and Løvseth, 2006; AS Standard Online, 2016; NORSOK, 2007*), the wind power law (*Furevik and Haakenstad, 2012; Manaster et al., 2019; Stull, 1988*), the logarithmic wind profile (*Stull, 1988*) and the Gryning profile (*Gryning et al., 2007*). The profile methods are listed in Table A.3 and A.4.

The NORSOK profile (*Andersen and Løvseth, 2006*) was developed for the Norwegian continental shelf based on comprehensive measurements from a tall mast on the island Frøya off the north-west coast of Norway. The NORSOK profile has been the basis behind the recommended practice for design of offshore structures in Norway

Method	Formula
NORSOK	$U_{100m} = U_{40m} \left( 1 + C \ln \frac{z}{z_r} \right)$ <p>where</p> $C = 5.73 \times 10^{-2} (1 + 0.15U_{40m})^{1/2}$ <p>Solved with respect to <math>U_{40m}</math> this gives the 3. order equation</p> $aU_{40m}^3 + bU_{40m}^2 + cU_{40m} + d = 0$ <p>where</p> $a = \left( \ln \frac{100}{40} \right)^2 \times 0.003283 \times 0.15$ $b = \left( \ln \frac{100}{40} \right)^2 \times 0.003283 - 1.0$ $c = 2U_{100m}$ $d = -U_{100m}^2$
Power law	$U_{40m} = U_{100m} \left( \frac{40}{100} \right)^\alpha$ <p>where <math>\alpha</math> depends on the atmospheric stability</p> <p><math>\alpha = 0.05</math> in neutral cases</p> <p><math>\alpha = 0.09</math> in stable cases</p> <p><math>\alpha = 0.04</math> in unstable cases</p>
Log wind	$U_{40m} = U_{100m} \frac{\ln(40m/z_0)}{\ln(100m/z_0)}$ <p><math>z_0</math> is set to 0.0002 m (a typical value over open ocean)</p>

Table A.3: Description of the NORSOK, Power law and Log wind profiles.

---

**Method Formula**


---

## Gryning

Neutral cases: Eq (21) by Gryning *et al.* (2007) (in the equations  $u_* = u_{*0}$ )

$$U(z) = (u_*/\kappa) \left( \ln \frac{z}{z_0} + \frac{z}{L_{\text{MBL}}} - \frac{z}{z_i} \frac{z}{2L_{\text{MBL}}} \right), \kappa = 0.41$$

where the length scale of the middle part of the boundary layer is parameterized as

$$L_{\text{MBL}} = \frac{u_*}{f} \left( (-2 \ln \frac{u_*}{fz_0} + 55) \exp\left(-\frac{(u_*/fL_{\text{MOL}})^2}{400}\right) \right)^{-1}$$

Stable cases, Eq (15) by Gryning *et al.* (2007):

$$U(z) = \frac{u_*}{\kappa} \left( \ln \frac{z}{z_0} + \frac{bz}{L_{\text{MOL}}} \left(1 - \frac{z}{2z_i}\right) + \frac{z}{L_{\text{MBL}}} - \frac{z}{z_i} \frac{z}{2L_{\text{MBL}}} \right)$$

where

$L_{\text{MOL}}$  is the Monin-Obukov length scale:

$$L_{\text{MOL}} = \frac{-U_*^3 T}{\kappa g Q}, \text{ where } Q \text{ is the kinematic heat flux (= heat flux}/\rho)$$

and  $g = 9.81 \text{ m s}^{-2}$  is the gravitational acceleration

Unstable cases, Eq. (19) by Gryning *et al.* (2007):

$$U(z) = \frac{u_*}{\kappa} \left( \ln \frac{z}{z_0} - \Psi\left(\frac{z}{L_{\text{MBL}}}\right) + \frac{z}{z_i} \left(1 + \frac{(1-12z/L_{\text{MOL}})^{2/3}-1}{8z/L_{\text{MOL}}}\right) + \frac{z}{L_{\text{MBL}}} - \frac{z}{z_i} \frac{z}{2L_{\text{MBL}}} \right)$$

where the stability correction is

$$\Psi = 1.5 \ln \left( \frac{1+x+x^2}{3} - \sqrt{3} \arctan \left( \frac{1+2x}{\sqrt{3}} \right) + \frac{\pi}{\sqrt{3}} \right) \text{ with } x = (1 - 12z/L_{\text{MOL}})^{1/3}$$

The Coriolis frequency is  $f = 1.46 \times 10^{-4} \sin(\phi)$ , where  $\phi$  is the latitude.

$z_i$  is the height of the boundary layer and is read from the model

The friction velocity  $u_*$  is retrieved from the model

$$(u_* = \sqrt{\tau/\rho}, \text{ where } \tau \text{ is the shear stress or vertical momentum flux})$$

$\rho$  is retrieved from model (= MSLP/ $T_{0m}R$ ), where  $R = 287.05$ .)

Stability conditions are determined from the criteria

(where  $\Delta T = T_{2m} - T_{0m}$ ):

$-1 \leq \Delta T < 0$ : neutral

$\Delta T > 0$ : stable

$\Delta T < -1$ : unstable

---

Table A.4: Description of the Gryning wind profile.

(DNVGL, 2017). In addition to being well documented and widely used, the advantage of this method is that it does not require any additional information which could be an additional source of uncertainty, but it also means that it does not take atmospheric stability into account.

The wind power law is

$$U_{10} = U_H \left( \frac{10}{H} \right)^\alpha \quad (\text{A.17})$$

Here,  $U_{10}$  and  $U_H$  are the wind speed in height 10 m and  $z = H$ , respectively, and the exponent  $\alpha$  determines the shear. *Hsu et al.* (1994) recommended  $\alpha = 0.11$  over marine surfaces, but for Norwegian offshore regions, a lower average value of 0.06 is found from a large data set of rawinsonde (*Furevik and Haakenstad*, 2012) and satellite data (*Manaster et al.*, 2019). Values for stable, unstable and near-neutral cases are given in Table A.2a.

The logarithmic wind profile (*Stull*, 1988) is given by

$$\frac{du}{dz} = \frac{u_*}{\kappa l} \quad (\text{A.18})$$

where  $u_*$  is the friction velocity,  $\kappa$  is von Kármán's constant ( $\kappa \approx 0.41$ ) and  $l$  is the turbulence length scale.

The Gryning profile (*Gryning et al.*, 2007) is based on *Panofsky* (1973). The profile assumes constant friction velocity in the surface layer and a linear reduction with height in the rest of the boundary layer. *Gryning et al.* (2007) separates the local length scale into three parts, representing the surface layer, the middle boundary layer and the upper boundary layer. The three length scales also differ with respect to atmospheric stability. The profile equation together with presumed constants needed to solve the equation, are based on profile measurements from the TV tower of Hamburg and the National Test Site for wind turbines in Høvsøre in Denmark, providing a profile description suitable for homogeneous terrestrial and rural terrain. The Gryning profile depends on a number of parameters that needs to be estimated from the model. These are the roughness length (available every hour), friction velocity and the height of the boundary layer (available 6-hourly). Based on this, we find an average reduction factor for the wind speed in stable, unstable and neutral cases which are used to reduce the 100 m observed value to 40 m. Fig. A.1 shows the density plot of wind speed reduced from 100m to 40m with the four different wind profile methods. The reduced values are plotted together with observed wind in 40m. All the profile methods show a correlation above 0.97, however the log-wind and power-law have a higher RMSE than NORSOK and Gryning, and a greater deviation for the upper percentiles. The Gryning and NORSOK both perform well, with a higher correlation in Gryning and a better fit to the upper percentiles in NORSOK. We could thus have chosen the Gryning profile instead of NORSOK, but the Gryning method adds extra complexity as it requires the friction velocity, the height of the boundary layer, as well as the roughness length, all parameters that are not yet evaluated in the NORA3 archive and quite complicated to simulate correctly (*Bourassa et al.*, 2014).

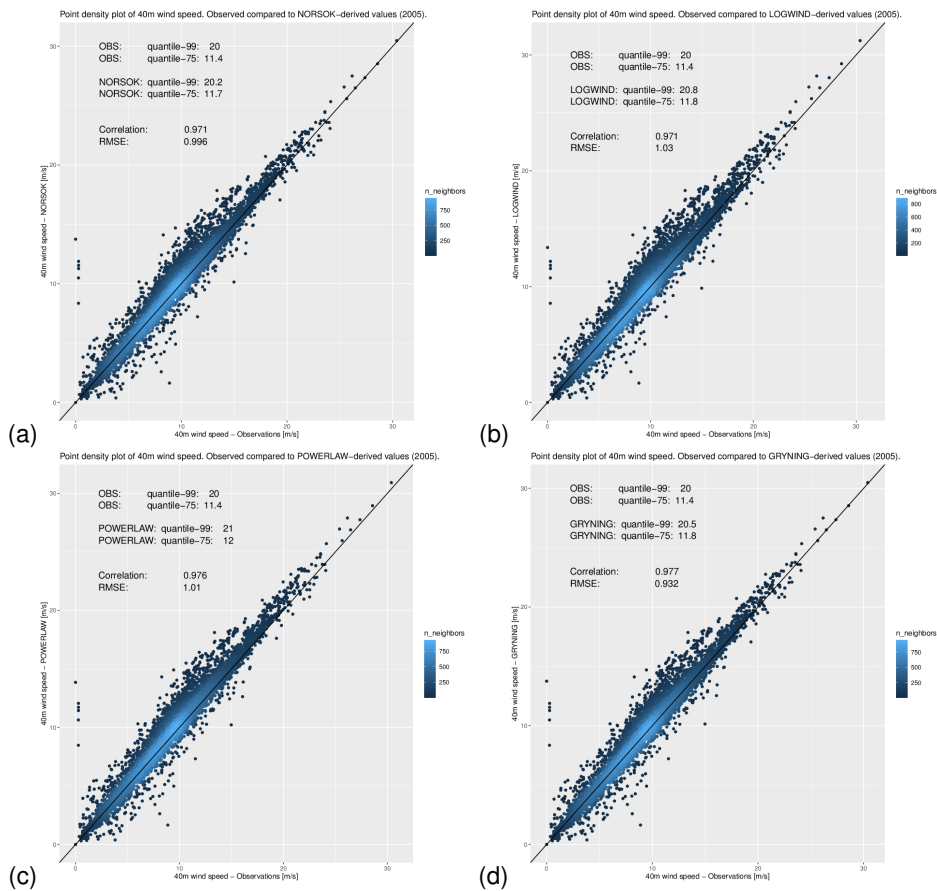


Figure A.1: Figure showing the density plot of different profile methods used to reduce wind from 100m height to 40m.

## A.6 Abbreviations and relevant information

---

AR	Atmospheric River
AROME	the Application of Research to Operations at MESoscale
ACCORD	A Consortium for CONvection-scale modelling Research and Development
ALADIN	Aire Limitée Adaptation Dynamique développement InterNational
CAMS	Copernicus Atmosphere Monitoring Service
CARRA	Copernicus Arctic Regional ReAnalysis
CERA	Coupled ECMWF ReAnalysis
CFSR	Climate Forecast System Reanalysis
CMIP	Coupled Model Intercomparison Project
CP	Convection Permitting
CPU	Central Processing Unit
ECMWF	European Centre for Medium-range Weather Forecasts
EDMF	Eddy Diffusivity Mass Flux
ERA	European ReAnalysis
ETS	Equitable Threat Score
EWA	European Wind Atlas
GMTED	Global Multi-resolution Terrain Elevation Data
HA	HARMONIE-AROME
HARATU	HARmonie with RAcmo TURbulence
HARMONIE-AROME	HIRLAM-ALADIN Regional/Mesoscale Operational NWP in Euromed
HIRLAM	High Resolution Limited Area Model
IFS	Integrated Forecasting System
IPCC	Intergovernmental Panel on Climate Change
ISBA	Interaction Soil Biosphere Atmosphere
JRA	Japanese ReAnalysis
LACE	Limited Area modeling in Central Europe
MACC	Monitoring Atmospheric Composition and Climate
MERRA	Modern-Era Retrospective analysis for Research and Applications
MET Norway	Norwegian Meteorological Institute (Europe and the Mediterranean area).

---

*Table A.5: Part 1: Acronyms and abbreviations used in the text.*

---

NCAR	National Center for Atmospheric Research
NCEP	National Centers for Environmental Prediction
NEWA	New European Wind Atlas
NH	Non-Hydrostatic
NORA10	10 km NORwegian hindcast Archive
NORA10EI	revised NORwegian hindcast Archive
NORA3	3 km NORwegian ReAnalysis
NORSEAWIND	NORthern SEas Wind Index Database
NORSOK	NORsk SOkkels Konkurransesisjon (The Norwegian shelf's competitive position)— Norwegian offshore standards
NSC	National Supercomputer Centre
NWP	Numerical Weather Prediction
ORAS	Ocean ReAnalysis System
PAMIP	Polar Amplification Model Intercomparison project
WAM	The WAve Model
WASA	Waves And Storms in the north Atlantic
WaSP	Wind Atlas analysis and application Programme
WRF	The Weather Research and Forecasting model
RMSE	Root-mean-square error
RRTM	Rapid Radiative Transfer Model
SURFEX	SURFace EXternalisée
YOPP	Year of Polar Prediction

---

*Table A.6: Part 2: Acronyms and abbreviations used in the text.*



## A.7 List of symbols

---

$a, b, c, d$	constants in the NORSOK equation
$A, B$	functions used in the definition of the vertical coordinate
$c_p$	constant pressure specific heat capacity for moist air
$c_{pa}$	constant pressure specific heat capacity for dry air
$c_v$	constant volume specific heat capacity for moist air
$c_{va}$	constant volume specific heat capacity for dry air
$c_*$	is defined as $\sqrt{(c_{pa}/c_{va})R_aT^*}$
$C$	constant in the NORSOK-equation
$\mathbf{d}$	a vertical momentum formulation
$D$	divergence
$D_3$	formulation used in the equation for vertical momentum, see Eq. 2.
$f$	Coriolis frequency
$\mathbf{F}$	external forces
$g$	acceleration of gravity
$H$	height
$l$	turbulence length scale
$L_{\text{MOL}}$	Monin-Obukhov length scale
$m$	the vertical derivative of hydrostatic pressure
$N_*$	is defined as $\sqrt{g^2/(c_{pa}T^*)}$
$p$	actual pressure
$p_s$	surface pressure
$\hat{q}$	nonhydrostatic pressure deviation (defined in an applicable way)
$Q$	kinematic heat flux
$r$	a tuning parameter used in the boundary relaxation
$r_s$	the ratio between the semi-implicit reference temperatures, ( $T_e^*$ and $T^*$ )
$R$	thermodynamic constant of moist air
$R_a$	thermodynamic constant of dry air
$\mathbf{R}$	the position vector of an air parcel
$\dot{s}$	vertical wind component in the hydrostatic model
$t$	time
$T^*$	the semi-implicit reference temperature
$T_e^*$	the semi-implicit reference temperature used for the term involved in the vertical propagation of elastic waves
$U$	wind speed
$u_*$	friction velocity
$\mathbf{V}$	wind velocity vector
$w$	vertical wind component
$\mathbf{X}$	model state (a prognostic variable)
$z_n$	the normalized distance from the boundary of the center zone to the border of the intermediate zone
$z_0$	roughness length

---

Table A.7: Symbols used in the text.

---

$\alpha$	atmospheric stability parameter
$\alpha_b$	formulation used in the boundary relaxation
$\eta$	hybrid vertical coordinate, terrain-following and pressure dependent
$\kappa$	von Kármán's constant
$\Lambda$	linear operator
$\pi$	hydrostatic pressure
$\rho$	air density
$\tau$	shear stress (vertical momentum flux)
$\phi$	latitude
$\psi$	Gryning stability correction

---

*Table A.8: Symbols used in the text (Greek letters).*

Partners involved in the different consortia listed in Table A.5 are given in the Table A.9 (Norman, 2021).

---

ALADIN:	Algeria, Austria, Belgium, Bulgaria, Croatia, Czech Republic, France, Hungary, Morocco, Poland, Portugal, Romania, Slovakia, Slovenia, Tunisia, and Turkey
LACE:	Austria, Croatia, Czech Republic, Hungary, Poland, Romania, Slovakia, and Slovenia
HIRLAM:	Denmark, Estonia, Finland, Iceland, Ireland, Lithuania, Netherlands, Norway, Spain, and Sweden

---

*Table A.9: Members of the meteorological consortia mentioned in the text.*

# Bibliography

- Aarnes, O. J., S. Abdalla, J.-R. Bidlot, and Ø. Breivik (2015), Marine wind and wave height trends at different ERA-Interim forecast ranges, *J Climate*, 28(2), 819–837, doi:10.1175/JCLI-D-14-00470.1. 3
- Alexandersson, H., T. Schmith, K. Iden, and H. Tuomenvirta (1998), Long-term trend variations of the storm climate over northwest Europe, *The Global Atmosphere-Ocean System*, 6(2), 97–120. 1.1.4
- Alpers, W., A. Ivanov, and J. Horstmann (2009), Observations of Bora events over the Adriatic Sea and Black Sea by spaceborne synthetic aperture radar, *Mon Wea Rev*, 137(3), 1150–1161, doi:10.1175/2008MWR2563.1. 1.1.3
- Andersen, O. J., and J. Løvseth (2006), The frøya database and maritime boundary layer wind description, *Marine Structures*, 19(2,3), 173–192, doi:10.1016/j.marstruc.2006.07.003. A.5, A.5
- Ardhuin, F., E. Rogers, A. V. Babanin, J.-F. Filipot, R. Magne, A. Roland, A. van der Westhuysen, P. Queffelecoul, J.-M. Lefevre, L. Aouf, and F. Collard (2010), Semiempirical dissipation source functions for ocean waves. Part I: Definition, Calibration and Validation, *J Phys Oceanogr*, 40(9), 1917–1941, doi:10.1175/2010JPO4324.1. 1.1.4, 2.1.3
- AS Standard Online (2016), Standard Norge Versjon 5.2: Action and action effects, N-003, *Tech. rep.*, Standard Norge, Postboks 242, 1326 Lysaker. A.5
- Avissar, R., and R. A. Pielke (1989), A parameterization of heterogeneous land surfaces for atmospheric numerical models and its impact on regional meteorology, *Mon Wea Rev*, 117(10), 2113–2136, doi:https://doi.org/fw4tpb. 2.1.1
- Azad, R., and A. Sorteberg (2017), Extreme daily precipitation in coastal western Norway and the link to atmospheric rivers, *J Geophys Res: Atmospheres*, 122(4), 2080–2095, doi:10.1002/2016JD025615. 1.1.2
- Balmaseda, M. A., A. Vidard, and D. Anderson (2008), The ECMWF ocean analysis system: ORA-S3, *Mon Wea Rev*, 136(8), 3018–3034, doi:10.1175/2008MWR2433. 1. 1
- Balmaseda, M. A., K. Mogensen, and A. T. Weaver (2013), Evaluation of the ECMWF ocean reanalysis system ORAS4, *Q J R Meteorol Soc*, 139(674), 1132–1161, doi:10.1002/qj.2063. 1

- Bénard, P., J. Vivoda, J. Mašek, P. Smolíková, K. Yessad, C. Smith, R. Brožková, and J.-F. Geleyn (2010), Dynamical kernel of the Aladin-NH spectral limited-area model: Revised formulation and sensitivity experiments, *Q J R Meteorol Soc*, 136(646), 155–169, doi:10.1002/qj.522. 2.1.2, A.3, A.3, 1, 2, 2, 3, 4, 5, 5, 5, A.3
- Benedict, I., K. Ødemark, T. Nipen, and R. Moore (2019), Large-scale flow patterns associated with extreme precipitation and atmospheric rivers over Norway, *Mon Wea Rev*, 147(4), 1415–1428, doi:10.1175/MWR-D-18-0362.1. 1.1.2
- Bengtsson, L., U. Andrae, T. Aspelien, Y. Batrak, J. Calvo, W. de Rooy, E. Gleeson, B. Hansen-Sass, M. Homleid, M. Hortal, K.-I. Ivarsson, G. Lendrink, S. Niemelä, K. P. Nielsen, J. Onvlee, L. Rontu, P. Samuelsson, D. S. Munoz, A. Subias, S. Tijm, V. Toll, X. Yang, and M. Körtzow. (2017), The HARMONIE-AROME model configuration in the ALADIN-HIRLAM NWP system, *Mon Wea Rev*, 145(5), 1919–1935, doi:10.1175/MWR-D-16-0417.1. 1.1.4, 2.1, 3
- Berge, E., Ø. Byrkjedal, Y. Ydersbond, and D. Kindler (2009), Modelling of offshore wind resources. Comparison of a meso-scale model and measurements from FINO 1 and North Sea oil rigs, *Tech. rep.*, Kjeller Vindteknikk, A.S., Kjeller, Norway. 1.1.4
- Bourassa, M. A., S. T. Gille, C. Bitz, D. Carlson, I. Cerovecki, C. A. Clayson, M. F. Cronin, W. M. Drennan, C. W. Fairall, R. N. Hoffman, G. Magnusdottir, R. T. Pinker, I. A. Renfrew, M. Serreze, K. Speer, L. D. Talley, and G. A. Wick. (2014), High-latitude ocean and sea ice surface fluxes: challenges for climate research, *Bull Am Meteor Soc*, 94(3), 403–423, doi:10.1175/BAMS-D-11-00244.1. A.5
- Bouteloup, Y., Y. Seity, and E. Bazile (2011), Description of the sedimentation scheme used operationally in all Météo-France NWP models, *Tellus*, 63(2), 300–311, doi:10.1111/j.1600-0870.2010.00484.x. A.3
- Breivik, Ø., Y. Gusdal, B. R. Furevik, O. J. Aarnes, and M. Reistad (2009), Nearshore wave forecasting and hindcasting by dynamical and statistical downscaling, *J Marine Syst*, 78, S235–S243, doi:10.1016/j.jmarsys.2009.01.025. 2.1.3
- Breivik, Ø., A. Carrasco, H. Haakenstad, O. J. Aarnes, A. Behrens, J.-R. Bidlot, J.-V. Björkqvist, P. Bohlinger, B. R. Furevik, J. Staneva, and M. Reistad (2022), The Impact of a Reduced High-wind Charnock Coefficient on Wave Growth With Application to the North Sea, the Norwegian Sea and the Arctic Ocean, *J Geophys Res: Oceans*, 127(3), e2021JC018196, doi:10.1029/2021JC018196. 1, 2.1.3, 2.2, 2.3
- Brousseau, P., Y. Seity, D. Ricard, and J. Léger (2016), Improvement of the forecast of convective activity from the AROME-France system, *Q J R Meteorol Soc*, 142(699), 2231–2243, doi:10.1002/qj.2822. 2.3
- Bubnová, R., G. Hello, P. Bénard, and J.-F. Geleyn (1995), Integration of the fully elastic equations cast in the hydrostatic pressure terrain-following coordinate in the framework of the ARPEGE/Aladin NWP system, *Mon Wea Rev*, 123(2), 515–535, doi:https://doi.org/d5m7wr. 2.1.2, A.3
- Byrkjedal, Ø., and R. Kravik (2009), Analyser av offshore modellsimuleringer av vind, *Tech. rep.*, Kjeller Vindteknikk AS, Kjeller, Norway. 1.1.4

- Byrkjedal, Ø., J. Hansson, and H. van der Velde (2015), Development of operational forecasting for icing and wind power at cold climate sites, in *IWAIS 2015–16th International Workshop on Atmospheric Icing of*, pp. 4, 16th International Workshop on Atmospheric Icing of Structures, IWAIS, Uppsala, Sweden, Kjeller, Norway. 1.1.4
- Catry, B., J.-F. Geleyn, F. Bouyssel, J. Cedilnik, R. Brožková, M. Derková, and R. Mladek (2008), A new formulation in a mountain drag parameterisation scheme, *Meteorologische Zeitschrift*, 17(2), 193–208, doi:10.1127/0941-2948/2008/0272. 2.1.2
- Caya, D., and R. Laprise (1999), A semi-implicit semi-lagrangian regional climate model: The Canadian RCM, *Mon Wea Rev*, 127(3), 341–362, doi:10/ddp92h. A.3
- Charnock, H. (1955), Wind stress on a water surface, *Q J R Meteorol Soc*, 81(350), 639–640, doi:10.1002/qj.49708135027. 3
- Christakos, K., B. R. Furevik, O. J. Aarnes, Ø. Breivik, L. Tuomi, and Ø. Byrkjedal (2020), The importance of wind forcing in fjord wave modelling, *Ocean Dyn*, 70(1), 57–75, doi:10.1007/s10236-019-01323-w. 2.3
- Cordeneanu, E., and J.-F. Geleyn (1998), Application to local circulations above the Carpathian-Black sea area of a NEP-type meso-scale model, *Contr. Atm. Phys*, 71(2), 191–212. 2.1.1
- Daley, R. (1991), *Atmospheric Data Analysis, Atmospheric and space science series*, vol. 2, 460 pp., Cambridge University Press, Cambridge. 2.3
- de Rooy, W. C., and A. P. Siebesma (2010), Analytical expressions for entrainment and detrainment in cumulus convection, *Q J R Meteorol Soc*, 136(650), 1216–1227, doi:10.1002/qj.640. 2.1.2, A.4
- de Rooy, W. C., P. Siebesma, P. Baas, G. Lenderink, S. R. de Roode, H. de Vries, E. van Meijgaard, J. F. Meirink, s. Tijm, and B. van't Veen (2022), Model development in practice: a comprehensive update to the boundary layer schemes in harmonie-arome cycle 40, *Geosci Model Dev*, 15(4), 1513–1543, doi:10.5194/gmd-15-1513-2022. 2.3
- Dee, D. P., S. M. Uppala, A. J. Simmons, P. Berrisford, P. Poli, S. Kobayashi, U. Andrae, M. A. Balmaseda, G. Balsamo, P. Bauer, P. Bechtold, A. C. M. Beljaars, L. van de Berg, J. Bidlot, N. Bormann, et al. (2011), The ERA-Interim reanalysis: Configuration and performance of the data assimilation system, *Q J R Meteorol Soc*, 137(656), 553–597, doi:10.1002/qj.828. 1, 1, 1.1.4, 2.1.1, 2.2, 3
- Degrauwe, D., S. Caluwaerts, F. Voitus, R. Hamdi, and P. Termonia (2012), Application of Boyd's periodization and relaxation method in a spectral atmospheric limited-area model. Part II: Accuracy analysis and detailed study of the operational impact, *Mon Wea Rev*, 140(10), 3149–3162, doi:10.1175/MWR-D-12-00032.1. 2.3
- DNVGL, A. (2017), Recommended practice, *DNVGL-RP-E307*, p. 29 pp. A.5

- Donelan, M. A., B. K. Haus, N. Reul, W. J. Plant, M. Stiassnie, H. C. Graber, O. B. Brown, and E. S. Saltzman (2004), On the limiting aerodynamic roughness of the ocean in very strong winds, *Geophys Res Lett*, 31(18), L18,306, doi:10.1029/2004GL019460. 3
- Durrán, D. R. (1986), Another look at downslope wind storms. Part I: The development of analogs to supercritical flow in an infinitely deep, continuously stratified fluid, *J Atmos Sci*, 43(21), 2527–2543, doi:https://doi.org/fcfq6n. 1.1.3
- Dyrørdal, A. V., F. Stordal, and C. Lussana (2018), Evaluation of summer precipitation from EURO-CORDEX fine-scale RCM simulations over Norway, *Int. J. Climatol.*, 38(4), 1661–1677, doi:10.1002/joc.5287. 1.1.2
- ECMWF (1989), Physical parameterization, ECMWF forecast model, *Research Manual RM-3, 3rd*, ECMWF, Shinfield Park, Reading, RG2 9AX, England. A.4
- ECMWF (2015), Operational implementation 12 May 2015. Part III: Dynamics and numerical procedures, *European Centre for Medium-Range Weather Forecasts IFS Doc. Cy41r1*, ECMWF, Shinfield Park, Reading, RG2 9AX, England. 2.1.2
- ECMWF (2020), IFS Documentation CY43r1, Part VII: ECMWF wave model., *ECMWF model documentation*, European Centre for Medium-Range Weather Forecasts, Shinfield Park, Reading, RG2 9AX, England. 3
- Eide, L. I., M. Reistad, and J. Guddal (1985), A database of computed wind and wave parameters for the North Sea, the Norwegian Sea and the Barents Sea for every 6 hours for the years 1955-1981 (In Norwegian), *Tech. rep.*, The Norwegian Meteorological Institute, P.O. 43, Blindern, 0313 OSLO. 1.1.4
- Eliassen, A. (1982), Vilhelm Bjerknes and his students, *Ann. Rev. Fluid Mech.*, 14, 1–11. 2.1
- Elvidge, A. D., and I. A. Renfrew (2016), The causes of Foehn warming in the lee of mountains, *Bull Am Meteor Soc*, 97(3), 455–466, doi:10.1175/BAMS-D-14-00194. 1. 1.1.3
- Faroux, S., A. T. K. Tchuente, J. L. Roujean, V. Masson, E. Martin, and P. L. Moigne (2013), ECOCLIMAP-II/Europe: a twofold database of ecosystems and surface parameters at 1 km resolution based on satellite information for use in land surface, meteorological and climate models, *Geosci Model Dev*, 6(2), 563–582, doi:10.5194/gmd-6-563-2013. A.4
- Flemming, J., A. Benedetti, A. Inness, R. J. Engelen, L. Jones, V. Huijnen, S. Remy, M. Parrington, M. Suttie, A. Bozzo, V.-H. Peuch, D. Akritidis, and E. Katragkou (2017), The CAMS interim reanalysis of carbon monoxide, ozone and aerosol for 2003-2015, *Atmospheric Chemistry and Physics*, 17(3), 1945–1983, doi:10.5194/acp-17-1945-2017. 1
- Francis, J. A., and S. J. Vavrus (2012), Evidence linking Arctic amplification to extreme weather in mid-latitudes, *GRL*, 39(6), L06,801, doi:10.1029/2012GL051000. 1.1.1



- Frogner, I.-L., U. Andrae, J. Bojarova, A. Callado, P. Escribá, H. Feddersen, A. Hally, J. Kauhanen, R. Randriamampianina, A. Singleton, G. Smet, S. van der Veen, and O. Vignes (2019), HarmonEPS-The HARMONIE Ensemble Prediction System, *Weather and Forecasting*, 34(6), 1909–1937, doi:10.1175/WAF-D-19-0030.1. 2.3
- Frogner, I.-L., A. T. Singleton, M. Ø. Køltzow, and U. Andrae (2019b), Convection-permitting ensembles: Challenges related to their design and use, *Q J R Meteorol Soc*, 145, 90–106, doi:10.1002/qj.3525. 2.3
- Furevik, B. R., and H. Haakenstad (2012), Near-surface marine wind profiles from rawinsonde and NORA10 hindcast, *J Geophys Res: Atmospheres*, 117(D23), 14, doi:10.1029/2012JD018523. A.5, A.5
- Furevik, B. R., H. Schyberg, G. Noer, F. Tveter, and J. Röhrs (2015), ASAR and ASCAT in Polar Low Situations, *J Atmos Ocean Tech*, 32(4), 783–792, doi:10.1175/JTECH-D-14-00154.1. 3
- Gaberšek, S., and D. R. Durran (2004), Gap flows through idealized topography. Part I: Forcing by large-scale winds in the nonrotating limit, *J Atmos Sci*, 61(23), 2846–2862, doi:10.1175/JAS-3340.1. 1.1.3
- Gelaro, R., W. McCarty, M. J. Suaáñez, R. Todling, A. Molod, L. Takacs, C. A. Randles, A. Darmenov, M. G. Bosilovich, R. Reichle, K. Wargan, L. Coy, R. Cullather, C. Draper, S. Akella, V. Buchard, A. Conaty, et al. (2017), The modern-era retrospective analysis for research and applications, version 2 (MERRA-2), *J Climate*, 30(14), 5419–5454, doi:10.1175/JCLI-D-16-0758.1. 1
- Gibson, J., P. Kållberg, S. Uppala, A. Nomura, A. Hernandez, and E. Serrano (1997), ERA Description In ECMWF ERA-15 Project Report Series, No. 1., *Tech. rep.*, European Centre for Medium-Range Weather Forecasts, ECMWF Shinfield, Reading, UK. 1
- Gryning, S.-E., E. Batchvarova, B. Brümmer, H. Jørgensen, and S. Larsen (2007), On the extension of the wind profile over homogeneous terrain beyond the surface boundary layer, *Boundary Layer Meteorol*, 124, 251–268, doi:10.1007/s10546-007-9166-9. A.5, A.5
- Günther, H., S. Hasselmann, and P. A. E. M. Janssen (1992), The WAM model cycle 4 (revised version), *Tech. Rep. 4*, Deutsches KlimaRechenZentrum, Hamburg, Germany. 1.1.4, 2.1.3, 3
- Gustafsson, N., and A. McDonald (1996), A comparison of the HIRLAM gridpoint and spectral semi-lagrangian models, *Mon Wea Rev*, 124(9), 2008–2022. A.2
- Haakenstad, H., and Ø. Breivik (2022), NORA3 Part II: Precipitation and temperature statistics in complex terrain modeled with a non-hydrostatic model, *Submitted to J Appl Meteorol and Climatol*. 1, 2.1.2, 2.2
- Haakenstad, H., Ø. Breivik, M. Reistad, and O. J. Aarnes (2020), NORA10EI: A revised regional atmosphere-wave hindcast for the North Sea, the Norwegian Sea and the Barents Sea, *IJC*, 40(10), 4347–4373, doi:10.1002/joc.6458. 1, 1.1.4, 2.2, 3

- Haakenstad, H., Ø. Breivik, B. R. Furevik, M. Reistad, P. Bohlinger, and O. J. Aarnes (2021), NORA3: A nonhydrostatic high-resolution hindcast of the North Sea, the Norwegian Sea and the Barents Sea, *JAMC*, 60(10), 1443–1464, doi:10.1175/JAMC-D-21-0029.1. 1, 1.1.4, 2.2
- Hahmann, A. N., T. Sīle, B. Witha, N. N. Davis, M. Dörrenkämper, Y. Ezber, E. García-Bustamante, J. F. González-Rouco, J. Fidel, J. Navarro, B. T. Olsen, and S. Söderberg (2020), The making of the new European wind atlas, Part 1: model sensitivity, *Geosci Model Dev*, 13(10), 5053–5078, doi:10.5194/gmd-2019-349. 1.1.4
- Hallerstig, M., L. Magnusson, E. W. Kolstad, and S. Mayer (2021), How grid-spacing and convection representation affected the wind speed forecasts of four polar lows, *Q J R Meteorol Soc*, 147(734), 150–165, doi:10.1002/qj.3911. 3
- Harstveit, K. (2005), Extreme value analysis of hindcast wind data from the maritime areas surrounding Norway, *Research Report 17*, The Norwegian Meteorological Institute, Oslo, Norway. 1.1.4
- Hasager, C. B., A. N. Hahmann, T. Ahsbahs, I. Karagali, T. Sile, M. Badger, and J. Mann (2020), Europe’s offshore winds assessed with synthetic aperture radar, ASCAT and WRF, *Wind Energ. Sci.*, 5(1), 375–390, doi:10.5194/wes-5-375-2020. 1.1.4
- Haug, O., and J. Guddal (1981), Hindcasting the wind and wave climate of Norwegian waters, *Tech. rep.*, The Norwegian Meteorological Institute, P.O. 43, Blindern, 0313 OSLO. 1.1.4
- Heikkilä, U., and A. Sorteberg (2012), Characteristics of autumn-winter extreme precipitation on the Norwegian coast identified by cluster analysis, *Clim. Dyn.*, 39, 929–939, doi:10.1007/s00382-011-1277-9. 1.1.2
- Hersbach, H., C. Peubey, A. Simmons, P. Berrisford, P. Poli, and D. Dee (2015), ERA-20CM: a twentieth-century atmospheric model ensemble, *Q J R Meteorol Soc*, 141(691), 2350–2375, doi:10.1002/qj.2528. 1
- Hersbach, H., B. Bell, P. Berrisford, S. Hirahara, A. Horányi, J. Muñoz-Sabater, J. Nicolas, C. Peubey, R. Radu, D. Schepers, A. Simmons, C. Soci, S. Abdalla, X. Abellan, G. Balsamo, P. Bechtold, G. Biavati, J. Bidlot, M. Bonavita, G. D. Chiara, P. Dahlgren, D. Dee, M. Diamantakis, R. Dragani, J. Flemming, R. Forbes, M. Fuentes, A. Geer, L. Haimberger, S. Healy, R. J. Hogan, E. Hólm, M. Janisková, S. Keeley, P. Laloyaux, P. Lopez, C. Lupu, G. Radnoti, P. de Rosnay, I. Rozum, F. Vamborg, S. Villaume, and J.-N. Thépaut (2020), The ERA5 global reanalysis, *Q J R Meteorol Soc*, 146(730), 1999–2049, doi:10.1002/qj.3803. 1, 1, 1.1.4, 3, A.4
- Hodges, K. I., R. W. Lee, and L. Bengtsson (2011), A comparison of extratropical cyclones in recent reanalyses ERA-Interim, NASA MERRA, NCEP CFSR, and JRA-25, *J Climate*, 24(18), 4888–4906, doi:10.1175/2011JCLI4097.1. 1.1.2
- Holthuijsen, L. H., M. D. Powell, and J. D. Pietrzak (2012), Wind and waves in extreme hurricanes, *J Geophys Res: Oceans*, 117(C9), doi:10.1029/2012JC007983. 3

- Holton, J. R. (1992), *An introduction to dynamic meteorology*, 511 pp., Academic Press Limited, 24-28 Oval Road, London NW1 7DX. 1.1.1, 1.1.3
- Hortal, M. (2002), The development and testing of a new two-time-level semi-Lagrangian scheme (SETTLS) in the ECMWF forecast model, *Q J R Meteorol Soc*, 128(583), 1671–1687, doi:10.1002/qj.200212858314. 2.1.2, A.3, A.3, A.3
- Hsu, S. A., E. A. Meindl, and D. B. Gilhousen (1994), Determining the power-law wind-profile exponent under near-neutral stability conditions at sea, *J Appl Meteor and Climatol*, 33(6), 757–765, doi:https://doi.org/drfdmxdx. A.5
- Inness, A., F. Baier, A. Benedetti, I. Bouarar, S. Chabrillat, H. Clark, C. Clerbaux, P. Coheur, R. J. Engelen, Q. Errera, J. Flemming, M. George, C. Granier, J. Hadji-Lazaro, V. Huijnen, D. Hurtmans, L. Jones, J. W. Kaiser, J. Kapsomenakis, K. Lefever, J. L. ao, M. Razinger, A. Richter, M. G. Schultz, A. J. Simmons, M. Suttie, O. Stein, J.-N. Thépaut, V. Thouret, M. Vrekoussis, and C. Zerefos (2013), The MACC reanalysis: an 8-year data set of atmospheric composition, *Atmospheric Chemistry and Physics*, 13(8), 4073–4109, doi:10.5194/acp-13-4073-2013. 1
- Inness, A., M. Ades, A. Agustí-Panareda, J. Barré, A. Benedictow, A.-M. Blechschmidt, J. J. Dominguez, R. Engelen, H. Eskes, J. Flemming, V. Huijnen, L. Jones, Z. Kipling, S. Massart, M. Parrington, V.-H. Peuch, M. Razinger, S. Remy, M. Schulz, and M. Suttie (2019), The CAMS reanalysis of atmospheric composition, *Atmospheric Chemistry and Physics*, 19(6), 3515–3556, doi:10.5194/acp-19-3515-2019. 1
- IPCC-AR5, C. W. T., R. K. Pachauri, and L. A. M. (eds.) (2014), IPCC, 2014: Climate change 2014: Synthesis report. Contribution of working groups I, II and III to the fifth assessment report of the intergovernmental panel on climate change, *Tech. rep.*, IPCC, Geneva, Switzerland. 1.1.2, 3
- Jackson, P. L., and D. G. Steyn (1994), Gap winds in a fjord. Part II: Hydraulic analog, *Mon Wea Rev*, 122(12), 2666–2676. 1.1.3
- Janssen, P. (2004), *The interaction of ocean waves and wind*, 300 pp., Cambridge University Press, Cambridge, UK. 2.3, 3
- Jasak, H., A. Jemcov, Z. Tukovic, et al. (2007), OpenFOAM: A C++ library for complex physics simulations, in *International workshop on coupled methods in numerical dynamics*, vol. 1000, pp. 1–20, IUC Dubrovnik Croatia. 2.3
- Kalnay, E. (2003a), *Handbook of weather, climate and water: Dynamics, Climate, Physical Meteorology, Weather system and Measurements*, Wiley-Interscience. 2.1
- Kalnay, E. (2003b), *Atmospheric Modeling, Data Assimilation and Predictability*, 341 pp., Cambridge University Press. 2.3
- Kalnay, E., M. Kanamitsu, R. Kistler, W. Collins, D. Deaven, L. Gandin, M. Iredell, S. Saha, G. White, J. Woollen, et al. (1996), The NCEP/NCAR 40-year reanalysis project, *Bull Am Meteor Soc*, 77(3), 437–472, doi:https://doi.org/fg6rf9. 1

- Khairoutdinov, M., and Y. Kogan (2000), A new cloud physics parameterization in a large-eddy simulation model of marine stratocumulus, *Mon Wea Rev*, 128(1), 229–243, doi:<https://doi.org/d6p75n>. A.4
- Kobayashi, S., Y. Ota, Y. Harada, A. Ebata, M. Moriya, H. Onoda, K. Onogi, H. Kamahori, et al. (2015), The jra-55 reanalysis: General specifications and basic characteristics, *J Meteorol Soc Jpn*, 93(1), 5–48, doi:10.2151/jmsj.2015-001. 1
- Køltzow, M., H. Schyberg, E. Støylen, and X. Yang (2022), Value of the Copernicus Arctic Regional ReAnalysis (CARRA) in representing near-surface temperature and wind speed in the north east European Arctic, *Accepted for publication in Polar Res.* 1.1.4, 2.3
- Komen, G. J., L. Cavaleri, M. Donelan, K. Hasselmann, S. Hasselmann, and P. A. E. M. Janssen (1994), *Dynamics and Modelling of Ocean Waves*, 532 pp., Cambridge University Press, Cambridge. 1.1.4, 2.1.3, 3, 3
- Kovats, R. S., R. Valentini, L. M. Bouwer, E. Georgopoulou, D. Jacob, E. Martin, M. Rounsevell, and J.-F. Soussana (2014), *Contribution of working group II to the Fifth Assessment Report of the Intergovernmental Panel on Climate Change. Europe. In Climate Change 2014: Impacts, adaptation, and vulnerability. Part B: Regional aspects*, 1267–1326 pp., Cambridge University Press, Cambridge, United Kingdom and New York, NY, USA. 1.1.1, 1.1.2
- Kuo, H. L. (1965), On the formation and intensification of tropical cyclone through latent heat release by cumulus convection, *J Atmos Sci*, 22(1), 40–63, doi:<https://doi.org/fkqrct>. 2.1.1
- Kuo, H. L. (1974), Further studies of the parameterization of the influence of cumulus convection on large-scale flow, *J Atmos Sci*, 31(5), 1232–1240, doi:<https://doi.org/fv9v29>. 2.1.1
- Laloyaux, P., E. de Boissesson, M. A. Balmaseda, J.-R. Bidlot, S. Broennimann, R. Buizza, P. Dalhgren, D. P. Dee, L. Haimberger, H. Hersbach, Y. Kosaka, M. Martin, P. Poli, N. Rayner, E. Rustemeier, and D. Schepers (2018), CERA-20C: a coupled reanalysis of the twentieth century, *Journal of Advances in Modeling Earth Systems*, 10(5), 1172–1195, doi:10.1029/2018MS001273. 1
- Laprise, R. (1992), The Euler equations of motion with hydrostatic pressure as an independent variable, *Mon Wea Rev*, 120(1), 197–207, doi:<https://doi.org/bh92k2>. 2.1.1, 2.1.2, A.3, A.3
- Lascaux, F., E. Richard, and J.-P. Pinty (2006), Numerical simulations of three different MAP IOPs and the associated microphysical processes, *Q J R Meteorol Soc*, 132(619), 1907–1926, doi:10.1256/qj.05.197. A.4
- Lenderink, G., and A. A. Holtslag (2004), An updated length-scale formulation for turbulent mixing in clear and cloudy boundary layers, *Q J R Meteorol Soc*, 130(604), 3405–3427, doi:10.1256/qj.03.117. 2.1.2, A.4

- Li, D., J. Staneva, J. R. Bidlot, S. Grayek, Y. Zhu, and B. Yin (2021), Improving regional model skills during typhoon events: A case study for super Typhoon Lingling over the northwest Pacific Ocean, *Frontiers in Marine Science*, 8, 42, doi:10.3389/fmars.2021.613913. 3
- Lock, S.-J., N. Wood, and H. Weller (2014), Numerical analyses of Runge-Kutta implicit-explicit schemes for horizontally explicit, vertically implicit solutions of atmospheric models, *Q J R Meteorol Soc*, 140(682), 1654–1669, doi:10.1002/qj.2246. 2.3
- Manaster, A., L. Ricciardulli, and T. Meissner (2019), Validation of High Ocean Surface Winds from Satellites Using Oil Platform Anemometers, *J Atmos Ocean Tech*, 36(5), 803–818, doi:10.1175/JTECH-D-18-0116.1. A.5, A.5
- Maronga, B., S. Banzhaf, C. Burmeister, T. Esch, R. Forkel, D. Fröhlich, V. Fuka, K. F. Gehrke, J. Geletlč, S. Giersch, T. Gronemeier, and co authors (2020), Overview of the PALM model system 6.0, *Geosci Model Dev*, 13(3), 1335–1372, doi:10.5194/gmd-13-1335-2020. 2.3
- Masson, V., P. L. Moigne, E. Martin, S. Faroux, A. Alias, R. Alkama, S. Belamari, A. Barbu, A. Boone, F. Bouyssel, P. Brousseau, E. Brun, J. C. Calvet, D. Carrer, B. Decharme, C. Delire, S. Donier, K. Essaouini, A. L. Gibelin, H. Giordani, F. Habets, M. Jidane, G. Kerdraon, E. Kourzeneva, M. Lafaysse, S. Lafont, C. L. Brossier, A. Lemonsu, J. F. Mahfouf, P. Marguinaud, M. Mokhtari, S. Morin, G. Pigeon, R. Salgado, Y. Seity, F. Taillefer, G. Tanguay, P. Tulet, B. Vincendon, V. Vionnet, and A. Voldoire (2013), The SURFEXv7.2 land and ocean surface platform for coupled or offline simulation of earth surface variables and fluxes, *Geosci Model Dev*, 6(4), 929–960, doi:10.5194/gmd-6-929-2013. 3, A.4
- McDonald, A., and J. E. Haugen (1992), A two time-level, three-dimensional, semi-Lagrangian, semi-implicit, limited-area gridpoint model of the primitive equations., *Mon Wea Rev*, 120(11), 2603–2621. A.3
- McDonald, A., and J. E. Haugen (1993), A two time-level, three-dimensional, semi-Lagrangian, semi-implicit, limited-area gridpoint model of the primitive equations. Part II: Extension to hybrid vertical coordinates, *Mon Wea Rev*, 121(7), 2077–2087. 2.1.1, A.2, A.3
- Mesinger, F., and A. Arakawa (1976), Numerical Methods Used in Atmospheric Models, *GARP Publications Series 17*, World Meteorological Organization. 2.1.1
- Mlawer, E. J., S. J. Taubman, P. D. Brown, M. J. Iacono, and S. A. Clough (1997), Radiative transfer for inhomogeneous atmospheres: RRTM, a validated correlated-k model for the longwave, *J Geophys Res*, 102(D14), 16,663–16,682. A.4
- Müller, M., Y. Batrak, J. Kristiansen, M. A. Ø. Kølitzow, G. Noer, and A. Korosov (2017a), Characteristics of a convective-scale weather forecasting system for the European Arctic., *Mon Wea Rev*, 145(12), 4771–4787, doi:10.1175/MWR-D-17-0194. 1. 1.1.4

- Müller, M., M. Homleid, K. I. Ivarsson, M. A. Ø. Køltzow, M. Lindskog, K. H. Midtbø, U. Andrae, T. Aspeli, L. Berggren, D. Bjørge, P. Dahlgren, J. Kristiansen, R. Randriamampianina, M. Ridal, and O. Vignes (2017b), AROME-MetCoOp: A Nordic convective-scale operational weather prediction model, *Wea Forecasting*, 32(2), 609–627, doi:10.1175/WAF-D-16-0099.1. 1.1.6, 2.1.2, A.4
- Neggens, R. A., M. Köhler, and A. C. M. Beljaars (2009), A dual mass flux framework for boundary layer convection. Part I: Transport, *J Atmos Sci*, 66(6), 1465–1487, doi:10.1175/2008JAS2635.1. 2.1.2, A.4
- Noilhan, J., and S. Planton (1989), A simple parameterization of land surface processes for meteorological models, *Mon Wea Rev*, 117(3), 536–549. 2.1.1
- Norman, H. (2021), ACCORD consortium aims to help citizens in Europe and North Africa mitigate the impact of weather and climate related threats, *Meteorological Technology International*. 2.1, A.7
- NORSOK (2007), NORSOK standard: Action and action effects, N-003, *Tech. rep.*, Norwegian Technology Standards Institution, Standard Norge, Postboks 242, 1326 Lysaker. A.5
- Onogi, K., H. Koide, M. Sakamoto, S. Kobayashi, J. Tsutsui, H. Hatsushika, T. Matsumoto, N. Yamazaki, H. Kamahori, K. Takahashi, K. Kato, R. Oyama, T. Ose, S. Kadokura, and K. Wada (2005), The JRA-25 reanalysis, *Q J R Meteorol Soc*, 131(613), 3259–3268, doi:10.1256/qj.05.88. 1
- Panofsky, H. (1973), Tower micrometeorology, *Technical Report*, American Meteorological Society. A.5
- Parish, T. R. (1982), Barrier winds along the Sierra Nevada mountains, *JAM*, 21(7), 925–930. 1.1.3
- Parish, T. R., and J. J. Cassano (2003), The role of katabatic winds on the Antarctic surface wind regime, *MWR*, 131(2), 317–333, doi:https://doi.org/fmw39t. 1.1.3
- Peixoto, J. P., and A. H. Oort (1992), *Physics of climate*, 520pp pp., American Institute of Physics, 335 E. 45th Street, New York, NY 10017-3483. 1.1.2
- Pinty, J.-P., and P. Jabouille (1998), A mixed-phase cloud parameterization for use in a mesoscale non-hydrostatic model: simulation of a squall line and of orographic precipitation, *Preprints of Conf. On Cloud Physics*, Everett, WA, *Amer. Meteor. Soc.*, pp. 217–220. A.4
- Poli, P., H. Hersbach, D. P. Dee, P. Berrisford, A. J. Simmons, F. Vitart, P. Laloyaux, D. G. H. Tan, C. Peubey, J.-N. Thépaut, Y. Trémolet, E. V. Bonavita, L. Isaksen, and M. Fisher (2016), ERA-20C: an atmospheric reanalysis of the twentieth century, *J Climate*, 29(11), 4083–4097, doi:10.1175/JCLI-D-15-0556.1. 1
- Powell, M., P. Vickery, and T. Reinhold (2003), Reduced drag coefficient for high wind speeds in tropical cyclones, *Nature*, 422, 279–283, doi:10.1038/nature01481. 3

- Rabier, F., H. Järvinen, E. Klinker, J.-F. Mahfouf, and A. Simmons (2000), The ECMWF operational implementation of four-dimensional variational assimilation. I: Experimental results with simplified physics, *Q J R Meteorol Soc*, 126(564), 1143–1170, doi:10.1002/qj.49712656415. 2.3
- Radnoti, G. (1995), Comments on a spectral limited-area formulation with time dependent boundary conditions applied to the shallow water equations, *Mon Wea Rev*, 123(10), 3122–3123, doi:https://doi.org/b83s7b. 2.1.2, A.3
- Reeve, M. A., and E. W. Kolstad (2011), The spitsbergen south cape tip jet, *Q J R Meteorol Soc*, 137(660), 1739–1748, doi:10.1002/qj.876. 1.1.3
- Reistad, M., Ø. Breivik, H. Haakenstad, O. J. Aarnes, B. R. Furevik, and J.-R. Bidlot (2011), A high-resolution hindcast of wind and waves for the North Sea, the Norwegian Sea, and the Barents Sea, *J Geophys Res*, 116(C5), 18 pp, C05,019, doi:10/fmnr2m. 1.1.4, 3
- Richardson, L. F. (1922), *Weather Prediction by Numerical Process*, 236 pp., Cambridge University Press, reprinted Dover, 1965, Cambridge. A.3
- Rienecker, M. M., M. J. Suarez, R. Gelaro, R. Todling, J. Bacmeister, E. Liu, M. G. Bosilovich, S. D. Schubert, L. Takacs, G.-K. Kim, et al. (2011), MERRA: NASA's Modern-Era Retrospective Analysis for Research and Applications, *J Climate*, 24(14), 3624–2648, doi:10.1175/JCLI-D-11-00015.1. 1
- Robert, A. (1981), A stable numerical integration scheme for the primitive meteorological equations, *Atmos. Ocean*, 19, 35–46. A.3
- Robert, A. (1982), A seim-Lagrangian and semi-implicit numerical integration scheme for the primitive meteorological equations, *J. Meteor. Soc. Japan*, 60(1), 319–325. A.3
- Rontu, L., K. Sattler, and R. Sigg (2002), Parametrization of subgrid-scale orography effects in HIRLAM, *Technical Report 56*, <http://hirlam.org>. 2.1.1
- Saha, S., S. Moorthi, H.-L. Pan, X. Wu, J. Wang, S. Nadiga, P. Tripp, R. Kistler, J. Woollen, D. Behringer, et al. (2010), The NCEP climate forecast system reanalysis, *Bull Am Meteor Soc*, 91(8), 1015–1057, doi:10.1175/2010Bams3001.1. 1
- Saha, S., S. Moorthi, X. Wu, J. Wang, S. Nadiga, P. Tripp, D. Behringer, Y.-T. Hou, H.-Y. Chuang, M. Iredell, et al. (2014), The NCEP climate forecast system version 2, *J Climate*, 27(6), 2185–2208, doi:10.1175/JCLI-D-12-00823.1. 1
- Sandvik, A. D., and K. Harstveit (2005), Study of a down slope windstorm over southern Norway, Rjukan, 16. January 2000, *met.no report 18*, The Norwegian Meteorological Institute, P.O. Box 43, Blindern, NO-0313 OSLO. 1.1.3
- Sass, B. H., L. Rontu, and P. Räisänen (1994), HIRLAM-2 Radiation scheme: Documentation and tests, *Technical report 16*, SMHI, S-60176 Norrköping, Sweden. 2.1.1

- Schepers, D., E. de Boissésou, R. Eresmaa, C. Lupu, and P. de Rosnay (2018), CERA-SAT: A coupled satellite-era reanalysis, *ECMWF Newsletter 155*, European Center for Medium-Range Weather Forecasts. 1
- Seity, Y., P. Brousseau, S. Malardel, G. Hello, P. Benard, F. Bouttier, C. Lac, and V. Masson (2011), The AROME-France Convective-Scale Operational Model, *Mon Wea Rev*, *139*(3), 976–991, doi:10.1175/2010MWR3425.1. 1.1.4, 2.1, 3
- Sharman, R. D., J. D. Doyle, and M. A. Shapiro (2012), An investigation of a commercial aircraft encounter with severe clear-air turbulence over western Greenland, *J Appl Meteor and Climatol*, *51*(1), 42–53, doi:10.1175/JAMC-D-11-044.1. 1.1.3
- Siebesma, A. P., C. S. Bretherton, A. Brown, A. Chlond, J. Cuxart, P. G. Dunkerke, H. Jiang, M. Khairoutdinov, D. Lewellen, C.-H. Moeng, E. Sanchez, B. Stevens, and D. Stevens (2003), A large eddy simulation intercomparison study of shallow cumulus convection, *J Atmos Sci*, *60*(10), 1201–1219, doi:https://doi.org/dkdbqx. A.4
- Siebesma, A. P., P. M. Soares, and J. Teixeira (2007), A combined eddy-diffusivity mass-flux approach for the convective boundary layer, *J Atmos Sci*, *64*(4), 1230–1248, doi:10.1175/JAS3888.1. 2.1.2, A.4
- Simmons, A. J., and D. M. Burridge (1981), An energy and angular-momentum conserving vertical finite-difference scheme and hybrid vertical coordinates, *Mon Wea Rev*, *109*(4), 758–766, doi:10/ddzqkq. 2.1.1
- Smith, D. M., R. Eade, M. B. Andrews, H. Ayres, A. Clark, S. Chripko, C. Deser, N. J. Dunstone, J. García-Serrano, G. Gastineau, L. S. Graff, S. C. Hardiman, B. He, L. Hermanson, T. Jung, J. Knight, X. Levine, G. Magnusdottir, E. Manzini, D. Matei, M. Mori, R. Msadek, P. Ortega, Y. Peings, A. A. Scaife, J. A. Screen, M. Seabrook, T. Semmler, M. Sigmond, J. Streffing, L. Sun, and A. Walsh (2022), Robust but weak winter atmospheric circulation response to future Arctic sea ice loss, *Nature Communications*, *13*(727), 1–15, doi:10.1038/s41467-022-28283-y. 1.1.1
- Smith, R. B. (1989b), Mountain-induced stagnation points in hydrostatic flow, *TEL*, *41*(3), 270–274, doi:10.3402/tellusa.v41i3.11839. 1.1.3
- Soares, P., P. Miranda, A. Siebesma, and J. Teixeira (2004), An eddy-diffusivity mass-flux parameterization for dry and shallow cumulus convection, *Q J R Meteorol Soc*, *130*(604), 3365–3383, doi:10.1256/qj.03.223. 2.1.2, A.4
- Solbrekke, I. M., A. Sorteberg, and H. Haakenstad (2021), The 3 km Norwegian reanalysis (NORA3) - a validation of offshore wind resources in the North Sea and the Norwegian Sea, *Wind Energ. Sci.*, *6*(6), 1501–1519, doi:10.5194/wes-6-1501-2021. 1, 3
- Stull, R. B. (1988), *An introduction to boundary layer meteorology*, 666 pp., Kluwer, New York. 1.1.3, A.3, A.5, A.5
- Sundqvist, H. (1993), Inclusion of ice phase of hydrometeors in cloud parameterization for mesoscale and largescale models, *Contr. Atm. Phys.*, *66*(1), 137–147. 2.1.1

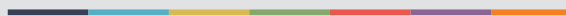


- Tanguay, M., A. Robert, and R. Laprise (1990), A semi-implicit semi-Lagrangian fully compressible regional forecast model, *Mon Wea Rev*, *118*, 1970–1980. A.3
- Tarback, E. J., and F. K. Lutgens (1990), *Earth science*, 659 pp., Macmillan Publishing Company, 866 Third Avenue, New York, New York 10022. 1.1.1
- Termonia, P., C. Fischer, E. Bazile, F. Bouyssel, R. Brožková, P. Bénard, B. Bochenek, D. Degrauwe, M. Derková, R. E. Khatib, R. Hamdi, J. Mašek, P. Pottier, N. Pristov, Y. Seity, P. Smolíková, O. Španiel, M. Tudor, Y. Wang, C. Wittmann, and A. Joly (2018), The ALADIN System and its canonical model configurations AROME CY41T1 and ALARO CY40T1, *Geosci Model Dev*, *11*(1), 257–281, doi: 10.5194/gmd-11-257-2018. 2.1.2, 2.1.2, A.3, A.3
- Thomas, E. E., M. Müller, P. Bohlinger, Y. Batrak, and N. Szapiro (2021), A Kilometer-Scale Coupled AtmosphereWave Forecasting System for the European Arctic, *Wea Forecasting*, *36*(6), 2087–2099, doi:10.1175/WAF-D-21-0065.1. 2.3
- Troen, I., and E. L. Petersen (1989), European wind atlas, *Tech. rep.*, Risø National Laboratory, Roskilde, Denmark. 1.1.4
- Uden, P., L. Rontu, H. Jarvinen, P. Lynch, J. Calvo, G. Cats, J. Cuxart, K. Eerola, C. Fortelius, J. A. Garcia-Moya, C. Jones, G. Lenderink, A. Mc-Donald, R. McGrath, B. Navascues, N. W. Nielsen, V. Odegaard, E. Rodriguez, M. Rummukainen, R. Room, K. Sattler, H. Savijarvi, B. H. Sass, B. W. Schreur, H. The, and S. Tijm (2002), Hirlam-5 scientific documentation, *Tech. Rep. GKSS 97/E/46*, SMHI, SMHI, SE-601 76 Norrköping, Sweden. 1.1.4, 2.1, 2.1.1, 3, A.2
- Uppala, S. M., P. W. Kållberg, A. J. Simmons, U. Andrae, V. D. C. Bechtold, M. Fiorino, J. K. Gibson, J. Haseler, A. Hernandez, G. A. Kelly, X. Li, K. Onogi, et al. (2005), The ERA-40 Re-analysis, *Q J R Meteorol Soc*, *131*(612), 2961–3012, doi: 10.1256/qj.04.176. 1, 1.1.4, 3
- Valkonen, T., P. Stoll, Y. Batrak, M. Køltzow, T. M. Schneider, E. E. Stigter, O. B. Aashamar, E. Støylen, and M. O. Jonassen (2020), Evaluation of a sub-kilometre NWP system in and Arctic fjord-valley system in winter, *Tellus*, *72*(1), 1–21, doi: 10.1080/16000870.2020.1838181. 2.3
- van Meijgaard, E., L. H. van Ulft, G. Lenderink, S. D. Roode, E. L. Wipfler, R. Boers, and R. M. A. van Timmermans (2012), Refinement and application of a regional atmospheric model for climate scenario calculations of Western Europe, *KVR Research Rep. 054/12*, Koninklijk Nederlands Meteorologisch Instituut. 2.1.2, A.4
- Vihma, T., R. Pirazzini, I. Fer, I. A. Renfrew, J. Sedlar, M. Tjernström, C. Lüpkes, T. Nygård, D. Notz, J. Weiss, D. Marsan, B. Cheng, G. Birnbaum, S. Gerland, D. Chechin, and J. C. Gascard (2014), Advances in understanding and parameterization of small-scale physical processes in the marine Arctic climate system: a review, *Atmos. Chem. Phys.*, *14*(17), 9403–9450, doi:10.5194/acp-14-9403-2014. 1.1.3
- Wamdi-Group, T. (1988), The WAM model—a third generation ocean wave prediction model, *J Phys Oceanogr*, *18*(12), 1775–1810, doi:https://doi.org/bhs3rr. 1.1.4, 2.1.3, 3

- Wang, X., Z. Zhang, X. Wang, T. Vihma, M. Zhou, L. Yu, P. Uotila, and D. V. Sein (2021), Impacts of strong wind events on sea ice and water mass properties in Antarctic coastal polynyas, *Climate Dynamics*, 57, 3505–3528, doi:10.1007/s00382-021-05878-7. 1.1.3
- WASA-group, T. (1998), Changing waves and storms in the northeast Atlantic?, *Bull Am Meteor Soc*, 79(5), 741–760. 1.1.4
- Wyser, K., L. Rontu, and H. Savijärvi (1999), Introducing the effective radius into a fast radiation scheme of a mesoscale model, *Contr. Atm. Phys*, 72(3), 205–218. 2.1.1
- Yang, X. (2005), Background blending using an incremental spatial filter., *Hirlam Newsletter*, 49, 3–11. 2.1.1
- Yang, X., K. P. Nielsen, B. Amstrup, C. Peralta, J. Høyer, P. N. Englyst, H. Schyberg, M. Homleid, M. Køltzow, R. Randriamampianina, P. Dahlgren, E. Støylen, T. Valkonen, B. Palmason, S. Thorsteinsson, J. Bojarova, H. Körnich, M. Lindskog, J. Box, and K. Mankoff (2020), C3S Arctic regional reanalysis - Full system documentation, *Technical documentation*, Copernicus Climate Change Service, ECMWF - Shinfield Park, Reading RG2 9AX, UK. 1.1.4, 2.3
- Zhu, Y., and R. E. Newell (1994), Atmospheric rivers and bombs, *Geophys Res Lett*, 21(18), 1999–2002, doi:10.1029/94GL01710. 1.1.2
- Zuo, H., M. A. Balmaseda, K. Mogensen, and S. Tietsche (2018), OCEAN5: The ECMWF ocean reanalysis system and its real-time analysis component, *Technical documentation*, European Centre for Medium-Range Weather Forecasts. 1
- Zweers, N. C., V. K. Makin, J. W. de Vries, and G. Burgers (2010), A sea drag relation for hurricane wind speeds, *Geophys Res Lett*, 37(21), L21,811, doi:10.1029/2010GL045002. 3



Graphic design: Communication Division, UIB / Print: Skjipes Kommunikasjon AS



[uib.no](http://uib.no)

ISBN: 9788230856239 (print)  
9788230852378 (PDF)